

# RESIDUAL STRESS CHARACTERIZATION IN A SINGLE FIBRE COMPOSITE SPECIMEN BY USING FBG SENSOR AND THE OLCR TECHNIQUE

THÈSE N° 3533 (2006)

PRÉSENTÉE LE 1<sup>ER</sup> JUIN 2006

À LA FACULTÉ SCIENCES ET TECHNIQUES DE L'INGÉNIEUR  
Laboratoire de mécanique et d'analyse de fiabilité  
SECTION DE GÉNIE MÉCANIQUE

ÉCOLE POLYTECHNIQUE FÉDÉRALE DE LAUSANNE

POUR L'OBTENTION DU GRADE DE DOCTEUR ÈS SCIENCES

PAR

**Fabiano COLPO**

Laurea in Fisica, Università degli studi di Milano, Italie  
et de nationalité italienne

acceptée sur proposition du jury:

Prof. P. Xirouchakis, président du jury  
Prof. I. Botsis, directeur de thèse  
Prof. P. Ermanni, rapporteur  
Prof. R.P. Salathé, rapporteur  
Prof. A. Vautrin, rapporteur



ÉCOLE POLYTECHNIQUE  
FÉDÉRALE DE LAUSANNE

Lausanne, EPFL

2006



*Lausanne, March 2006*

*Ai miei genitori, Renata e Gabriele  
e a mia moglie Rita.  
Con immenso amore,  
Fabiano*



# Abstract

The purpose of this thesis is to characterize internal strains in polymeric materials due to consolidation. In view of this, optical Fiber Bragg Grating sensors are an excellent non-destructive tool for internal strain characterization and damage detection in composite materials and structures. Fiber Bragg Gratings (FBG), have become increasingly used in engineering applications because of their inherent advantages with respect to traditional sensors. They can provide an important tool in experimental mechanics to perform key experiments that are difficult or impossible with other standard techniques. In this respect, they are ideally suited as strain measuring devices in composites, where they can be embedded non-invasively during fabrication. In view of this, the main goal of this thesis is the development of an experimental methodology to characterize the residual stresses that are generally present in many materials and is a complex problem to solve in micro-mechanics. The work is presented in three interrelated parts.

Long-gauge-FBGs (Bragg grating of  $\simeq 24$  mm) are introduced in cylindrical specimens of epoxy. In this configuration the fiber is simultaneously a reinforcement and a sensor in a single fiber composite. Because the epoxy matrix shrinks during the polymerization process, the optical sensor undergoes substantial non-uniform strain along the fiber. The response of the FBG to a non-uniform strain distribution is investigated by using an Optical Low-Coherence Reflectometry (OLCR) based technique which allows a direct reconstruction of the optical period along the grating without any a priori assumption about the strain field. A comparison with the most common reconstruction inverse technique T-Matrix is also proposed, showing that it generally introduces greater errors without ensuring the uniqueness of the solution. The OLCR permits in fact the direct measurement of the axial evolution of the residual strain along the core of the reinforcing fiber, thus providing important information on the internal state of stress of the specimen at a given stage of its preparation and, later on, during its service life. In addition, the measured strain distribution evolves along the fiber direction following a fourth-order function, which clearly presents a plateau over a 20 mm range at the center of the specimen. In particular, the maximum strain level reached after the matrix solidification is  $-2000 \mu\epsilon$  which increases up to  $-6000 \mu\epsilon$  at the end of the post-curing process of the resin. This value is consistent with the volume reduction of the free resin provided by the producer and equal to 2 %. This strain corresponds to -450 MPa axial compressive stress on the embedded reinforcing fiber.

The implementation of FBG sensors to study the changes in the stress field when a crack is present in the sample is addressed next. Bragg wavelength distributions have been measured as a function of the depth of machined circular cracks in the radial direction of the cylinder. Three different crack depths (namely 7.5 mm, 11 mm and 12 mm) have been machined in the central section of the specimen. First, these measurements give an indication about the zone of influence of the reinforcing fiber on the residual stresses and, secondly, they permit the characterization of the effect of a mechanically induced crack on the initial residual stress state. In particular, only the stress relaxation due to the introduction of the deepest transversal crack significantly affects the FBG response with a related wavelength variation of 3 nm. These data are used as input to deduce the radial evolution of the stress field by adapting and improving the Crack Compliance (C.C.M) inverse Method to retrieve the stress field within a composite starting from a measurement of strain. A rigorous analytical approach to predict the residual stress field is described and verified numerically and experimentally. A very good agreement is found between experimental and numerical values, thus proving the reliability of the experimental approach.

As last topic in this work, the response of a long FBG to the transverse crack propagation is monitored experimentally by using the OLCR and modeled numerically. Firstly, a Compact-Tension specimen submitted to a cyclic fatigue test is chosen with the FBG glued on its back-face and normal to the crack direction. A simple analytical model predict the FBG response as the crack advances. Secondly, long- FBG is embedded in a Compact-Tension specimen of the same dimensions. In particular when the natural crack overpasses the fiber, the grating can be used to measure the bridging forces between fracture surfaces and/or to measure the relative opening of the crack. Reconstruction of the FBG signal with T-matrix indicate problems associated to stress distributions due to highly non-uniform strain field. In this way, the FBG becomes the excellent candidate to study a number of interesting problems in the field of the fracture mechanics applications.

**Keywords:** Residual stresses, FBG, OLCR Technique, Crack Compliance Method, damage detection

# Version abrégée

Le but de cette thèse est la caractérisation des contraintes internes dans les matériaux composites induites pendant le durcissement. Les fibres optiques intégrant des réseaux de Bragg sont des excellents outils non-destructifs pour la caractérisation des contraintes internes et la détection d'endommagements dans les matériaux composites ou les structures. Les réseaux de Bragg (FBG), sont devenus de plus en plus utilisés dans des applications de haute technologie en raison de leurs avantages intrinsèques par rapport aux senseurs traditionnels. Ils peuvent fournir un support important dans le domaine de la mécanique expérimentale pour réaliser des expériences qui sont difficiles, voire impossibles, à mettre en œuvre avec d'autres techniques standards. A ce sujet, ils conviennent particulièrement comme dispositifs de mesure dans le cas de contraintes dans les matériaux composites, où ils peuvent être intégrés de façon non-intrusive pendant le processus de fabrication. Pour cette raison, l'un des buts principaux de cette thèse est le développement d'un procédé expérimental fiable, afin de caractériser les contraintes résiduelles qui sont généralement présentes dans beaucoup de problèmes complexes de la micromécanique. Le travail est présenté en trois parties principales.

Des longs FBGs (réseaux de 24 mm de longueur) sont introduits dans des spécimens cylindriques d'époxyde. Dans cette configuration la fibre est simultanément renfort et senseur dans un composite dit Single Fiber. Puisque la matrice époxyde se rétrécit pendant le procédé de polymérisation, le senseur optique subit une substantielle compression non-uniforme le long de la fibre. La réponse du FBG à une distribution non-uniforme de contrainte est étudiée en utilisant une technique basée sur la réflectométrie optique à basse cohérence (OLCR) qui permet une reconstruction directe de la période optique le long du réseau sans aucune hypothèse à priori sur le champ de déformation. Une comparaison avec la technique de reconstruction T-Matrix est aussi proposée. On montre qu'elle introduit des erreurs plus grands sans assurer l'unicité de la solution. Cela permet une mesure directe de la distribution de déformation tout le long du réseau, et donc fournit des informations très importantes sur l'état des contraintes internes du spécimen à chaque étape de sa préparation et, plus tard, pendant toute sa durée de vie. D'ailleurs la distribution de déformation évolue selon une fonction du quatrième ordre qui présente un plateau de 20 mm d'amplitude au centre du spécimen. En particulier, après durcissement, la valeur de déformation est  $-2000 \mu\epsilon$  qui augmente jusqu'à  $-6000 \mu\epsilon$  à la fin de la post-cuisson. La valeur mesurée correspond à la variation volumique de la résine fournie par le producteur qui est égale à 2 %. Cette valeur correspond à des contraintes compressives

de -450 MPa.

L'utilisation des senseurs de Bragg pour étudier les modifications du champ de contrainte lorsque des endommagements sont présents dans l'échantillon est ensuite présenté. Des distributions de longueur d'onde de Bragg ont été mesurées pour différentes profondeurs de fissures circulaires usinées radialement dans le cylindre. Trois différentes longueurs de fissure (7.5 mm, 11 mm and 12 mm) ont été introduites dans la section centrale du spécimen. Par rapport à l'état de contrainte initial, ces mesures donnent premièrement une indication au sujet de la zone d'influence de la fibre de renfort sur les contraintes résiduelles et, deuxièmement, elles permettent la caractérisation de l'effet d'une fissure introduite mécaniquement. En particulier les mesures indiquent que seulement la fissure la plus profonde influence considérablement la distribution de contraintes (3 nm de variation dans la longueur d'onde de Bragg). Par ailleurs ces mesures sont employées comme données de base dans la détermination de l'évolution radiale du champ de contrainte. Pour cela, on a adapté et amélioré la méthode inverse de la compliance (C.C.M), initialement utilisée pour retrouver le champ de contrainte dans un matériau composite à partir d'une mesure ponctuelle de déformation. Une approche analytique rigoureuse pour prédire le champ de contraintes résiduelles est exposée et ensuite vérifiée numériquement et expérimentellement.

Comme dernière expérience de travail, des réseaux de Bragg ont été utilisés pour détecter et prédire la longueur d'une fissure réelle qui se propage dans un spécimen. Un spécimen du type Compact-Tension soumis à un essai cyclique de fatigue est choisi dans ce cas avec le FBG collé sur la face extérieure perpendiculaire à la direction de propagation de la fissure. Un modèle analytique simple est utilisé pour évaluer la longueur de la fissure. Dans un deuxième cas d'étude, on utilise un réseau de Bragg à la fois comme renfort et comme senseur, après l'avoir incorporé dans un spécimen du type Compact Tension avec les mêmes dimensions et pré-fissuré. En particulier, lorsque la fissure dépasse la position de la fibre, le senseur peut être utilisé pour mesurer les forces pontantes entre les lèvres de la fissure. La reconstruction du signal du réseau avec T-Matrix montre des problèmes quand on est en présence de hauts gradients de déformation. A travers ces expériences, les FBGs montrent d'être d'excellents candidats pour l'étude de problèmes de grand intérêt dans le domaine de la mécanique de la rupture.

**Mots clés:** Contraintes résiduelles, FBG, technique OLCR, méthode de la compliance, détection d'endommagement



# Estratto

Lo scopo di questo lavoro di tesi é la caratterizzazione delle deformazioni interne in materiali a matrice polimerica a seguito del processo di polimerizzazione. A tal proposito, le fibre ottiche contenenti sensori di Bragg sono uno strumento eccellente e non distruttivo per la caratterizzazione delle deformazioni interne e la detezione di danneggiamento nel caso dei materiali compositi e delle strutture. I sensori ottici di Bragg (FBG) sono sempre piú usati in applicazioni ingegneristiche grazie ai loro intrinseci vantaggi rispetto ad altri sensori ritenuti oggi piú tradizionali. Gli FBGs sono infatti in grado di fornire un supporto importante nel caso della meccanica sperimentale, dove possono essere usati in esperimenti chiave che sono difficili o impossibili da realizzare con altre tecniche. In quest'ottica, essi sono particolarmente adatti per misurare le deformazioni nei materiali compositi, dove possono essere inglobati in maniera relativamente non invasiva durante il processo di fabbricazione. Tenuto conto di queste premesse, il risultato principale di questa tesi é lo sviluppo di una metodologia sperimentale per caratterizzare gli stress residui presenti in molti materiali e che rimane ancora un problema da risolvere nel caso della micromeccanica. Il seguente lavoro é sviluppato in tre parti interconnesse tra loro.

Reticoli di Bragg cosiddetti lunghi ( $\simeq 24$  mm) sono introdotti in provette cilindriche di materiale epossidico. In questa configurazione la fibra é simultaneamente rinforzo e sensore in un composito detto a fibra singola. Poiche l'eossidico si contrae durante il processo di polimerizzazione, il sensore ottico subisce una sostanziale deformazione non uniforme lungo la fibra. La risposta del reticolo a tale distribuzione non uniforme di deformazione é investigata usando una tecnica basata sull'interferometria ottica a bassa coerenza (OLCR) la quale permette una ricostruzione diretta del periodo ottico lungo il reticolo senza alcuna assunzione a priori riguardante il campo di deformazione. Un confronto con la piú comune tecnica di ricostruzione chiamata T-Matrix é anche proposta, mostrando che quest'ultima generalmente introduce un errore maggiore senza per altro garantire l'unicitá della soluzione trovata. La tecnica OLCR permette infatti la misura diretta dell'evoluzione assiale della deformazione residua lungo il cuore della fibra di rinforzo, fornendo in questo modo una informazione sullo stato di stress interno della provetta ad un dato momento della sua preparazione e, in seguito, durante il suo utilizzo. Inoltre, la distribuzione di deformazione misurata evolve lungo la direzione della fibra seguendo una funzione del quarto ordine, che presenta chiaramente un plateau su una regione di 20 mm al centro della provetta. In particolare, il massimo valore

di deformazione raggiunto dopo la solidificazione della matrice é  $-2000 \mu\epsilon$  che aumenta fino a  $-6000 \mu\epsilon$  alla fine del processo di post-trattamento termico. Tale valore é in accordo con la riduzione volumetrica della sola matrice epossidica fornita direttamente dal produttore ed uguale a 2 %. Questa deformazione corrisponde a  $-450 \text{ MPa}$  di stress compressivi sulla fibra di rinforzo.

L'implementazione di sensori di Bragg per studiare i cambiamenti nel campo di stress quando una frattura é presente nella provetta é l'argomento affrontato in seguito. Distribuzioni di lunghezze d'onda di Bragg sono state misurate in funzione della profonditá di fessure circolari intagliate meccanicamente in direzione radiale al cilindro. Tre differenti fessure (7.5 mm, 11mm e 12 mm) sono state realizzate al centro del cilindro. Inizialmente, tali misure hanno dato una indicazione per quanto riguarda l'influenza della fibra di rinforzo sul campo residuo di stress e, successivamente, hanno permesso di caratterizzare gli effetti dovuti all'introduzione di una fessura artificiale sullo stato iniziale di stress. In particolare, solo il rilassamento dovuto all'introduzione di una profonda fessura trasversale influenza in maniera significativa la risposta del reticolo di Bragg con una corrispondente variazione di lunghezza d'onda di 3 nm. Questi dati sono usati come input per dedurre l'evoluzione radiale del campo di stress adattando e migliorando il metodo inverso della Compliance (C.C.M.) per risalire al campo di stress all'interno di un composito partendo dalla misura di deformazione. Un approccio analitico rigoroso per predire il campo di stress residuo é altresí descritto e poi verificato per via numerica e sperimentale. Un accordo molto buono tra valori numerici e sperimentali é stato trovato, garantendo cosí l'affidabilitá dell'approccio sperimentale proposto.

Come ultimo argomento affrontato in questo lavoro, si é monitorata sperimentalmente attraverso la tecnica OLCR e in seguito modellata numericamente, la risposta di un reticolo di Bragg durante la propagazione di una frattura che si propaga trasversalmente al reticolo stesso. Per prima cosa, una provetta di tipo Compact Tension sottoposta a un ciclo di fatica é stata scelta, con il reticolo di Bragg incollato sulla faccia esterna trasversale alla direzione di propagazione della fessura. In seguito, un FBG lungo, é stato inserito in una provetta Compact Tension delle stesse dimensioni. In particolare, quando la fessura oltrepassa la fibra, il sensore puó essere usato per misurare le forze pontanti tra le superfici della frattura e/o l'apertura relativa tra le faccia della fessura. La ricostruzione del segnale riflesso attraverso la tecnica T-Matrix ha evidenziato alcuni problemi associati a distribuzioni di stress dovuti a campi di deformazione altamente non uniformi. In questo modo, i sensori di Bragg possono essere considerati un eccellente candidato per studiare un numero interessante di problemi nel campo delle applicazioni relative alla meccanica della frattura.

**Parole chiave:** Stress residui, FBG, tecnica OLCR, metodo della Compliance, detezione di danneggiamento

# Acknowledgements

First of all, I would like to thank Prof. John Botsis for being more than a thesis supervisor during these years at EPFL with his human qualities and kindness. He gave me unique opportunities to study and learn new branches of applied mechanics and numerical analysis, leading enthusiastically my research activity and always providing new ideas, suggestions and insights.

I am grateful to Prof. René Salathé from the Laboratory of Applied Optics at EPFL, for his competence, support and advice in the optical domain. I thank all the members of the jury, especially Prof. Paolo Ermanni from the Department of Mechanical and Process Engineering at ETH Zurich, Prof. Alain Vautrin from the Mechanics and Materials Department at ENSM Saint-Etienne, and Prof. Paul Xirouchakis from the Laboratory of Computed-aided Design and Production at EPFL for presiding the jury. Finally, I wish to acknowledge the EPFL and the Swiss National Science Foundation (Grant N° 200020-103624) for the financial support they provided to me during these years.

Several people contributed to the achievement of this work. Special recognition goes to my colleagues, in particular Dr. Laurent Humbert, Gabriel Dunkel, Larissa Sorensen, Dr. Joël Cugnoni, Dr. Massimo Facchini and one of my best friends, Matteo Galli, for sharing with me a part of their precious time, for their friendship and their availability and for creating a lively and nice place and a great team. Thanks to all other people with whom I interacted during my period at EPFL, especially all the members of LMAF, Laboratory of Applied Mechanics and Reliability Analysis and the Atelier group, particularly Gino Crivellari, Marc Jeanneret and Nicolas Favre for their outstanding work in preparing the moulds and the fixtures used in the experiments, despite the infamous quality of the drawings. This work has also benefited from the collaboration with Dr. Philippe Giaccari who patiently introduced to me to the optical low coherence reflectometry and other optical techniques.

Personally, I would like to remember all people with whom I interacted during my PhD –the list would be too long and incomplete– for understanding, support, interest and affection.

Last but not least, a very special thanks to my mother and father for their support in my long university years and most of all to my wife, Rita, for her love and for bearing with me all this time. This work is dedicated to you.



*“In motu igitur sanguinis explicando easdem offendimus insuperabiles difficultates, quae nos impediunt omnia plane opera Creatoris accuratius prescrutari; ubi perpetuo multo magis summam sapientiam cum omnipotentia coniunctam admirari ac venerari debemus, cum ne sumum quidem ingenium humanum vel levissimae vibrillae veram structuram percipere atque explicare valeat.”*

*Leonhard Euler (1707-1783).*

*“Mathematics seems to endow one with something like a new sense.”*

*Charles Darwin (1809-1882).*

*“È nelle difficoltà che si prova la fedeltà e la costanza*

*–Omnia possum in Eo qui me confortat (St.Paul, Philipp. 4,13)–.”*

*Francesca Cabrini (1850-1917).*

*“Ci sono solo due cose infinite: l’universo e la stupidità dell’uomo.*

*Il fatto é che della prima non sono del tutto certo.”*

*Albert Einstein (1879-1955).*



# Contents

<b>1</b>	<b>Introduction</b>	<b>1</b>
1.1	Composite materials: a first approach . . . . .	1
1.2	Objectives of the present work . . . . .	3
1.3	Thesis structure . . . . .	4
<b>2</b>	<b>State of the art</b>	<b>7</b>
2.1	Residual stresses: an overview . . . . .	7
2.2	Experimental methods used to measure residual stresses . . . . .	9
2.2.1	The use of FBGs to measure residual stresses in composite . . . . .	11
<b>3</b>	<b>Optical methods: FBG and OLCR technique</b>	<b>15</b>
3.1	General description . . . . .	15
3.2	FBG working principles . . . . .	15
3.3	OLCR Technique . . . . .	18
3.4	Preliminary test: residual strain distribution in a block of epoxy . . . . .	20
3.5	The transfer matrix (T-Matrix) approach to compute the FBG spectra . . . . .	25
<b>4</b>	<b>Materials and methods</b>	<b>31</b>
4.1	The single fiber composite (SFC) specimen: the difficulties in treating the problem . . . . .	31
4.2	Specimen preparation . . . . .	32
4.3	Specimen geometry . . . . .	34
<b>5</b>	<b>Residual axial strain and stress field in a SFC specimen</b>	<b>37</b>
5.1	Axial strain evolution for different FBG positions . . . . .	37
5.2	Dimensional effect on the residual axial strain field . . . . .	38
5.3	The effect of the coating on the axial strain distribution . . . . .	41
<b>6</b>	<b>Determination of the radial stress evolution</b>	<b>45</b>
6.1	The Crack Compliance (C.C.) Method . . . . .	45
6.2	The influence of the specimen radius $r_m$ on the radial distribution of stresses . . . . .	50
6.3	Effect of a longitudinal crack on the residual stress field . . . . .	53

<b>7 FEM analysis</b>	<b>55</b>
7.1 The matrix shrinkage function $S_m$ . . . . .	56
7.1.1 Introduction to the Weight Function method to calculate the Crack Opening Displacement (C.O.D.) . . . . .	57
7.1.2 Weight functions . . . . .	59
7.1.3 Calculation of crack opening displacement . . . . .	60
7.1.4 C.O.D. General formulation . . . . .	62
7.1.5 Determination of the weight function associated to the reinforced cylin- drical specimen geometry . . . . .	63
7.1.6 The virtual crack extension method to compute $K_I$ : stiffness derivative formulation . . . . .	68
7.2 FE analysis of residual stresses . . . . .	69
7.2.1 The axysymmetric model . . . . .	70
7.2.2 The fiber-matrix interface shear stress . . . . .	74
7.3 Finite Element modeling of the longitudinal crack . . . . .	76
<b>8 Analytical modeling of residual stresses</b>	<b>79</b>
8.1 The concentric cylinder model of Y. Mikata and M. Taya . . . . .	79
8.2 The asymptotic solution based model of E.S. Folias . . . . .	85
8.3 The energetic approach of M.Y. Quek . . . . .	88
<b>9 Crack-fiber interaction</b>	<b>95</b>
9.1 Introduction . . . . .	95
9.2 Notes on fatigue fracture . . . . .	96
9.3 Optical FBG sensor glued on the back face of the specimen . . . . .	98
9.4 3-D Finite Element modeling of the CT-specimen . . . . .	102
9.4.1 3-D model parameterization . . . . .	102
9.5 Analytical modeling of the CT-specimen . . . . .	109
9.6 CT-specimen containing an embedded optical fiber . . . . .	112
<b>10 Summary and future work</b>	<b>121</b>
10.1 Summary . . . . .	121
10.2 Perspectives . . . . .	122
<b>Appendix</b>	<b>124</b>
<b>A The T-Matrix reconstruction based approach for the analysis of other dis- tributions of strain</b>	<b>125</b>
<b>Bibliography</b>	<b>131</b>



# List of Tables

6.1	Values of the coefficients $A_i$ calculated via the C.C. method for the specimen $S1$ .	50
6.2	Values of the coefficients $A_i$ calculated via the C.C. method for the specimen $SS1$ .	52
7.1	Coefficients $m_{i,k}$ determined to fit the functions drawn in Fig.7.10.	67
7.2	Coefficients $a, b, c, d$ used in the function $S_m(r, z)$ .	71
7.3	Coefficients $a', b', c', d', e', f', g'$ used in the function $S_m(r, z)$ .	71
9.1	Parameters used in the fatigue crack propagation test to obtain a stable crack evolution in the specimen	97



# List of Figures

1.1	Example of carbon-fiber reinforced composite pieces used in different applications	2
1.2	Experimental configuration used to retrieve the residual strain and stress field by FBG sensors: <b>a)</b> an epoxy cylinder with a radially machined deep crack; <b>b)</b> an epoxy cylinder of the same length but shorter radius; <b>c)</b> an epoxy cylinder with a longitudinally machined deep crack. . . . .	5
1.3	Structure of the thesis . . . . .	6
2.1	The different types of residual stresses. $\sigma^I$ refers to macro residual stresses, $\sigma^{II}$ are micro residual stresses that vary on the scale of an individual grain and $\sigma^{III}$ are micro residual stresses that exist within a grain, essentially generated by presence of dislocations or others crystalline defects. . . . .	8
2.2	Typical reflected spectra of a FBG subjected to <b>a)</b> homogeneous strain; <b>b)</b> non-uniform strain; . . . . .	12
3.1	Scheme of an optical fiber. Typical dimensions are indicated. . . . .	16
3.2	Structure of an optical fiber with an embedded FBG. The external plastic coating surrounding the glass guiding part of the fiber is not indicated here. . .	16
3.3	FBG working principle. The broadband light $\text{in}(\lambda)$ is launched into the fiber core. $r(\lambda)$ and $t(\lambda)$ are the reflected and transmitted signals respectively, around the Bragg wavelength $\lambda_{B0}$ . $\Lambda$ is the grating period. In particular, when the grating is stretched, the reflected Bragg peak simply shifts or presents multiple peaks depending whether the deformation it undergoes is uniform or not. . . . .	17
3.4	Simplified scheme of the OLCR-setup. . . . .	19
3.5	Principle of OLCR-based method to reconstruct the strain distribution from FBG impulse response measurements. . . . .	19
3.6	Plots of the amplitude (top) and the phase (bottom) of the impulse response for not embedded (grey line) and embedded (black line) FBG. The OPLD scale distance corresponds to the optical path length difference in vacuum between the reference and the test arm . . . . .	20
3.7	Corresponding reflection intensity spectra (top) and local Bragg wavelength (bottom) for not embedded (grey line) and embedded (black line) FBG . . . .	21

3.8	View of the mould used to prepare the block specimens in the so called "horizontal configuration". . . . .	21
3.9	Scheme of the block specimen (dimensions are in mm). The location of the FBG is also indicated. . . . .	22
3.10	Typical FBG reflected spectra during the three stages of the specimens fabrication. . . . .	23
3.11	Local Bragg wavelength distributions $\lambda_B(z)$ calculated for three processing time. The corresponding spectra are shown in Fig.3.10. . . . .	24
3.12	Axial strain distribution measured before and after post-curing for the block specimen realized in the horizontal configuration. . . . .	25
3.13	FBG slicing in sub-sections for the T-Matrix method [34] . . . . .	26
3.14	Spectrum and local Bragg evolution reconstructed with the OLCR technique. The spectrum corresponds to real one measured with a simple spectrometer. . . . .	27
3.15	Interpolation of the local Bragg wavelength evolution of Fig.3.14 by two slightly different piecewise constant functions. . . . .	28
3.16	Comparison between the reconstructed spectrum via the OLCR and layer-peeling algorithm (solid line) and the spectrum retrieved by using the T-Matrix approach (dashed line). . . . .	29
3.17	Comparison between the reconstructed spectrum via the OLCR and layer-peeling algorithm (solid line) and the spectrum retrieved by using the T-Matrix approach (dashed line) when the piecewise function does not corresponds exactly to the $\lambda_B(z)$ evolution of Fig.3.14. . . . .	30
4.1	<b>a)</b> Typical transverse section of a unidirectional composite [22] and <b>b)</b> schematic of the SFC cylindrical specimen extracted from the real material. Dimensions are in mm. . . . .	31
4.2	Stand used to strip the acrylate coating from the fiber by mean of sulfuric acid bath ( $H_2SO_4$ , 96%). . . . .	33
4.3	Comparison between the geometry of the block and the new cylindrical geometry. Two possible locations of the FBG are also shown: when it is centrally (black line) and partially (grey line) embedded. Dimensions are in mm. . . . .	34
4.4	Parts of the mould used to realize the block <b>a)</b> and the cylinder <b>b)</b> in the horizontal configuration. See also Fig.3.8 for more details. . . . .	35
4.5	Direct comparison between the measured axial strain distribution before and after post-curing for the block and the cylindrical specimen produced in the horizontal configuration. . . . .	35
4.6	Mould used to prepare the cylindrical specimen in the "Vertical configuration".	36
4.7	Axial strain distribution measured before and after post-curing for a cylindrical specimen realized in the mould of Fig.4.6 and FBG centrally located. . . . .	36
5.1	Axial strain distribution obtained for the cylindrical specimen of 40 mm length measured before and after post-curing. . . . .	37

5.2	Axial stress distribution obtained for the cylindrical specimen of 40 mm length and 12.5 mm radius after the post-cure treatment. . . . .	38
5.3	Axial evolution of strain along the fiber for three different cylinder lengths after the post-curing treatment. . . . .	39
5.4	Evolution of the reflected spectra during the preparation processes of the specimen <i>S1</i> . . . . .	40
5.5	Internal sections of the forming parts of the mould showed in Fig.4.6. . . . .	41
5.6	Locations of radius <i>a</i> ) and of the length <i>b</i> ) measurements. . . . .	42
5.7	Evolution of the axial strain distribution before and after post-curing when the coating is kept around the optical fiber. The result is obtained by superposition of two different gratings of 15-mm length and located in two different positions. . . . .	42
5.8	Strain distribution measured at the center of a cylindrical specimen when the interface conditions between fiber and surrounding coating fail. An inversion on the behavior is observed. . . . .	43
5.9	Schematic of an optical fiber with an FBG. The recoated region around the grating shows the difference in thickness that in general exists between the coated and the recoated part. . . . .	44
6.1	Configuration used for C.C. method tests . . . . .	46
6.2	Plot of the measured local Bragg wavelength distributions $\lambda_B(z)$ for increasing notch depth $a_T$ . The corresponding strain profiles are deduced by using Eq.3.2.4. In particular, since the reference local Bragg $\lambda_{B0}(z)$ is in this application a constant distribution, the strain evolutions are equal to the form of the different $\lambda_B(z)$ . . . . .	46
6.3	Form of the first sixteen Legendre polynomials used as a base to decompose the stress $\sigma_z^m(r)$ . . . . .	47
6.4	Application of the superposition principle to calculate ( $\epsilon_{measured}$ ) used in the Eq.6.1.2 . . . . .	48
6.5	Local Bragg distribution $\lambda_B(z)$ obtained with only one cut of depth $\bar{a}_T = 12mm$ . Slightly differences in comparison with Fig.6.2 can be attributed to the machining processing. . . . .	49
6.6	Radial evolution of the stress $\sigma_z^m(r)$ in the plane $z=0$ . . . . .	50
6.7	Evolution of the axial stress distribution as a function of the specimen radius. . . . .	51
6.8	Measured strain distribution before and after cutting a circumferential cut of 3 mm depth for the post-cured specimen SS1. . . . .	52
6.9	Shift of the principal Bragg peak due to the longitudinal cut. A slightly variation of the Bragg wavelength is measured after a cut depth of $a_L = \frac{r_m}{2}$ (dashed line). A greater shift is detected for the deeper crack $a_L = r_m - 2r_f$ (dotted line). . . . .	53
6.10	Maximum peak variation due to the light polarization changes. The curves represent the same sensor response centered at the wavelength of 1294.15 nm, and recorded for two different states of polarization. . . . .	54

7.1	Crack Opening Displacement (the double of the vertical displacement of any single surface of the crack) for the specimen S1 and a crack depth of 11.5 mm.	58
7.2	Three different modes of loading that can be applied to a crack [77]. . . . .	58
7.3	Superposition principle: the global system of forces acting on the fracture surfaces of a body is viewed as a sum of single distributions, one representing the far stress field $\sigma_\infty(x)$ , one the bridging forces $\phi(x)$ and one term that guaranties the equilibrium conditions without influencing the fracture opening (two auto-compensating actions) [77]. . . . .	59
7.4	<b>a)</b> Crack submitted to a dipole force and in <b>b)</b> submitted to a distribution of forces $\phi(x)$ . . . . .	60
7.5	Cracked body loaded with a force P and a dipole F. $\Delta_P$ and $\Delta_F$ are the displacement in the direction of the forces and $d$ is the distance before deformation [11]. . . . .	61
7.6	Reinforced cylindrical specimen modeled to calculate the weight function. . . .	64
7.7	<b>a)</b> One eighth of the 3-D view of the cylindrical specimen. The simulated $rz$ -plane is highlighted with bold lines. <b>b)</b> Example of the mesh in the model. The applied symmetry conditions are indicated by using triangular symbols. . .	65
7.8	Particular of the mesh implemented in the FE model used to calculate the value of $K_I$ . The $J$ -contour integral based on the Virtual Crack Extension Method approach is the routine used by the FE codes to calculate $K_I$ . . . . .	66
7.9	Evolution of $H$ as a function of $(\frac{c}{a})$ for different values of $(\frac{a}{b})$ . . . . .	66
7.10	The different evolutions of the functions $h_i$ for the considered configuration. . .	67
7.11	Virtual crack extension method working principle: <b>a)</b> initial conditions and <b>b)</b> after virtual crack advance [4]. . . . .	69
7.12	<b>a)</b> Scheme of the two-phase composite modeled in the present analysis and <b>b)</b> the associated 2-D section meshed with axisymmetric elements. . . . .	70
7.13	Comparison between the experimental (black line) and the numerical (grey line) axial strain distribution for the specimen S1. . . . .	72
7.14	The experimental stress evolution $\sigma_z^m(r)$ (dotted line) is compared with the numerical evolution when $R(r)$ is taken in its general form or when the radial effect is neglected (dashed line). . . . .	72
7.15	Particular of the Fig.7.14 where is highlighted the effect on the stress evolution due to introduction of a radial effect in the general expression of $S_m$ . . . . .	73
7.16	Evolution of the axial stress distribution as a function of the specimen radius. The distribution obtained for the bigger and smaller radius are compared with those ones calculated via the C.C. method. . . . .	73
7.17	Axial and transversal stress evolutions in the plane $z = 0$ . . . . .	74
7.18	<b>a)</b> Photo of a coordinate measuring machine. <b>b)</b> Comparison between the simulated and the measured cylindrical profile by CMM. . . . .	75
7.19	Evolution of the fiber/matrix interface shear stress. The mesh refinement of Kovalev (insert) has been used to catch the correct shear distribution at the specimen end. . . . .	75

7.20	A quarter of the 3-D model used to simulate the effect of the longitudinal crack.	76
7.21	Complete strain evolution simulated without longitudinal cut (continuous line) and with a cut of depth $a_L = r_m - 2r_f$ (dashed line). The axial relaxation corresponds to the one measured by the FBG. . . . .	77
7.22	Component in the x-direction of the fiber displacement after machining the longitudinal crack. . . . .	78
8.1	Four-phase model [56]. . . . .	80
8.2	Simulation of the axial stress distribution along the fiber. Comparison with the model of Mikata and Taya . . . . .	84
8.3	Geometrical and loading configurations [32]. . . . .	85
8.4	Definition of local coordinates system in the region of interest [33]. . . . .	86
8.5	Comparison between the shear distribution of stresses provided by the FE model (continuous line) and the asymptotic approach (dashed dotted line) adopted by Folias along the fiber-matrix interface of the cylindrical specimen. . . . .	89
8.6	The composite specimen used by Quek in its thermal stress problem [66]. . . . .	89
8.7	Comparison between the shear distribution of stresses provided by the FE model (continuous line), the asymptotic approach (dashed dotted line) adopted by Folias and the distribution based on the energetic approach of Quek (dotted line) along the fiber-matrix interface of the cylindrical specimen. . . . .	93
9.1	CT-specimen's geometry with an embedded optical fiber. Dimensions are in [mm]. $D_N$ may be changed to check the influence of the fiber position on the final results. . . . .	96
9.2	Cyclic load-time profile used in laboratory experiment. . . . .	97
9.3	CT-specimen used in the preliminary test. The optical fiber containing a 1.4 mm-length FBG is positioned on the back face of the specimen and glued using epoxy. . . . .	98
9.4	Compact tension specimen during the test of fatigue crack propagation. The final length $a$ of the fracture before stopping the test was 25.6 mm. . . . .	99
9.5	Special stand used to manually load the compact tension specimen. . . . .	100
9.6	Strain measured at the origin of the system of coordinates shown in Fig.9.3 by using a 1.4-mm-long-grating. The results correspond to two different tests (A and B) performed on the same specimen and in the same conditions. . . . .	100
9.7	Strain measured along the axial direction $z$ by using a 13-mm-long-grating. The grating center is slightly displaced respect to the origin of the coordinate system. . . . .	101
9.8	A quarter of the modeled CT-specimen. . . . .	102
9.9	First approach used to model the traction applied to the CT-specimen via the contact tool and the distributed coupling between a reference point and a rigid surface. . . . .	103

9.10	Illustration of the load transfer process from the reference point to the hole's surface. . . . .	103
9.11	Comparison between the numerical simulation (continuous line) and the two experimental results coming out from the 1,4-mm-long grating placed at 4 mm from the origin of the system of coordinates along the z-direction. . . . .	104
9.12	Comparison between the numerical (continuous lines) and the experimental (bold line) distributions obtained by the 13-mm-long grating along the axial direction z. . . . .	104
9.13	Schematic explaining the possible error committed in the vertical alignment of the optical fiber. Depending on the grating position, the variation in the strain response could be important. . . . .	105
9.14	Numerical strain evolution (continuous line) for a short grating located at 4 mm along the axial direction z and the possible corresponding variations (dashed lines)) due to a misalignment of the fiber. . . . .	106
9.15	Four different shapes of the crack front simulated in the FE model. . . . .	107
9.16	Plot of the crack fronts shown in Fig.9.15. . . . .	107
9.17	Strain evolutions as functions of the front shapes represented in Fig.9.16. . . . .	108
9.18	Simulated crack fronts used to underline the dependence of the strain on the derivative of the fracture profile. . . . .	108
9.19	Strain evolutions as functions of the front shapes represented in Fig.9.18. . . . .	109
9.20	The CT-specimen viewed as part of a beam. The strain $\epsilon$ and the stress $\sigma$ are supposed to vary linearly along the section. . . . .	110
9.21	Evolution of the maximum value of strain calculated at the origin of the coordinates as function of the crack length $a$ by using the FE model (black line) and the proposed new approach (grey line) respectively . . . . .	111
9.22	Fatigue crack propagation test on a CT-specimen with an embedded optical fiber. A natural crack is visible in the notch. . . . .	113
9.23	Evolution of the maximum value of strain calculated during the specimen preparation. . . . .	113
9.24	Comparison between the experimental (dashed line) and numerical (continuous line) maximum strain values for a crack length $a$ of 21.6 mm. . . . .	114
9.25	Comparison between the experimental (dashed line) and numerical (continuous line) maximum strain values for a crack length $a$ of 22.85 mm. . . . .	114
9.26	Comparison between the experimental (dashed line) and numerical (continuous line) maximum strain values for a crack length $a$ of 24.4 mm. . . . .	115
9.27	Profile of the curved crack front interacting with the reinforcing glass optical fiber. The black line behind the fiber can be explained noting that the fracture front is not coplanar anymore when pass the fiber. In the region of conjunction a sort of deep valley is created thus reflecting the light in a different direction. . . . .	116



9.28	Evolution of the maximum strain value calculated during the specimen preparation. Since the grating length is 13 mm, the complete wavelength evolutions along the gratings are presented in the insets of the figure. Notice that a practically constant distribution of wavelength corresponds to a constant strain in the central region of the specimen. . . . .	116
9.29	Comparison between the experimental (bold lines) and numerical (normal lines) strain distributions along the axial direction $z$ (i.e. along the core of the fiber) for a crack length $a$ of 21.6 mm measured by a13-mm-long-grating. Each curve refers to a given applied load: 10 N (lower curves) 50 N (in the middle) and 100 N (upper curves). . . . .	117
9.30	Comparison between the experimental (bold lines) and numerical (normal lines) strain distributions along the axial direction $z$ (i.e. along the core of the fiber) for a crack length $a$ of 22,85 mm measured by a13-mm-long-grating. Each curve refers to a given applied load: 10 N (lower curves) 50 N (in the middle) and 100 N (upper curves). . . . .	117
9.31	Comparison between the experimental (bold lines) and numerical (normal lines) strain distributions along the axial direction $z$ (i.e. along the core of the fiber) for a crack length $a$ of 24.1 mm measured by a13-mm-long-grating. Each curve refers to a given applied load: 10 N (lower curves) 50 N (in the middle) and 100 N (upper curves). . . . .	118
9.32	Numerical (normal lines) strain distributions along the axial direction $z$ (i.e. along the core of the fiber) for a crack length $a$ of 24.4 mm measured by a13-mm-long-grating. Each curve refers to a given applied load: 10 N (lower curves) 50 N (in the middle) and 100 N (upper curves). This case was experimentally analyzed only by using a short grating but the entire distributions are reported for thoroughness. Let notice the exact form of the fracture front simulated by the model. . . . .	118
9.33	Comparison between the experimental (bold lines) and numerical (normal lines) strain distributions along the axial direction $z$ (i.e. along the core of the fiber) for a crack length $a$ of 24.6 mm measured by a13-mm-long-grating. Each curve refers to a given applied load: 10 N (lower curves) 50 N (in the middle) and 100 N (upper curves). . . . .	119
9.34	A photograph of a cracked compact tension specimen. The crack has exceed the fiber and it work as a bridgingbetween the two surfaces of the fracture. The bridging force along the fiber can be calculated using the deformation data plotted in Fig.9.33. . . . .	119
A.1	Reflected spectrum from an FBG of 25-mm-length embedded in a cylindrical specimen with a machined circular crack of-12-mm depth. . . . .	125
A.2	The Gaussian piecewise constant evolution chosen to represent a realistic distribution of the Bragg wavelength along the FBG. The center of the grating corresponds to the center of the specimen. . . . .	126

A.3	Comparison between the measured spectrum (grey line) and the reconstructed spectrum (dashed line) via the T-Matrix approach in the case of the cylinder with a circular radial crack. . . . .	127
A.4	Spectrum and local Bragg wavelength evolution retrieved via the OLRC in the case of the cracked CT-specimen reinforced with an embedded optical fiber. . .	128
A.5	Piecewise constant function used to approximate the local Bragg wavelength evolution along the core of the embedded optical fiber. . . . .	129
A.6	Comparison between the real measured spectrum (grey line) and the simulated one (dashed line) via the T-Matrix reconstruction method. . . . .	130

# Chapter 1

## Introduction

### 1.1 Composite materials: a first approach

Most of the products we see every day are made of monolithic materials. That means that the individual components consist either of a single material (an unreinforced plastic), or of a combination of materials that are assembled in such a way that the individual components are indistinguishable (e.g. a metal alloy).

Composites, on the other hand, consist of two or more materials combined in such a way that the individual elements are easily distinguishable. In fact, while in the more familiar world of metals the mixing of different materials typically forms bonds at the atomic level (alloys), composites typically form molecular bonds in which the original components retain their identity and mechanical properties. The properties of that new structure are then dependent on the properties of the constituent materials as well as the properties of their interface.

The individual materials that make up composites are called constituents. Most composites have two constituents: a binder or matrix and a reinforcement. The reinforcement is usually much stronger and stiffer than the matrix, and gives to the composite its good properties. The matrix holds the reinforcements in an orderly pattern. Because the reinforcements are usually discontinuous, the matrix also helps to transfer load among the reinforcements. Reinforcements basically come in three forms: particulate, discontinuous fibers and continuous fibers. A particle has roughly equal dimensions in all directions, though it doesn't have to be spherical. Gravel, microballoons and resin powder are examples of particulate reinforcements. Reinforcements become fibers when one dimension is long compared to others. Discontinuous reinforcements (chopped fibers, milled fibers, or whiskers) vary in length from a few millimeters to a few centimeters. Most fibers are only a few microns in diameter, so it doesn't take much length to make the transition from particle to fiber. With either particles or short fibers, the matrix must transfer the load at very short intervals. Thus, the composite properties cannot come close to the reinforcement properties. With continuous fibers, however, there are few if any breaks in the reinforcements. Composite properties are much higher, and continuous fibers are therefore used in most high performance components. A common example of a composite is concrete. In fact, it consists of a binder (cement) and a reinforcement (gravel).

Adding another reinforcement (rebar) transforms concrete into a three-phase composite. Matrix materials are usually some type of plastic and these composites are often called reinforced plastics. There are other types of matrices, such as metal or ceramic, but plastics are by far the most common. There are also many types of plastics, but the two most common plastic matrices are epoxy resins and polyester resins.

Even if the use of composites is increasing in all products (from sporting goods to automobiles and aircrafts to satellites), today, when we speak about composites materials, or just composites, we are referring to the highly engineered combinations of polymer resins and reinforcing materials such as glass or carbon fibers. More specifically, a fiberglass composite structure is a combination of glass fibers of various lengths and resins such as vinyl ester or polyester. The term FRP is often used, meaning Fiber Reinforced Plastic. FRP is a very general term for many different combinations of reinforcement materials and bonding resins. The term composites has thus become extremely useful to describe many materials with many different properties targeted at an even larger number of applications. To show how composites have changed our world, look no further than under the hood of a modern car or observe a sport motorbike (Fig.1.1) and realize that most of what you can see are components made of composite materials.



**Figure 1.1:** *Example of carbon-fiber reinforced composite pieces used in different applications*

Actually, due to their high strength and stiffness coupled with a low density, composites materials offer designers an increasing number of possibilities in terms of material and system

solutions. Moreover, they present other benefits such as high processibility, thermal and acoustic insulating properties and, depending on the constituents, resistance to environmental factors (corrosion, chemical wear, thermal effect). Finally, composites cost trends are highly favorable, especially when the total cost of fabrication is considered.

These are some of the reasons that justify why each year composites find new ways into hundreds of new applications providing highly reliable products to be used in extremely demanding conditions which no single material can stand by itself.

## 1.2 Objectives of the present work

The lifetime of a structural component depends on the interaction between its internal defects and the surrounding stresses that result both from the external loading and the composite processing. In the latter case, they remain present when the applied forces are removed and are for this reason named residual stresses. Especially for FRP material, just the fabrication process can induce an appreciable amount of residual stresses, for instance as a consequence of the rate of solidification or due to the differences in coefficient of expansion/contraction of the constituents. Although residual stresses are quite difficult to predict and to measure reliably, their magnitude and distribution are generally critical for the performance of composites because they significantly influence the quality and the behaviour of the target structural material. This explains why residual stresses have to be considered while designing a component.

In this frame, the scope of this thesis research is principally to develop a reliable procedure involving a long Fiber Bragg Grating (FBG) sensors in combination with more other traditional techniques to retrieve the non-uniform residual strain and stress fields generated during the fabrication of a composite. In particular, the response of an FBG to a non-uniform strain distribution is investigated using a technique developed at EPFL based on a Optical Low-Coherence Reflectometry (OLCR) and combined with a reconstruction algorithm called layer-peeling. This new approach has the main advantage of providing the direct reconstruction of the optical period along the grating without any a priori assumption on the form of the axial strain field applied to the fiber. More details on FBG working principles and on the OLCR technique will be given in Chapter 3 of this thesis. The same technique will be also implemented to monitor any possible variations of these residual fields as a consequence of an applied external load and to detect the presence of damage (e.g. cracks) generated and propagated within the material.

These tasks involve different steps. First, work is done to better characterize the response of long fiber Bragg grating to a non-uniform axial strain, particularly in applications where the sensor is embedded. Secondly, after designing an appropriate experimental setup, FBG are used in conjunction to a typical technique of the fracture mechanics and called Crack Compliance Method (C.C.M.) to retrieve the transversal evolution of the strain field. The advantages and the drawbacks presented by the FBG sensor for this kind of applications are also considered by comparing it with other type of strain gages commonly used in this domain. Thirdly, fiber Bragg gratings are employed in cases closer to real structural sensing applica-

tions. In particular, an example is chosen in relatively novel experimental configuration when using long FBG: a compact tension specimen reinforced with an optical fiber where a natural crack is generated and propagated during a fatigue test.

Thus, this study addresses long-FBG related issues in the mechanics of composites at various level, ranging from sensing response to applicability in both fundamental laboratory experiment and advanced sensing response analyses.

### 1.3 Thesis structure

The thesis is divided into nine chapters. After an introduction chapter containing the statement of the objectives, Chapter 2 is dedicated to a wide review of the state of the art on the different techniques used to measure residual stresses. The experimental methods used in this work are exposed in Chapter 3: FBG sensors and the OLCR apparatus applied to measure non-uniform strain and stress distributions. Some results from a preliminary test will also be presented. An effective, non-destructive experimental method is illustrated, combining an optical interferometric technique with embedded sensors to investigate the behaviour of a composite subjected to a non-uniform residual stress distribution.

In Chapter 4, the materials and the protocol chosen to prepare the specimens are illustrated. In particular will be justified the choice of the kind of specimen, its geometry and dimensions. The experimental measurements to retrieve the axial strain and stress field on a Single Fibre Composite (SFC) specimen are recovered in Chapter 5. A first analysis of how the specimen dimensions affect the residual axial strain field will also taken into account.

The presentation of the Finite Element (FE) model based on an equivalent thermo-mechanical approach represents the main part of the Chapter 6. The simulations are performed using both 2-D (axisymmetric) and complete 3-D configurations, obtaining thus, the verification of the experimental results and assessing the reliability of the employed optical method.

Chapter 7 reveals some practical advantages which come from the use of a embedded long-FBG's as a strain sensors. The new experimental setup proposed to apply the Crack Compliance Method to the cylindrical specimen allows one to greatly simplify that methodology reducing the experimental errors and the time necessary to perform the experiment itself. This way, the radial evolution of the residual stress is retrieved in particular for two specimen of different radii, showing thus the applicability of the technique. A third configuration is finally analyzed: the effect of a longitudinal machined crack along the specimen [Fig.1.2] .

In this case a wide use of the FE modelling was necessary to explain the results and to model the considered phenomena.

Because the characterization of residual stresses is not new, in the available literature it is easy to find different approaches to deal with this subject. Chapter 8 highlights three analytical models considered as the most representative in the domain and dealing with similar problems or aspects treated in this work. A comparison between the analytical predictions, the experimental and finite element results is presented with the aim of generalizing the analysis of the residual stress problem, at least in the case of a model composite specimen.

Chapter 9 documents further experiments carried out using FBG sensor to measure internal

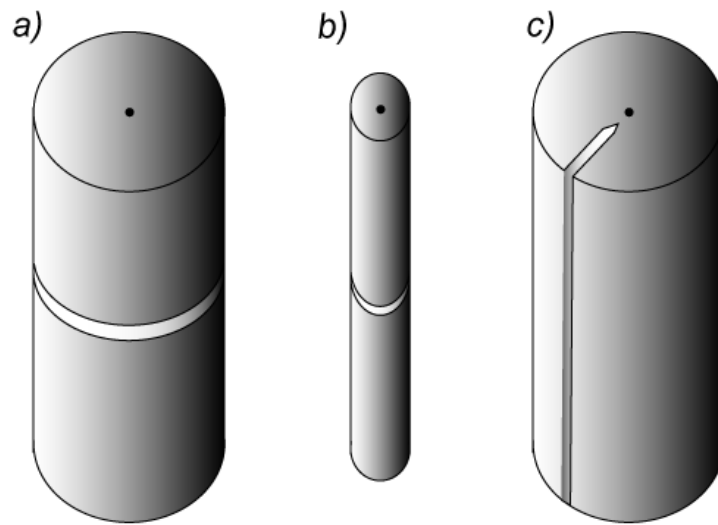


**Figure 1.2:** *Experimental configuration used to retrieve the residual strain and stress field by FBG sensors: a) an epoxy cylinder with a radially machined deep crack; b) an epoxy cylinder of the same length but shorter radius; c) an epoxy cylinder with a longitudinally machined deep crack.*

strain in composite: a FBG is simply glued on the back side or embedded in a compact tension specimen and subjected to different load conditions. The measurement results are used to validate a proposed new analytical model, based on the beam theory which can be used to predict the length of a fracture produced within the specimen when loaded in a mode I configuration.

Finally, a summary and suggestions for further work are given in the conclusions. The overall structure of the thesis is illustrated in Fig.1.3 with the connections between the related topics additionally highlighted.

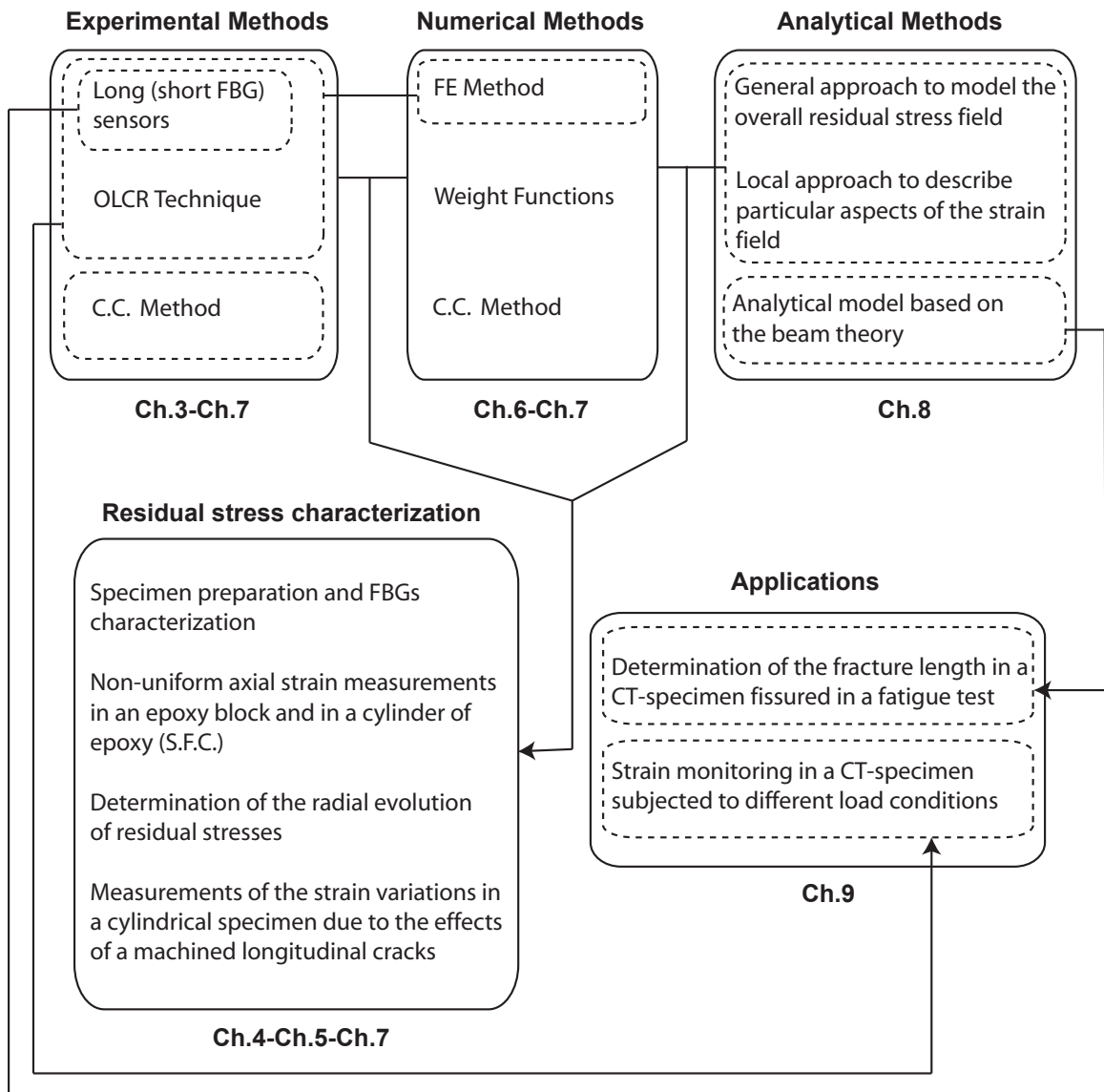


**Figure 1.3:** *Structure of the thesis*



## Chapter 2

# State of the art

### 2.1 Residual stresses: an overview

Residual stresses are self-equilibrated stresses supported by a body and that remain embedded inside the component even after the forces causing the stresses are removed. They superimpose on applied stresses and are generally more difficult to predict. A common manifestation of residual stresses is for example the warping of laminate composites without the application of any external load. Moreover, they can also aggravate the failure of a component, and often may cause fatigue failure, quench cracking and stress corrosion cracking.

The subject has been investigated in a number of numerical/experimental works in the past. In general residual stresses can be classified by the scale over which they self-equilibrate, or according to the method by which they are measured. Macroscopic residual stresses occur over large distances (several millimetres) while microscopic residual stresses operate over the grain scale of the material Fig.2.1. Barnes, for instance, discussed the different kinds of residual stresses present in continuous carbon-fiber-reinforced thermoplastic composites [7]. In his paper, he has indicated three levels of stresses to be distinguished in laminated structures: the micro-stresses existing between individual fibers within a ply, the macro-stresses which form on the ply-to-ply scale in multiaxial laminates, and at a much larger scale a third level of stresses due to differential thermal histories of parts of a laminate during the cooling stage. In order to optimize material quality and minimize component weight, a better understanding of the role of residual stresses is then required.

Residual stresses originate from a variety of sources: macroscopic stresses can arise from heat treatment, machining, secondary processing and assembly. Micro-structural stresses result typically from the coefficient of thermal expansion mismatch between constituents, differences in yield stress or stiffness or phase transformations (e.g. cure shrinkage). Both types may be present at any one time in a material or component [82].

The numerical study of Stone and co-workers [76] is dedicated to the residual stresses associated with post-cure shrinkage of adjacent layers in composite tubes. Specifically, the authors developed a model that takes into consideration the material shrinkage occurring after gelation. Other investigators have addressed the problem of local thermal stresses occurring in

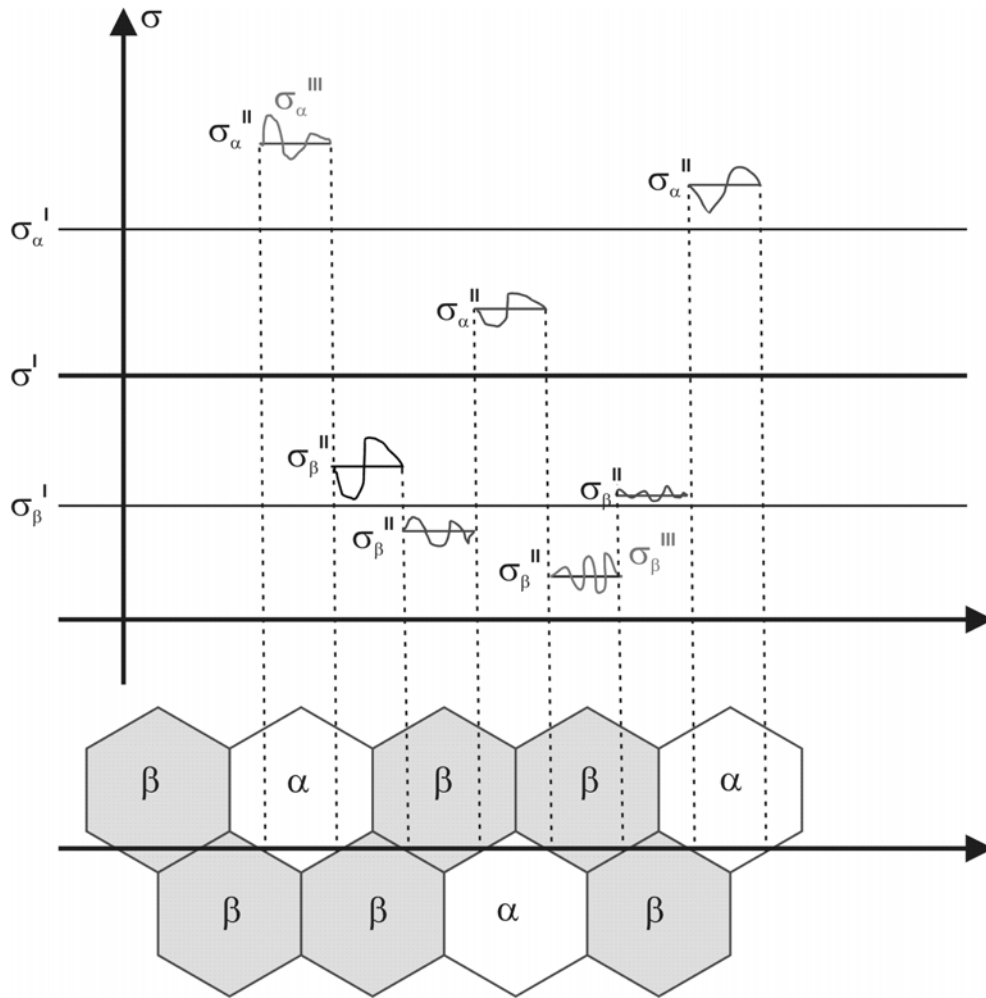


**Figure 2.1:** The different types of residual stresses.  $\sigma^I$  refers to macro residual stresses,  $\sigma^{II}$  are micro residual stresses that vary on the scale of an individual grain and  $\sigma^{III}$  are micro residual stresses that exist within a grain, essentially generated by presence of dislocations or others crystalline defects.

composite materials by use of concentric circular cylinders models. Modelling of (thermal) residual stresses has thus been achieved for unidirectional fiber-reinforced composites of infinite length and two-dimensional solutions (generalized plane strain) can be found in the papers of Mikata and Taya [56] and Anifantis [5]. In particular the work of Mikata and Taya is compared to the pioneering approach of Eshelby [25, 26] who developed a technique to treat the residual stresses caused by a difference in the thermal contraction of the constituents of a composite.

For a finite specimen length, closed-form solutions based on a more general three-dimensional approach have recently been derived by Folias [33] and Quek [66]. For the single fiber push-out problem, Chai and Mai [17] proposed a theoretical model of stress transfer across fiber/matrix interface in consideration of interface roughness and thermal residual stresses. It has also been reported that residual stresses significantly affect interfacial debonding behaviour and the stress transfer between fiber and matrix.

All the analytical models formulated for the estimation of residual stresses are usually developed based on significant assumptions about the geometry and the constitutive laws of the components (i.e linear elastic behaviour). Although such strong hypothesis limit the applicability of these models (residual stress may often exceed the elastic limit of the constituents) they certainly constitute an efficient and easy-to-use guide for preliminary study.

A much more powerful technique of investigating residual stresses is provided by finite element modelling, which has been massively used with increasing calculating power of computers [49]. Numerical models can provide significant results only if pertinent experimental strategies are followed in parallel and, at the same time, experiments need the guideline provided by numerics. This implies, among other things, that one must improve measurement techniques in order to obtain a greater confidence in the results provided by existing experimental methods.

## 2.2 Experimental methods used to measure residual stresses

Nowadays, a large number of destructive and non-destructive residual stress measurement techniques are available. Certain methods are convenient for overall stress measurements whereas others are restricted to specific regions of the specimen. In particular, layer-removal, hole drilling and crack compliance techniques [83, 60, 29] are well established for measurement of residual stresses in metallic, polymeric materials. The basis of these methods is the monitoring of changes in component distortion, either during the generation of the residual stresses, or afterwards, by deliberately removing material to allow the stresses to relax. Moreover, the experimental measurements are typically performed over a small area of the tested specimen. In the hole drilling method for instance [31], a strain-gage rosette is used to measure surface strains that result when sub-surface stress is released due to the drilling of a small hole. These strains, are then related to the state of stress in the hole region prior to the stress relaxation. The method is cheap, widely used, and it has been easily applied to polymeric samples [31, 51]. Nevertheless, although it is possible to deduce the variation in stress with depth by incrementally deepening the hole, it is difficult to obtain reliable measurements much beyond a depth equal to the diameter. Moreover, if the residual stresses

exceed about the 50% of the yield stress, then errors can arrive due to the localized yielding [63, 64]. Finally, while the method has been used to assess the levels of stress in coatings [31, 19], it is not really practical for thin ( $< 100 \mu m$ ), or for brittle coatings.

A similar technique, the crack compliance method, involves cutting a small slot to monitor the relaxation of stress in the vicinity of the crack using a strain gage. By steadily increasing the depth of the slot it is possible to resolve the stress field normal to the crack as a function of depth for relatively simple stress distribution. This technique has been successfully applied especially with metals [28, 62], even if the experimental procedure involved can become complicated. Another interesting method frequently used to measure residual stresses especially within coatings and layers [83], is the measurement of curvature. The deposition of a layer can induce stresses which causes substrate to curve. The resulting changes in curvature during deposition make it possible to calculate the corresponding variation in stress as a function of the deposit thickness. This approach can present some ambiguity, because the stress distribution associated with a given curvature is not unique.

Alternatively, non-destructive methods (such as diffraction, magnetic, electrical, ultrasonic, photoelastic, thermo-elastic techniques) can be used if experimental data are required in a larger area of the specimen. Each method presents its own merits, applicability and restrictions. Within the diffraction based methods it is possible to enumerate:

- Electron diffraction
- X-Ray diffraction
- Neutron diffraction
- Hard X-Ray diffraction

but they all present the fundamental drawback of being limited to materials presenting a crystalline structure. Using diffraction, it is only possible to determine the lattice strain for a given plane spacing in the direction of the bisector of the incident and diffracted beams. In order to calculate the strain (or stress) tensor at a sampling gage location at least six independent measurements of strain in different directions are required [21, 45]. Finally the equipment needed to perform the experiments is quite expensive and sometimes the errors generated in the measurement process can be of the same order of magnitude or even greater than the measured strain itself.

Magnetic methods are based on the monitoring the alteration of the magnetic domain orientation in magnetostrictive materials. The magnetic anisotropy induced by the applied stress leads to the rotation of an induced magnetic field away from the applied direction [3, 16]. By following these small rotations, both the principle stress directions and the size of the principle stress differences can be measured. Unfortunately, magnetic methods are sensitive to both stress and the component microstructure, which must therefore be accounted for using calibration experiments. The problem of the microstructural changes during the experiments affects the electrical methods too, which happen while measuring variations in the electrical

conductivity or magnetic permeability in a composite on which are induced by the so called eddy currents[3, 16].

By the ultrasonic methods, a measure of the stress averaged along the wave path is retrieved by evaluation of the changes in the ultrasonic speed observed when a material is subjected to a strain [70]. Ultrasonic wave velocities can depend on microstructural inhomogeneities [6, 69, 70] and there are difficulties in separating the effects of multiaxial stresses.

When the elastic deformation of a composites generates a small changes in temperature (e.g. 1 mK for MPa steel) then, with an appropriate infrared camera, it is possible to map the thermal variations undergoes by the material obtaining thus an indication of concomitant variations in stresses [3]. Piezospectroscopic technique are based on the Raman spectra measurement[3, 69]. In fact, characteristic Raman or fluorescence luminescence lines shift linearly with variations in the hydrostatic stresses. The methods are useful because these spectral shifts can be easily and accurately measured. Furthermore, given the optical transparency of some matrix material such as epoxy [6, 22], it is even possible to obtain subsurface information. The transparency is also an important characteristic that belongs to materials showing photoelastic properties. When the light goes through a stressed material there is an anisotropic change in its speed that gives rise to an interference fringe patterns when such objects are viewed between crossed polarizers. The stresses applied on the material are deduced by a correct interpretation of these fringes.

To complete this short introduction about the techniques that can be used to measure residual stresses a particular attention has to be done to the interferometric or optical technique, overall because FBG and the OLCR are part of this category. In a classical interferometer [3], two beams of coherent light, henceforth referred to as the illumination and reference beams, are combined and the resulting wavefront is passed to a detector. In a speckle pattern interferometry, one or both beams exhibit speckle patterns due to the reflection of said beam(s) from a diffusely reflecting surface. When these two beams form an image on a charged coupled device (CCD), an interferogram results. Recording the changes in the phase angle of the interference signal as a consequence of an applied stress on the surface, allows one to retrieve the variation in the path length and then the strain. This is the working principle of the ESPI (electronic speckle interferometry) [71] which has been also used in combination with the hole drilling method [75] to measure corresponding surface stress relaxation [78].

### 2.2.1 The use of FBGs to measure residual stresses in composite

Embedded optical fiber Bragg grating (FBG) sensors are well suited for single and multiplexed strain measurements in composite structures. They have attracted particular attention over the two last decades in the aerospace industry, manufacturing process monitoring, structural health monitoring and non-destructive testing. This is essentially due to their ability to perform direct strain measurement inside host structures at a desired location, providing valuable information about the local deformation state in complex structures. Moreover, when the FBG is written in an optical fiber it does not affect its mechanical properties, thus

allowing it to play at the same time the role of a reinforcement and a relatively non-invasive sensor.

Initial experiments with FBG $\tilde{O}$ s were conducted in the 1980 $\tilde{O}$ s as a consequence of the work of Hill et al.[39] demonstrating the photosensitivity of germanium-doped glass fibers and their capacity to support permanent gratings. Further studies have shown their advantages over conventional sensors: they are generally smaller (i.e. a  $125\mu\text{m}$  diameter for a standard telecom fiber) and more flexible, lighter, immune to electromagnetic interference, can withstand corrosive environments and high temperatures. In addition, FBG sensors provide localized measurements with high sensitivity, reproducibility and linearity of response at selected grating locations in the host structure. They also show an intrinsic self-referencing capability, are not susceptible to power fluctuations and can be easily multiplexed in the wavelength domain, allowing several sensors to be addressed in a single fiber.

The use of FBG $\tilde{O}$ s for uniform axial strain (tension or compression) and/or temperature sensing have been fully investigated in the past [23, 37] and several practical arrangements have been reported for the simultaneous measurements of strain and temperature [48]. One traditionally employs short gage length FBG $\tilde{O}$ s, fabricated in low-birefringence standard single mode (SM) fibers. The measurement principle is simply based on the determination of the shift of the Bragg peak reflected by the grating Fig.2.2a) which gives an indication about the axial deformation applied to the fiber.

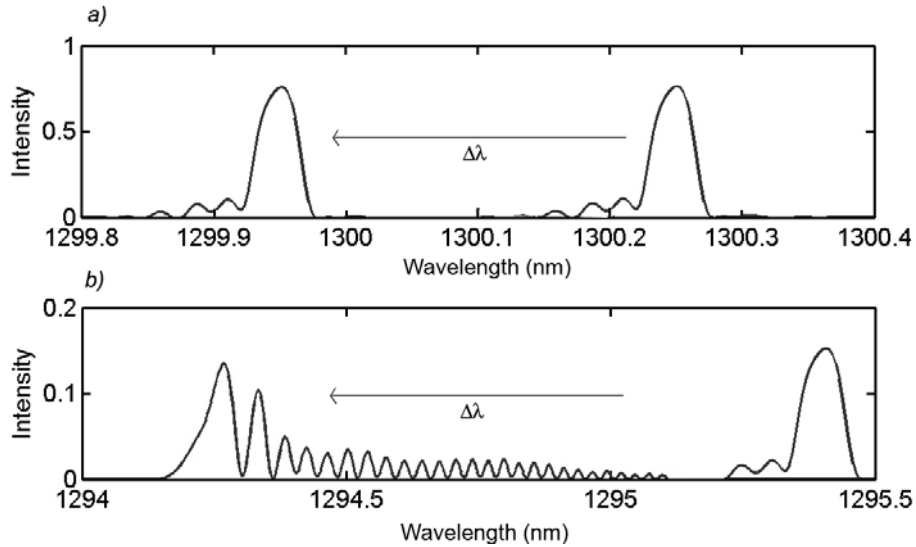


**Figure 2.2:** Typical reflected spectra of a FBG subjected to **a)** homogeneous strain; **b)** non-uniform strain;

However, in several configurations of interest a three-dimensional state of strain prevails around a FBG [67]. An important example is the residual strain field arising during the consolidation of a multi-layered composite material. When a FBG is subjected to non-negligible transversal strains, its optical response is generally affected. Thus, transversal strains essentially induce birefringence in the fiber core, which may lead to the separation of the initial

Bragg peak into two distinct ones along two polarization axes (i.e. the slow and fast eigenmodes). The relative wavelength difference of the two peaks depends upon the difference between the transversal strain components. Consequently, FBG sensors appear to be suitable for monitoring transversal strain differences provided that Bragg peaks are sufficiently separated to be distinguished.

While the advantages of embedded FBG over other techniques are very clear, it is important to underline that, due to its relatively greater dimensions respect to the usual reinforcements used with the composites, the optical fiber acts mechanically as an elastic inclusion with interfacial conditions that must be addressed. Correct evaluation of strains in the structure thus requires an adequate modeling of the load transfer between the optical fiber and the host material. Then, given the complex microstructures of the composite materials, numerical models are normally used to interpret the experimental results.

When a non-homogeneous strain field is present around the sensing region (e.g. strain gradients generated by the presence of heterogeneities) the FBG's spectral response is particularly modified (see Chapter 3 for more details). The initial Bragg peak splits into multiple secondary peaks distributed over a larger spectral range. The grating is said to be chirped and the FBG's spectrum becomes more complicated and in general can not be directly interpreted and related to the strain distribution along the grating length (Fig.2.2*b*). This is particularly evident in long gage length sensors. Existing techniques (e.g. see Measures [53]) can easily predict spectra modifications corresponding to a given strain distribution. However, the reverse problem, which is of interest, i.e. the determination of an arbitrary strain profile from a measured spectrum, always requires assumptions about the strain profile [61]. The use of the OLCR measurement and reconstruction technique easily overcomes the problem, providing the reconstruction of the optical period and the related strain distribution along the grating without any a priori assumption on the strain profile itself [35]. Distributed strain sensing with long-gage-length FBG sensors is part of the current research and will be addressed for relevant mechanical applications.





## Chapter 3

# Optical methods: FBG and OLCR technique

### 3.1 General description

Currently, there are different kinds of optical fibers with different diameters (the most common are between  $125\ \mu\text{m}$  and  $400\ \mu\text{m}$ ) available on market. They are composed of different materials (plastic or glass) and designed to work at different wavelengths. In this case only monomode optical glass fibers commonly used in telecom applications will be taken into account. In particular, for these applications standard wavelengths are 1300 and 1500 nm but in this specific case only fibers working at 1300 nm will be taken into account.

The optical fibers are composed of a  $9\ \mu\text{m}$  diameter core where the light is guided through the entire length of the fiber. Around the core there is an optical coating (cladding) whose function is to assuring the guiding properties of the fiber. Its diameter is in general  $125\ \mu\text{m}$ . In fact, even though these two parts are made of the same glass, the fiber core is doped in order to have an index of refraction slightly higher respect to the cladding. Finally, to protect the fiber from surface abrasion and exposure to moisture and then increase its resistance, an external plastic coating of  $250\ \mu\text{m}$  is applied all around the fiber (Fig.3.1). The two most widespread types of coating are acrylate and polymide, the latter being more high temperature resistant and thinner than the former.

### 3.2 FBG working principles

A fiber Bragg grating can be defined as a spatial modulation (or quasi periodic modulation) of the refractive index created along a desired length of the core of an optical fiber [9, 16](Fig.3.2) obtained by means of the two-beam interference technique or phase mask method [40]. The fabrication process is based on the photosensitivity property of the germanium-doped silica glass fiber core [39]. Co-dopants such as boron can also be added to enhance the photosensitivity phenomenon. Depending on UV laser beam characteristic, exposure time and dopants used, the most common types of reported gratings are homogeneous, apodized, index and/or

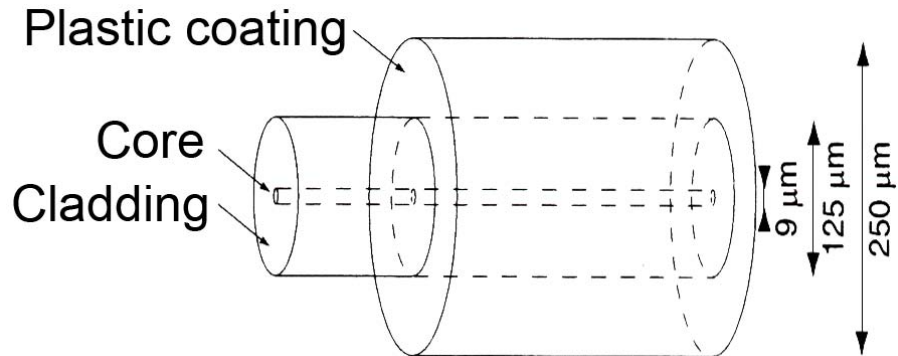


**Figure 3.1:** Scheme of an optical fiber. Typical dimensions are indicated.

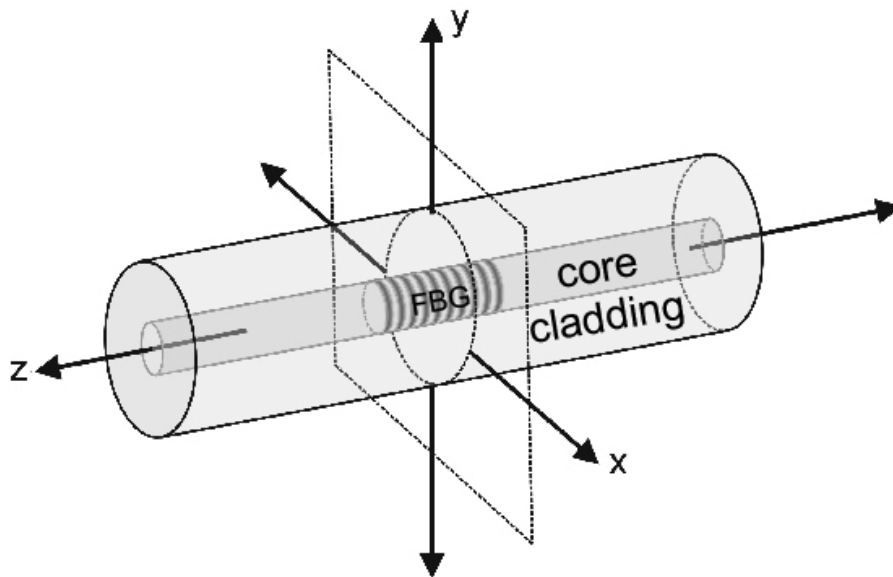


**Figure 3.2:** Structure of an optical fiber with an embedded FBG. The external plastic coating surrounding the glass guiding part of the fiber is not indicated here.

period chirped gratings [24]. Only homogeneous gratings inscribed in low birefringence single mode (SM) fibers are considered here. For an homogeneous grating, the FBG reflected signal is comprised of a main, relatively narrow, peak centred at the Bragg wavelength  $\lambda_{B0}$ , which is related to the product of the mean effective refractive index  $n_{eff}$  and the grating period  $\Lambda$  through the Bragg condition [53]

$$\lambda_{B0} = 2n_{eff}\Lambda \quad (3.2.1)$$

Note that, for weakly guiding fiber (as those used in these applications)  $n_{eff} \simeq n_0(x, y) \simeq n_{co}$ , where  $n_0(x, y)$  is the index profile of the unperturbed fiber and  $n_{co}$  is the index of the fiber core [73]. In principle, the transmitted spectrum of a fiber grating is complementary to the reflected one [53].

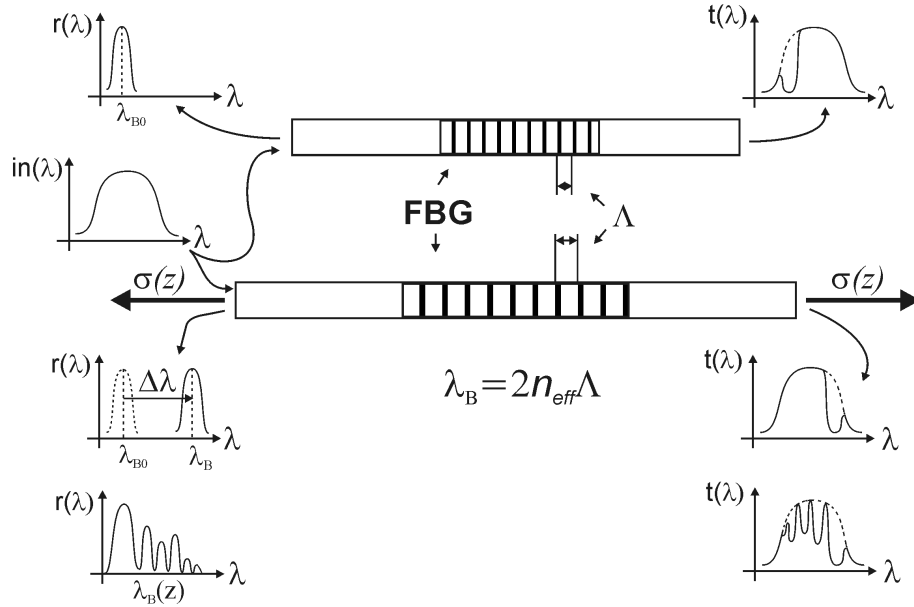


**Figure 3.3:** *FBG working principle.* The broadband light  $in(\lambda)$  is launched into the fiber core.  $r(\lambda)$  and  $t(\lambda)$  are the reflected and transmitted signals respectively, around the Bragg wavelength  $\lambda_{B0}$ .  $\Lambda$  is the grating period. In particular, when the grating is stretched, the reflected Bragg peak simply shifts or presents multiple peaks depending whether the deformation it undergoes is uniform or not.

However, it is not generally the case because of the transmission losses due to connections (or those coming from coupling to cladding modes in the case of multi-mode (MM) fibers) [74]. The spectral response of the FBG is influenced by the environmental conditions. In particular, both strain and thermal variations in the grating region induce changes in the effective index of the fiber and the grating period, resulting in a modification of the Bragg condition. Thus, when the grating is subjected to uniform changes in strain and/or temperature all grating periods experience the same changes resulting in a shift of the Bragg wavelength without modification of the spectrum shape.

For a non-uniform variation of applied load or temperature, the resulting Bragg wavelength becomes a function of the position  $z$  along the grating. Assuming constant temperature and neglecting all birefringence and dispersion effects in the fiber, the three-dimensional load-induced Bragg wavelength shift can be described by the following equation [72]

$$\frac{\lambda_B(z) - \lambda_{B0}(z)}{\lambda_{B0}(z)} = \frac{\Delta\lambda_B(z)}{\lambda_{B0}(z)} = \epsilon_z(z) - \frac{n_{eff}^2}{2}(p_{12}\epsilon_z(z) + \frac{1}{2}(p_{11} + p_{12})(\epsilon_x(z) + \epsilon_y(z))) \quad (3.2.2)$$

where  $p_{11}$ ,  $p_{12}$  are the Pockels strain-optic constants of the undisturbed fiber and  $\epsilon_x(z)$ ,  $\epsilon_y(z)$ ,  $\epsilon_z(z)$  are the principal strain components within the SM fiber core. The subscript  $z$  stands here for the axial direction. The function  $\lambda_{B0}$  indicates that a non-uniform Bragg wavelength may exist at the chosen reference state. When the experimental conditions are such that  $\epsilon_{x,y}(z) = -\nu_f\epsilon_z$ , where  $-\nu_f$  is the Poisson's ratio of the fiber, equation (3.2.2) can be simplified to

$$\frac{\Delta\lambda_B(z)}{\lambda_{B0}(z)} = [1 - \frac{n_{eff}^2}{2}((1 - \nu_f)p_{12} - \nu_f p_{11})]\epsilon_z(z) \quad (3.2.3)$$

This corresponds to the assumptions of Butter and Hocker describing strain effect on the fiber [15]. Finally, for axial strain measurements, equation (3.2.3) is often presented in this more compact form

$$\frac{\Delta\lambda_B(z)}{\lambda_{B0}(z)} = (1 - p_e)\epsilon_z(z) \quad (3.2.4)$$

where  $p_e$  is the effective photo-elastic coefficient which can be easily determined experimentally ( $\cong 0.22$  in the case of the fiber considered here).

### 3.3 OLCR Technique

As indicated in equation (3.2.4), the strain distribution along the grating requires the knowledge of the local Bragg wavelengths corresponding to the actual state and the reference state. According to the coupled mode theory [74, 41, 24], light propagation through a FBG can be described by a coupling between the forward-propagation fundamental guided mode and its backward-propagating counterpart. This implies the introduction of a unique complex coupling coefficient  $q(z)$  to be determined from pertinent experimental data. The novel optical low coherence reflectometer (OLCR) apparatus, designed at EPFL, allows one to measure precisely the FBG complex impulse response  $h(t)$  (where  $t$  represents the time variable) with high precision and low noise (generally below -120 dB). Details can be found in [36]. The incident light is sent into the reflectometer where it is split by a 3-dB coupler into two equal beams which illuminate the reference and test arms. The latter contains the FBG. In the reference arm, light is reflected by a mirror which is mounted on a translating stage. By moving the mirror, one interrogates the FBG on its overall length. Then, the total backward signal recorded by a dual phase lock-in amplifier included in the detection system (Fig. 3.4)

that directly extracts the amplitude and phase information of  $h(t)$ . Once  $h(t)$  is measured, one calculates the spectral response  $r(\lambda)$  of the grating by Fourier transform and  $q(z)$  can be retrieved from  $r(\lambda)$  using the layer-peeling reconstruction algorithm [36, 73]. Finally, the retrieval of the local Bragg wavelength  $\lambda_B(z)$  is obtained by the derivative of the phase of the complex coupling coefficient  $\phi(z)$  through the following equation

$$\lambda_B(z) = 2n_{eff}\Lambda_d \left( 1 + \frac{\Lambda_d}{2\pi} \frac{d\phi(z)}{dz} \right)^2 \quad (3.3.1)$$

where  $\Lambda_d$  is the design grating period [34, 36]. A simple schematic of the OLCR setup and the associated reconstruction process are summarized in Fig.3.4 and Fig.3.5.

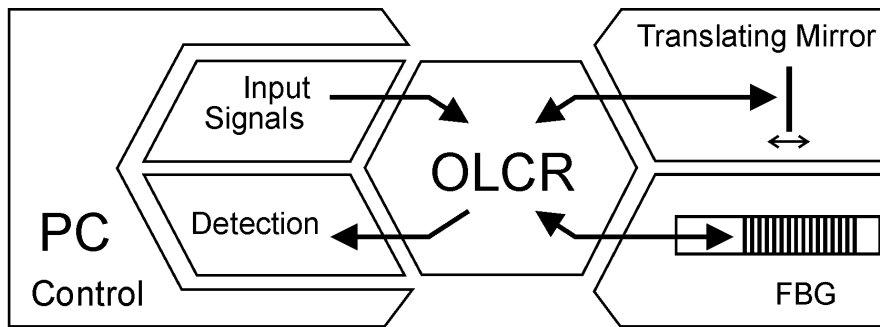


Figure 3.4: Simplified scheme of the OLCR-setup.

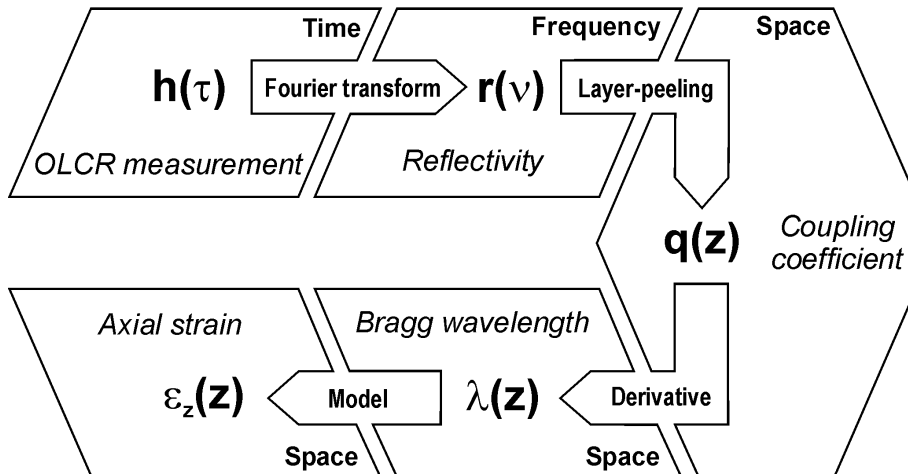
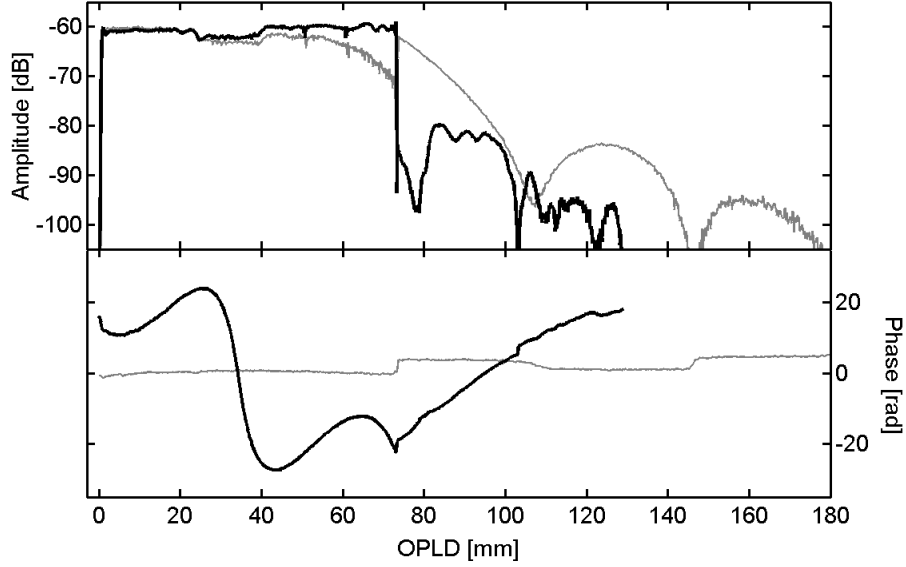


Figure 3.5: Principle of OLCR-based method to reconstruct the strain distribution from FBG impulse response measurements.

Some examples of measurements conducted with the OLCR system are illustrated in Fig.3.6 and Fig.3.7. Given in Fig.3.6 are the amplitude (top) and phase (bottom) of the FBG impulse

response. The curves in light line (bold line) correspond to a non-embedded (embedded) FBG sensor. In Fig.3.7 the reflection intensity spectra (top) and local Bragg wavelengths (bottom) are depicted for the FBG configurations considered in Fig.3.6



**Figure 3.6:** Plots of the amplitude (top) and the phase (bottom) of the impulse response for not embedded (grey line) and embedded (black line) FBG. The OPLD scale distance corresponds to the optical path length difference in vacuum between the reference and the test arm

### 3.4 Preliminary test: residual strain distribution in a block of epoxy

The proposed OLCR technique is initially used to determine the residual strain field generated around an optical fiber embedded in an easier to make rectangular  $25 \times 25 \times 40$  mm block of epoxy with the aim of examining and ensuring the reproducibility of the results [20]. The same geometry was successfully used in the previous work of Bosia et al. [10] to study the sensitivity of the FBG to transversal loading in PM fibers. The mould especially designed to prepare the specimens is depicted in Fig.3.8.

The fiber is placed along the longitudinal axis of symmetry ( $z$ ) and a 24-mm long FBG is located at the center of the specimen as indicated in Fig.3.9.

Acting as a cylindrical elastic inclusion which is more rigid than the surrounding matrix, the fiber clearly promotes the development of additional residual stresses in the neighbouring region. They are mainly caused by the volume shrinkage of the epoxy resin during curing and post-curing treatment and by the mismatch between the elastic and thermal properties of the two constituents. In particular, due to the polymerization, the epoxy matrix undergoes a substantial volume reduction: this effect is shown by the analysis of the FBG reflected spectra

§3.4. PRELIMINARY TEST: RESIDUAL STRAIN DISTRIBUTION IN A BLOCK OF EPOXY21

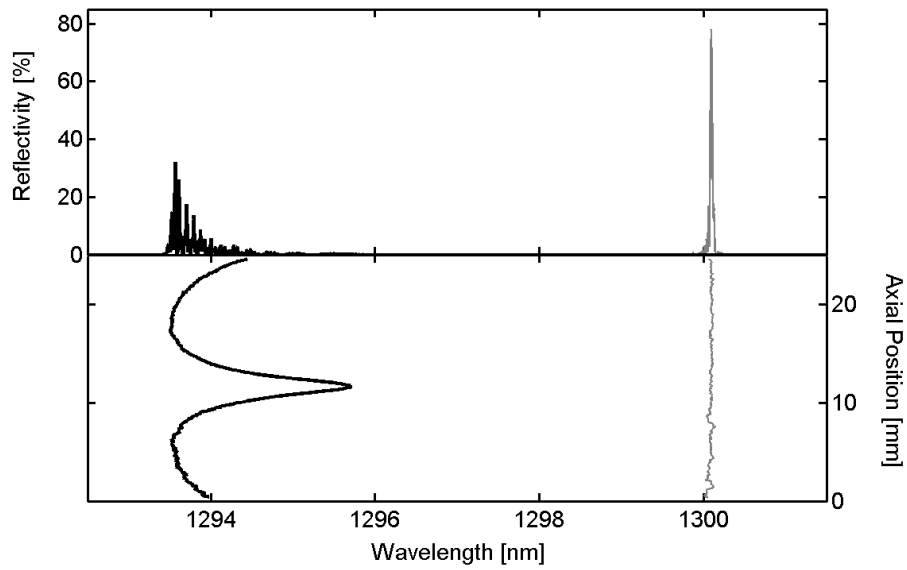


**Figure 3.7:** Corresponding reflection intensity spectra (top) and local Bragg wavelength (bottom) for not embedded (grey line) and embedded (black line) FBG

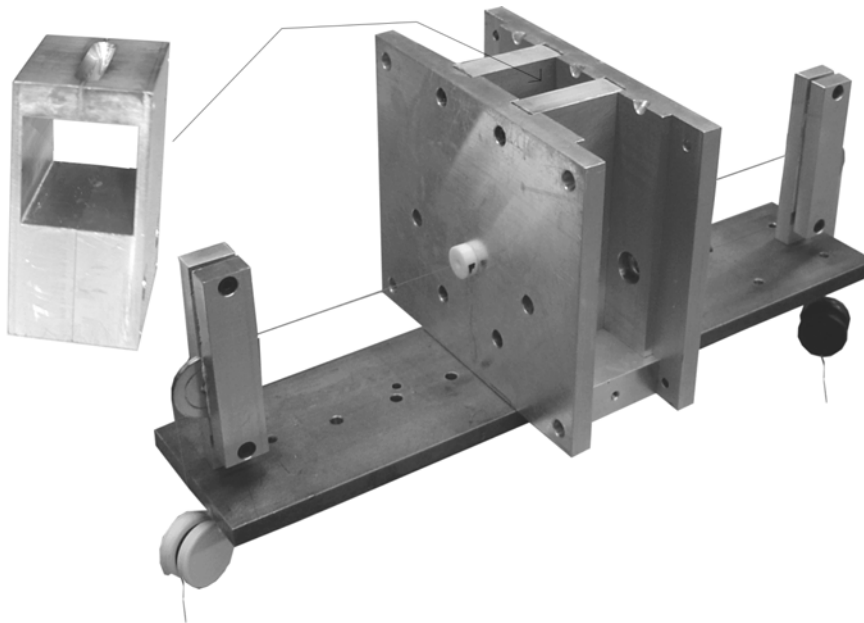


**Figure 3.8:** View of the mould used to prepare the block specimens in the so called "horizontal configuration".

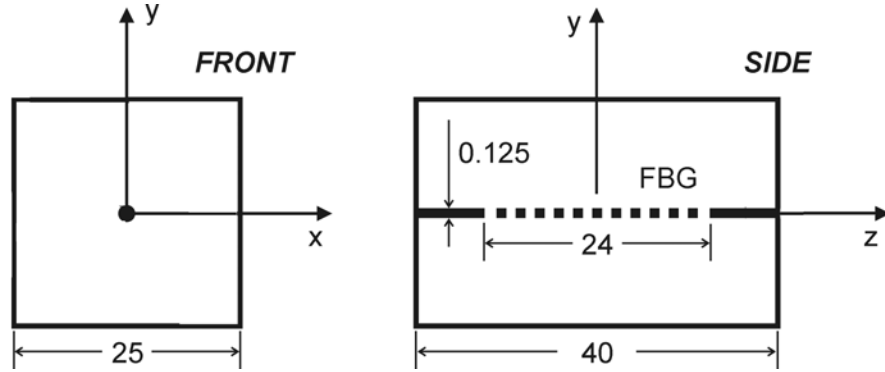


**Figure 3.9:** Scheme of the block specimen (dimensions are in mm). The location of the FBG is also indicated.

when they are reconstructed for three important steps of the specimen preparation: before embedding, two hours after curing and two hours after post-curing.

From the previous results, it appears that the specimen sustains an important non-uniform compressive strain during fabrication, shown by the shape and the position of the resulting reflected spectra Fig.3.10.

The maximum shift of the Bragg wavelength peak provides an idea of the maximum value of deformation applied to the grating whereas the distribution of the reflected wavelengths gives information on the non-uniformity of the strain profile applied along its length. The OLCR measurements allow to express the local Bragg wavelength distribution  $\lambda_B(z)$ , as a function of  $z$  along the grating length at different stages of the manufacturing process Fig.3.11. When the new  $\lambda_B(z)$  is known, the corresponding strains are calculated by the relation 3.2.4 and represented in Fig.3.12 for a typical case.

It is important to notice the form of the strain profile, with a maximum compressive strain of  $-2000 \mu\epsilon$  and  $-6000 \mu\epsilon$  at the centre, after the curing and the post-curing process respectively. It is also important to underline that the values of strain can be calculated with a maximum resolution of  $30 \mu\epsilon$  due to the physical limit of the OLCR apparatus (the source bandwidth) which enables to measure the Bragg wavelength with a resolution higher than  $25 \text{ nm}$ . At the moment, another important limit of this kind of system is the possibility to do measurements in dynamic configuration. This is due to the high sensibility of the interference-based system to the influence of external actions, which can produce a noise which make impossible to come out the measurement process itself. Nevertheless, despite these drawbacks, in literature there is no notice of better instruments (in terms of resolution) to perform distributed measurements at least for static or quasi-static experimental configurations.



§3.4. PRELIMINARY TEST: RESIDUAL STRAIN DISTRIBUTION IN A BLOCK OF EPOXY<sup>23</sup>

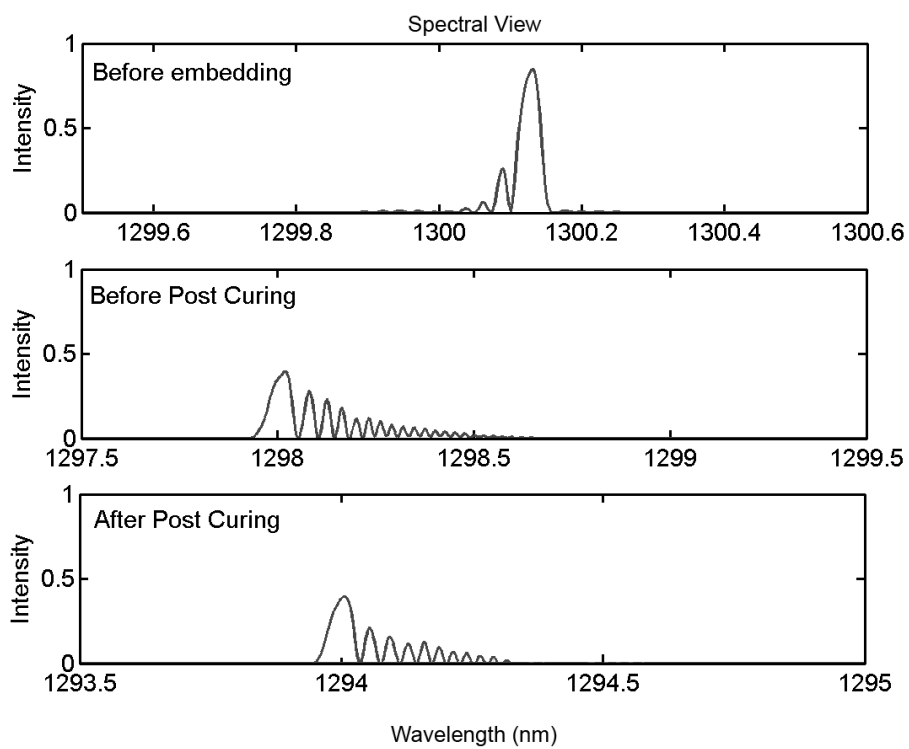


**Figure 3.10:** Typical FBG reflected spectra during the three stages of the specimens fabrication.

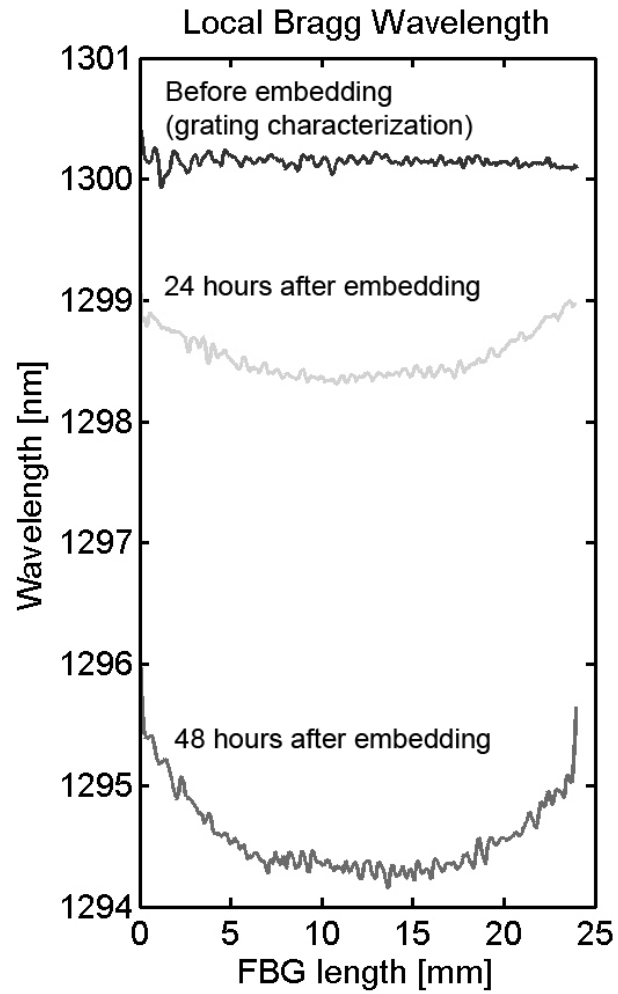


**Figure 3.11:** Local Bragg wavelength distributions  $\lambda_B(z)$  calculated for three processing time. The corresponding spectra are shown in Fig.3.10.

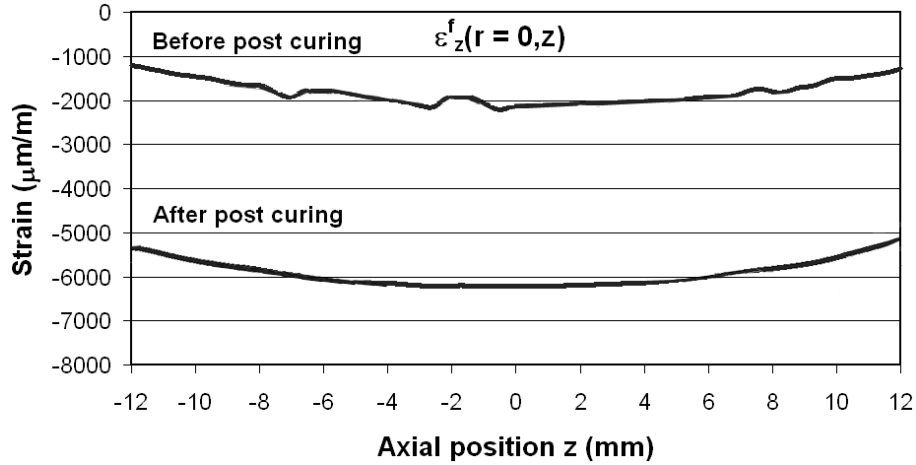


**Figure 3.12:** Axial strain distribution measured before and after post-curing for the block specimen realized in the horizontal configuration.

### 3.5 The transfer matrix (T-Matrix) approach to compute the FBG spectra

The main advantage presented by the OLCR technique to characterize FBG's is the possibility to directly retrieve the local Bragg wavelength distribution by using the layer peeling reconstruction algorithm and, consequently, the exact spectrum of a uniform and non-uniform deformed grating.

Nevertheless, there are a variety of methods to compute the reflection and the transmission spectra of non-uniform gratings [24, 34, 73] but their performances depend on the knowledge of the grating parameters and on the exact deformation (i.e. the wavelength distribution due to an applied load) along the sensor length.

One of the preferred technique is called the transfer matrix method (T-Matrix) where, based on an inverse scattering approach, one first divides the grating into smaller sections each one treated as simple uniform grating, yielding the overall FBG spectrum by matrix multiplication.

For a uniform grating, the coupling coefficient  $q(z)$  is considered constant over a limited range  $0 \leq z \leq L$  where  $L$  is the grating length. The coupled-mode equations can be solved analytically where, in particular, the amplitude and the power reflection coefficients  $r(\hat{\sigma})$  and  $R(\hat{\sigma}) = |r(\hat{\sigma})|^2$  can be written as follows [24, 34, 74, 73]

$$r(\hat{\sigma}) = \frac{-|q| \sinh(\gamma L)}{\hat{\sigma} \sinh(\gamma L) + i\gamma \cosh(\gamma L)} \quad (3.5.1)$$

$$R(\hat{\sigma}) = \frac{\sinh^2(\gamma L)}{\cosh^2(\gamma L) - \left(\frac{\hat{\sigma}}{|q|}\right)^2} \quad (3.5.2)$$

where, for a single-mode reflection grating,  $\gamma = \sqrt{|q|^2 - \hat{\sigma}^2}$ ,  $\hat{\sigma} = \delta + \sigma$ ,  $\delta = \beta - \frac{\pi}{\Lambda_d}$ ,  $\sigma = \frac{2\pi}{\lambda} dn_{eff}$ ,  $\beta = \frac{2\pi n_{eff}}{\lambda}$  and  $|q| = \frac{\pi}{\lambda} \eta dn_{eff}$  with  $\eta$  defined as the fringe visibility coefficient. In particular the plot of  $R(\hat{\sigma})$  corresponds to the FBG spectrum (in reflection), where the maximum value of reflectivity  $R_{MAX}$  is given by

$$R_{MAX} = \tanh^2(|q|L) \quad (3.5.3)$$

To correctly apply the T-Matrix method, the grating has to be divided in a sufficiently large number of sections  $N$  so that each section can be treated as approximately uniform and characterized by a coupling coefficient  $q_j$  and thickness  $\Delta_j$  (see Fig.3.13). The knowledge of

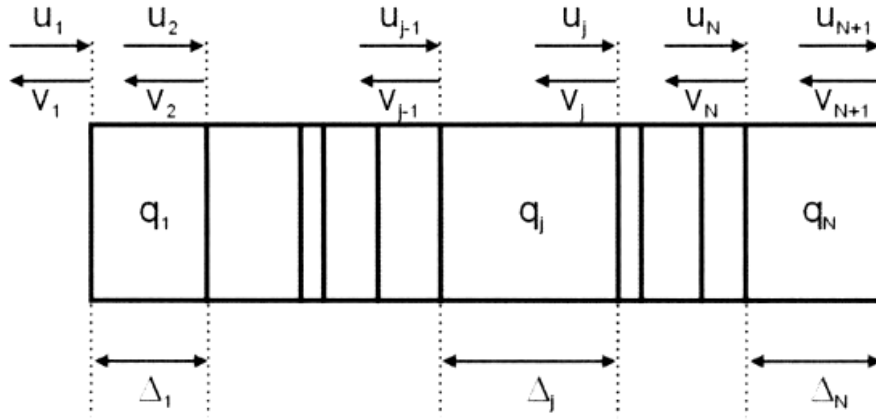


**Figure 3.13:** FBG slicing in sub-sections for the T-Matrix method [34]

the fields  $u_j$  and  $v_j$  at the entrance of section  $j$  allows to find the fields  $u_{j+1}$   $v_{j+1}$  at the layer output. Here  $u_j$  and  $v_j$  represent the forward and backward propagating field envelopes in the layer of thickness  $\Delta_j$  mutually coupled by the coupled mode equations.

The interaction between two layers can be expressed in the form of a transfer matrix relation

$$T_j = \begin{bmatrix} \cosh(\gamma_j \Delta_j) - i \frac{\hat{\sigma}}{\gamma_j} \sinh(\gamma_j \Delta_j) & \frac{q_j^*}{\gamma_j} \sinh(\gamma_j \Delta_j) \\ \frac{q_j}{\gamma_j} \sinh(\gamma_j \Delta_j) & \cosh(\gamma_j \Delta_j) + i \frac{\hat{\sigma}}{\gamma_j} \sinh(\gamma_j \Delta_j) \end{bmatrix} \quad (3.5.4)$$

The fields  $u_1$ ,  $v_1$  and  $u_{N+1}$ ,  $v_{N+1}$  at the grating entrance and output respectively, are then related to each other by

$$\begin{bmatrix} u_{N+1} \\ v_{N+1} \end{bmatrix} = T_N \cdot \dots \cdot T_j \cdot \dots \cdot T_1 \begin{bmatrix} u_1 \\ v_1 \end{bmatrix} = T \begin{bmatrix} u_1 \\ v_1 \end{bmatrix} = \begin{bmatrix} T_{11} & T_{12} \\ T_{21} & T_{22} \end{bmatrix} \begin{bmatrix} u_1 \\ v_1 \end{bmatrix} \quad (3.5.5)$$

Since the reconstruction grating problem is a boundary value problem, the reflection coefficient amplitude  $r(\hat{\sigma})$  of a fiber grating of length  $L$  (see Fig.3.2) can be found by assuming a forward-going wave incident from  $z = -\infty$  (corresponding to the limit condition  $u_1 = 1$ ) and requiring that no backward-going wave exists for  $\frac{L}{2} \leq z$  (i.e.  $v_{N+1} = 0$ ). Moreover, since  $r(\hat{\sigma}) = \frac{v_1}{u_1}$  from the boundary conditions is easy to verify that  $r(\hat{\sigma}) = \frac{-T_{21}}{T_{22}}$ . The number of

section needed for the piecewise-uniform calculation is determined by the required accuracy. Nevertheless,  $N$  may not be made arbitrarily large, since the coupled mode theory approximations are not valid when a uniform grating section is only a few grating periods long. Thus the condition to be fulfilled is  $\Delta_j \gg \Lambda$  which means that  $N \ll \frac{2n_{eff}L}{\lambda_D}$ . It is easy to understand that the last request can be a problem when the evolution  $q(z)$  presents high gradients and then the dimension of  $\Delta_j$  have to be decreased in order to consider the grating as uniform in any sub-domain.

It is important to underline that though all the physical parameters of the grating are known, the T-Matrix method allows to calculate the complex spectral response  $r(\nu)$  only if the complex coupling coefficient  $q(z)$  is defined all over the grating length. In other words the reconstruction process is possible only if the exact local Bragg wavelength distribution (which is related to the phase derivative of  $q(z)$ ) is provided as an input data. In this case the indirect T-Matrix method and the direct layer-peeling reconstruction process give the same results (the only difference is the time necessary for the complete reconstruction which is shorter in the case of the layer-peeling approach).

In Fig.3.14 are shown the spectrum and the wavelength distribution of a grating embedded in block of epoxy similar to that one presented in Fig.3.9. As expected, the reconstruction of the

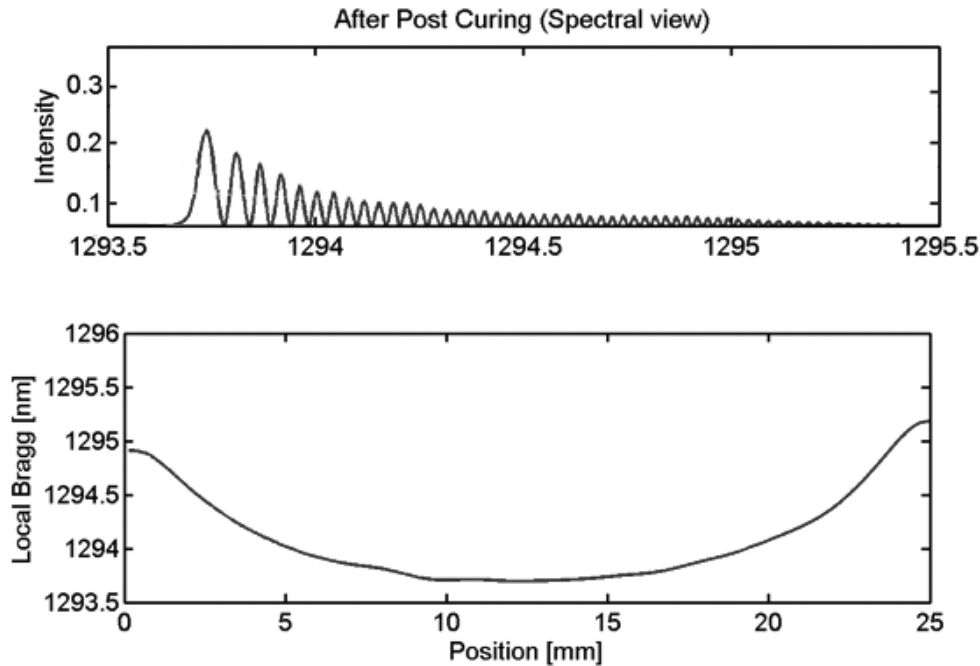


**Figure 3.14:** *Spectrum and local Bragg evolution reconstructed with the OLCR technique. The spectrum corresponds to real one measured with a simple spectrometer.*

same grating via T-Matrix is in good agreement with the results obtained by the OLCR and the layer-peeling approach (Fig.3.16). Since the physical parameters used in the two methods are the same, the differences in the spectra can be attributed to the approximation in defining

the chirp function (the variation in the phase of the coupling coefficient) which comes from a direct interpolation of the local Bragg distribution of Fig.3.14 (see Fig.3.15 a)). It is then

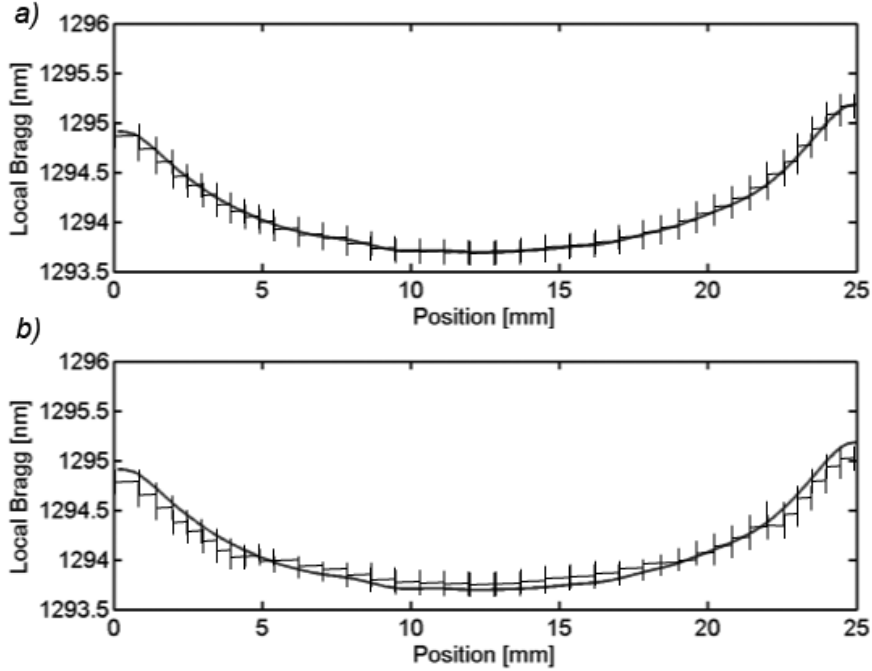


**Figure 3.15:** Interpolation of the local Bragg wavelength evolution of Fig.3.14 by two slightly different piecewise constant functions.

clear that the major problem in using the simple T-Matrix approach without the information provided by the OLCR is the knowledge of the grating chirp function. If no indication is given about the local Bragg distribution along the grating for example as a consequence of an external applied load, the only way to guess the wavelength distribution is to use the FE element method. Starting from an initial possible distribution a minimization procedure is then used to find the best wavelength evolution which allows to retrieve the real reflected spectrum. Unfortunately, because in practice this corresponds to solve an inverse problem it is not unrealistic that the distribution giving the best spectrum's fit does not correspond to the real deformation applied on the sensor. From a mechanical point of view this corresponds to determine a strain distribution which is not the real one. In order to show the importance of well defining the initial local Bragg distribution, if the piecewise function used to interpolate  $\lambda_B(z)$  of Fig.3.14 is slightly changed (Fig.3.15 b)) the differences between the real and simulated spectra become more important (Fig.3.17).

Other examples where the T-matrix based approach fails by introducing greater errors while the OLCR based technique overcomes all the problem's difficulties can be found in Appendix A.

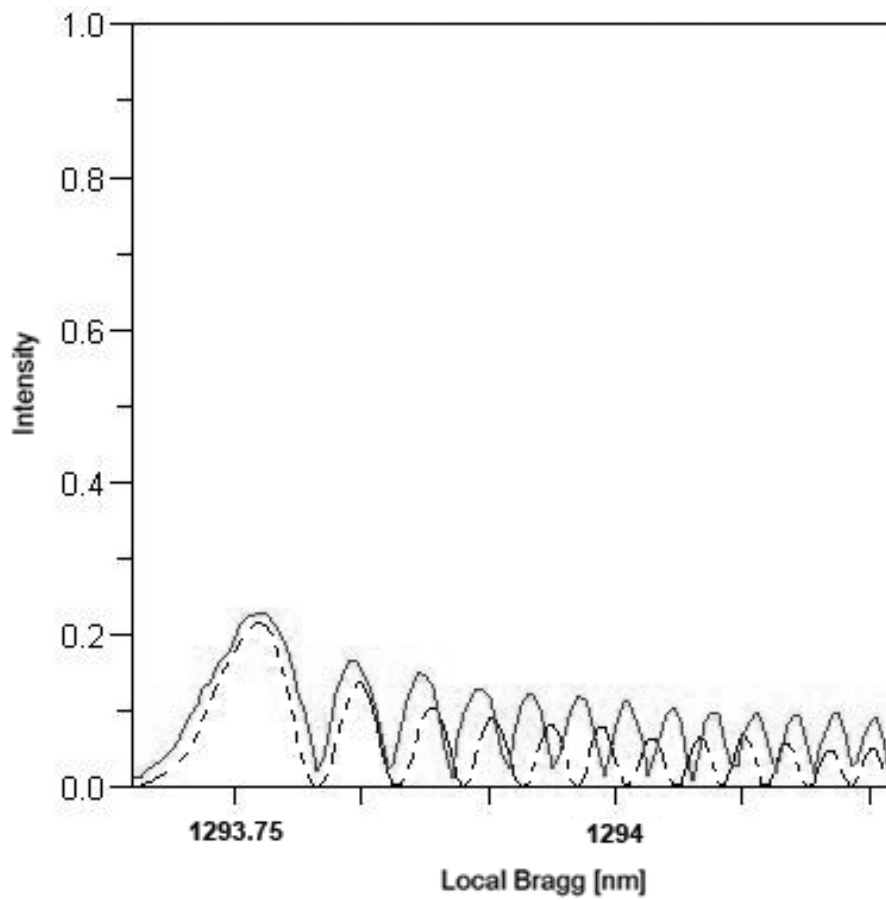


**Figure 3.16:** Comparison between the reconstructed spectrum via the OLCR and layer-peeling algorithm (solid line) and the spectrum retrieved by using the T-Matrix approach (dashed line).

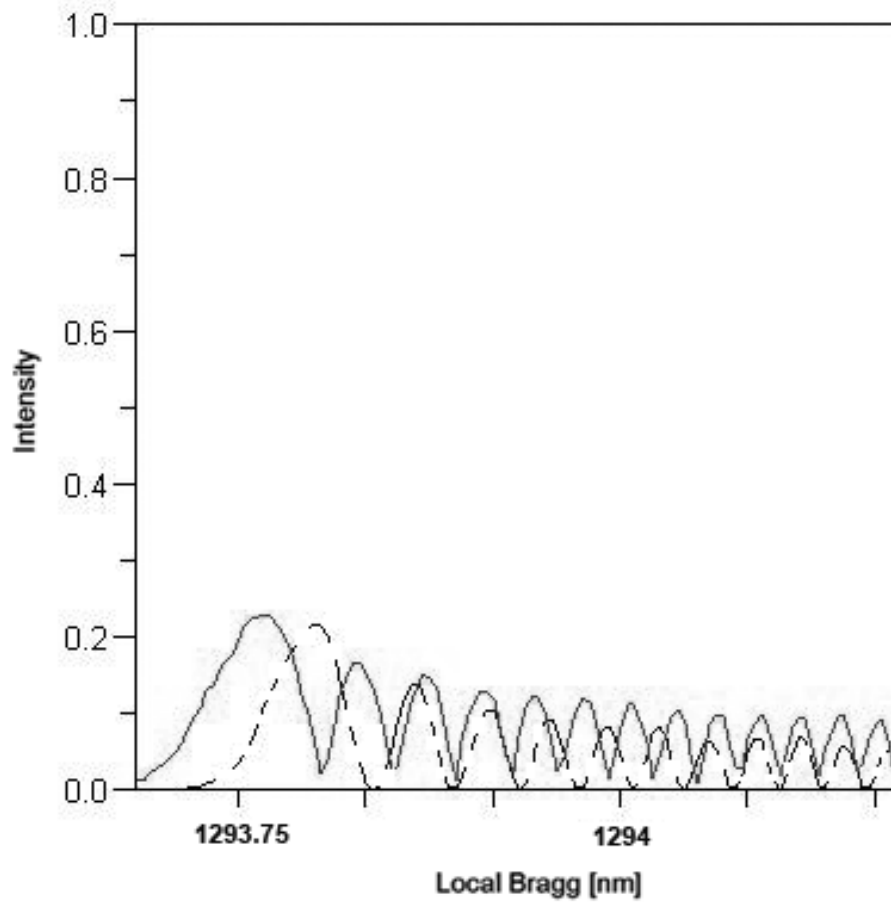


**Figure 3.17:** Comparison between the reconstructed spectrum via the OLCR and layer-peeling algorithm (solid line) and the spectrum retrieved by using the T-Matrix approach (dashed line) when the piecewise function does not correspond exactly to the  $\lambda_B(z)$  evolution of Fig.3.14.



## Chapter 4

# Materials and methods

### 4.1 The single fiber composite (SFC) specimen: the difficulties in treating the problem

Designing an experiment to characterize the mechanisms that govern the behaviour of a composite structure is generally a difficult task to achieve in practice. The complex morphology often makes the local strain/stress field very difficult to analyze because the position as well as the contour of the different constitutive phases of the composite (matrix and reinforcement) are generally not well defined. Moreover, there are many other parameters (e.g. interface properties) which interact in a complicated manner thus making the study unrealizable. Alternatively, one can simplify and reduce the geometric complexity without appreciable loss of generality by considering a specific portion of the real composite structure. In that sense the block specimen previously presented represents a simplified approach in the study of the composite behavior. It may be considered as a basic component or element from which a real composite can be assembled.

To further simplify the geometry, one may instead use a cylindrical specimen, thus providing an axisymmetric unit cell that represents the composite material (Fig.4.1). This configuration is referred to as a single-fiber composite specimen (SFC).

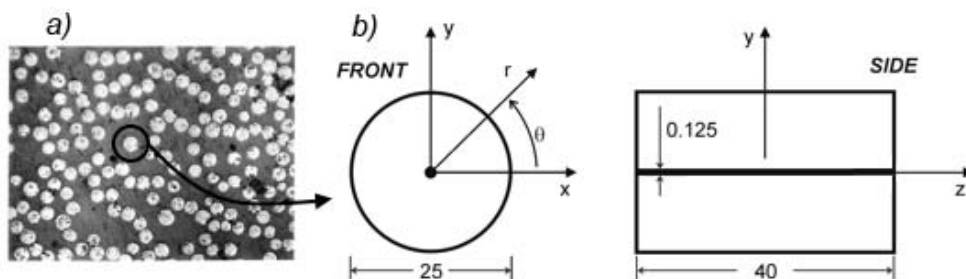


**Figure 4.1:** *a)* Typical transverse section of a unidirectional composite [22] and *b)* schematic of the SFC cylindrical specimen extracted from the real material. Dimensions are in mm.

Such a configuration has been used by several researchers in the past (see for example [13, 12]) for typical fiber pull-out and push-out tests. It has also proven to be very convenient especially to investigate residual stresses in fiber-reinforced composite materials [32, 56] and will be adopted here.

In the present case, the outer radius of the matrix cylinder is taken much larger than the radius of the fiber, corresponding to a small fiber volume fraction of  $2.5E-5$ . Clearly, this is not a representative volume element of a fiber-reinforced composite such as the one depicted in Fig.4.3a). Nevertheless, such choice is motivated by the fact that this configuration eliminates free surface effects and creates high level of residual stresses in the fiber. In this work, the chosen specimen length and diameter correspond to those presented in Fig.4.3. This can be viewed as the limiting case of a single fiber in an infinite matrix. Note that such a configuration allows further comparison with the theoretical results of Mikata and Taya [56], at least in the central region far from the specimen's ends. It is expected that the initial length chosen for the cylinder ( $L = 40 \text{ mm}$ ) is large enough with respect to the specimen radius to be able to neglect the ends effects in the central region of interest. In other words, the choice of  $L$  is motivated by the objective of obtaining generalized plane strain conditions and consequently constant residual stresses in a large portion of the fiber. This point is discussed in the next chapter.

## 4.2 Specimen preparation

All the specimens fabricated and tested in this work contain a standard optical glass fiber of  $125 \mu\text{m}$  (Fig.3.2) in diameter centrally located along the axial direction and embedded in an epoxy matrix as indicated in Fig.3.9.

The optical fiber-host system is viewed as a two phase composite, for which the fiber volume fraction is very small compared with that of the epoxy. The optical fiber, supplied by Avensins Inc., is equipped with a FBG of 24 mm in length, whose center coincides initially with the center of the specimen and the origin of the system of coordinates (Fig.3.9). Before positioning the fiber and pre-straining it to  $870 \mu\epsilon$  to obtain a correct alignment, its acrylate coating is stripped along the entire embedded length ( $L=40 \text{ mm}$ ) using a hot sulphuric acid bath (Fig.4.2).

The stripped surface is also cleaned by mean of successive baths in ethyl alcohol to assure clean interface conditions.

To prepare the epoxy, an established standard protocol is followed [2], that uses a mixture of  $DER^{TM}330$ ,  $DER^{TM}732$  Dow Epoxy resins and  $DEH^{TM}26$  curing agent in respective weight proportions of 70 : 30 : 10. Once the polymerization process is completed at room temperature (24 hours), the specimen is removed from the mould and placed in an oven for post-curing at  $60^\circ$  for 9 hours. It is then left to cool inside the oven until room temperature is reached. The material properties considered for the epoxy matrix are  $E_m = 2.35 \text{ GPa}$ ,  $\nu_m = 0.38$ . In particular, the Young modulus  $E_m$  has been experimentally determined according to ASTM test procedures [1]. For the glass fiber these parameters are 72 GPa and 0.17 respectively, and they have been directly provided by the manufacturer. When the specimen preparation

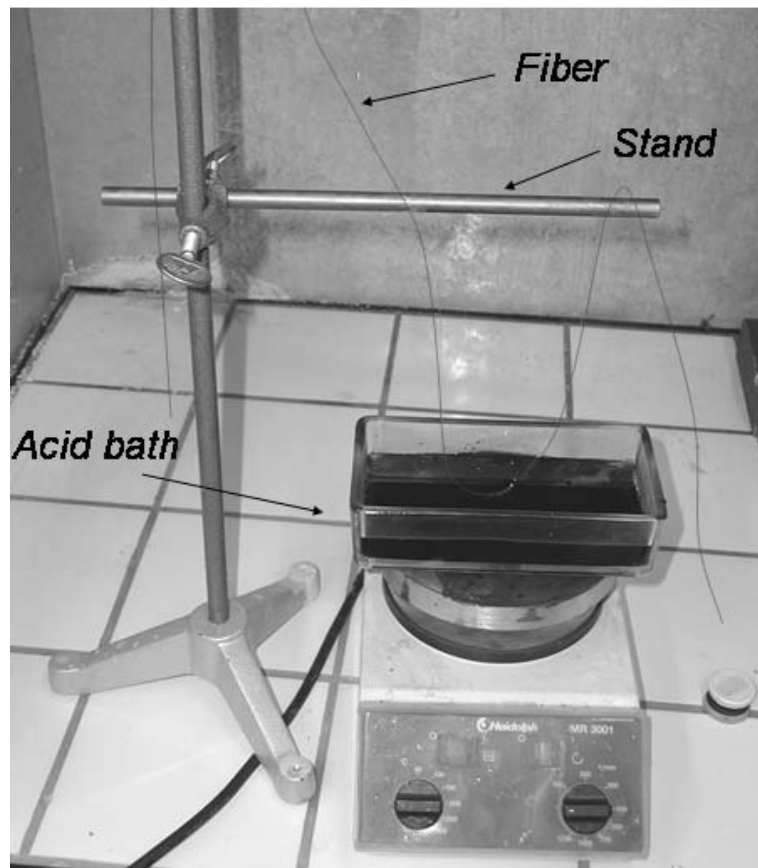


**Figure 4.2:** Stand used to strip the acrylate coating from the fiber by mean of sulfuric acid bath ( $H_2SO_4$ , 96%).

is completed, precise measurements of both length and position of the grating with reference to one end of the specimen are carried out using the OLCR apparatus [77].

### 4.3 Specimen geometry

After the preliminary tests on the block specimen presented in Chapter 3, a second kind of specimen was manufactured. The new geometry is a cylinder with a radius of 12.5 mm and length of 40 mm. Due to the cylindrical symmetry conditions, this configuration is simpler to use in numerical simulations and also allows the results to be compared with existing analytical models. Moreover, the specimen dimensions are such that they can be directly compared with the data obtained from the block sample (Fig.4.3).

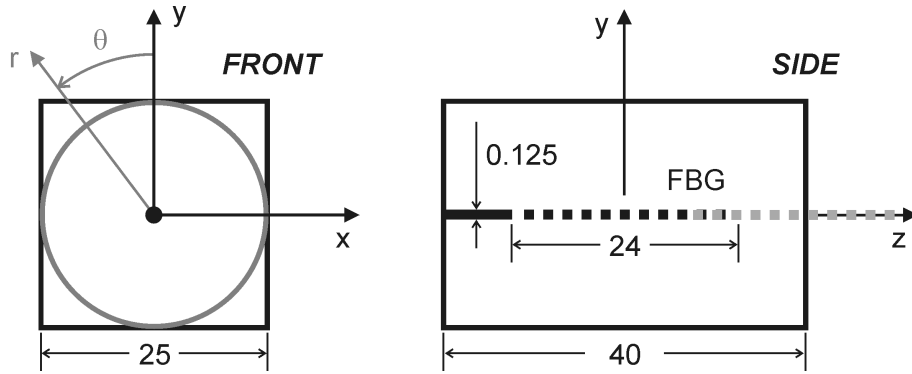


**Figure 4.3:** Comparison between the geometry of the block and the new cylindrical geometry. Two possible locations of the FBG are also shown: when it is centrally (black line) and partially (grey line) embedded. Dimensions are in mm.

To prepare the cylinder the same mould designed for the the block was used, by simply changing the forming parts as indicated in Fig4.4. A second series of preliminary tests were conducted by using this cylindrical geometry. By using the OLCR technique the residual strain distribution along the grating length was also retrieved in this case. As indicated in Fig.4.5, no appreciable differences are present between the two geometries, thus meaning that in this particular case, the block and the cylinder can be considered equivalent.

In order to verify that the shape of the strain distribution Fig.4.5 does not depend on the specimen orientation (gravity effect), a special mould has been designed such that the new orientation of the fiber is vertical (Fig4.6). As depicted in Fig.4.7 the OLCR analysis reveals that, also in this last case, the influence of specimen orientation during polymerization does not play an important role on the level and on the form of the residual strain distribution inside the sample (Fig.4.7).

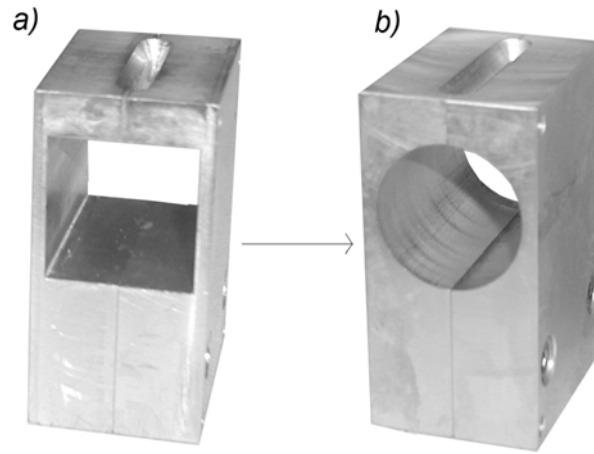


**Figure 4.4:** Parts of the mould used to realize the block **a)** and the cylinder **b)** in the horizontal configuration. See also Fig.3.8 for more details.

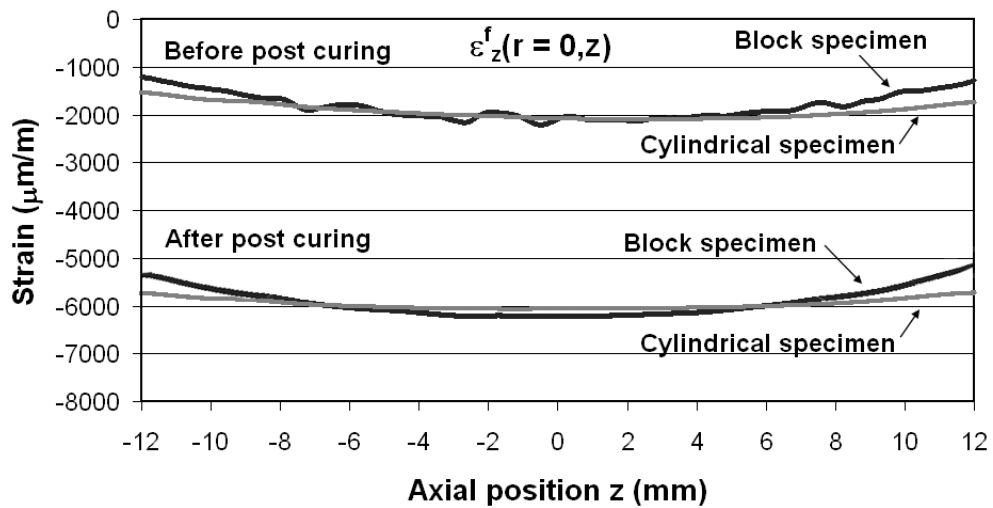


**Figure 4.5:** Direct comparison between the measured axial strain distribution before and after post-curing for the block and the cylindrical specimen produced in the horizontal configuration.



**Figure 4.6:** *Mould used to prepare the cylindrical specimen in the "Vertical configuration".*

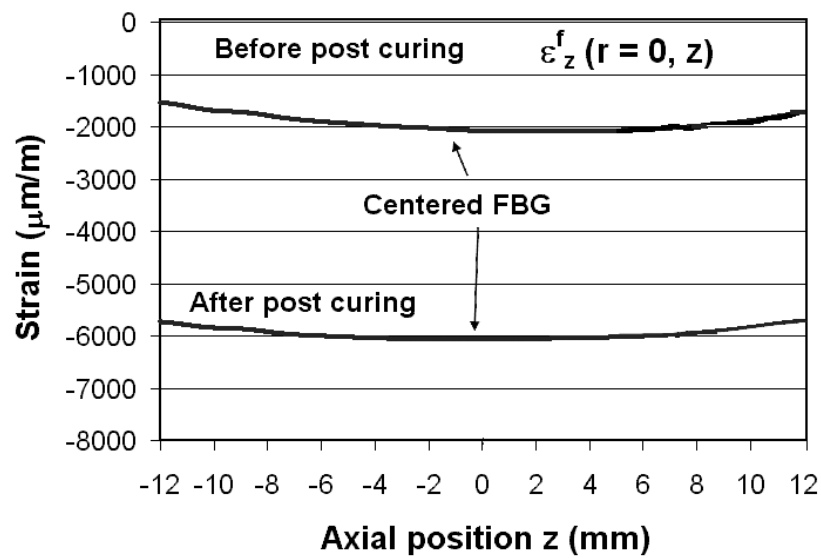


**Figure 4.7:** *Axial strain distribution measured before and after post-curing for a cylindrical specimen realized in the mould of Fig.4.6 and FBG centrally located.*

## Chapter 5

# Residual axial strain and stress field in a SFC specimen

### 5.1 Axial strain evolution for different FBG positions

Since the FBG can be precisely located in different positions along the main axis of symmetry of the cylinder (from the center to the outside) (Fig.4.3), the complete strain distribution along the entire length of the embedded optical fiber core has been experimentally determined. This is accomplished by using two specimens: one with the FBG covering the region  $z = \pm 12\text{mm}$  (centered) and one with the FBG in the  $z = 5$  to  $z = 30$  region ( $\frac{2}{3}$  inside and  $\frac{1}{3}$  outside). By superimpose the response of these two sensors, and assuming symmetry about  $z = 0$ , one obtains the strain distribution along the entire length of the specimen. The strain curves obtained before curing and after post-curing all along the specimen length are depicted in Fig.5.1

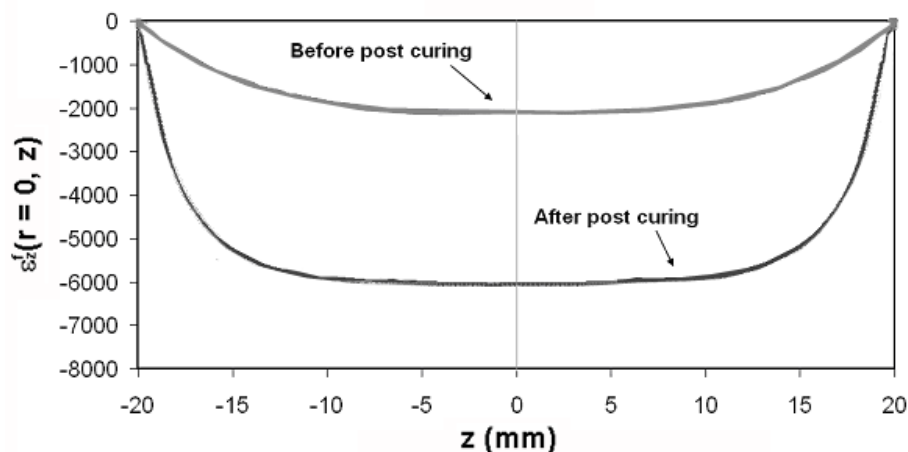


**Figure 5.1:** Axial strain distribution obtained for the cylindrical specimen of 40 mm length measured before and after post-curing.

One can observe that after the complete matrix consolidation, the strains (i.e. the local Bragg wavelengths) evolve in the axial direction following a fourth-order distribution. By considering Hooke's law and taking into account the geometrical dimensions of the specimen and the mechanical parameters of the materials, the maximum compressive stress value is found to be  $-450$  MPa. The complete stress distribution for a post-cured specimen is represented in Fig.5.2. All these data are employed as appropriate boundary conditions for the analysis of

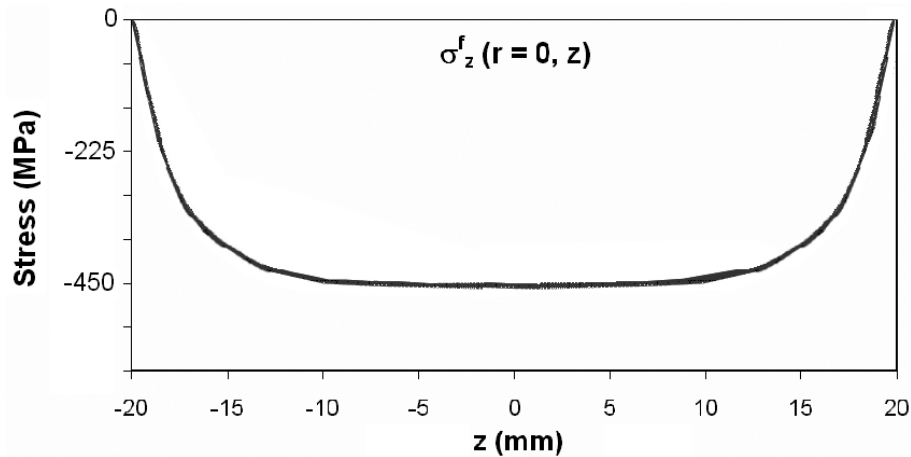


**Figure 5.2:** Axial stress distribution obtained for the cylindrical specimen of 40 mm length and 12.5 mm radius after the post-cure treatment.

the residual strain and stress field in the surrounding epoxy host by using the finite element method.

## 5.2 Dimensional effect on the residual axial strain field

While the level of residual stresses within a composite principally depends on the material properties and on the manufacturing process, their distribution is mainly influenced by the form of the specimen [8].

In order to investigate the geometrical influence on the axial residual stress distribution and, at the same time, verify if the initial dimensions of the specimen allow an acceptance of generalized plane strain hypothesis at least at the center of the specimen as mentioned the section 4.1. Cylindrical specimens of three different lengths  $L$  have been fabricated, namely  $L = 40$  mm, 20 mm, 10 mm. The radius  $r$  is kept constant and equal to 12.5 mm. For convenience the samples are denoted  $S1$ ,  $S2$  and  $S3$  respectively. As seen in paragraph 5.1, the measurement of the strain along the specimen length can be obtained by superposition of the results coming from two different gratings located at different positions in two specimens of the same dimensions. In the case of the specimens  $S2$  and  $S3$ , the grating length (24 mm) exceeds the specimen length and the complete strain curve along the embedded part of fiber can be retrieved by only one cylindrical sample of each type.

In Fig.5.3, strain measurements are plotted and compared for the three specimens  $S1$ ,  $S2$



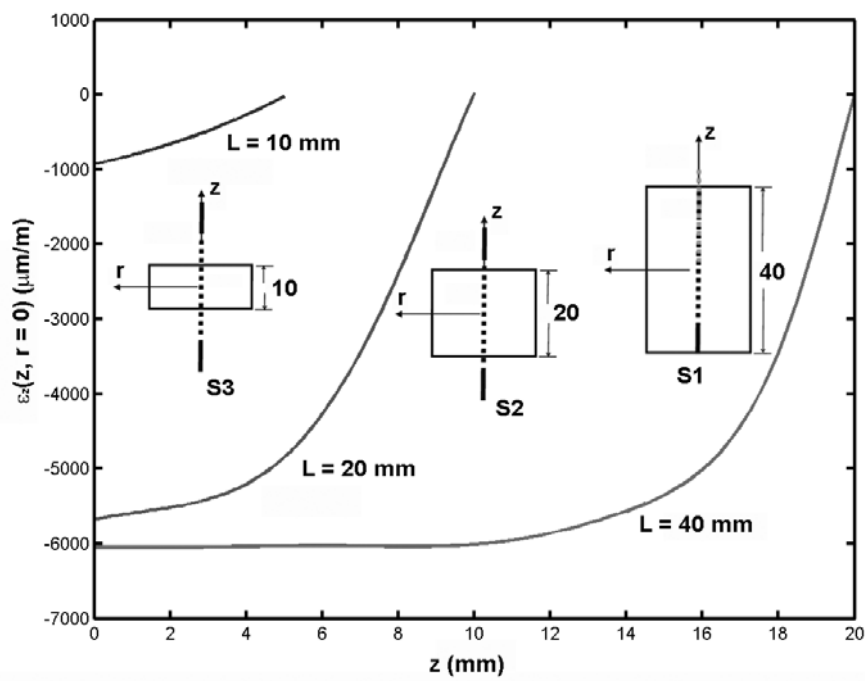


**Figure 5.3:** Axial evolution of strain along the fiber for three different cylinder lengths after the post-curing treatment.

and  $S3$ ; note that symmetrical distributions with respect to the plane  $z = 0$  were obtained. In particular, the axial strain calculated for the specimen  $S1$  reaches a plateau of  $-6000 \mu\epsilon$  when  $z \leq 10 \text{ mm}$ . In this region a generalized plane strain state prevails indicating that the border effects are not appreciable at a distance greater than 10 mm from the specimen ends. It is also noticed that the derivative of the strain curves averaged over the last 5 mm ( $L = L - 5$ ) tends to reach a constant value for specimens of at least 20 mm (the corresponding curves are not reported here), indicating comparable border effects in regions of the same relative size. However, when the length of the specimen decreases, the size of the plateau as well as the maximum level of strain (see Fig.5.3) both decreases. For the smallest specimen  $S3$ , one notices that a region of constant strain does not appear, and a maximum strain value of  $-1000 \mu\epsilon$  is registered at the center of the specimen. This comparison justifies the choice of the  $S1$  sample geometry for further testing.

The previous curves provide a very good indication on the substantial level of volume reduction undergone by the specimens during the production. This contraction is in practice entirely transmitted to the fiber in the case of the specimen  $S1$  and  $S2$ . This effect is clearly highlighted by the spectra presented in Fig.5.4 and here reported only for the specimen  $S1$ . The total wavelength shift of the main peak of  $6.4 \text{ nm}$  corresponds to  $6.100 \mu\epsilon$  via Eq.3.2.4. A simple verification of this affirmation can be easily obtained by comparing the volume

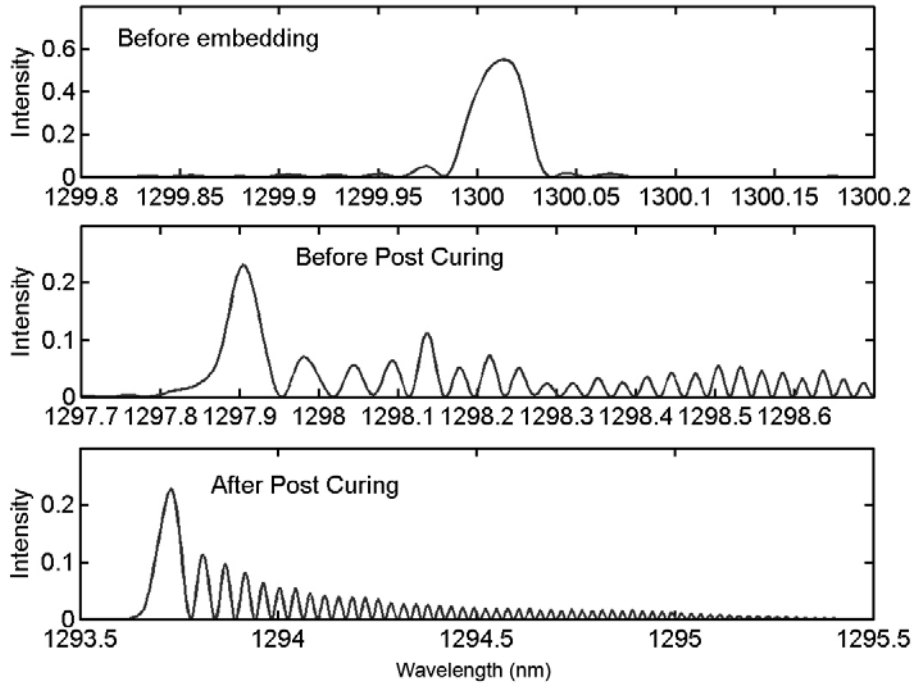


**Figure 5.4:** Evolution of the reflected spectra during the preparation processes of the specimen  $S1$ .

reduction of the epoxy resin evaluated and provided by the producer [2] and that measured via the FBG. The volume reduction of the resin in the mixture used during the test is equal to

2%. In the same time, the volume reduction of the specimen  $S1$  can be simply approximated by

$$\frac{\Delta V}{V} = 3 \frac{\Delta L}{L} \quad (5.2.1)$$

In the considered case,  $\frac{\Delta L}{L}$  exactly corresponds to the strain value measured via the FBG at the center of the specimen and found to be  $-6000 \mu\epsilon$ . Multiplying by three this strain we obtain (taking into account the possible errors) the volume reduction of the resin, thus attesting on the reliability of the measurement provided by the proposed optical method. Alternatively (see Fig.5.5), the same results can be retrieved in an independent manner by

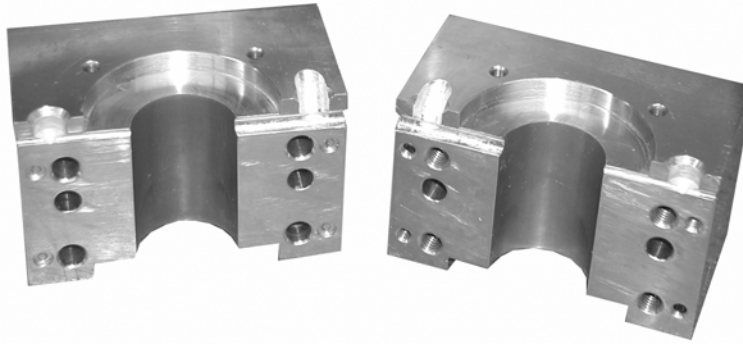


**Figure 5.5:** *Internal sections of the forming parts of the mould showed in Fig.4.6.*

directly measuring the variation in length  $\frac{\Delta L}{L}$  and in the radius  $\frac{\Delta r}{r}$  undergone by the cylinder during the polymerization process of the matrix. The shape of reference has been assumed equal to the internal cavity of the mould (Fig.4.6).

To calculate the volume contraction of the cylindrical sample, a series of precise measurements have been made in order to evaluate the variations in length along the axial and the transversal direction. In particular, the radial contraction has been calculated by averaging the results obtained of five different, equally-spaced, transversal sections while, for the axial contraction, six longitudinal planes separated by an angle of  $60^\circ$  have been taken into account. (Fig.5.6) The measurements revealed that a radial strain  $\frac{\Delta r}{r} = -0.0068$  and axial strain  $\frac{\Delta L}{L} = -0.0067$  occur in the transversal and longitudinal directions respectively. An experimental volume contraction of 2.06% is then recovered, exactly as indicated by the producer and previously measured by the FBG.

### 5.3 The effect of the coating on the axial strain distribution

If the plastic protective coating is not stripped from the fiber before the embedding process, the sensitivity of the fiber Bragg grating is greatly influenced and the data provided by the sensor will be very difficult to be interpreted. The coating tends in fact to reduce the stress transfer between the matrix and the fiber by partially absorbing the deformation applied on the reinforcement. The axial strain determined in a three-phase composite (ma-

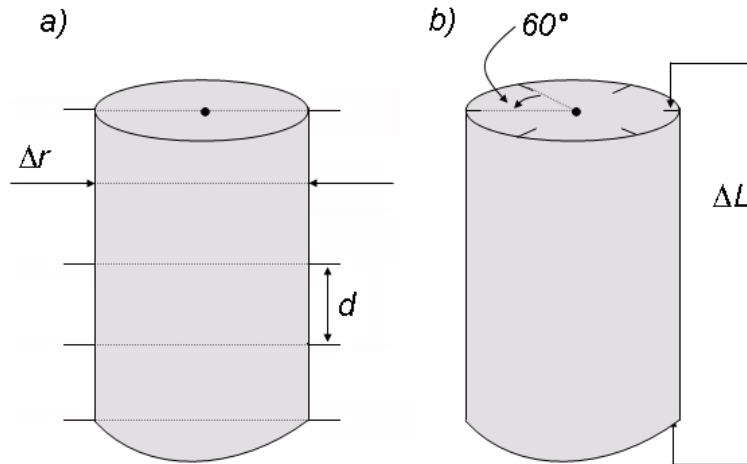


**Figure 5.6:** Locations of radius *a)* and of the length *b)* measurements.

trix+coating+glass fiber) via the FBG are lower than those measured in the case of a stripped optical fiber. The shape of the strain evolution along the longitudinal direction of the specimen is also very different (see Fig5.7). This experiment also indicates that the interface

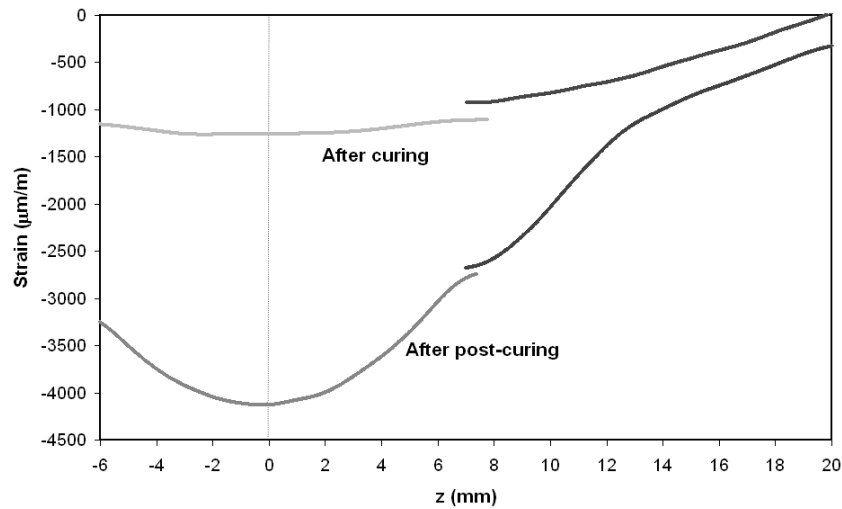


**Figure 5.7:** Evolution of the axial strain distribution before and after post-curing when the coating is kept around the optical fiber. The result is obtained by superposition of two different gratings of 15-mm length and located in two different positions.

properties between the glass and the epoxy are better than those between the glass and the coating. During matrix consolidation the coating follows the deformation of the epoxy and de-cohesion zones between plastic and glass may appear.

In some cases, the interface between the coating and the fiber is highly weakened and the fiber may have less of a reinforcement effect, thus allowing the resin free to contract in the axial

direction. An inversion in the strain generation process can be observed with a maximum level of compressive strain reached this time at the end of the curing period and not at the end of the post-curing treatment Fig.5.8. Indeed, though in the literature there is an indica-

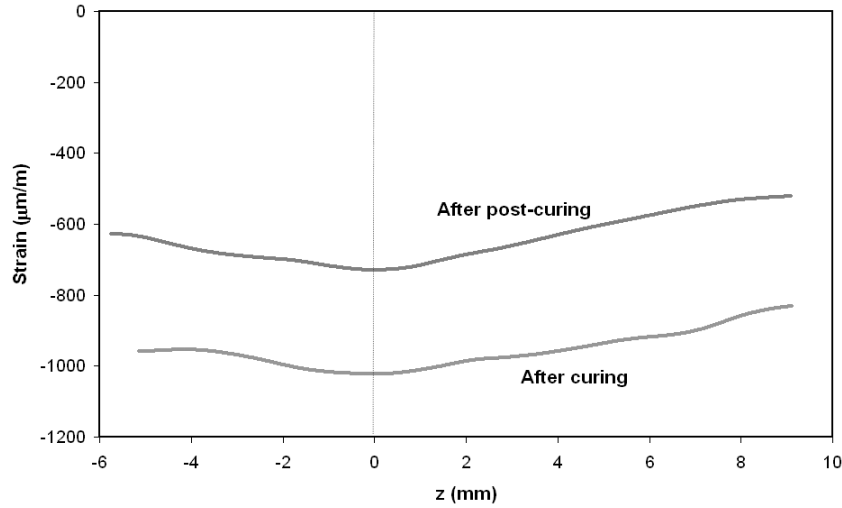


**Figure 5.8:** *Strain distribution measured at the center of a cylindrical specimen when the interface conditions between fiber and surrounding coating fail. An inversion on the behavior is observed.*

tion on the mechanical properties of the coating ( $E_c = 700$  MPa and  $\nu_c = 0.38$ ) absolutely no information on the interface characteristics between coating and fiber are given. These characteristics are particularly important because they are responsible for the transmission of information from the matrix to the Bragg sensor. Experimentally it is very difficult to evaluate these properties and some preliminary results [17, 18] obtained by pulling a coated optical fiber have revealed that a variation in the interface behavior could change even from fibers coming from the same batch. Due to the uncontrollable properties of the glass-coating interface, it is extremely difficult to conduct reproducible specimens of this type (compare Fig.5.7 and Fig.5.8).

Another problem coming from the use of a coated fiber is related to the thickness of the plastic coating. Around the grating region the thickness may significantly change with respect to the average thickness of the coating all along the rest of the waveguide Fig.5.9. This is a consequence of the fabrication process of the FBG. When the gratings are written into an optical fiber, the region chosen to receive the sensor the fiber is stripped of its original acrylate coating so that the laser used with the phase-mask method can correctly focus on the fiber core with an enough power. When the writing process is completed, the fiber is then recoated to protect the FBG. The recoated parts are generally thicker but not always the same, and the mechanical properties likely differ due to the processing of the recoating itself. This implies supplementary problems, because it is now more difficult to justify a measure of a lower level of strain applied on the grating. In fact this can be attributed either to a higher thickness of the coating, to a failure in the interface between plastic and glass or to the different properties of

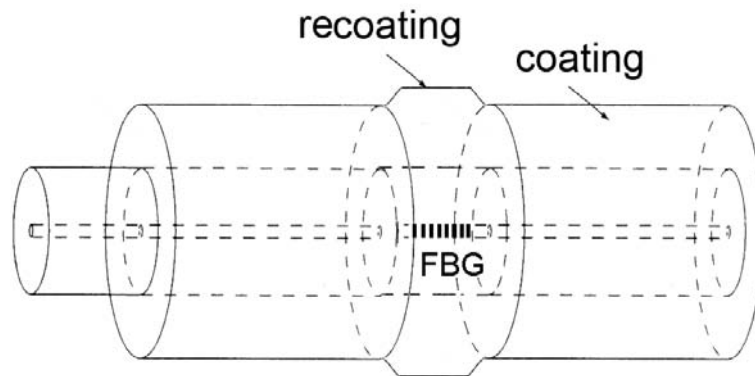


**Figure 5.9:** *Schematic of an optical fiber with an FBG. The recoated region around the grating shows the difference in thickness that in general exists between the coated and the recoated part.*

the recoated part. Consequently, it is not easy to decouple the problem and determine which cause principally affects the reduction in strain and each case must be analyzed individually. Since the coating does not assure a reproducibility of the experimental results, this investigation of the fiber coating influence, reinforces the decision to embed bare fiber sensors into the epoxy specimen.

## Chapter 6

# Determination of the radial stress evolution

Since the FBG only provides information regarding the axial the strain evolution along the fiber (equation 3.2.4), another experiment is necessary to derive the radial evolution of the residual strains. The residual stress distribution in the epoxy cylinder (at the experimental level) is calculated combining the strain measurements provided by the fiber Bragg grating with a typical technique well known in the fracture mechanics domain as the "crack compliance method" (C.C. method for simplicity). In particular, due to the ability of the grating to provide distributed measurements of strain along a given direction, the system involved in the C.C. method can be immediatly assembled and subsequently solved, thus providing the stress evolution normal to the crack.

### 6.1 The Crack Compliance (C.C.) Method

The approach for the residual stress measurement by the crack compliance method involves measuring strain at selected locations while a cut of progressively increasing depth ( $a_T$ ) is introduced into the part Fig.6.1. The material can simply be mechanically removed, or other techniques like electron-discharge machining or chemical attack can be adopted depending on the constituents of the specimen's matrix. This experimental technique introduced by Cheng and Finnie [28, 29] and largely applied by Prime and co-workers [63, 62, 64, 65], has been implemented for a number of plane and axisymmetric configurations and extensively validated. Following the proposed method a new experiment has been designed and realized.

A series of circumferential concentric thin cuts have been machined in the center of a post-cured specimen S1 as indicated in Fig.6.2. In particular, to avoid an excessive heating in the contact region between the cutting blade and the cylindrical specimen, a machine equipped with a water-cooling system has been used.

It is possible to observe in Fig.6.2 that the mechanical stress relaxation due to the introduction of deep transverse cuts, ( $a_T > 11$ ) significantly affects the FBG response. Such changes can be clearly detected (more than 5-6% in the strain values) up to a distance of about 10

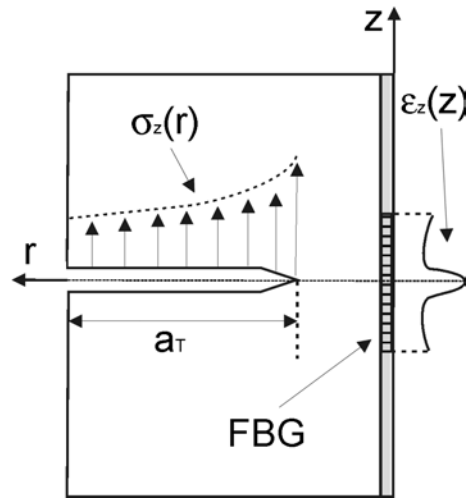


Figure 6.1: Configuration used for C.C. method tests

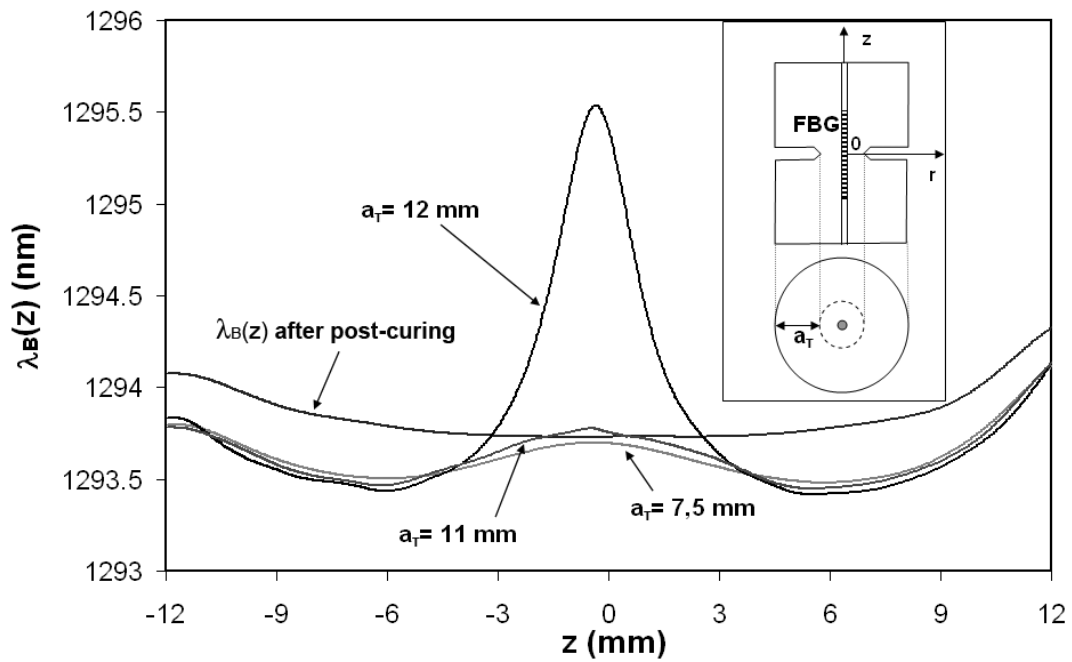


Figure 6.2: Plot of the measured local Bragg wavelength distributions  $\lambda_B(z)$  for increasing notch depth  $a_r$ . The corresponding strain profiles are deduced by using Eq.3.2.4. In particular, since the reference local Bragg  $\lambda_{B0}(z)$  is in this application a constant distribution, the strain evolutions are equal to the form of the different  $\lambda_B(z)$



FBG diameters from the center of the cylinder. The Bragg wavelength and the corresponding strain distribution obtained for  $a_T = 12 \text{ mm}$  is used to calculate the original residual stress field that is now relaxed.

The residual stress component normal to the crack plane,  $\sigma_z^m(r, z = 0)$ , is calculated by assuming that the original residual stress profile along a cut of depth  $a_T = \bar{a}_T$  can be represented by a series expansion

$$\sigma_z^m(r, z = 0) = \sum_{i=0}^n A_i P_i(r) \quad r_m - \bar{a}_T \leq r \leq r_m \quad (6.1.1)$$

where  $A_i$  are the unknown coefficients associated to the  $i^{\text{th}}$  polynomial term  $P_i$ . In relation 6.1.1 the orthogonal polynomials  $P_i$  are defined over the interval  $r_m - \bar{a}_T \leq r \leq r_m$  ( $r_m$  is the matrix radius). Note that Legendre polynomials have been used because they provide the best approximation of  $\sigma_z^m$  [28] (Fig.6.3).

For each applied function  $P_i(r)$  to the faces of the cut, the corresponding strain values

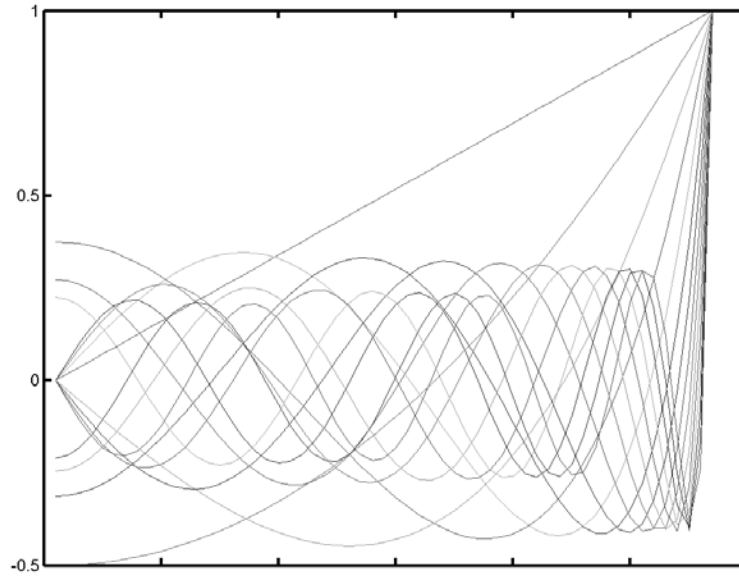


**Figure 6.3:** Form of the first sixteen Legendre polynomials used as a base to decompose the stress  $\sigma_z^m(r)$ .

at given location  $z_j$  along the Bragg grating are calculated by appropriate finite element simulations. These "numerical" strains are denoted as the compliance functions  $C_i(z_j; \bar{a}_T)$ .

From linear superposition principle the total strain in the fiber  $\epsilon_z^f$  at  $z = z_j$  is given by

$$\epsilon_z^f(z_j; \bar{a}_T) = \sum_{i=0}^n A_i C_i(z_j; \bar{a}_T) = [C_{ji}] \begin{pmatrix} A_0 \\ \cdots \\ \cdots \\ A_N \end{pmatrix} = [C_{ji}](A) \quad (6.1.2)$$

Notice that in Eq.6.1.2,  $[C_{ji}]$  is the  $J \times (N+1)$  compliance matrix where the  $i^{th}$  column vector  $[C_i(z_1; \bar{a}_T), \dots, C_i(z_J; \bar{a}_T)]^T$  is composed of the values of the compliance function  $C_i(z_j; \bar{a}_T)$  when evaluated at  $J$  selected positions along the grating. The sampling point  $z_j$  are selected within the domain  $0 \leq z_j \leq 4$  divided in  $(J-1)$  equally spaced intervals. Even though in literature [29, 30] a maximum order  $N = 11$  of the Legendre polynomials is indicated as sufficient to describe the correct evolution of the stress field, in practice for the considered cut depth  $\bar{a}_T$  of 12 mm,  $N = 15$  and  $J = 50$  are found to be the best values to obtain an accurate solution of the system. The coefficients  $A_i$  are determined by a least square fit that minimizes the error between the measured strains and those given by Eq.6.1.2. The stress evolution  $\sigma_z^m$  is finally retrieved via Eq.6.1.1. This leads to

$$(A) = ([C]^T [C])^{-1} [C]^T (\epsilon_{measured}) \quad (6.1.3)$$

where the experimental values of strains  $(\epsilon_{measured}) = [\epsilon_z^{meas}(z_1), \dots, \epsilon_z^{meas}(z_J)]^T$  are evaluated at the sampling point  $z_j$  from the response of the FBG shown in Fig.6.2 when the cut depth  $\bar{a}_T = 12 \text{ mm}$ . Note that  $(\epsilon_{measured})$  are obtained by using a spline fitting of the experimental strain distribution. More precisely, as indicated by the superposition principle in Fig.6.4, the column vector  $(\epsilon_{measured})$  has been retrieved as a difference between the measured strain distribution at the end of the post-curing process (case a) and the strain distribution along the grating after the cut of depth  $\bar{a}_T$  (case b).

The problem of finding the stress released due to machining can be viewed as a problem of

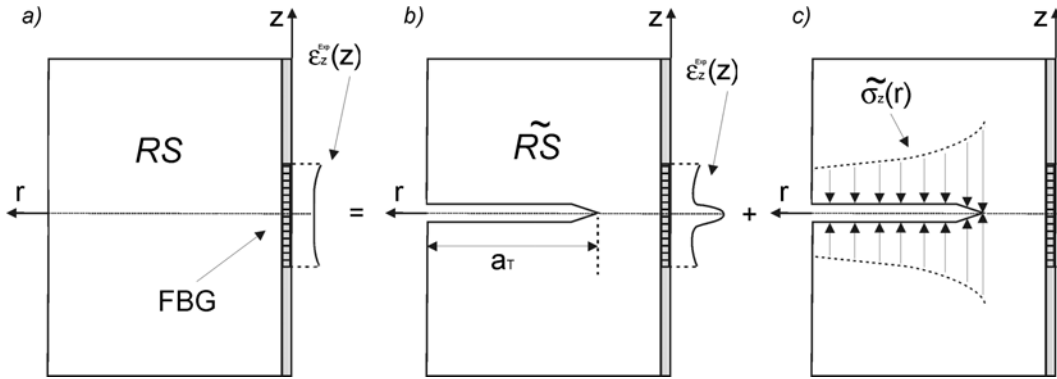


**Figure 6.4:** Application of the superposition principle to calculate  $(\epsilon_{measured})$  used in the Eq.6.1.2

finding a stress distribution  $\tilde{\sigma}_z(r)$  that, when applied on the fracture surfaces, allows one to

eliminate the effect of the cutting by closing the fracture. When this stress distribution is added to the modified residual stress field  $\bar{RS}$ , the initial residual stress field  $RS$  within the specimen should be retrieved. Since the embedded grating sensor provides information on the state of stress at the end of the post-curing (case *a*) in Fig.6.4 and after cutting (case *b*) in Fig.6.4, the experimental strain distribution that has to be used in Eq.6.1.2, corresponding to the (case *c*), can be easily retrieved.

It is important to underline that by selecting a series of distinct points along the grating where the strain is experimentally evaluated from the FBG response, the solution of the system 6.1.2 can be obtained with only one cut Fig.6.5. In the classical C.C. method however, to get the coefficient  $A_i$  one has to introduce a great number of cuts because the strain value is only read by one strain gage glued on the specimen. This leads to a great improvement of the method, overall by reducing the number of cracks (only one) needed to solve the system 6.1.2 and consequently the correlated experimental errors.

The number  $N$  which indicates the higher polynomial degree taken in the expansion 6.1.1,

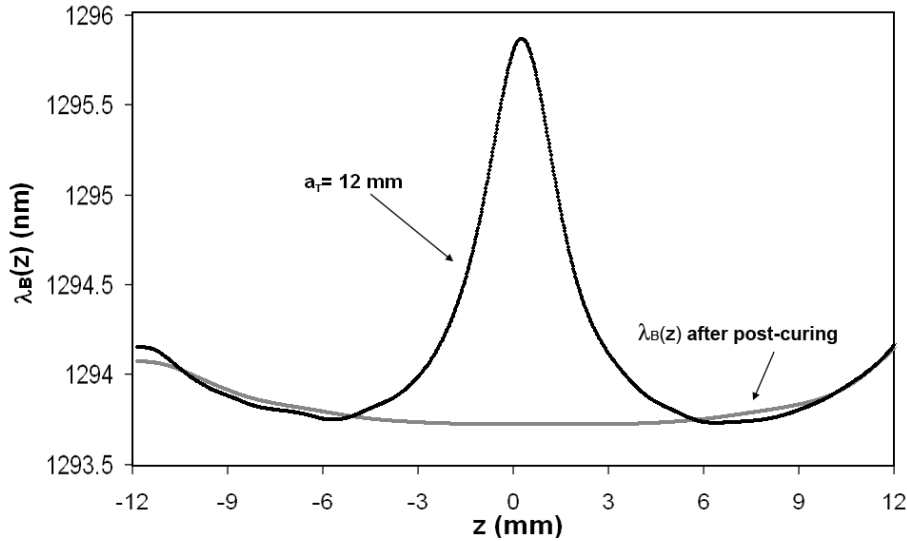


**Figure 6.5:** Local Bragg distribution  $\lambda_B(z)$  obtained with only one cut of depth  $\bar{a}_T = 12\text{mm}$ . Slightly differences in comparison with Fig.6.2 can be attributed to the machining processing.

has to be chosen in order to minimize the total fitting error which has two constituents: the first is related to the capacity of the chosen series to represent the actual strain profile (i.e. the completeness of the series) while the second comes from the conditions of inversion of the matrix  $C_{ji}$  which may magnify the errors initially created in the strain profile.

A plot of the determined  $\sigma_z(r)$  is presented in Fig.6.6. The distribution plotted in Fig.6.6 highlights the effect of the stress transfer which takes place from the reinforcing fiber to the epoxy matrix. During the curing process, the matrix around the fiber shrinks, but the full or free contraction of the matrix is constrained as a consequence of being bonded to the fiber. At the same time, as a result, the matrix is stressed in tension in a direction parallel to the fiber axis. The fiber is compressed by the constrained shrinkage of the matrix. This results

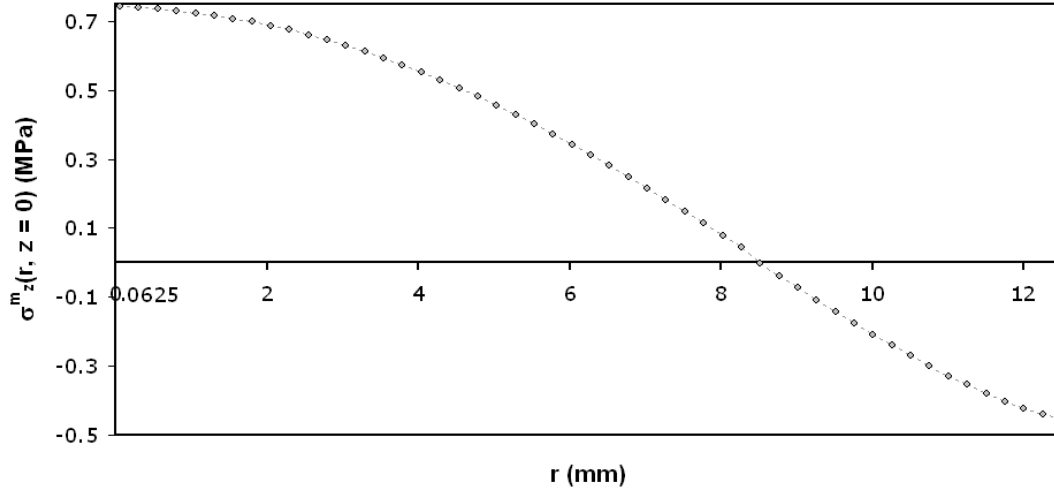


**Figure 6.6:** Radial evolution of the stress  $\sigma_z^m(r)$  in the plane  $z=0$

in residual axial compressive stresses in the fiber, which reach a maximum at mid-length and decrease to zero at the fiber ends.

The modified version of the C.C. method works very well and, more importantly, is able to describe the physics of the problem. The values calculated for the coefficients  $A_i$  are finally presented in Table 6.1. Notice that their amplitudes tend to decrease especially from the 11<sup>th</sup> term of the series ([29, 30]) up to the last coefficient which can be practically neglected. This is a confirmation that  $N = 15$  is a number of Legendre polynomials sufficient to describe reliably the researched radial stress distribution.

	$A_0$	$A_1$	$A_2$	$A_3$	$A_4$	$A_5$	$A_6$
<b>Values</b>	-0.2413	0.9273	-1.2749	-0.5892	1.3418	-0.9499	0.2638
	$A_7$	$A_8$	$A_9$	$A_{10}$	$A_{11}$	$A_{12}$	$A_{13}$
	0.3188	-0.4941	0.3985	-0.2332	0.1049	-0.0363	0.0092
	$A_{14}$	$A_{15}$					
	-0.0015	0.0001					

**Table 6.1:** Values of the coefficients  $A_i$  calculated via the C.C. method for the specimen S1.

## 6.2 The influence of the specimen radius $r_m$ on the radial distribution of stresses

In the previous paragraph, the radial stress evolution  $\sigma_z^m(r)$  has been obtained for a cylinder of 40 mm length and a radius  $r_m$  of 12.5 mm (specimen S1). The effect of the radius  $r_m$  on the residual stress profile is investigated in this section.

Equilibrium of residual stresses in the fiber  $\sigma_z^f(r)$  and in the matrix domain  $\sigma_z^m(r)$  requires that

$$\int_0^{2\pi} \int_0^{r_f} \sigma_z^f(r) r dr d\theta = \int_0^{2\pi} \int_{r_f}^{r_m} \sigma_z^m(r) r dr d\theta \quad (6.2.1)$$

Equation 6.2.1 simply states that the averaged residual stress on any transversal section of the cylinder is always zero. Nevertheless, probably due to a lack of information in the literature (available experimental data are not exhaustive) the evolution of the function  $\sigma_z^m(r)$  is not well established. A relation of proportionality between  $\sigma_z^f(r)$  and  $\sigma_z^m(r)$  is generally assumed

$$\sigma_z^f(r) = const = K \sigma_z^m(r) \quad (6.2.2)$$

where  $K$  is an appropriate constant which depends on the volume ratio of the two components. Unfortunately, the previous assumption may lead to a significant error in the evaluation of  $\sigma_z^m(z)$  for large radii  $r_m$  of the cylinder, because  $\sigma_z^f(r)$  is generally assumed constant on the fiber cross-section. Nevertheless, relation 6.2.2 holds when the external radius of the specimen is "sufficiently" small.

In order to prove this assertion, the evolution of the residual stresses  $\sigma_z^m(z)$  has also been experimentally obtained by using (Fig.6.7) a specimen of external radius  $r_m = 4mm$  (indicated here as SS1). The length of the specimen is kept constant at 40 mm. Following the previously described C.C. method the residual radial stress evolution has been calculated for the cylinder SS1 and is presented in Fig.6.7. This figure compares the stress distributions and highlights the errors made by assuming the relationship 6.2.2. One notes that for large radii,

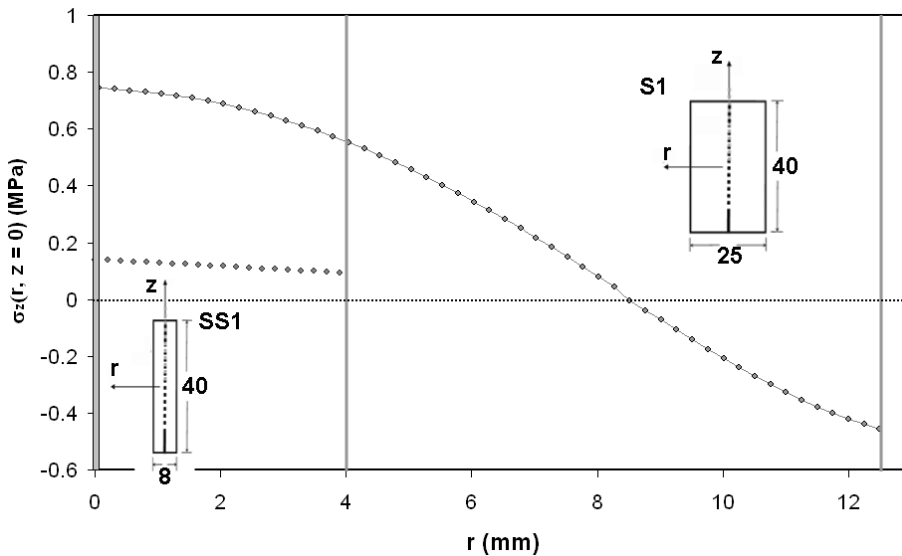


**Figure 6.7:** Evolution of the axial stress distribution as a function of the specimen radius.

the function  $\sigma_z^m(r)$  has negative values in the domain  $\frac{2}{3}r_m \leq r \leq r_m$  whose size is about one third of the specimen radius. Positive values are encountered only in the remaining region. This is one real case for which the assumption 6.2.2 completely fails.

When the radius  $r_m$  decreases, the shape of the function  $\sigma_z^m(r)$  completely changes. Experimental results for the specimen SS1 indicate an approximately positive constant value of the residual stress  $\sigma_z^m(r)$  across the matrix domain, attesting to the validity of relation 6.2.2. Note that relation 6.2.1 which makes not assumptions about of the form  $\sigma_z^m(r)$  and  $\sigma_z^f(r)$ , is satisfied by all the distributions plotted in Fig.6.7.

It is also important to underline that in Fig.6.8 the maximum strain level reached at the center of the specimen SS1 is close to the one obtained for the specimen S1 (see Fig.6.5). This

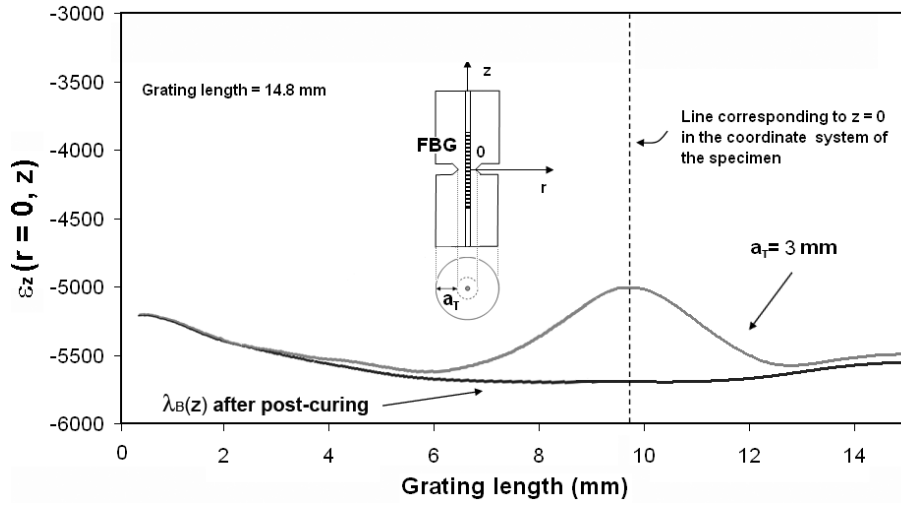


**Figure 6.8:** Measured strain distribution before and after cutting a circumferential cut of 3 mm depth for the post-cured specimen SS1.

results indicate that the radius does not considerably the strain distribution built up along the fiber. This means that only the contraction of the matrix in the axial direction  $z$  has, a priori, a significant role in the generation of the residual stress field. Along the transversal direction  $r$  however, the epoxy matrix can contract freely only respecting Poisson' ratio.

To complete this analysis, the coefficients  $A_i$  calculated via the C.C. method in the case of the cylinder SS1 are finally presented in the Table6.2

	$A_0$	$A_1$	$A_2$	$A_3$	$A_4$	$A_5$	$A_6$
<b>Values</b>	0.1339	-0.0323	-0.0164	0.0131	-0.0063	-0.0005	0.0050
	$A_7$	$A_8$	$A_9$	$A_{10}$	$A_{11}$	$A_{12}$	$A_{13}$
	-0.0062	0.0053	-0.0034	0.0018	-0.0007	0.0002	0.0000
	$A_{14}$	$A_{15}$					
	0.0000	0.0000					

**Table 6.2:** Values of the coefficients  $A_i$  calculated via the C.C. method for the specimen SS1.

### 6.3 Effect of a longitudinal crack on the residual stress field

In the second section of this chapter, the axial stress relaxation along the radial direction is obtained by introducing a circumferential crack in the specimen. In this section the relaxation effect of the hoop stresses on the FBG response is investigated. This can be considered as a natural extension of the application of the C.C. method to the cylindrical geometry [65], and at the same time allows for a verification of the FBG sensor's behavior when submitted to transverse stress variations. However, while the FBG response is relatively simple to interpret when an axisymmetric transversal crack is machined into the specimen (because the variations in the grating response only depend on the axial effects), it maybe more difficult to understand in the case of a longitudinal crack. This is mainly due to the loss of the corresponding axisymmetric conditions around the optical fiber [80].

Two successive longitudinal (L) cuts of depth  $a_L = \frac{r_m}{2}$  and  $a_L = r_m - 2r_f$  have been machined (see the insert of Fig.6.9). In each case, a relaxation time of two hours has been allowed before

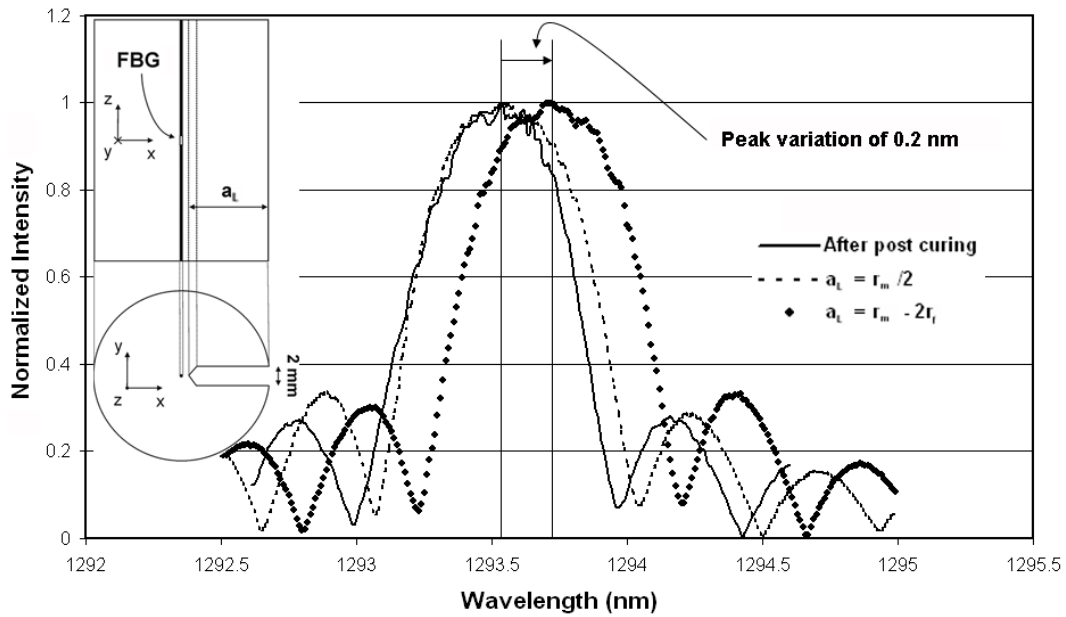


**Figure 6.9:** Shift of the principal Bragg peak due to the longitudinal cut. A slightly variation of the Bragg wavelength is measured after a cut depth of  $a_L = \frac{r_m}{2}$  (dashed line). A greater shift is detected for the deeper crack  $a_L = r_m - 2r_f$  (dotted line).

the measurements. A grating length of 1.5 mm has been used because the spectrum in this case is composed by a single peak, whose modification is generally easier to control and to understand. Moreover, since the strain distribution along the axial direction is well known, a single short grating is sufficient to capture the maximum strain variation at least in the central region of the specimen. Using the 1.5 mm long FBG, the spectral response due to the axial strain relaxation is plotted in Fig.6.9.

The main effect revealed by the test, is a significant shift towards longer wavelengths of the

grating spectrum (see Fig.6.9). This is seen in the case of the deepest crack, while nearly negligible variations are created by the initial crack length. One notes a strain relaxation of  $50 \mu\text{m}/\text{m}$  is detected when  $a_L = \frac{r_m}{2}$  and a greater strain variation ( $190 \mu\text{m}/\text{m}$ ) is measured when  $a_L = r_m - 2r_f$ .

Particular attention has to be paid to verify the presence of any possible birefringence affect. In fact, due to the loss of axial symmetry on a given transversal section of the cylinder, the in-plane stress relaxation can generate a deformation of the fiber section in such a way that its shape differs from a circle. As a consequence, two privileged light propagations directions can be identified and the out-coming light (i.e. the related grating spectrum) becomes polarization state dependent and the optical fiber is said to present a state of birefringence. However, as shown in Fig.6.10, the peak modifications due to the polarization changes are comprised in a range of 25 pm, which is compatible with the laser wavelength fluctuations. No measurable birefringence state is then detected within the fiber, probably because its stiffness is too high compared to that one of the resin, thus becoming the fiber insensitive at least to the transverse deformation of the matrix. This result is particularly important, because represents the experimental evidence that the hypothesis of Butter and Hocker [15] used in Chapter 3 to model the relation between the applied strain and the FBG response (i.e. the Bragg wavelength shift) is valid. In practice, it is an affirmation of the fact that, for this kind of geometry and constitutive materials, only the axial shrinkage produces important modifications on the physical state of the reinforcing fiber.

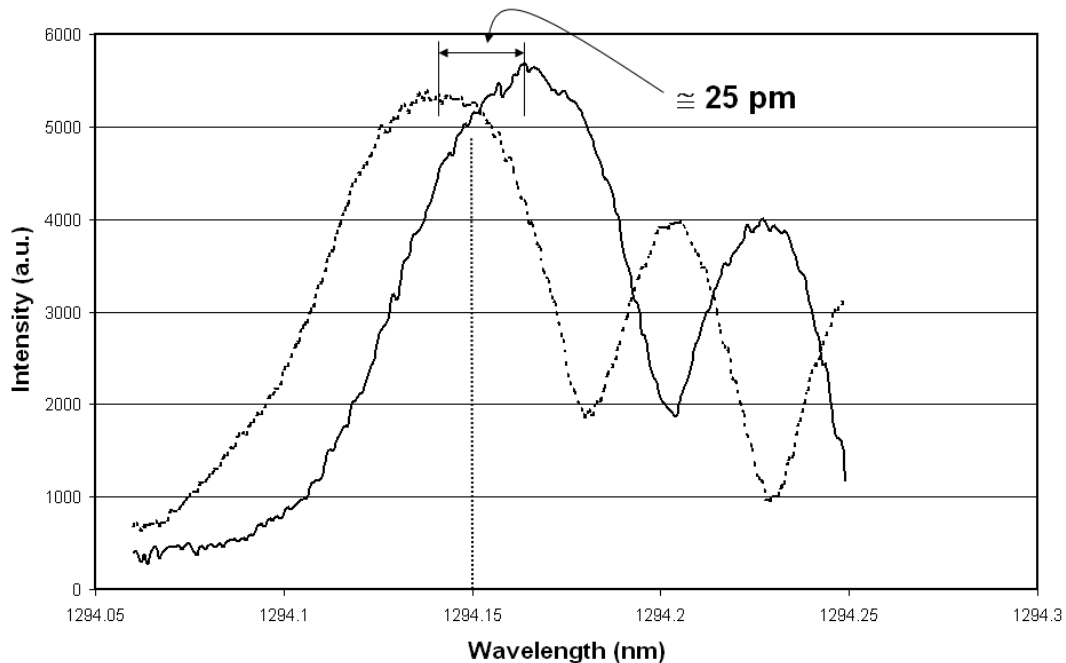


**Figure 6.10:** Maximum peak variation due to the light polarization changes. The curves represent the same sensor response centered at the wavelength of 1294.15 nm, and recorded for two different states of polarization.



## Chapter 7

# FEM analysis

In the engineering domain, finding solutions to complex structural problems easily becomes very difficult and at times impossible by analytical methods. A possible solution can be found by the numerical methods among which one of most powerful is the Finite Element Method (FEM) [42]. Nowadays, FEM is used in different kinds of applications ranging from stress analysis, heat transfer, fluid flow and so on.

The basis of the FEM is the Ritz-Galerkin method where, for a given loading conditions, a displacement field satisfying the weak formulation of the problem and the essential boundary conditions are assumed over a certain body.

In practice, a entire body is divided into smaller elements, connected to each others at particular points called nodes. The ensemble of all nodes and elements constitutes the FE mesh. Finally, a displacement field is assumed for each individual element.

The approach is based on the assumption of simple displacement over the elements and an integration process is carried-out over the entire body. In particular, the displacement field over a certain element is approximated by a polynomial function of a given order. Then, the global approximated displacement field is calculated by taking a linear combination of these local functions ("shape" functions), each of which presents the characteristic of being equal to one at the corresponding node of the FEM mesh and equal to zero in the all other nodal points.

A system of  $N$  equations with  $N$  unknowns has to be solved, where  $N$  corresponds to the number of degree of freedom in the FEM mesh (i.e. the number of nodes times the number of displacement components per nodes). In some cases this system can be non-linear and an iterative method has to be used to calculate the solution of the discrete variational problem. In the finite-displacement formulation the equations of equilibrium for the entire structure are obtained by combining (in the sense of the virtual work principle) the equilibrium equations of each node in such way that continuity conditions are assured at each node.

Depending on the particular application involved, and for a given set of boundary conditions, field parameters such as stress, strain, displacement, temperature distribution, flow velocities, etc can be retrieved. Given the number of degrees of freedom typically involved in these kind of problems the calculation power of computers is absolutely necessary to elaborate and solve

the system associated to the FEM method.

One parameter that influences the results of the FEM solution is the mesh quality. A first indication on that point is represented by the element distortion which has to be reduced to the minimum. The error of the FEM approximation also depends on the size of the element used to divide the body or the considered structure in a given number of simpler sub-domains. The mesh has to be sufficiently refined, especially in regions where the researched fields may vary with high gradient, for instance near concentrated loads or in the vicinity of the holes, where stress concentration can occur .

The use of quadratic elements, which have a higher number of nodes per element and consider parabolic shape functions, generally increases the precision of the results but with a higher computational cost. Another possibility is the implementation of special elements (e.g. singular elements), specially designed to capture field singularities in particular geometrical zones of the body.

In the end, no simple rule exists for choosing the size of the mesh or the kind of element that must to be used in a finite element model, and only a posteriori parametric study can provide information on the reliability of the FEM solution.

## 7.1 The matrix shrinkage function $S_m$

To model the matrix volumetric shrinkage effect, the problem is considered analogous to a thermo-elastic one [44]. The analogy with a thermo-mechanical problem is particularly helpful because at the moment it is the only possibility for numerically generating a stress field within a material which respects the conditions equivalent to a chemical shrinkage (e.g. there are no forces applied on the contour of the body). Nevertheless, the elastic properties of the material are considered temperature independent and not to change as the degree of cure advances during post-curing. As a consequence, the only residual stresses are those associated with curing shrinkage of the epoxy when the system returns to room temperature.

To simulate the frozen-in strains, a matrix shrinkage function  $S_m(r, z)$  is introduced in the general stress-strain relations as follows

$$\begin{pmatrix} \epsilon_r(z, r) \\ \epsilon_\theta(z, r) \\ \epsilon_z(z, r) \\ \epsilon_{rz}(z, r) \end{pmatrix}^{(m)} = \frac{1}{E_m} \begin{pmatrix} 1 & -\nu_m & -\nu_m & 0 \\ -\nu_m & 1 & -\nu_m & 0 \\ -\nu_m & -\nu_m & 1 & 0 \\ 0 & 0 & 0 & 2(1 + \nu_m) \end{pmatrix} \begin{pmatrix} \sigma_r(z, r) \\ \sigma_\theta(z, r) \\ \sigma_z(z, r) \\ \sigma_{rz}(z, r) \end{pmatrix}^{(m)} + \alpha_m \Delta T(r, z) \begin{pmatrix} 1 \\ 1 \\ 1 \\ 0 \end{pmatrix} + S_m(r, z) \begin{pmatrix} 1 \\ 1 \\ 1 \\ 0 \end{pmatrix} \quad (7.1.1)$$

where  $\alpha_m \Delta T(r, z)$  takes into account a possible temperature variation  $\Delta T$  and  $\alpha$  is the coefficient of thermal expansion (CTE) of the material. In the present case,  $\alpha_m \Delta T(r, z) = 0$  because all the strain measurements have been performed at the same controlled room temperature. A similar relation holds for the fiber domain by replacing the letter  $m$  by  $f$  in

relation 7.1.1, except for the last term which is set to zero because the fiber is taken to have zero chemical shrinkage (i.e.  $S_f(r, z) = 0$ ).

Based on the FBG measurement (axial and radial strain evolution) and physical boundary conditions (for a sufficiently large matrix radius the shrinkage function has to correspond to the uniform free linear contraction of about  $-6000\mu m$  in the plane  $z = 0$ ), the following form can be assumed for the function  $S_m$  (i.e. for the evolution of the residual strain field)

$$S_m(r, z) = Z(z)R(r) = \left[ a \left( \frac{z}{20} \right)^4 + b \left( \frac{z}{20} \right)^2 + c \right] [1 + df(r)] \quad (7.1.2)$$

where the constant parameters  $a$ ,  $b$ ,  $c$  and  $d$  have to be determined and  $f(r)$  is a polynomial function linked to the derivative of the crack opening displacement C.O.D. [4] (which corresponds to a strain). Notice that the form of the function  $Z(z)$  can be obtained by an interpolation of the strain distribution provided by the FBG, while the determination of  $R(r)$  requires the data obtained by using the Crack Compliance method.

The C.O.D represents the axial displacement of the crack surfaces expressed as a function of the radius  $r$  of the cylindrical specimen. In particular, the C.O.D. depends on the amplitude and shape of the stress profile along the radial direction (i.e.  $\sigma_r^m(z)$ ). By using the Weight Function Method [46, 27, 79] the C.O.D. can be calculated by

$$C.O.D. = u_z^m(\sigma_z^m(r), r, a) = \frac{2}{E'_m} \int_r^a \left[ \int_0^s h(r, s) \sigma_z^m(r) dr \right] h(r, s) ds \quad (7.1.3)$$

where  $h(r, s)$  is an appropriate weight function whose form has been calculated via FE simulations for the considered composite cylinder,  $\sigma_z^m(r)$  is the stress distribution given by 6.1.1 and  $E' = \frac{E_m}{1+\nu_m^2}$  ( $E_m$  and  $\nu_m$  are the Young modulus and the Poisson ratio of the epoxy matrix). More details on the determination of the C.O.D. and the appropriate weight function for the reinforced cylinder will be given in the subsequent paragraph.

The C.O.D. due to the residual stress  $\sigma_z^m(r)$  applied on the crack surfaces is plotted in Fig.7.1 showing that its form is compatible with the stress distribution of Fig.6.6

### 7.1.1 Introduction to the Weight Function method to calculate the Crack Opening Displacement (C.O.D.)

In the linear elastic fracture mechanics domain the stress field presents a singularity near the crack tip. In order to characterize this field a special parameter  $K$  named Stress Intensity Factor (S.I.F.) was introduced, giving an indication of the field singularity amplitude around the crack front.

There are three different types of loading that a crack can experience as Fig.7.2 illustrates. Mode I loading, where the principal load is applied normal to the crack plane, tends to open the crack. Mode II corresponds to in-plane shear loading and tends to slide one crack face with respect to the other. Mode III refers to out-of-plane shear. A cracked body can be loaded in any one of these modes, or a combination of two or three modes. Because the problems dealing with the mode I displacement are the most frequent in fracture mechanics, they will be taken into account in this exposition.

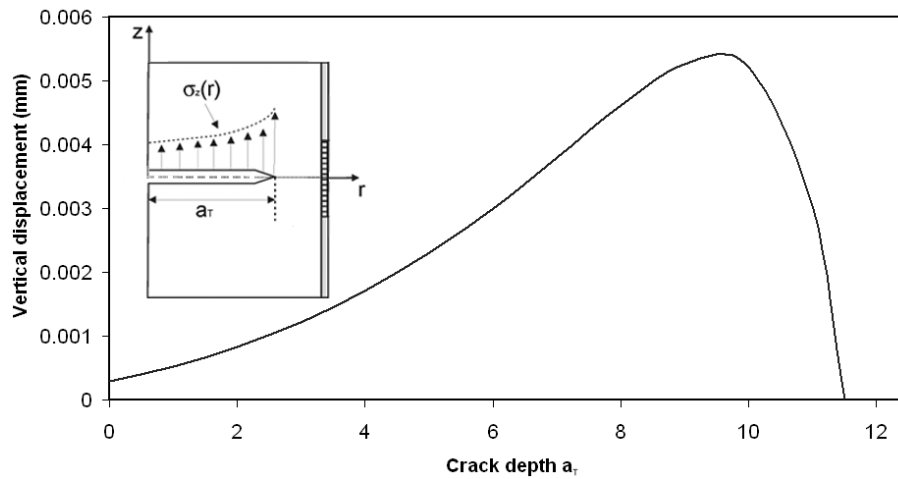


**Figure 7.1:** Crack Opening Displacement (the double of the vertical displacement of any single surface of the crack) for the specimen S1 and a crack depth of 11.5 mm.

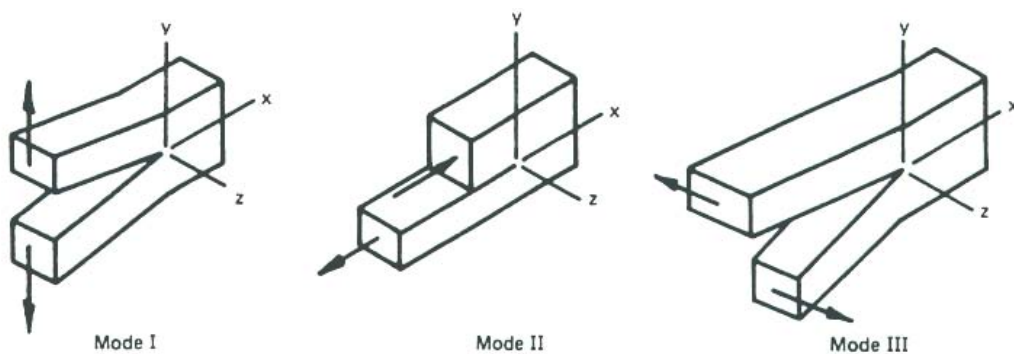


**Figure 7.2:** Three different modes of loading that can be applied to a crack [77].

The weight functions, first introduced by Paris [58] and developed later by Bueckner [14] and Rice [68], are nowadays largely used in the linear elastic fracture field with the overall aim to calculate the Stress Intensity Factor. To use the weight function method the hypothesis of the superposition principle is usually applied to the system of forces acting on the fracture (Fig.7.3) There are typically far-field applied forces and the bridging forces. Also, the specimen

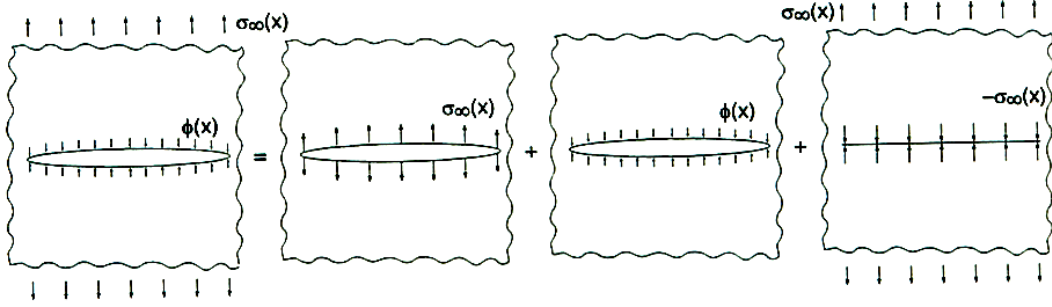


**Figure 7.3:** *Superposition principle: the global system of forces acting on the fracture surfaces of a body is viewed as a sum of single distributions, one representing the far stress field  $\sigma_\infty(x)$ , one the bridging forces  $\phi(x)$  and one term that guaranties the equilibrium conditions without influencing the fracture opening (two auto-compensating actions) [77].*

is considered homogeneous far from the fracture and characterized by an effective Young modulus  $E'$ , where  $E' = E$  in the case of plane stress conditions or  $E' = \frac{E}{1+\nu^2}$  in the plane strain conditions. The description that follows is a summary of a wider theory presented by Tada [79] and by Botsis [11].

### 7.1.2 Weight functions

Consider a dipole force applied on a surface of a crack, as illustrated in Fig.7.4a). This system generates a stress intensity factor that can be expressed as follows:

$$K_I(F, a) = \frac{2F}{\sqrt{\pi a}} \Phi\left(\frac{x}{a}, \frac{a}{w}\right) \quad (7.1.4)$$

where  $\Phi\left(\frac{x}{a}, \frac{a}{w}\right)$  is a given function depending only on the system geometry that can be calculated analytically or numerically ([27]). Nevertheless, for the most common specimen geometries in literature it easy to find the complete expression of  $\Phi$  (see for example [79]). In particular, a weight function  $g^{SIF}(x, a, w)$  can be defined as the function providing the SIF for a unit dipole force:

$$g^{SIF}(x, a, w) = \frac{2F}{\sqrt{\pi a}} \Phi\left(\frac{x}{a}, \frac{a}{w}\right) \Big|_{F=1} \quad (7.1.5)$$

$g^{SIF}(x, a, w)$  is often indicated as the influence function or Green's function of a given specimen geometry. Similarly, it is possible to calculate the SIF for any type of distribution  $\phi(x)$  acting on the fracture surfaces (Fig.7.4b)):

$$K_I(\phi, a) = \int_{c_1}^{c_2} \phi(x) g^{SIF}(x, a, w) dx = \int_{c_1}^{c_2} \frac{2\phi(x)}{\sqrt{\pi a}} \Phi\left(\frac{x}{a}, \frac{a}{w}\right) \quad (7.1.6)$$

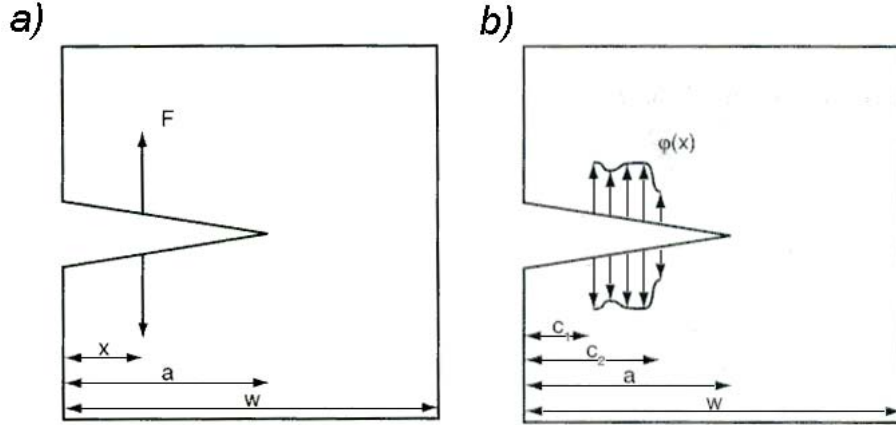


**Figure 7.4:** a) Crack submitted to a dipole force and in b) submitted to a distribution of forces  $\phi(x)$ .

### 7.1.3 Calculation of crack opening displacement

Consider a cracked body submitted to a load  $P$  and to a virtual dipole force  $F$  as indicated in Fig.7.5. Though only the mode I will be considered here, the other two modes can be treated similarly. Defining  $U_T$  as the elastic strain energy, for a specimen of unit thickness under constant load the energy release rate (ERR)  $G$  is

$$G(P, F, a) = \left. \frac{\partial U_T}{\partial a} \right|_{forces} \quad (7.1.7)$$

Since the SIF is due to the entire system of forces, namely

$$K_I(P, F, a) = K_I(P, a) + K_I(F, a) \quad (7.1.8)$$

from the relation  $G = \frac{K_I^2}{E'}$  we have the following relation

$$G(P, F, a) = \frac{K_I^2}{E'} = \frac{[K_I(P, a) + K_I(F, a)]^2}{E'} \quad (7.1.9)$$

In particular, since  $U_T$  is composed of two parts (that of the bulk material  $U_T^{NOCRACK}$  and that due to the crack), taking into account the previous relations the expression of  $U_T$  becomes

$$U_T = U_T^{NOCRACK} + \int_0^a \frac{\partial U_T}{\partial a'} da' = U_T^{NOCRACK} + \int_0^a G da' \quad (7.1.10)$$

According to the theorem of Castigliano, the displacement of a point in the direction of the applied load at that point is given by the derivative of  $U_T$  with respect to the load applied at that point. If no force is applied on the considered point, it is possible to consider a virtual force in the direction of the desired displacement. In this particular case, the derivative of the energy is calculated as the limit as virtual force goes to zero.

In the case of Fig.7.5, the displacement  $\Delta_P$  is given by

$$\Delta_P = \Delta_P^{NOCRACK} + \int_0^a \frac{\partial G(P, F, a')}{\partial P} da' \quad (7.1.11)$$

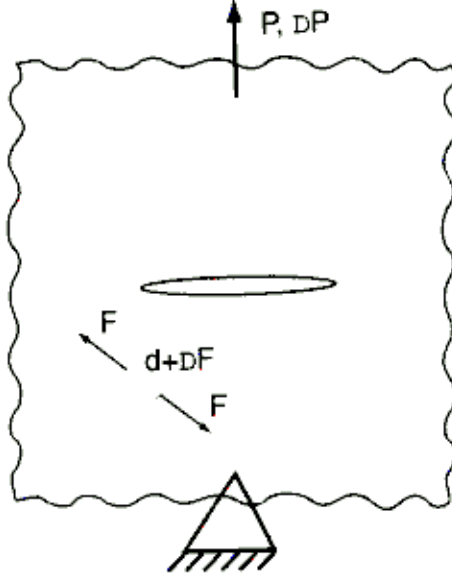


**Figure 7.5:** Cracked body loaded with a force  $P$  and a dipole  $F$ .  $\Delta_P$  and  $\Delta_F$  are the displacement in the direction of the forces and  $d$  is the distance before deformation [11].

where  $\Delta_P^{NOCRACK} = \frac{\partial U_T^{NOCRACK}}{\partial P}$ . In particular, taking into account Eq.7.1.9 we have:

$$\frac{\partial G(P, F, a)}{\partial P} = \frac{2}{E'} [K_I(P, a) + K_I(F, a)] \left[ \frac{\partial K_I(P, a)}{\partial P} \right] \quad (7.1.12)$$

and via Eq.7.1.11

$$\Delta_P = \Delta_P^{NOCRACK} + \frac{2}{E'} \int_0^a [K_I(P, a') + K_I(F, a')] \left[ \frac{\partial K_I(P, a')}{\partial P} \right] da' \quad (7.1.13)$$

A similar expression can be calculated for  $\Delta_F$ :

$$\Delta_F = \frac{\partial U_T^{NOCRACK}}{\partial F} + \frac{2}{E'} \int_0^a [K_I(P, a') + K_I(F, a')] \left[ \frac{\partial K_I(P, a')}{\partial F} \right] da' \quad (7.1.14)$$

and taking into account that  $K_I(F, a) \rightarrow 0$  when  $F \rightarrow 0$ , the last equation can be re-written as

$$\Delta_F = \Delta U_T^{NOCRACK} + \frac{2}{E'} \int_0^a K_I(P, a') \left[ \frac{\partial K_I(P, a')}{\partial F} \right] da' \quad (7.1.15)$$

If the displacement is determined on the fracture surfaces (i.e. we calculate the C.O.D.  $u_F$ ) then  $\Delta^{NOCRACK} = 0$ . In this case

$$u_F = \frac{2}{E'} \int_0^a K_I(P, a') \left[ \frac{\partial K_I(P, a')}{\partial F} \right] da' \quad (7.1.16)$$

### 7.1.4 C.O.D. General formulation

The formalism presented in the previous section can be easily generalized to a distribution of forces  $P_i(i) = (1, \dots, N)$  applied on the body. For the Eq.7.1.13 and Eq.7.1.14 we have respectively:

$$\Delta_{P_i} = \Delta_P^{NOCRACK} + \frac{2}{E'} \int_0^a K_I(P_1, \dots, P_N, a') \left[ \frac{\partial K_I(P, a')}{\partial P} \right] da' \quad (7.1.17)$$

$$\Delta_F = \Delta_F^{NOCRACK} + \frac{2}{E'} \int_0^a K_I(P_1, \dots, P_N, F, a') \left[ \frac{\partial K_I(F, a')}{\partial F} \right] da' \quad (7.1.18)$$

where

$$K_I(P_1, \dots, P_N, a) = \sum_1^N K_I(P_i, a) \quad (7.1.19)$$

Then, the expression of C.O.D. is

$$u_F = \frac{2}{E'} \int_{x_1}^a K_I(P_1, \dots, P_N, F, a') \frac{\partial K_I(F, a')}{\partial F} da' \quad (7.1.20)$$

where  $x_1$  corresponds to the position we want to know the value of  $u_F$ . Notice that  $\frac{\partial K_I(F, a')}{\partial F} = 0$  if  $a' \leq x_1$ . Taking  $\frac{\partial K_I(F, a')}{\partial F} = g^{SIF}(x_1, a, w)$  it is possible to define a weight function for the C.O.D. measured at the point  $x_1$  and due to a force applied in the point  $x_0$ :

$$g^{C.O.D.}(x_0, x_1, a, w) = \frac{2}{E'} \int_{\max(x_0, x_1)}^a g^{SIF}(x_0, a', w) g^{SIF}(x_1, a', w) da' \quad (7.1.21)$$

Calculating now the C.O.D. at the point  $x_1$  of the crack face due to a continuous distribution of pressure  $\phi(x)$  over the faces of the crack (we neglect the index of  $u$  because is not useful any more) we obtain

$$u(\phi, x, a, w) = \int_0^a g^{C.O.D.}(x_0, x_1, a, w) dx_0 \quad (7.1.22)$$

or, by using Eq.7.1.21

$$u(\phi, x_0, a, ) = \frac{2}{E'} \int_0^a \phi(x_0) \left( \int_{\max(x_0, x_1)}^a g^{SIF}(x_0, a', w) g^{SIF}(x_1, a', w) da' \right) dx_0 \quad (7.1.23)$$

which can be written in the following final form

$$u(\phi, x_0, a, ) = \frac{2}{E'} \int_{\max(x_0, x_1)}^a \left[ \int_0^{a'} g^{SIF}(x_0, a', w) \phi(x_0) dx_0 \right] g^{SIF}(x_1, a', w) da' \quad (7.1.24)$$

The last expression allows one to calculate the C.O.D. in any point along a given fracture within a body undergoing a load  $\sigma_\infty$  far from the crack region and a load  $\phi(x')$  on the fracture faces.

Since the C.O.D is in general taken from the middle plane of the fracture, for the reasons of notations we take  $g(x, a, w) = 2g^{SIF}(x_1, a, w)$ , thus obtaining

$$u(x, a, w) = u_\infty - \frac{4}{E'} \left\{ \int_x^a \left[ \int_0^{a'} g(x', a', w) \phi(x') dx' \right] g(x, a', w) da' \right\} \quad (7.1.25)$$



where

$$u_{\infty}(x, a, w) = \frac{4}{E'} \left\{ \int_x^a \left[ \int_0^{a'} g(x', a', w) \sigma_{\infty}(x') dx' \right] g(x, a', w) da' \right\} \quad (7.1.26)$$

Notice that considering a system of cylindrical coordinate  $(r, \theta, z)$ , changing  $a'$  with  $s$ , the name of the weight function  $g$  with  $\frac{h}{2}$  and taking  $\phi(x') = \sigma_z^m(r)$  the Eq.7.1.25 becomes exactly the Eq.7.1.3 previously presented ( $u_{\infty} = 0$  because there is not remote load).

### 7.1.5 Determination of the weight function associated to the reinforced cylindrical specimen geometry

In the previous paragraphs has been illustrated how it is possible calculate the C.O.D. of a fracture via the weight functions method. Using this method it is indispensable for determining the weight function associated to the considered geometry.

As said before, the weight function  $g(x, a)$  can be interpreted as the Green's function for a stress intensity factor problem. This means that the weight function corresponds to the stress intensity factor (SIF)  $K_I$  caused by a pair of normal forces  $P$  ( $P = 1$ ) acting at the point  $x'$ . If we express the single force  $P$  in terms of the Dirac delta function by a stress distribution

$$\phi(x) = P\delta(x - x') \quad (7.1.27)$$

and introduce this into Eq.7.1.6, we obtain:

$$K_I = P \int_0^a g(x, a) \delta(x - x') dx = P g(x', a) \quad (7.1.28)$$

and for a unit force

$$K_I = g(x', a) \quad (7.1.29)$$

By using this relation the problem of finding the weight function for a specific geometry is then changed into the calculation of the stress intensity factor for the same geometry. This is very useful in all the cases where an analytical expression of the weight function is not known but has to be determined. In fact, by mean of finite element (FE) simulations the stress intensity factor can be easily identified because the values of  $K_I$  are directly provided by the numerical model.

For the particular case of the cylindrical reinforced specimen used in this work, no calculation of the weight function is reported in the literature. It is then necessary to use the FE analysis to obtain one possible expression for the Green's function of this specimen.

There are many books [27, 79] and reference articles [46, 50, 54, 81] where it is possible to find suggestions or indications suggesting the mathematical form that is more adapted to this geometry. In this case  $K_I$  should be calculated using the following formula [79]:

$$K_I = \frac{2P}{\sqrt{\pi a}} \frac{H\left(\frac{c}{a}, \frac{a}{w}\right)}{\left(1 - \frac{a}{w}\right)^{\frac{3}{2}} \sqrt{1 - \left(\frac{a}{w}\right)^2}} = P g\left(\frac{c}{a}, \frac{a}{w}\right) \quad , P \text{ is a concentrated force } (P = 1) \quad (7.1.30)$$

where

$$H\left(\frac{c}{a}, \frac{a}{w}\right) = h_1\left(\frac{a}{w}\right) + h_2\left(\frac{a}{w}\right)\left(\frac{c}{a}\right) + h_3\left(\frac{a}{w}\right)\left(\frac{c}{a}\right)^2 + h_4\left(\frac{a}{w}\right)\left(\frac{c}{a}\right)^3 \quad (7.1.31)$$

and  $h_i$  are polynomials of the fifth order

$$h_i = \sum_{k=0}^5 m_{i,k} \left(\frac{a}{w}\right)^k, \quad i = 1, 4 \quad (7.1.32)$$

The geometrical parameters used in Eq.7.1.30 can be found in Fig.7.6 where the load position  $x'$  has been indicated by  $c$ . To define the exact form of the function  $H$  (and then  $h_i$ ) it is

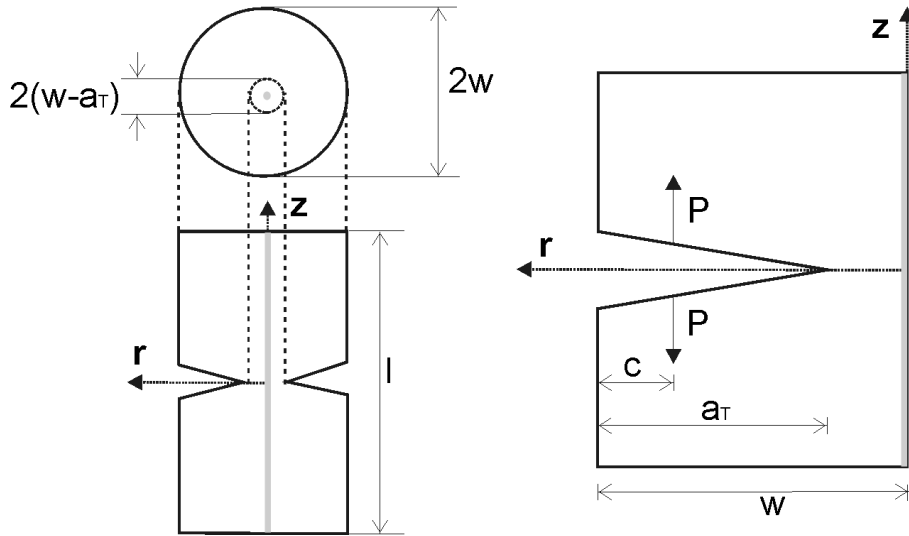


**Figure 7.6:** Reinforced cylindrical specimen modeled to calculate the weight function.

necessary to use a finite element model to calculate the stress intensity factor  $K_I$  at a given point close to the crack tip for different combinations of the ratios  $\left(\frac{c}{w}\right)$  and  $\left(\frac{a}{w}\right)$  varying in an established range compatible with the dimension of the specimen. When  $K_I$  is determined, by using Eq.7.1.30 also the corresponding value of  $H$  can be easily calculated. In particular, at each fixed value of  $\left(\frac{a}{w}\right)$ , the FE model provides the value of  $K_I$  at every corresponding variation of  $\left(\frac{c}{w}\right)$ . This way,  $H$  can then be drawn as a function of  $\left(\frac{c}{a}\right)$  and any  $\left(\frac{a}{w}\right)$  (i.e. at each fixed crack length  $a_T$ ). Solving the system

$$\begin{pmatrix} 1 & \left(\frac{c_1}{a_T}\right) & \left(\frac{c_1}{a_T}\right)^2 & \left(\frac{c_1}{a_T}\right)^3 \\ 1 & \left(\frac{c_2}{a_T}\right) & \left(\frac{c_2}{a_T}\right)^2 & \left(\frac{c_2}{a_T}\right)^3 \\ 1 & \dots & \dots & \dots \\ 1 & \dots & \dots & \dots \\ 1 & \dots & \dots & \dots \\ 1 & \left(\frac{c_n}{a_T}\right) & \left(\frac{c_n}{a_T}\right)^2 & \left(\frac{c_n}{a_T}\right)^3 \end{pmatrix} \begin{pmatrix} h_1 \\ h_2 \\ h_3 \\ h_4 \end{pmatrix} = \begin{pmatrix} H\left(\frac{c_1}{a_T}, \frac{a_T}{w}\right) \\ H\left(\frac{c_2}{a_T}, \frac{a_T}{w}\right) \\ \dots \\ \dots \\ H\left(\frac{c_n}{a_T}, \frac{a_T}{w}\right) \end{pmatrix} \quad (7.1.33)$$

the function  $h_i$  can be described as a function of  $(\frac{a}{b})$  and finally calculated by the determination of the coefficients  $m_{i,k}$  as suggested in Eq.7.1.32 via a simple polynomial interpolation. It is important to notice here that the system 7.1.33 is an over-determined system (we have more equations than unknowns); its solution is thus obtained via a minimization procedure (least square fit) in order to reduce the numerical error in the determination of the coefficients  $h_i$ .

With reference to the cylindrical specimen used in the tests of Chapter five and six, it has been simplified by modeling the geometry by an axisymmetric model Fig.7.7 (more details on the model itself will be given in the subsequent section). It is important to underline that

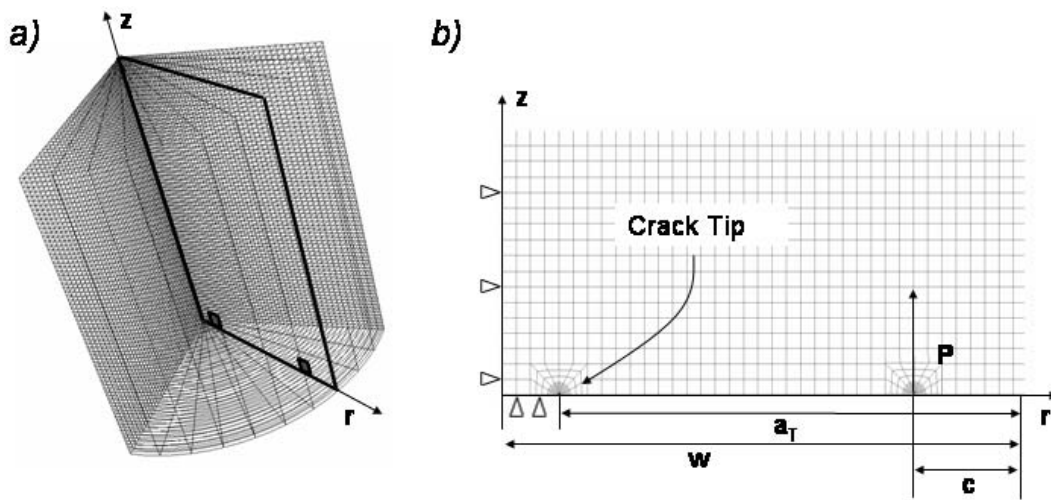


**Figure 7.7:** a) One eighth of the 3-D view of the cylindrical specimen. The simulated  $rz$ -plane is highlighted with bold lines. b) Example of the mesh in the model. The applied symmetry conditions are indicated by using triangular symbols.

particular attention has been taken to mesh the region around the application point of the force  $P$  and around the crack tip, in order to increase the precision in the calculation of the desired quantities (see Fig.7.7b)).

The length of the fracture  $a_T$  is chosen to vary between 2.5 mm and 11 mm (conforming to the experiments presented in Chapter 6), so the corresponding range of  $(\frac{a}{w})$  is taken between 0.2 and 0.88. The step depends on how many points of measure are needed to make the calculations sufficiently accurate. At each value of  $(\frac{a}{w})$ ,  $(\frac{c}{a})$  is varied between 0.15 and 0.9, so at any corresponding length of fracture  $a$  it is necessary to vary the position of  $c$  of the dipole of charges  $P$  to obtain the desired ratio for  $(\frac{c}{a})$ . At any combination of  $c$  and  $a$  the FE model provides the value of  $K_I$  along a given path around the crack tip (Fig.7.8). By using the finite element simulations the system 7.1.33 can be completed. Finally their solutions allow to find the function  $H$  and  $h_i$  (Fig.7.9 and Fig.7.10). The polynomial fit of the data plotted in Fig.7.10 as expressed in Eq.7.1.32, gives the values of the coefficients  $m_{i,k}$  Table 7.1. The complete analytical expression of the functions  $h_i$  have been obtained and presented

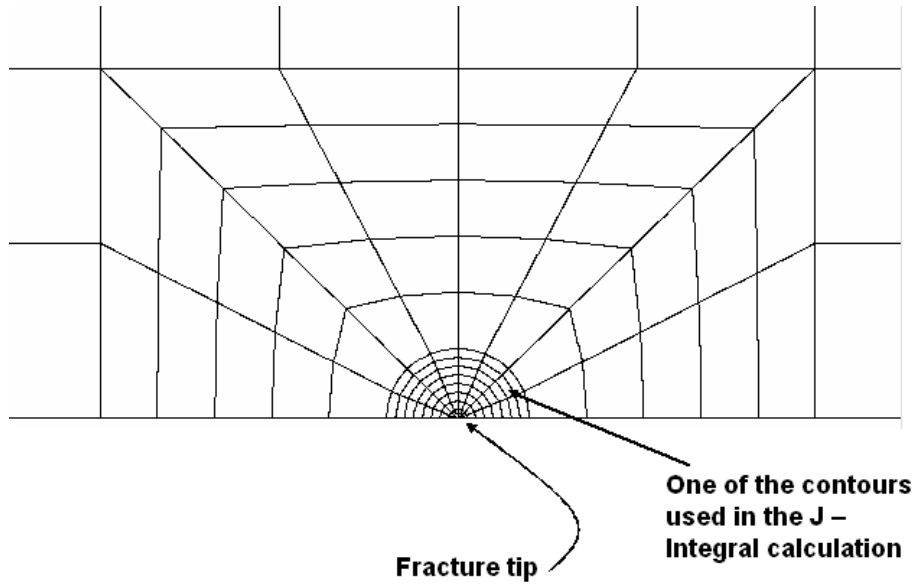


**Figure 7.8:** Particular of the mesh implemented in the FE model used to calculate the value of  $K_I$ . The J-contour integral based on the Virtual Crack Extension Method approach is the routine used by the FE codes to calculate  $K_I$ .

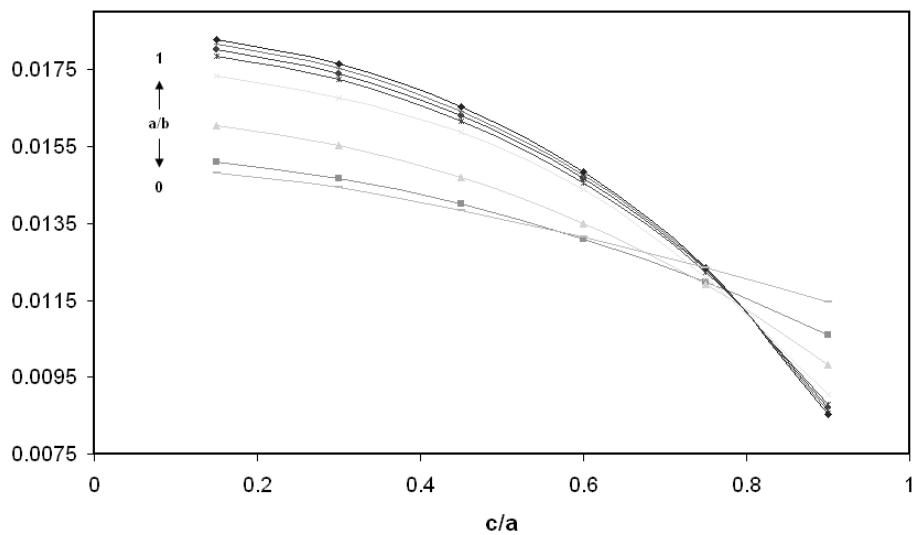


**Figure 7.9:** Evolution of  $H$  as a function of  $(\frac{c}{a})$  for different values of  $(\frac{a}{b})$ .

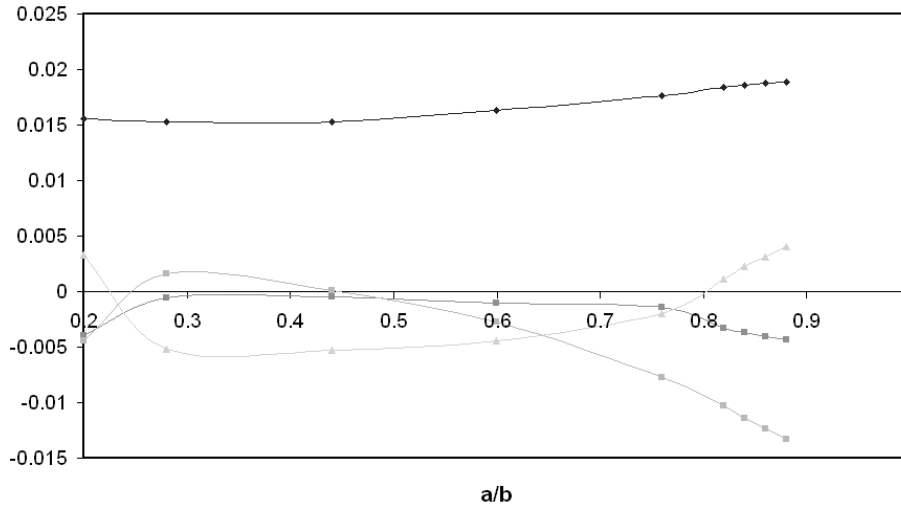


**Figure 7.10:** The different evolutions of the functions  $h_i$  for the considered configuration.

$m_{i,k}$						
	0.01691	-0.00633	-0.01354	-0.07338	-0.07601	-0.02592
	-0.05924	0.58313	-2.19723	3.94309	-3.38017	1.10485
	0.13688	-1.40646	5.28842	-9.50370	8.19110	-2.70225
	-0.10356	1.04646	-3.93487	7.04412	-6.09661	2.03193

**Table 7.1:** Coefficients  $m_{i,k}$  determined to fit the functions drawn in Fig.7.10.

in Eq.7.1.34

$$\begin{aligned}
h_1 &= 0.01691 - 0.00633 \left(\frac{a}{w}\right) - 0.01354 \left(\frac{a}{w}\right)^2 + 0.07338 \left(\frac{a}{w}\right)^3 - 0.07601 \left(\frac{a}{w}\right)^4 + 0.02592 \left(\frac{a}{w}\right)^5 \\
h_2 &= -0.05924 + 0.58313 \left(\frac{a}{w}\right) - 2.19723 \left(\frac{a}{w}\right)^2 + 3.94309 \left(\frac{a}{w}\right)^3 - 3.38017 \left(\frac{a}{w}\right)^4 + 1.10485 \left(\frac{a}{w}\right)^5 \\
h_3 &= 0.13688 - 1.40646 \left(\frac{a}{w}\right) + 5.28842 \left(\frac{a}{w}\right)^2 - 9.50370 \left(\frac{a}{w}\right)^3 + 8.19110 \left(\frac{a}{w}\right)^4 - 2.70225 \left(\frac{a}{w}\right)^5 \\
h_4 &= -0.10356 + 1.04646 \left(\frac{a}{w}\right) - 3.93487 \left(\frac{a}{w}\right)^2 + 7.04412 \left(\frac{a}{w}\right)^3 - 6.09661 \left(\frac{a}{w}\right)^4 + 2.03193 \left(\frac{a}{w}\right)^5
\end{aligned} \tag{7.1.34}$$

By combining Eq.7.1.34, Eq.7.1.31 and Eq.7.1.32 the explicit expression of  $g(x, a)$  can be finally retrieved.

In particular, it is easy to calculate the analytical expression of the function  $H$  in the limiting cases corresponding to  $\left(\frac{a}{w}\right) \rightarrow 0$  and  $\left(\frac{a}{w}\right) \rightarrow 1$ . In the first case we have

$$H = m_{1,0} + m_{2,0} \left(\frac{c}{a}\right) + m_{3,0} \left(\frac{c}{a}\right)^2 + m_{4,0} \left(\frac{c}{a}\right)^3 \tag{7.1.35}$$

while for  $\left(\frac{a}{w}\right) \rightarrow 1$ , the function  $H$  assumes the following form:

$$H = \sum_{k=0}^5 m_{1,k} + \sum_{k=0}^5 m_{2,k} \left(\frac{c}{a}\right) + \sum_{k=0}^5 m_{3,k} \left(\frac{c}{a}\right)^2 + \sum_{k=0}^5 m_{4,k} \left(\frac{c}{a}\right)^3 \tag{7.1.36}$$

### 7.1.6 The virtual crack extension method to compute $K_I$ : stiffness derivative formulation

The Virtual Crack Extension approach was one of the first FE methods used to inferring energy release rate in elastic bodies. It can be also used in the case of non-linear behavior and large deformations at the crack tip.

Consider a two-dimensional cracked body with unit thickness subjected to Mode I loading. The potential energy of the body, in terms of the finite element solution, is given by

$$\Pi = \frac{1}{2} [u]^T [K] [u] - [u]^T [F] \tag{7.1.37}$$

where  $\Pi$  is the potential energy,  $[u]$  the global displacement,  $[K]$  the stiffness matrix and  $[F]$  the global force applied to the structure. We recall here that the energy release rate can be defined [4, 42] as the derivative of  $\Pi$  with respect to crack area  $s$ , for both fixed load and fixed displacement conditions. In particular for fixed load conditions (more convenient in this instance), we have for  $G$

$$G = - \left( \frac{\partial \Pi}{\partial s} \right)_{load} = - \frac{\partial [u]^T}{\partial s} ([K] [u] - [F]) - \frac{1}{2} [u]^T \frac{\partial [K]}{\partial s} [u] + [u]^T \frac{\partial [F]}{\partial s} \tag{7.1.38}$$

Because in the FE formulation we have  $[K] [u] = [F]$ , the first term in Eq.7.1.38 must be zero. In the absence of tractions on the crack face, the third term also vanishes, since load are held constant. Thus the energy release rate is given by

$$G = \frac{K_I^2}{E'} = - \frac{1}{2} [u]^T \frac{\partial [K]}{\partial s} [u] \tag{7.1.39}$$

This way, the energy release rate is proportional to the derivative of the stiffness matrix with respect to the crack length.

Suppose that we have generated a finite element mesh for a body with crack length  $a$  and we wish to extend the crack by  $\Delta a$ . It would not be necessary to change all of the elements in the mesh; we could accommodate the crack growth by moving elements near the crack tip and leaving the rest of the mesh intact. Fig.7.11 illustrates such a process, where element inside the contour  $\Gamma_0$  are shifted by  $\Delta a$ , and elements outside the contour  $\Gamma_1$  are unaffected.

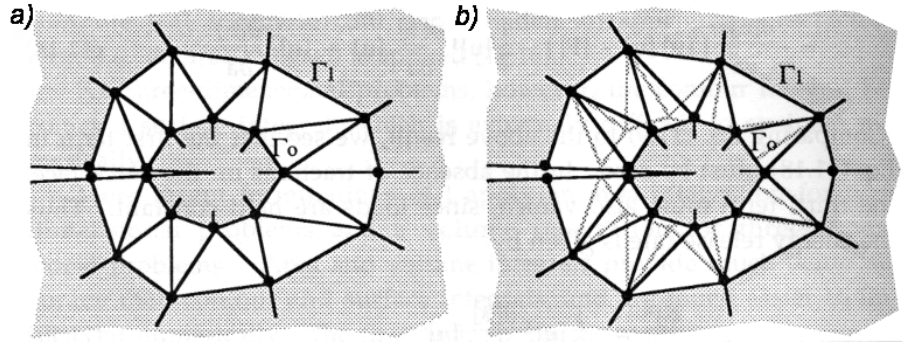


**Figure 7.11:** *Virtual crack extension method working principle: a) initial conditions and b) after virtual crack advance [4].*

Each of the elements between  $\Gamma_0$  and  $\Gamma_1$  is distorted, such that its stiffness changes. The energy release is related to this change in element stiffness:

$$G = -\frac{1}{2}[u]^T \left( \sum_{i=1}^{N_c} \frac{\partial [k_i]}{\partial a} \right) [u] \quad (7.1.40)$$

where  $[k_i]$  are the elemental stiffness matrices and  $N_c$  is the number of elements between the contour  $\Gamma_0$  and  $\Gamma_1$ . Parks [59] demonstrated that Eq.7.1.40 is equivalent to the  $J$ -integral. The value of  $G$  (or  $J$ ) is independent of the choice of the inner and outer contours.

It is important to note that in a virtual crack extension analysis, it is not necessary to generate a second mesh with a slightly longer crack. It is sufficient merely to calculate the changes in element stiffness matrices corresponding to shifts in the nodal coordinates. One of the problems with the stiffness derivative approach is that it involves cumbersome numerical differencing. Nevertheless, though more recent formulations of the virtual crack extension method overcome these difficulties, it remains the basis for calculating the SIF of cracked bodies by using FE method.

## 7.2 FE analysis of residual stresses

The main application of FEM analysis in this work is the determination of the complete residual strain field generated during the polymerization process within a SFC specimen based on the experimental results obtained from the FBGs. The commercial FEM code Abaqus [38] is

used for simulations.

As indicated in Fig.7.12a) the specimen is considered to be cylindrical fiber-reinforced com-

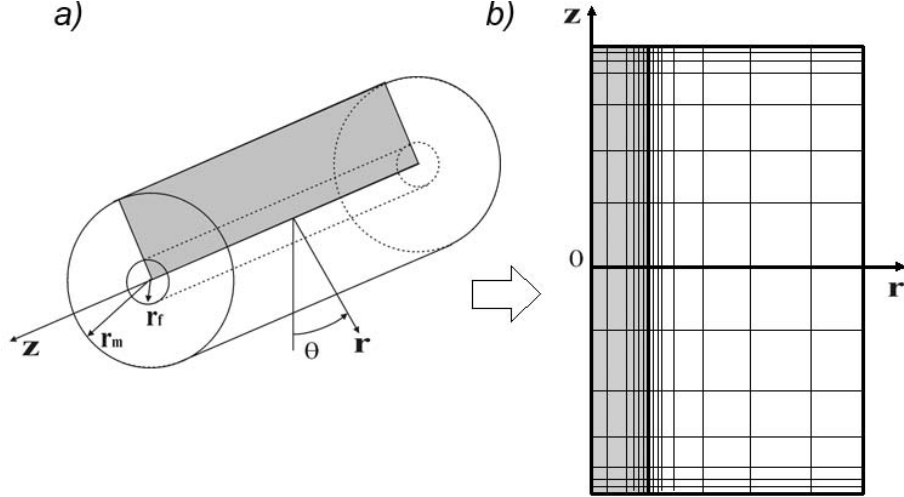


**Figure 7.12:** *a) Scheme of the two-phase composite modeled in the present analysis and b) the associated 2-D section meshed with axisymmetric elements.*

posite consisting of two concentric cylinders. The fiber is the central cylinder of radius  $r_f = 0.0625$  mm. The matrix domain corresponds to the annulus of inner radius  $r_f$  and outer radius  $r_m = 12.5$  mm. The fiber and the matrix are considered to have a perfect interface. In particular, for the two materials, the stress equilibrium equations are written in the cylindrical coordinate system  $(r, \theta, z)$  shown in Fig.7.12a) as follows

$$\begin{aligned} \frac{1}{r} \frac{\partial(r\sigma_{rr}^{(i)})}{\partial r} + \frac{\partial\tau_{rz}^{(i)}}{\partial z} - \frac{\sigma_{\theta\theta}}{r} &= 0 \\ \frac{1}{r} \frac{\partial(r\tau_{rz}^{(i)})}{\partial r} + \frac{\partial\sigma_{zz}^{(i)}}{\partial z} &= 0 \end{aligned} \quad i = m, f \quad (7.2.1)$$

### 7.2.1 The axisymmetric model

Due to the simple geometry of the considered specimen, an axisymmetric finite element model is used to retrieve the residual strain state in the specimen. The assumed axisymmetric mode of deformation states that the non-zero stress components  $(\sigma_r, \sigma_\theta, \sigma_z, \tau_{rz})$  and displacement components  $(u_r, u_z)$  do not vary with  $\theta$ . The problem can be then considered as two-dimensional and only the  $rz$ -plane shown in Fig.7.12b) needs to be meshed. Along the longitudinal and transversal directions, the matrix domain is discretized into  $300 \times 300$  elements. For the fiber  $300 \times 30$  elements are used. The mesh is constructed with 8-node quadratic axisymmetric quadrilateral elements and is refined toward the ends and at the fiber-matrix interface to accommodate potentially strong variations of the field quantities. In addition, different types of mesh and elements have been compared to check their influence on the simulation results.



The constitutive law that governs the behavior of the model is based on relation 7.1.1 where the function  $S_m(r, z)$  is given by 7.1.2. We are reminding that the optimized coefficients  $a, b, c, d$  can be found using a procedure that minimizes the difference between the calculated and measured strains along the grating. Moreover, the stresses calculated with the model have also to match the experimental stress evolutions presented in Fig.6.7.

In order to correctly describe the overall residual stress field within the specimen, it is also necessary to calculate the function  $f(r)$  in Eq.7.1.2. As indicated in the first paragraph of this chapter the form of  $f(r)$  is calculated by interpolating the derivative of the C.O.D. sketched in Fig.7.1.3. In particular it is found that a polynomial of the sixth order is enough to fit the first derivative of the crack opening displacement, namely

$$f(r) = a' + b' \left( \frac{r}{r_m - r_f} \right) + c' \left( \frac{r}{r_m - r_f} \right)^2 + d' \left( \frac{r}{r_m - r_f} \right)^3 + e' \left( \frac{r}{r_m - r_f} \right)^4 + f' \left( \frac{r}{r_m - r_f} \right)^5 + g' \left( \frac{r}{r_m - r_f} \right)^6 \quad (7.2.2)$$

The best values found for the parameters  $a, b, c, d$  and  $a', b', c', d', e', f', g'$  are reported in Table 7.2 and in Table 7.3 respectively.

$a$	$b$	$c$	$d$
2.1	0.014	-6.42	0.00015

**Table 7.2:** Coefficients  $a, b, c, d$  used in the function  $S_m(r, z)$ .

$a'$	$b'$	$c'$	$d'$	$e'$	$f'$	$g'$
5.6	3	-317	1342.2	-2345.8	1897.2	-585.5

**Table 7.3:** Coefficients  $a', b', c', d', e', f', g'$  used in the function  $S_m(r, z)$ .

The complete expression of the function  $S_m$  can be retrieved and then used in the finite element model to describe the strain and the stress fields within the whole cylindrical specimen.

The simulated strain distribution along the fiber for the specimen S1 is presented in Fig.7.13 and as expected, it correctly matches the experimental measurements. In Fig.7.14 and in Fig.7.15 the simulated stress distribution  $\sigma_z^m(r)$  has been obtained when the function  $R(r)$  in the expression of  $S_m$  is taken constant (i.e.  $d = 0$ ) or in its general form ( $d \neq 0$ ). This indicates that, for the considered geometry, only the axial function  $Z(z)$  plays a significant role in the characterization of the matrix shrinkage effect. In particular if the radius of the cylinder is reduced to 4 mm the function  $Z(z)$  correctly fits the experimental results without an appreciable difference (see 7.16). Nevertheless in a region close to the fiber (see 7.15) the radial dependence of the function  $S_m$  helps in reducing the error between the numerical and the experimental results. Finally, Fig.7.17 summarizes the radial dependency of the transverse field at  $z = 0$  that is in relatively good agreement with available results in the literature [43].

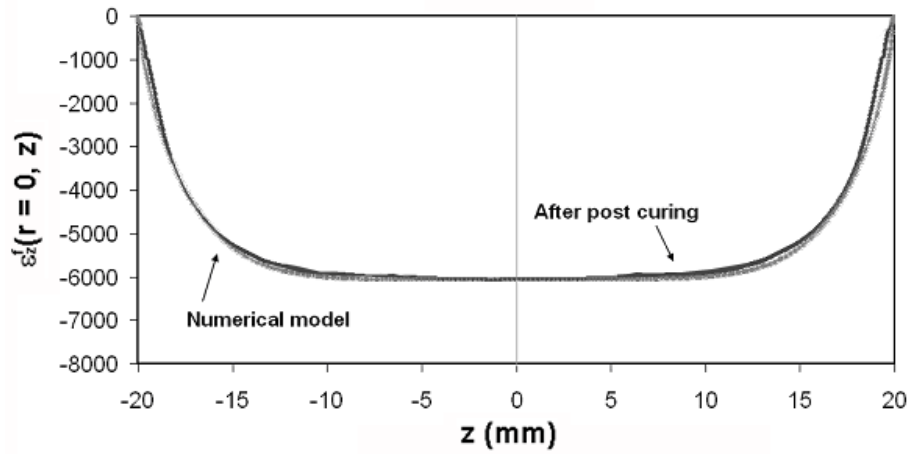


**Figure 7.13:** Comparison between the experimental (black line) and the numerical (grey line) axial strain distribution for the specimen S1.

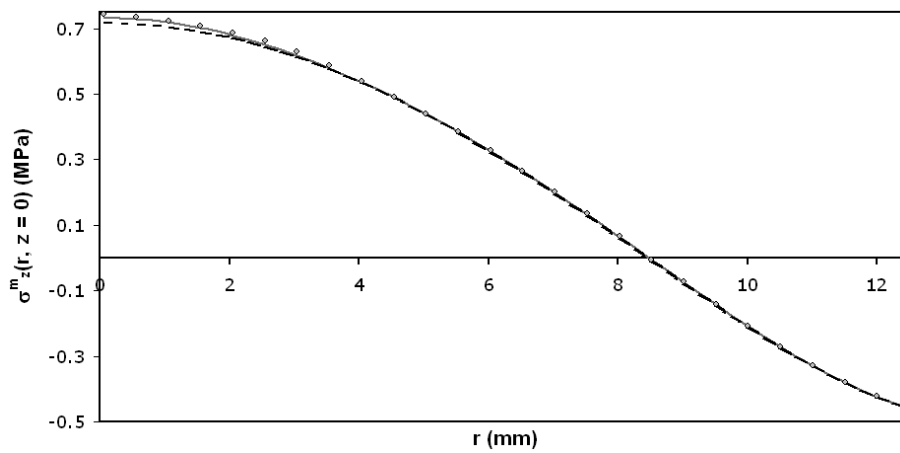


**Figure 7.14:** The experimental stress evolution  $\sigma_z^m(r)$  (dotted line) is compared with the numerical evolution when  $R(r)$  is taken in its general form or when the radial effect is neglected (dashed line).

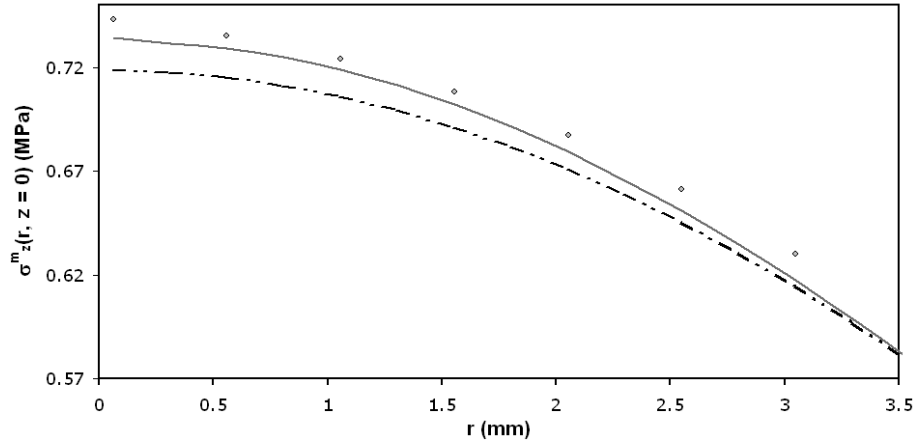


**Figure 7.15:** Particular of the Fig.7.14 where is highlighted the effect on the stress evolution due to introduction of a radial effect in the general expression of  $S_m$ .

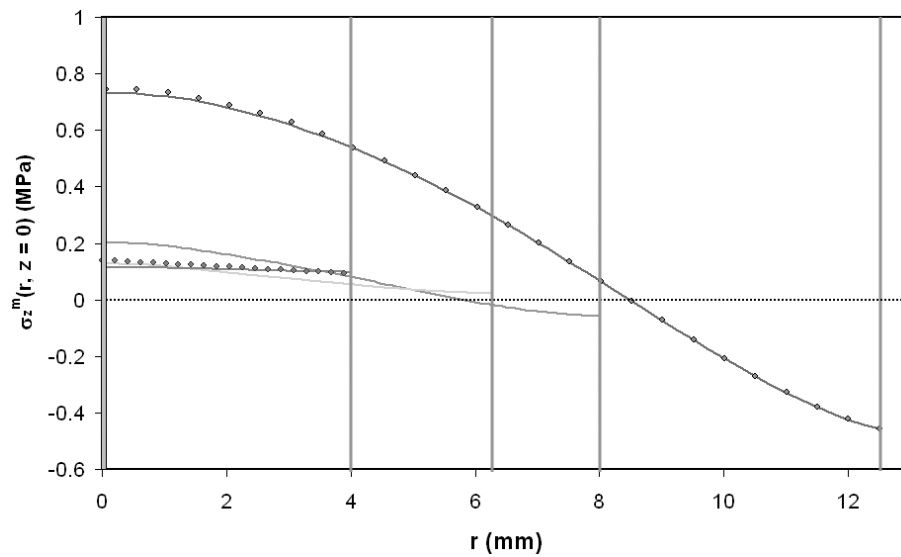


**Figure 7.16:** Evolution of the axial stress distribution as a function of the specimen radius. The distribution obtained for the bigger and smaller radius are compared with those ones calculated via the C.C. method.

To have another independent experimental result to guaranty the quality of the numerical

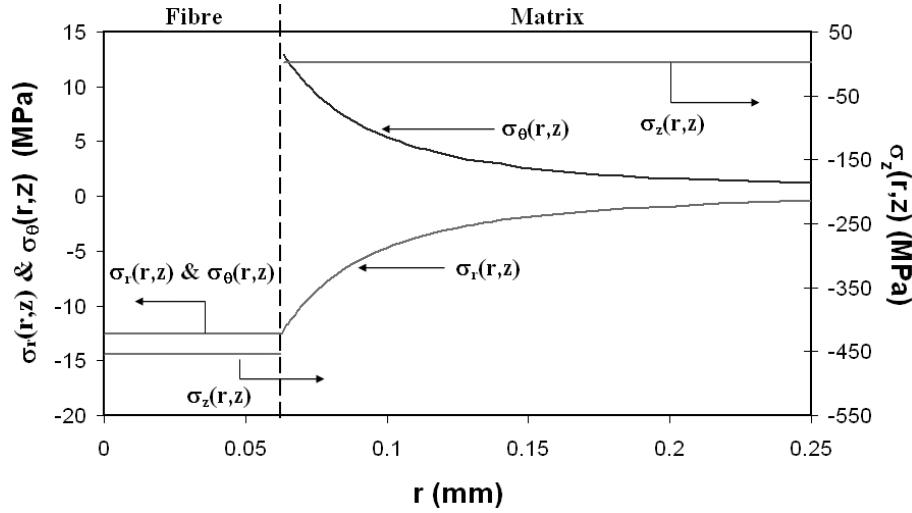


**Figure 7.17:** Axial and transversal stress evolutions in the plane  $z = 0$ .

simulation, after the post-cure treatment the deformed shape of the cylindrical specimen  $S1$  has been reconstructed by using a Coordinate Measuring Machine (CMM) (Fig.7.18 *a*) with a resolution of  $\mu m$  and is compared with FE prediction. As shown in Fig.7.18 *b*), even if some differences (generally at the ends of the specimen) are present due to the simplified assumption used in defining Eq.7.1.2 (i.e. the variable separation is likely valid only at the center of the specimen) the simulated data are in good agreement with the measured ones.

## 7.2.2 The fiber-matrix interface shear stress

In Fig.7.19, the shear stress  $\tau_{r,z}(z)$  is plotted at the fiber matrix interface for the specimen  $S1$ . The plot clearly shows higher shear stresses towards the free surface. That is the region where the fiber intersects the specimen free ends. Note that the maximum shear value reached generally increases as long as the FE mesh is simply refined towards the end in the region of singularity. This is an example of a classical numerical problem that arrives when using the finite element approach.

Nevertheless, from a physical point of view, the shear stress has to be exactly zero on the free surface, otherwise the model solution is acceptable only at a certain distance from the specimen ends.

It is sometimes possible to correct this problem by using singular elements ([38]), whose interest is to eliminate the singularity, providing thus a valid finite value of the desired quantity. This requires the a priori knowledge of the order of singularity at the point of interest. When the singularity's order is unknown it is possible to obtain the desired shear stress value by using a sufficiently refined radial mesh centered at the point of singularity as indicated by Kovalev [47]. Even if the number of elements in this last case is higher than that used in the case of the singular elements, the problem of the singularity can be eliminated. In our case we

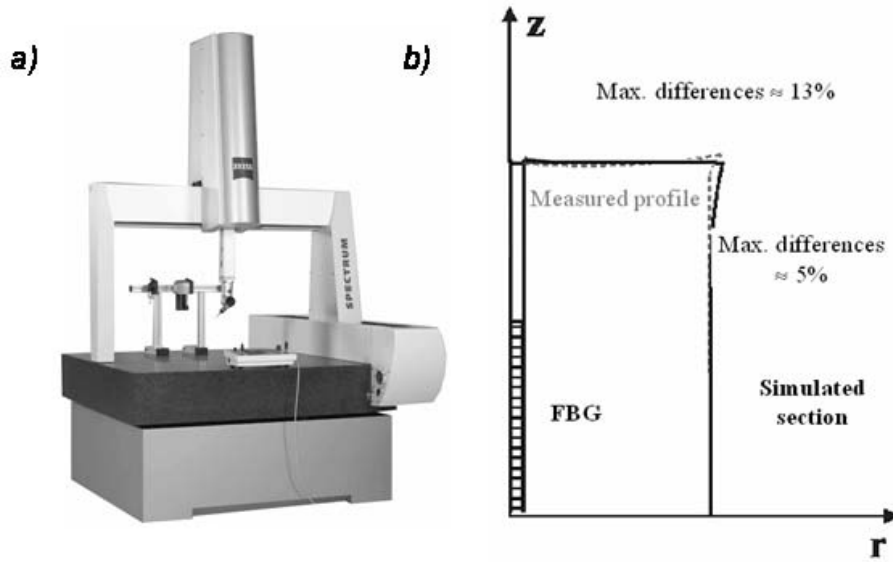


**Figure 7.18:** a) Photo of a coordinate measuring machine. b) Comparison between the simulated and the measured cylindrical profile by CMM.

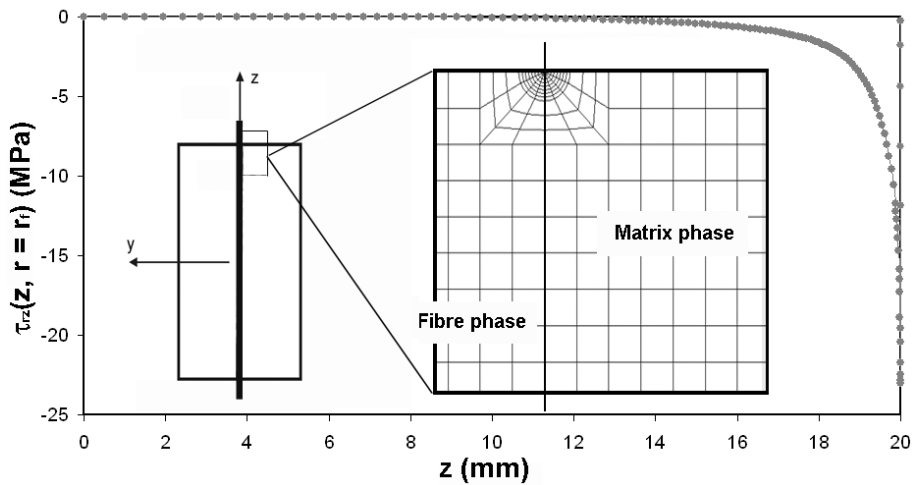


**Figure 7.19:** Evolution of the fiber/matrix interface shear stress. The mesh refinement of Kovalev (insert) has been used to catch the correct shear distribution at the specimen end.

have adopted the mesh refinement suggested by Kovalev. The benefits are visible in Fig.7.19 where the distribution of the shear stress is correctly matched by the model; the shear stress drops in fact to zero at the specimen ends.

### 7.3 Finite Element modeling of the longitudinal crack

Since the introduction of the longitudinal crack breaks the axial symmetry of the specimen  $S1$  (see the insert of Fig.6.9), a more complex 3-D mesh of  $S1$  is required to explain the measured axial strain relaxation along the grating. Nevertheless, taking into account the symmetries along the axial direction and the crack plane, only a quarter of the cylinder need to be meshed (Fig.7.20).

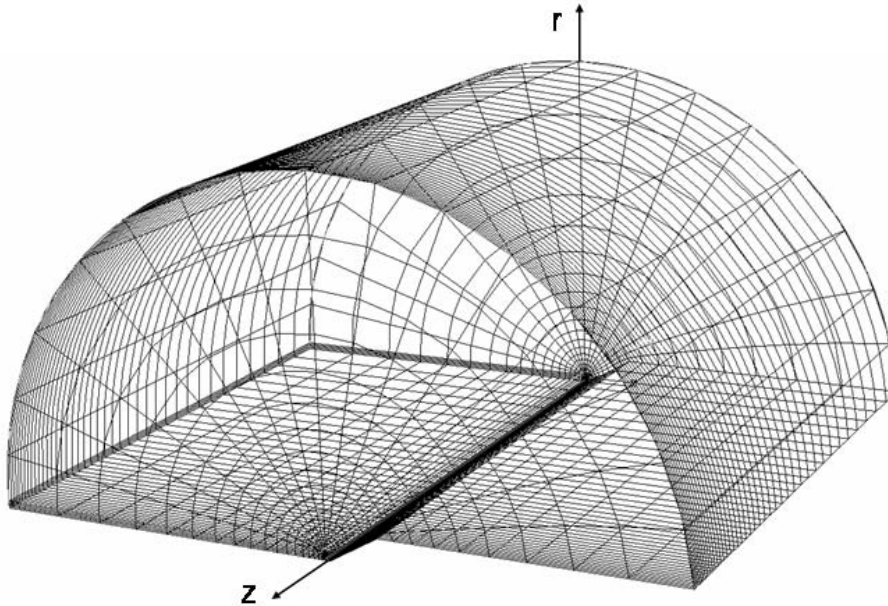


**Figure 7.20:** A quarter of the 3-D model used to simulate the effect of the longitudinal crack.

The mesh is constructed with 20-node quadratic hexaedric elements for the matrix and with 15-node quadratic triangular prisms for the fiber. As in the axisymmetric case, the mesh is refined towards the ends of the specimen and in the fiber region in order to capture any variations of the field quantities.

Based on the superposition principle, (see insert of Fig.7.21) the strain distribution due to the longitudinal crack has been calculated as the difference between the one obtained with the un-cracked 3-D model (subjected to the function  $S_m(r, z)$ ) and the one due to relaxed hoop stress  $\epsilon_\theta(r)$  imposed along the crack surfaces.

Note that the hoop stress evolution  $\epsilon_\theta(r)$  is numerically identified via the finite element

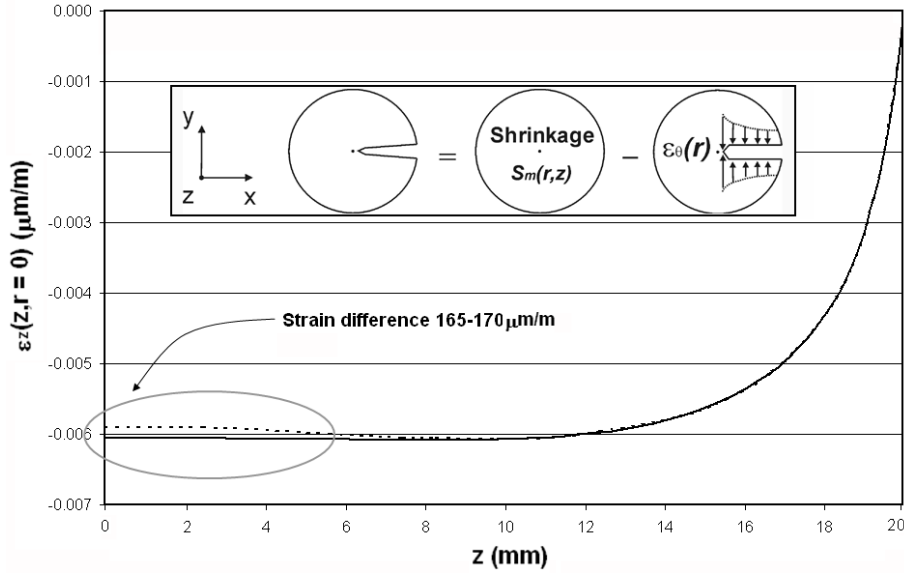


**Figure 7.21:** Complete strain evolution simulated without longitudinal cut (continuous line) and with a cut of depth  $a_L = r_m - 2r_f$  (dashed line). The axial relaxation corresponds to the one measured by the FBG.

analysis dealing with the axisymmetric model (see. Fig.7.17). In particular

$$\epsilon_r(r, z = 0) = p \frac{r_f^2}{r_m^2 - r_f^2} \frac{r_e^2 - r^2}{r^2} \quad \text{Lamé, 1852} \quad (7.3.1)$$

where  $p$  is the constant radial pressure applied at the fiber/matrix interface and equal to 13 MPa. As shown in Fig.7.21 finite element simulations indicate an axial strain strain relaxation of about  $170 \mu m$  in the central region of the specimen. As expected, the compressive stress due to the matrix shrinkage is not equally distributed on the fiber surface ( $\theta$  dependency). Consequently the cylindrical specimen is subjected to a bending which slightly deforms the fiber and relax the strain, overall in a region of 6 mm length close to the plane  $z = 0$  (see Fig.7.22). The strain variation calculated by the model is  $165-175 \mu m$ , which is compatible with that measured by the FBG sensor. A difference of 10 % is observed between the numerical and the experimental results. It can be attributed to an imperfect alignment of the fiber along the axial direction or by some possible changes in the interface properties between the epoxy matrix and the glass fiber produced during the cutting process or during the bending deformation.

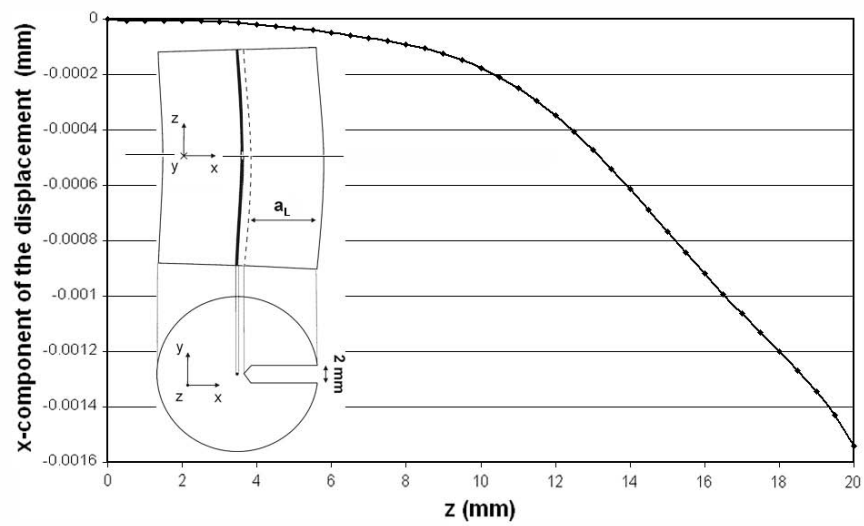


**Figure 7.22:** Component in the  $x$ -direction of the fiber displacement after machining the longitudinal crack.



## Chapter 8

# Analytical modeling of residual stresses

Composite materials are inherently inhomogeneous, in term of both elastic and inelastic properties. One consequence of this is that, on applying a load, a non-uniform distribution of stress is set up within the composite. Much effort has been devoted to understanding and predicting this distribution, as it determines how the material will behave and can be used to explain the superior properties of composites over conventional material. In this chapter a brief survey is given of the methods used for modeling the residual stress distribution in composites. These techniques range widely in nature and complexity. Some are more suited for certain types of composites and attention is drawn to areas of particular relevance to fiber-reinforced polymer matrix composites.

Even though the presented models may involve mathematical approximations ranging from the good to a very poor they generally present the capability of well estimating the partitioning of load between the constituents of composites subjected to external load. In the same time the analytical model solutions can be used as an ulterior verification of the finite element results. Moreover, even if the analytical models are rather limited in terms of properties which can predict or are computationally daunting, they generalize many problems dealing with residual stresses providing solutions applicable to different experimental cases. Nevertheless the experimental information remains particularly important because it represents the final validation of the analytical model prediction.

### 8.1 The concentric cylinder model of Y. Mikata and M. Taya

In their original approach, Mikata and Taya [56] have studied the general stress field in a coated continuous fiber composites represented by a four-phase model that consists of fiber, coating, matrix, and the remaining surrounding composite body. The composites is then simulated by four concentric long circular cylinders as shown in Fig.8.1. The surrounding body with the composite properties (outermost cylinder), matrix, coating, fiber (innermost cylinder) are denoted by domain, 1,2,3 and 4 respectively, and their radii by  $r_1, r_2, r_3$  and  $r_4$ . The

diameter of the fiber and matrix (including a coated fiber) are denoted by  $d, D$  respectively and the coating thickness by  $c$ . Since the surrounding body is assumed of infinite dimension,

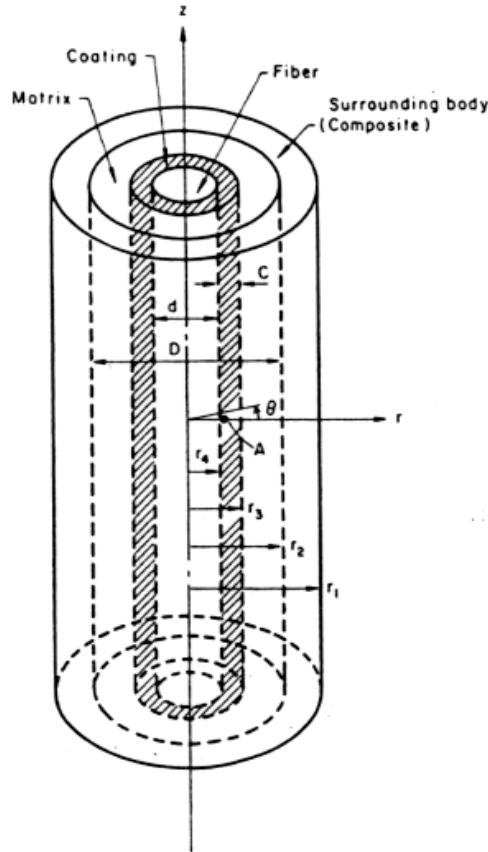


**Figure 8.1:** *Four-phase model [56].*

$r_1$  will be considered infinite at the end of the formulation. Moreover, the concentric material are regarded as infinitely long also in the axial direction  $z$ , thus meaning that the region of interest is assumed to be sufficiently far from the ends to ensure a generalized plane strain mode of deformation.

The general solution of the problem is calculated when the entire body (four cylinders) are subjected to three independent boundary conditions, axisymmetric temperature change,  $\Delta T(r)$ , uniaxial applied stress  $\sigma_{0z}$  and biaxial applied stress  $\sigma_{0r}$  where  $r$  and  $z$  are the radial and axial components referred to cylindrical coordinates  $(r, \theta, z)$ . In general, all the materials are assumed to be transversely isotropic both in stiffness and thermal expansion, where  $(r, \theta)$  corresponds to the transverse plane. As a special case, an explicit close form solution is given considering a uniform temperature change  $\Delta T$  applied to a continuous fiber embedded in an infinite matrix. In this extreme case, the materials used in the two-phase model are taken isotropic homogeneous.

For the  $n^{th}$  domain the general equilibrium equations are given by

$$\begin{aligned} \frac{1}{r} \frac{\partial(r\sigma_{rr}^{(n)})}{\partial r} + \frac{1}{r} \frac{\partial(\tau_{r\theta}^{(n)})}{\partial \theta} + \frac{\partial\tau_{rz}^{(n)}}{\partial z} - \frac{\sigma_{\theta\theta}}{r} &= 0 \\ \frac{1}{r^2} \frac{\partial(r^2\tau_{\theta r}^{(n)})}{\partial r} + \frac{1}{r} \frac{\partial(\sigma_{\theta\theta}^{(n)})}{\partial \theta} + \frac{\partial\tau_{\theta r}^{(n)}}{\partial z} &= 0 \\ \frac{1}{r} \frac{\partial(r\tau_{zr}^{(n)})}{\partial r} + \frac{1}{r} \frac{\partial(\tau_{z\theta}^{(n)})}{\partial \theta} + \frac{\partial\sigma_{zz}^{(n)}}{\partial z} &= 0 \end{aligned} \quad (8.1.1)$$

Due to the axisymmetry of the problem (i.e.the considered geometry is symmetric respect to the z-axis as are the applied forces and/or displacement), the displacement field in the  $n^{th}$  domain can be expressed as

$$\begin{aligned} u_r^{(n)} &= u_n(r) \\ u_\theta^{(n)} &= 0 \\ u_z^{(n)} &= w_n(z) \end{aligned} \quad (8.1.2)$$

Taking into account the stress-strain relations and the strain-displacement relations, via a substitution one obtains the following stress-displacement equations:

$$\begin{aligned} \sigma_{rr}^{(n)} &= C_{11}^{(n)} \frac{\partial u_n}{\partial r} + C_{12}^{(n)} \frac{u_n}{r} + C_{13}^{(n)} \frac{\partial w_n}{\partial z} - \beta_1^{(n)} T_n \\ \sigma_{\theta\theta}^{(n)} &= C_{12}^{(n)} \frac{\partial u_n}{\partial r} + C_{11}^{(n)} \frac{u_n}{r} + C_{13}^{(n)} \frac{\partial w_n}{\partial z} - \beta_1^{(n)} T_n \\ \sigma_{zz}^{(n)} &= C_{13}^{(n)} \frac{\partial u_n}{\partial r} + C_{13}^{(n)} \frac{u_n}{r} + C_{33}^{(n)} \frac{\partial w_n}{\partial z} - \beta_3^{(n)} T_n \\ \sigma_{rz}^{(n)} &= \sigma_{\theta z}^{(n)} = \sigma_{r\theta}^{(n)} = 0 \end{aligned} \quad (8.1.3)$$

where

$$\begin{aligned} \beta_1^{(n)} &= (C_{11}^{(n)} + C_{12}^{(n)})\alpha_{nT} + C_{13}^{(n)}\alpha_{nL} \\ \beta_3^{(n)} &= 2C_{12}^{(n)}\alpha_{nT} + C_{33}^{(n)}\alpha_{nL} \end{aligned} \quad (8.1.4)$$

with  $C_{i,j}^{(n)}$  elastic constant of the  $n^{th}$  material and  $\alpha_{nT}$  and  $\alpha_{nL}$  the thermal expansion coefficients of the  $n^{th}$  material along the transverse ( $r$ ) and longitudinal ( $z$ ) direction respectively. The governing equations of the problem can be derived in term of displacement from Eq.8.1.1 and Eq.8.1.2 obtaining thus

$$\begin{aligned} \frac{d^2 u_n}{dr^2} + \frac{1}{r} \frac{du_n}{dr} - \frac{u_n}{r^2} &= l_n \frac{dT_n}{dr} \\ \frac{d^2 w_n}{dz^2} & \end{aligned} \quad (8.1.5)$$

where

$$l_n = \frac{\beta_1^{(n)}}{C_{11}^{(n)}} \quad (8.1.6)$$

The boundary conditions for this problem are given by:

$$\begin{aligned}
\sigma_{rr}^n &= \sigma_{0r}, & \text{at } r &= r_1 \\
u_1 = u_2, \quad w_1 = w_2, \quad \sigma_{rr}^{(1)} &= \sigma_{rr}^{(2)}, & \text{at } r &= r_2 \\
u_2 = u_3, \quad w_2 = w_3, \quad \sigma_{rr}^{(2)} &= \sigma_{rr}^{(3)}, & \text{at } r &= r_3 \\
u_3 = u_4, \quad w_3 = w_4, \quad \sigma_{rr}^{(3)} &= \sigma_{rr}^{(4)}, & \text{at } r &= r_4
\end{aligned} \tag{8.1.7}$$

$$\int_0^{r_4} \sigma_{zz}^{(4)} r dr + \int_{r_4}^{r_3} \sigma_{zz}^{(3)} r dr + \int_{r_3}^{r_2} \sigma_{zz}^{(2)} r dr + \int_{r_2}^{r_1} \sigma_{zz}^{(1)} r dr = + \int_0^{r_1} \sigma_{0z} r dr \tag{8.1.8}$$

The general solution to Eq.8.1.5 if given by

$$\begin{aligned}
u_n(r) &= A_n r + \frac{B_n}{r} + \frac{r}{2} \int g_n(r) dr - \frac{1}{2r} \int r^2 g_n(r) dr \\
w_n(z) &= H_n z + F_n
\end{aligned} \tag{8.1.9}$$

where  $A_n, B_n, H_n$  and  $F_n$  are unknown constants which will be determined considering the appropriate boundary conditions, Eq.8.1.6 and Eq.8.1.7, while  $g_n(r) = l_n \frac{dT_n}{dr}$ . More details on the solution process exposed by Mikata and Taya can be directly found in their paper and in the cited references.

More attention has to be paid to the explicit close form solution proposed in the case of a single inhomogeneity problem (i.e. continuous fiber embedded in an infinite matrix) because allows a direct comparison between the results of the present analysis and those obtained by the finite element model exposed in chapter 7.

To this end, we consider the case of uniform temperature change  $\Delta T$ . The domains of the matrix, fiber and the radius of the fiber are denoted by 1,2 and  $r_2$ , respectively. The displacement and the stress fields in each domain are now expressed as

$$\begin{aligned}
\sigma_{rr}^{(1)} &= C_{11}^{(1)} \left( A_1 - \frac{B_1}{r^2} \right) + C_{12}^{(1)} \left( A_1 + \frac{B_1}{r^2} \right) + C_{13}^{(n)} H - \beta_1^{(1)} \Delta T \\
\sigma_{\theta\theta}^{(1)} &= C_{12}^{(1)} \left( A_1 - \frac{B_1}{r^2} \right) + C_{11}^{(1)} \left( A_1 + \frac{B_1}{r^2} \right) + C_{13}^{(n)} H - \beta_1^{(1)} \Delta T
\end{aligned} \tag{8.1.10}$$

$$\begin{aligned}
\sigma_{zz}^{(1)} &= 2C_{13}^{(1)} A_1 + C_{33}^{(1)} H - \beta_3^{(1)} \Delta T \\
\sigma_{rr}^{(2)} &= A_2 (C_{11}^{(2)} + C_{12}^{(2)}) + C_{13}^{(3)} H - \beta_1^{(2)} \Delta T \\
\sigma_{\theta\theta}^{(2)} &= A_2 (C_{11}^{(2)} + C_{12}^{(2)}) + C_{13}^{(2)} H - \beta_1^{(2)} \Delta T \\
\sigma_{zz}^{(2)} &= 2C_{13}^{(2)} A_2 + C_{33}^{(2)} H - \beta_3^{(2)} \Delta T
\end{aligned} \tag{8.1.11}$$

When the material 1 and 2 are isotropic both in stiffness and in thermal expansion the following relations have to be satisfied by the coefficients

$$\begin{aligned}
C_{11}^{(1)} = C_{33}^{(1)} &= 2\mu_1 + \lambda_1, & C_{12}^{(1)} = C_{13}^{(1)} &= \lambda_1 \\
C_{11}^{(2)} = C_{33}^{(2)} &= 2\mu_2 + \lambda_2, & C_{12}^{(2)} = C_{13}^{(2)} &= \lambda_2 \\
\alpha_{1T} = \alpha_{1L} &= \alpha_1, & \alpha_{2T} = \alpha_{2L} &= \alpha_2 \\
\beta_1^{(1)} = \beta_3^{(1)} &= (2\mu_1 + 3\lambda_1)\alpha_1, & \beta_1^{(2)} = \beta_3^{(2)} &= (2\mu_2 + 3\lambda_2)\alpha_2
\end{aligned} \tag{8.1.12}$$

where  $\mu_1, \lambda_1, \alpha_2$  and  $\mu_2, \lambda_2, \alpha_2$  are Lamé constants and the thermal expansion coefficient of the materials 1 and 2 respectively. In particular we remind that the Lamé coefficients are related to the Young modulus ( $E$ ) and to the Poisson ratio ( $\nu$ ) of the material by the following relations:

$$\begin{aligned} \lambda_i &= \frac{E_i \nu_i}{(1 + \nu_i)(1 - 2\nu_i)} \\ \mu_i &= \frac{E_i}{2(1 + \nu_i)} \end{aligned} \quad i=1,2 \quad (8.1.13)$$

A substitution process permits to find that

$$\begin{aligned} A_1 &= H = \alpha_1 \Delta T \\ A_2 &= \frac{(2\mu_1 - \lambda_2)\alpha_1 + (2\mu_2 + 3\lambda_2)\alpha_2}{2(\mu_1 + \mu_2 + \lambda_2)} \Delta T \\ B_1 &= -\frac{2\mu_2 + 3\lambda_2}{2(\mu_1 + \mu_2 + \lambda_2)} (\alpha_1 - \alpha_2) \Delta T r_2^2 \end{aligned} \quad (8.1.14)$$

Finally, taking into account the previous relations, the expressions giving the stresses in two constitutive phases of the composite under consideration are

$$\begin{aligned} \sigma_{rr}^{(1)} &= \frac{\mu_1(2\mu_2 + 3\lambda_2)}{\mu_1 + \mu_2 + \lambda_2} (\alpha_1 - \alpha_2) \Delta T \frac{r_2^2}{r} \\ \sigma_{\theta\theta}^{(1)} &= -\sigma_{rr}^{(1)} \\ \sigma_{zz}^{(1)} &= 0 \\ \sigma_{rr}^{(2)} &= \frac{\mu_1(2\mu_2 + 3\lambda_2)}{\mu_1 + \mu_2 + \lambda_2} (\alpha_1 - \alpha_2) \Delta T \\ \sigma_{\theta\theta}^{(2)} &= \sigma_{rr}^{(2)} \\ \sigma_{zz}^{(2)} &= \frac{(\mu_1 + \mu_2)(2\mu_2 + 3\lambda_2)}{\mu_1 + \mu_2 + \lambda_2} (\alpha_1 - \alpha_2) \Delta T \end{aligned} \quad (8.1.15)$$

The axial residual stress  $\sigma_z^f(r = 0, z)$  predicted by the finite element model and due to the matrix shrinkage effect (function  $S_m$ ) is then compared with the distribution provided by the last equation in 8.1.15, where in the term  $(\alpha_1 - \alpha_2)\Delta T$ ,  $\alpha_2$  is assumed equal to zero because the fiber is free of residual stresses.

The two distributions of stresses along the fiber is given in Fig.8.2. Even though the problem developed and solved by Mikata and Taya is only an ideal treatment of our case because the real specimen has a finite dimensions, a good agreement is presented in a region of 20 mm length at the center of the cylinder. This is an indirect confirmation of the fact that at the center of the sample a plane strain mode of deformation can be reasonably assumed to describe the behavior of the composite. In fact, if in its central section the real cylinder is modeled by a 2-D generalized plane strain model where the function  $S_m$  is substituted by its constant value of  $-6000\mu m$ , it easy to verify that the numerical radial distribution of stresses exactly corresponds to that one given by the first relation in Eq.8.1.15.

This affirmation has another important consequence: if the cylindrical fiber reinforced specimen is viewed as a holy cylinder where the inclusion is substituted by an equivalent pressure

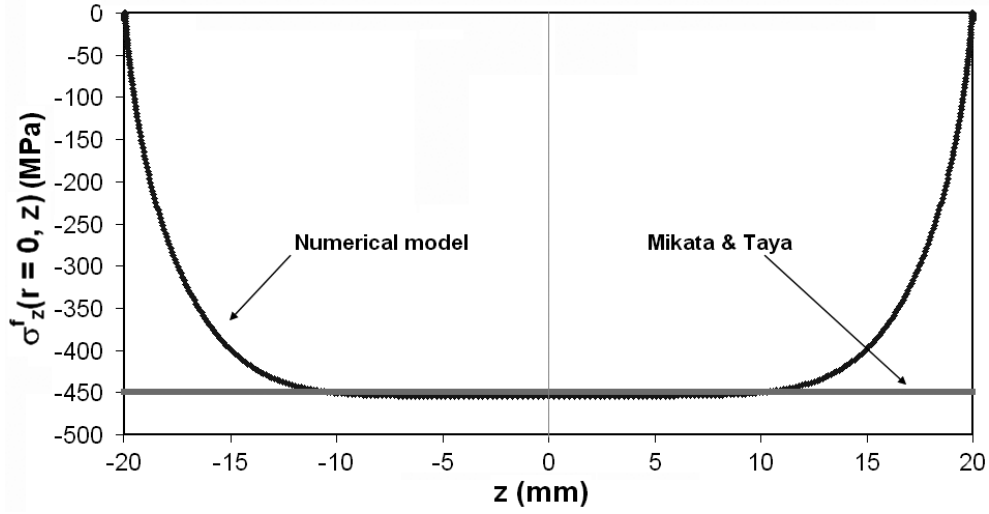


**Figure 8.2:** Simulation of the axial stress distribution along the fiber. Comparison with the model of Mikata and Taya

$p$  which represents the presence of the fiber, the same radial evolution can be expressed as (Eq.7.3.1):

$$\sigma_{rr}(r, z = 0) = p \frac{r_f^2}{r_m^2 - r_f^2} \frac{r_e^2 - r^2}{r^2} \quad \text{Lamé, 1852} \quad (8.1.16)$$

that for an infinity matrix becomes

$$\sigma_{rr}(r, z = 0) = p \frac{r_f^2}{r^2} \quad (8.1.17)$$

On the other hand, taking into account the analogy between the residual stress problem and its analysis via an equivalent thermo-elastic approach using the shrinkage function  $S_m$ , along the circular section  $z=0$  of the cylindrical specimen the first relation presented in 8.1.15 can be written as:

$$\sigma_{rr}^{(1)} = \frac{\mu_1(2\mu_2 + 3\lambda_2)}{\mu_1 + \mu_2 + \lambda_2} S_m(r = r_f, z = 0) \frac{r_f^2}{r} \quad (8.1.18)$$

Finally, by comparison of the two last relations, we arrive at this important result

$$\frac{\mu_1(2\mu_2 + 3\lambda_2)}{\mu_1 + \mu_2 + \lambda_2} S_m(r = r_f, z = 0) = p \quad (8.1.19)$$

This equation clearly states that the pressure acting transversally to the fiber-matrix interface and due to the presence of the inhomogeneity (the reinforcing fiber) can be directly calculated from the material properties of the composite constituents and the FBG measurements. Moreover, this result can be also verified by using the FE simulations. In this last case the numerical pressure is found to be equal to 13.056 MPa while experimentally  $p$  results equal to 12.999 MPa thus demonstrating the validity of Eq. 8.1.19

## 8.2 The asymptotic solution based model of E.S. Folias

Though the model proposed by Mikata and Taya permits a verification of the FE prediction at the center of the modeled specimen their results are not applicable to fiber of finite length such as used in the fiber pull- and push-out test. On the other hand, the analysis developed by Folias provides a verification of the model prediction at the two ends of the specimen since it gives an approximation of the shear stress distribution along the fiber matrix interface. In particular, utilizing the form of a general 3-D solution, the author investigates (exclusively at the analytical level) the whole stress field in the neighborhood of the intersection of a cylindrical inclusion and a free surface Fig.8.3. The inclusion is assumed to be of a homogeneous and

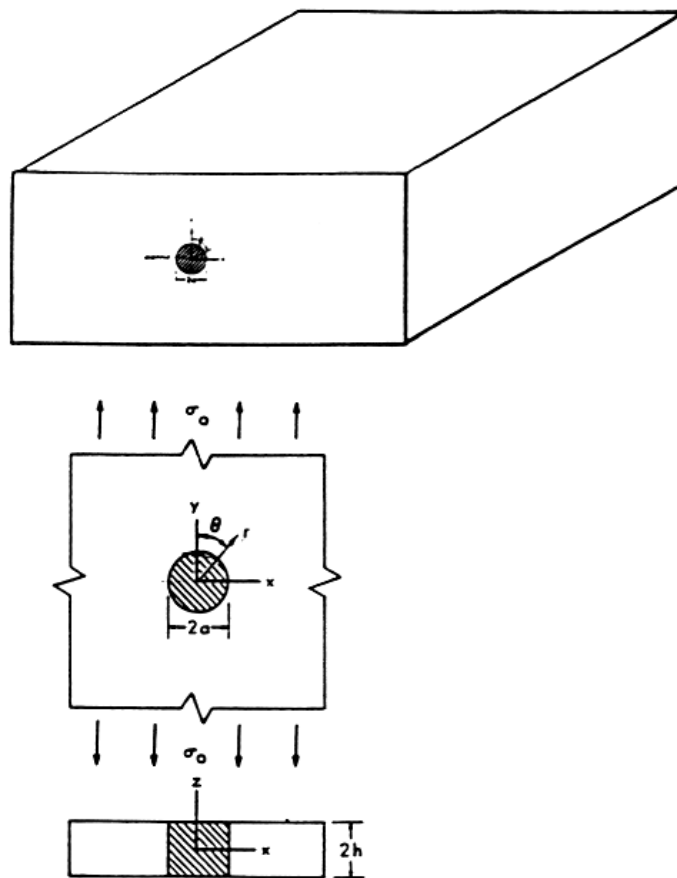


**Figure 8.3:** Geometrical and loading configurations [32].

isotropic material and the problem solution is obtained when it is embedded in an homogeneous plate of arbitrary thickness. The stress field is induced by uniform tension applied on the plate at point far remote from the inclusion even if a generalization to a thermo-mechanical load would be possible only modifying the stress-strain relation. Nevertheless, the analysis revealed that the stresses at the corner (see Fig.8.4) is proportional to  $\varrho^{\alpha-2}$  where  $\varrho$  is the radius from the corner and  $\alpha$  represents the order of singularity of the field. In particular,

the characteristic values of  $\alpha$  only depend on the material properties of the composite's constituents. In the subsequent a simple introduction on the key points of the model will be

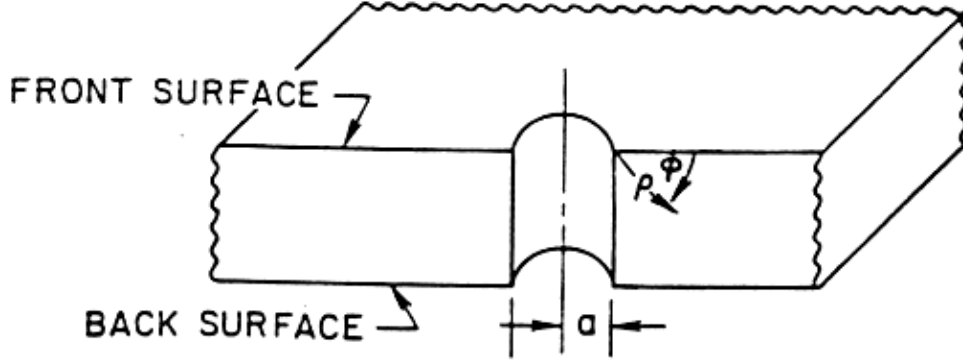


**Figure 8.4:** Definition of local coordinates system in the region of interest [33].

illustrated, while for more mathematical details we directly send to the original article [32] and to the related references.

The main objective of the Folias analysis was to derive an asymptotic solution (describing the stress and the strain fields) valid in the immediate vicinity of the corner points where the interface meets the free surface of the plate. For this purpose, the complementary displacement field is assumed to have the following form in the two constituents (matrix and fiber):

$$\begin{aligned} u^{(k)} &= \frac{1}{1-2\nu_k} \frac{\partial}{\partial x} \left( 2(1-\nu_k)f_2^{(k)} + h \frac{\partial f_1^{(k)}}{\partial z} + z \frac{\partial f_2^{(k)}}{\partial z} \right) \\ v^{(k)} &= \frac{1}{1-2\nu_k} \frac{\partial}{\partial y} \left( 2(1-\nu_k)f_2^{(k)} + h \frac{\partial f_1^{(k)}}{\partial z} + z \frac{\partial f_2^{(k)}}{\partial z} \right) \\ w^{(k)} &= \frac{1}{1-2\nu_k} \frac{\partial}{\partial z} \left( -2(1-\nu_k)f_2^{(k)} + h \frac{\partial f_1^{(k)}}{\partial z} + z \frac{\partial f_2^{(k)}}{\partial z} \right) \end{aligned} \quad k=m,f \quad (8.2.1)$$

where the functions  $f_1^{(k)}$  and  $f_2^{(k)}$  are three dimensional harmonic functions. In particular it is assumed that:

$$f_j^{(k)} = r^{-1/2} H_j^{(k)}(r-a, h-z) e^{i2\theta} \quad (8.2.2)$$

and the functions  $H_j^{(k)}$  must satisfy the following equation:

$$\frac{\partial^2 H_j^{(k)}}{\partial (r-a)^2} + \frac{\partial^2 H_j^{(k)}}{\partial (h-z)^2} - \frac{15}{4(a+r-a)^2} H_j^{(k)} = 0 \quad (8.2.3)$$

Considering now a convenient change in the local coordinate system (see Fig.8.4), the last relation can be written as follow

$$\frac{\partial^2 H_j^{(k)}}{\partial \varrho^2} + \frac{1}{\varrho} \frac{\partial H_j^{(k)}}{\partial \varrho} + \frac{1}{\varrho^2} \frac{\partial^2 H_j^{(k)}}{\partial \phi^2} - \frac{15 H_j^{(k)}}{4a^2(1+(\varrho/a)\cos\phi)^2} = 0 \quad (8.2.4)$$



Under the assumption that the radius of the inclusion is sufficiently large, so that the condition  $\varrho \ll a$  is meaningful, the solution is chosen to be of the following form:

$$H_j^{(k)} = \sum_{n=0}^{\infty} \varrho^{\alpha+n} F_{jn}^k(\phi), \quad \text{with } \alpha \text{ appropriate constant} \quad (8.2.5)$$

Omitting the tedious and rather complicated mathematical procedure, it is finally possible to construct the following series expansion in ascending power of  $\varrho$

$$H_j^{(k)} = \varrho^\alpha (A_j^{(k)} \cos(\alpha\phi) + B_j^{(k)} \sin(\alpha\phi)) + \varrho^{\alpha+1} (C_j^{(k)} \cos(\alpha+1)\phi + D_j^{(k)} \sin(\alpha+1)\phi) + O(\varrho^{\alpha+2}) \quad (8.2.6)$$

where the constant  $\alpha$ ,  $A_j^{(k)}$ ,  $B_j^{(k)}$ ,  $C_j^{(k)}$ ,  $D_j^{(k)}$ , have to be determined from the boundary conditions.

In particular all terms up to the order  $O(\varrho^{\alpha-2})$  are satisfied if one assumes that

$$\begin{aligned} B_1^{(m)} &= 0 \\ -h(\alpha+1)A_1^{(m)} - B_2^{(m)} &= 0 \\ A_1^{(f)} \sin(\alpha\pi) - B_1^{(f)} \cos(\alpha\pi) &= 0 \\ (A_2^{(f)} - h(\alpha+1)B_1^{(f)}) \tan(\alpha\pi) - B_2^{(f)} + h(\alpha+1)A_1^{(f)} &= 0 \end{aligned} \quad (8.2.7)$$

and similarly, the displacement and boundary conditions at the cylindrical surface are verified if also the subsequent combination vanishes

$$\begin{aligned} &\frac{1}{1-2\nu_m} \left( (-\alpha-1+2\nu_m)A_2^{(m)} \tan\left(\frac{\alpha\pi}{2}\right) - (-\alpha-1+2\nu_m)B_2^{(m)} + h(\alpha+1) \left[ A_1^{(m)} + B_1^{(m)} \tan\left(\frac{\alpha\pi}{2}\right) \right] \right) \\ &- \frac{1}{1-2\nu_f} \left( (-\alpha-1+2\nu_f) \left[ A_2^{(f)} \tan\left(\frac{\alpha\pi}{2}\right) B_2^{(f)} \right] + h(\alpha+1) \left[ A_1^{(f)} + B_1^{(f)} \tan\left(\frac{\alpha\pi}{2}\right) \right] \right) = 0 \\ &\frac{1}{1-2\nu_m} \left( (\alpha-2+2\nu_m)A_2^{(m)} + (\alpha-2+2\nu_m)B_2^{(m)} \tan\left(\frac{\alpha\pi}{2}\right) + h(\alpha+1) \left[ A_1^{(m)} \tan\left(\frac{\alpha\pi}{2}\right) \right] - B_1^{(m)} \right) \\ &- \frac{1}{1-2\nu_f} \left( (\alpha-2+2\nu_f) \left[ A_2^{(f)} + B_2^{(f)} \tan\left(\frac{\alpha\pi}{2}\right) \right] + h(\alpha+1) \left[ A_1^{(f)} \tan\left(\frac{\alpha\pi}{2}\right) - B_1^{(f)} \right] \right) = 0 \\ &\alpha A_2^{(m)} - (1-\alpha) \tan\left(\frac{\alpha\phi}{2}\right) B_2^{(m)} + \\ &- \beta \left( \alpha A_2^{(f)} + \alpha \tan\left(\frac{\alpha\phi}{2}\right) B_2^{(f)} - \tan\left(\frac{\alpha\phi}{2}\right) \left[ A_2^{(f)} \sin(\alpha\phi) - B_2^{(f)} \cos(\alpha\phi) \right] \right) = 0 \\ &- (\alpha-1)A_2^{(m)} \tan\left(\frac{\alpha\phi}{2}\right) + (\alpha-2)B_2^{(m)} + \\ &- \beta \left( \left[ -(\alpha-1) \tan\left(\frac{\alpha\phi}{2}\right) + \sin(\alpha\phi) \right] A_2^{(f)} + [(\alpha-1) - \cos(\alpha\phi)] B_2^{(f)} \right) = 0 \end{aligned} \quad (8.2.8)$$

where for simplicity it is defined

$$\beta \equiv \frac{1-2\nu_m}{1-2\nu_f} \frac{\mu_f}{\mu_m} \quad (8.2.9)$$

The characteristic value  $\alpha$  may now be determined by setting the determinant of the algebraic system 8.2.7-8.2.8 equal to zero. Once the roots have been determined, the complete

displacement and stress fields can be constructed in ascending powers of  $\varrho$ . The stress field given in the term of the local system of coordinates indicated in Fig.8.4 is reported below.

$$\begin{aligned}
\sigma_{rr}^{(m)} &= 2\mu^{(m)}(\alpha - 1)A_n\varrho^{\alpha-2}(B[2\cos(\alpha - 2)\phi - (\alpha - 2)\sin\phi\sin(\alpha - 3)\phi] - (\alpha + 1)* \\
&\quad * [\sin(\alpha - 2)\phi + (\alpha - 2)\sin\phi\cos(\alpha - 3)\phi])\cos(2n\theta) \\
\sigma_{\theta\theta}^{(m)} &= 4\nu_1\mu_1(\alpha - 1)A_n\varrho^{(\alpha-2)}(B\cos(\alpha - 2)\phi - (\alpha + 1)\sin(\alpha - 2)\phi)\cos(2n\theta) \\
\sigma_{zz}^{(m)} &= 2\mu_1(\alpha - 1)A_n\varrho^{(\alpha-2)}(B(\alpha - 2)\sin\phi\sin(\alpha - 3)\phi + (\alpha + 1)[(\alpha - 2)\sin\phi\cos(\alpha - 3)\phi \\
&\quad - \sin(\alpha - 2)\phi])\cos(2n\theta) \\
\tau_{rz}^{(m)} &= 2\mu_1(\alpha - 1)A_n\varrho^{(\alpha-2)}(B[\sin(\alpha - 2)\phi + (\alpha - 2)\sin\phi\cos(\alpha - 3)\phi] + \\
&\quad - (\alpha + 1)(\alpha - 2)\sin\phi\sin(\alpha - 3)\phi)\cos(2n\theta) \\
\tau_{r\theta}^{(m)} &= \tau_{\theta r}^{(m)} = 0
\end{aligned} \tag{8.2.10}$$

or in summary

$$\sigma_{i,j}^{(m)} = \varrho^{(\alpha-2)}F(\phi, \theta) \tag{8.2.11}$$

In particular for the case of only one fiber embedded in the matrix the value of  $n$  is 0. Moreover, after the examination of the stress field, the analysis clearly shows that in the neighborhood where the fiber meet the free surface the stress evolves proportionally to  $\varrho^{(\alpha-2)}$  and that, for certain material properties, it may become singular.

Following the Folias procedure (i.e. solving the system given by 8.2.7 plus 8.2.8), the characteristic value of  $\alpha$  corresponding to the cylindrical geometry and material properties of the specimen analyzed in this work is found to be 1.62948.

This pure analytical solution is compared with the same value of singularity that corresponds to the distribution of shear given by the FE model (Fig.7.19). In fact the numerical value of  $\alpha$  can be easily extracted from the numerical solution because simply corresponds to the slope of the shear distribution  $\tau_{rz}^{numerical}(z)$  when plotted in a log-log scale. This value is 1.6232 showing a very good agreement (the difference is of the order of 1,6%) with the analytical solution of Folias.

The two distributions are plotted in Fig.8.5 with the zone of superposition between the curves included in a circle. Unfortunately, even if the model of Folias represents a good step towards the exact characterization of the shear stress distribution, the proposed models fails at the very ends of the specimen since the analytical distribution doesn't return to zero (as it has to physically). The singularity problem remains thus confining the asymptotic solution in a region at a certain distance from the entry singular point  $\varrho = 0$ .

A possible solution to this important question will be exposed in the next paragraph with the energetic approach of Quek.

### 8.3 The energetic approach of M.Y. Quek

As we have seen before, several methods have been developed or are suited for characterize thermal residual stresses in a single fiber composite specimen. These include finite element

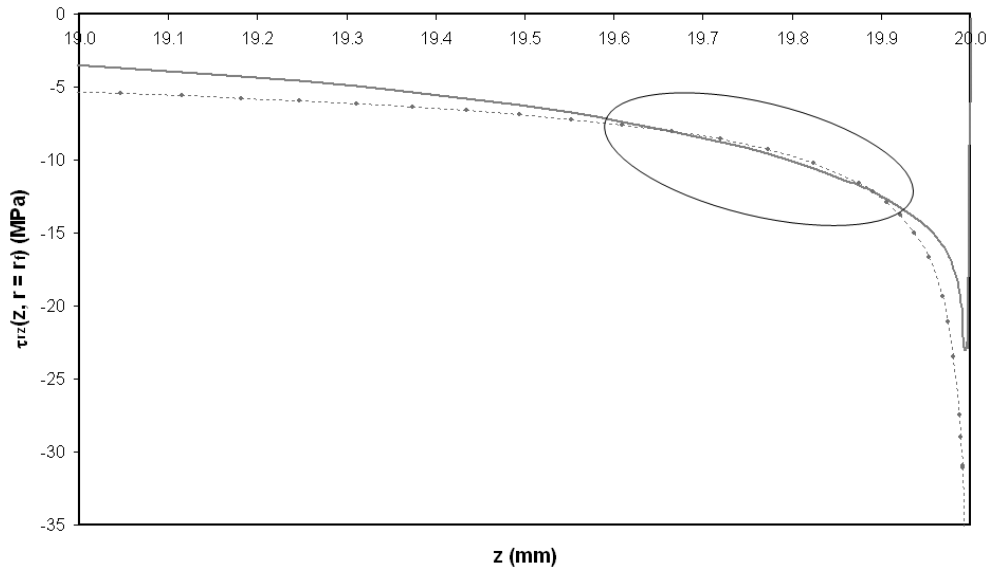


**Figure 8.5:** Comparison between the shear distribution of stresses provided by the FE model (continuous line) and the asymptotic approach (dashed dotted line) adopted by Folias along the fiber-matrix interface of the cylindrical specimen.

method, cylinder theory in which thermal stresses are determined for an infinitely long fiber surrounded by a matrix, elasticity solution and so on. The theoretical model proposed by Quek and developed for the analysis of the thermal stresses in fiber of finite length is based on the complementary energy approach, in particular on the minimization of the total complementary energy of the system. These direct method where the forces and not the displacements are treated as unknowns is preferable because it doesn't require the use of assumed high-order displacement fields to obtain greater accuracy in the stresses reducing the problem's complexity considerably. In Fig.8.6 is presented the geometry and the system of coordinates adopted by Quek in his analysis. In the present approach, the complete axisymmetric state

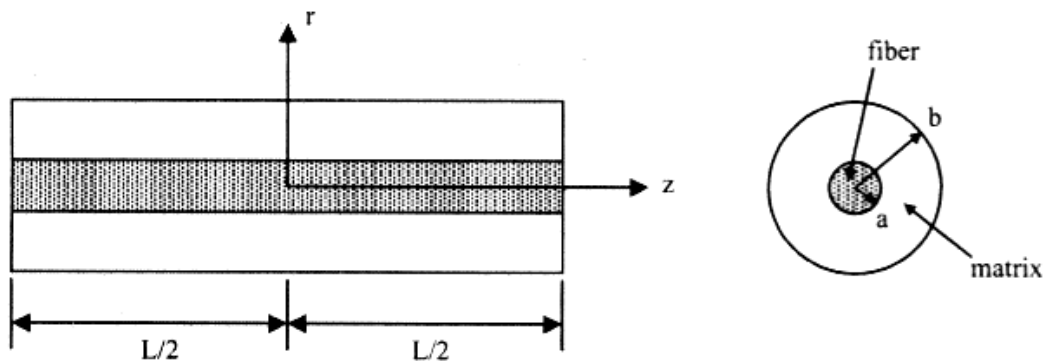


**Figure 8.6:** The composite specimen used by Quek in its thermal stress problem [66].

of stress in the fiber and matrix is derived by assuming stress functions

$$\begin{aligned}\phi_f &= f_1(r)g_1(z) + h_1(z) \\ \phi_m &= f_2(r)g_2(z) + h_2(z)\end{aligned}\quad \begin{array}{l} f \text{ and } m \text{ state for fiber and matrix respectively} \\ \end{array} \quad (8.3.1)$$

which are not known a priori. The function  $f_i(r)$  ( $i = 1, 2$ ) are functions of the radial direction  $r$ , and  $g_i(z)$  and  $h_i(z)$  are functions of the axial direction  $z$  only. Moreover they exactly satisfy the equilibrium equations in the fiber end in the matrix domain.

In terms of the Airy stress function, the stresses in the composite constituents can be expressed as

$$\begin{aligned}\sigma_j^z &= \left( \frac{d^2 f_i}{dr^2} + \frac{1}{r} \frac{df_i}{dr} \right) g_i(z) \\ \tau_j^{rz} &= -\frac{df_i}{dr} \frac{dg_i}{dz} \\ \sigma_j^r &= \sigma_j^\theta = f_i^r \frac{d^2 g_i}{dz^2} + \frac{d^2 h_i}{dz^2}\end{aligned}\quad \begin{array}{l} j = m, f \\ \end{array} \quad (8.3.2)$$

Utilizing the free state of stress at the matrix surface and enforcing stress continuity at the fiber-matrix interface, the number of unknown function can be reduced to  $f_1(r)$ ,  $f_2(r)$  and  $g_1(z)$ . The unknown functions  $f_1(r)$  and  $f_2(r)$  can be obtained in terms of a constant  $C_1$  by applying the appropriate boundary conditions that is fiber and matrix axial stress maximum at the plane of symmetry and zero at the ends of the composite. The function  $g_1(z)$  is finally determined by minimizing the total complementary energy in the fiber and matrix. Once these functions are known the axial, radial and the shear stress evolution at the fiber matrix interface can be easily retrieved by a substitution process.

Following the procedure indicated by the author the thermal stresses induced in the fiber and in the matrix are found to be:

$$\begin{aligned}\sigma_f^z &= C_1 g_1(z) \\ \tau_f^{rz} &= -\frac{C_1 r}{2} \frac{dg_1}{dz} \\ \sigma_f^r &= \sigma_f^\theta = \frac{C_1}{4} \left( r^2 - 2\gamma b^2 \ln \left( \frac{b}{a} \right) \right) + \frac{d^2 g_1}{dz^2}\end{aligned}\quad \begin{array}{l} \text{for the fiber} \\ \end{array} \quad (8.3.3)$$

and

$$\begin{aligned}\sigma_m^z &= -\gamma C_1 g_1(z) \\ \tau_m^{rz} &= -\left( \frac{\gamma C_1}{2r} \right) (r^2 - b^2) \frac{dg_1}{dz} \\ \sigma_m^r &= \sigma_m^\theta = -\frac{\gamma C_1}{4} \left( r^2 - b^2 - 2b^2 \ln \left( \frac{r}{b} \right) \right) + \frac{d^2 g_1}{dz^2}\end{aligned}\quad \begin{array}{l} \text{for the matrix} \\ \end{array} \quad (8.3.4)$$

where  $\gamma = (a^2/(b^2 - a^2))$  and  $C_1$  is a constant. A first observation can be done: comparing the first equation of 8.3.3 and 8.3.4 we retrieve the relation 6.2.2, which states that the axial evolutions of stresses in the fiber and matrix are proportional and are constant all along any transversal plane. We have experimentally and numerically demonstrated that this affirmation is valid only for short matrix radii and fails when the radius is greater than 6 mm (at least in

the case of a SFC specimen). In view of this, the comparison between the FE model and the analytical approach of Quek has a sense only if it is done in a region close to the reinforcing fiber.

In the following, the composite's constituents will be considered homogeneous and isotropic with a linear elastic behavior. The thermo-elastic strain-stress are:

$$\begin{aligned}\epsilon_j^z &= \frac{1}{E_j}[\sigma_j^z - \nu_j(\sigma_j^r + \sigma_j^\theta)] + \alpha\Delta T \\ \epsilon_j^r &= \frac{1}{E_j}[\sigma_j^r - \nu_j(\sigma_j^z + \sigma_j^\theta)] + \alpha\Delta T \\ \epsilon_j^\theta &= \frac{1}{E_j}[\sigma_j^\theta - \nu_j(\sigma_j^z + \sigma_j^r)] + \alpha\Delta T \\ \gamma_j^{r,z} &= \frac{\tau_j^{rz}}{\mu_j}\end{aligned}\tag{8.3.5}$$

where  $\mu$ ,  $E$  and  $\nu$  are the shear modulus, modulus of elasticity and Poisson's ratio, respectively. The two unknowns that remain to determine are the constant  $C_1$  and the function  $g_1(z)$ . The solution to  $g_1(z)$  may be obtained by minimizing the total complementary energy

$$\Pi^* = U^* + V^*\tag{8.3.6}$$

where  $U^*$  is the complementary strain energy and  $V^*$  is the complementary potential energy of an eventual load externally applied. In the present case, since the surface of the matrix and the ends of the fiber are free of any traction,  $V^*$  is equal to zero.

The total complementary energy then reduces to the complementary strain energy only, and can be expressed as

$$\begin{aligned}U^* &= \int \int \int_v \left( \frac{1}{2}\sigma_f^z\epsilon_f^z + \frac{1}{2}\sigma_f^r\epsilon_f^r + \frac{1}{2}\sigma_f^\theta\epsilon_f^\theta + \tau_f^{rz}\epsilon_f^{rz} \right) + \\ &+ \left( \frac{1}{2}\sigma_m^z\epsilon_m^z + \frac{1}{2}\sigma_m^r\epsilon_m^r + \frac{1}{2}\sigma_m^\theta\epsilon_m^\theta + \tau_m^{rz}\epsilon_m^{rz} \right) r dr d\theta dz\end{aligned}\tag{8.3.7}$$

Taking into account 8.3.3, 8.3.4 and 8.3.5 and performing the integration with respect to  $r$ , the expression for  $U^*$  may be written as

$$U^* = 2\pi \int \int_0^L F[C_1, g_1(z), g_1'(z), g_1''(z)] dz\tag{8.3.8}$$

Using standard calculus of variations, the Euler-Lagrange equations is:

$$-\frac{d^2}{dz^2} \left( \frac{\partial F}{\partial g_1''(z)} \right) + \frac{d}{dz} \left( \frac{\partial F}{\partial g_1'(z)} \right) - \frac{\partial F}{\partial g_1(z)}\tag{8.3.9}$$

where  $F$  is the expression within the square brackets in Eq.8.3.8. Performing the differentiation term by term in Eq.8.3.9 we obtain a fourth-order differential equation in  $g_1(z)$  as

$$D_1 \frac{d^4 g_1}{dz^4} - D_2 \frac{d^2 g_1}{dz^2} + D_3 g_1 + \frac{D_4}{C_1}\tag{8.3.10}$$

The coefficients D1-D4 depends on the material properties and geometry of the specimen and their explicit expression can be found in the original article of Quek [66].

It easy to verify that general solution to Eq.8.3.10 is given by

$$g_1(z) = \cosh(\bar{\alpha}z)(A\cos(\bar{\beta}z) + B\sin(\bar{\beta}z)) + \sinh(\bar{\alpha}z)(C\cos(\bar{\beta}z) + D\sin(\bar{\beta}z)) - \frac{D_4}{D_3} \frac{1}{C_1} \quad (8.3.11)$$

where  $\bar{\alpha}$  and  $\bar{\beta}$  are the roots of characteristic equation. Considering the following boundary conditions (in particular the last two conditions give both zero axial and shear stress at the ends of the fiber)

$$\begin{aligned} g(0) &= 1 \\ g'(0) &= 0 \\ g(L/2) &= 0 \\ g'(L/2) &= 0 \end{aligned} \quad (8.3.12)$$

the coefficient  $A$ ,  $B$ ,  $C$  and  $D$  can be determined. To obtain the constant  $C_1$ , Eq.8.3.11 and its derivatives has to be first substituted into Eq.8.3.8 and the integration performed with respect to  $z$ . Finally, minimizing the the complementary strain energy setting  $dU^*/dC_1 = 0$  enables the constant  $C_1$  to be determined. The complete solution to  $g_1(z)$  is then obtained and a back-substitution into Eq.8.3.3 and Eq.8.3.4 yields the residual stresses in the fiber and matrix.

Due to the complexity of the mathematics involved, to solve practically the problem and then calculate the distributions of stresses a symbolic mathematical software Methamatica 5 was used. In particular, even though the model of Quek is based on some simplified assumptions, the most interesting result deals with the form of the shear stress distribution provided by this approach. The analytical form of  $\tau_j^{rz}$  and calculated from equation Eq.8.3.3 or Eq.8.3.4, as in the real physical case peaks at some distance into the interface from the fiber ends and return exactly to zero at the entry point. This distribution is then compared with the same evolution provided via the FE model based on the  $S_m$  shrinkage function and they are finally depicted in Fig.8.7, where, for completeness, it has been also included the asymptotic evolution of Folias. It is worthy to note that the maximum values reached by the peaks in the case of the two finite distributions are slightly different even if they they are not located in the same position along the interface. Nevertheless this an encouraging result in the assessment of a certain reliability in the finite element prediction overall in a region very difficult to study at the numerical level. In practice the numerical distribution shows an average behavior between the real case (it presents a peak before the specimen end and finishes to zero) and the tendency to go to infinity because of the presence of the singularity.

Finally, with an interesting parametric study based on the Quek model (variation of the fiber length, matrix radius, Young modulus and coefficient of thermal expansion) it is possible to verify how thermal stresses (i.e. the residual stresses) in composites are dependent on the material properties of the constituents and more importantly on the geometry.

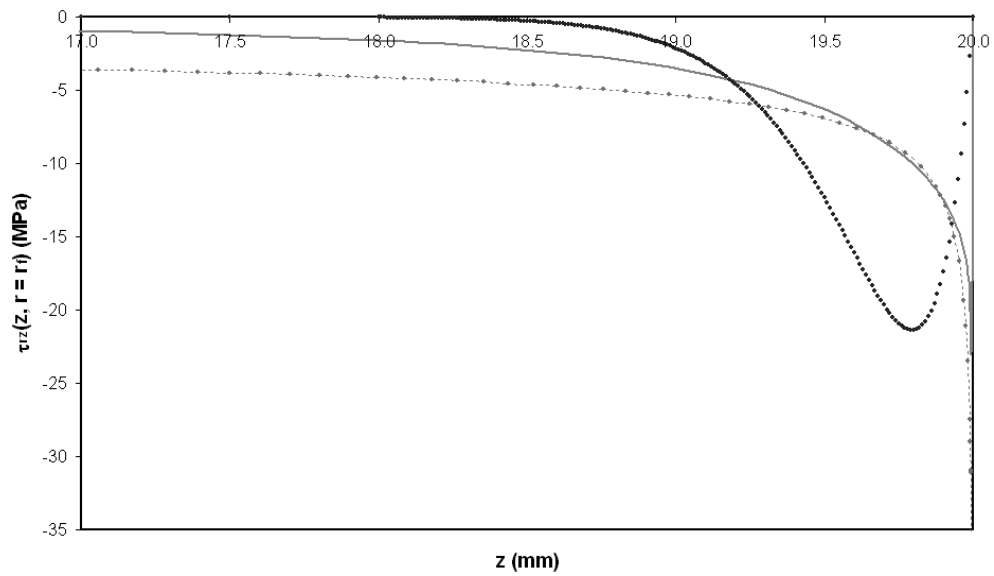


**Figure 8.7:** Comparison between the shear distribution of stresses provided by the FE model (continuous line), the asymptotic approach (dashed dotted line) adopted by Folias and the distribution based on the energetic approach of Quek (dotted line) along the fiber-matrix interface of the cylindrical specimen.





# Chapter 9

## Crack-fiber interaction

### 9.1 Introduction

The benefits of using FBG sensors and the OLCR technique to interpret their signal response has been widely illustrated in the first part of this thesis. This combination of results is particularly useful in the domain of the composite materials thanks to its capability to provide distributed measurements of strain at the grating location in a completely non-invasive manner. Starting from the FBG measurement, the characterization of the residual stress field inside a composite was successfully treated and the convergence between experimental, numerical and analytical results was finally obtained.

Another important aspect related to the fiber Bragg gratings is that they play also the role of reinforcement when embedded into a composite. This allows the creation of self-diagnostic materials which can be easily monitored during their service life via the optical sensor. Any change in the composite properties or functionalities could be rapidly detected preventing failures and possible dangerous situations.

In order to demonstrate this last assertion another important experiment has been conceived and realized in the framework of this research. Based on the information acquired with the SFC specimen, a new specimen called compact tension (CT-specimen) was built (Fig.9.1) with the aim to enlarge the use of the FBG sensor to detect the presence and the effects of a real crack propagating in the material. The crack was generated and propagated by submitting the specimen to a fatigue test, where a symmetrical cyclic load was imposed on the sample.

Since the CT-specimen is made of epoxy following the same preparation protocol adopted in the case of the cylinders, the first measurements of strain (performed without the crack) give a good indication on the level of residual stresses within the sample for the new geometry. In addition, the characteristic dimension of the sample have been defined on the ASTM international norm.

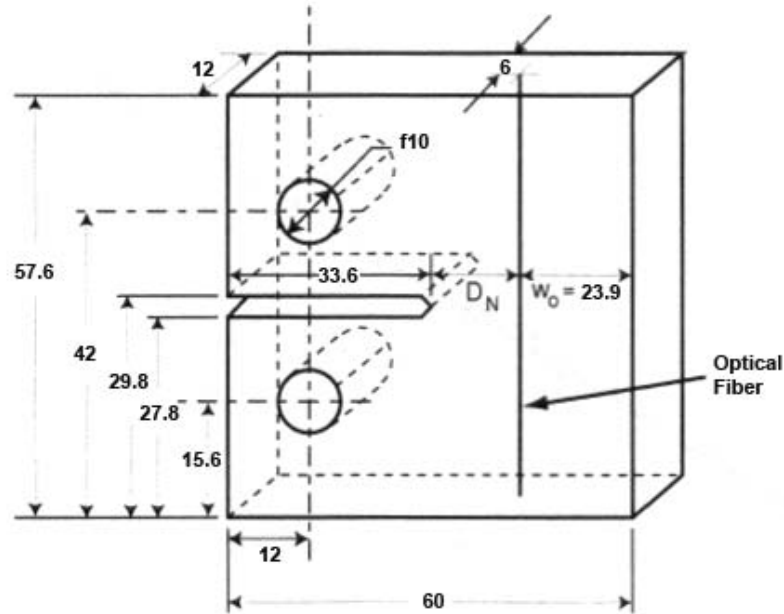


**Figure 9.1:** *CT-specimen's geometry with an embedded optical fiber. Dimensions are in [mm].  $D_N$  may be changed to check the influence of the fiber position on the final results.*

## 9.2 Notes on fatigue fracture

It is well recognized that when a body or structural component is subjected to a cyclic load, a nucleation of damage initiates at stress concentration points within the body. Voids, slip lines, microcracks, etc. appear and the process of rupture starts. Some time later, if the corresponding stress intensity factor (SIF) is large enough, a macroscopic crack generally propagates until a catastrophic fracture occurs destroying the body. This phenomenon is called fatigue crack propagation (FCP).

In the laboratory environment these observations can be reproduced by using a smooth or notched specimen under a cyclic load, however it remains a formidable problem since a unique solution valid for all possible specimen geometries does not exist. Empirical treatments have been developed which cover specific structural components and/or materials systems under well defined load time profiles. A typical profile is shown in Fig.9.2.

The parameters that completely characterize the load profile are

- Load ratio  $R = \frac{P_{Min}}{P_{Max}}$
- Frequency  $\nu$  [cycles/second]

If the frequency is known, the number of cycles  $N$  and the time  $t$  are related by  $N = \nu t$ . In general it is possible to distinguish two type of cyclic fatigue:

- Low cycle fatigue
- High cycle fatigue

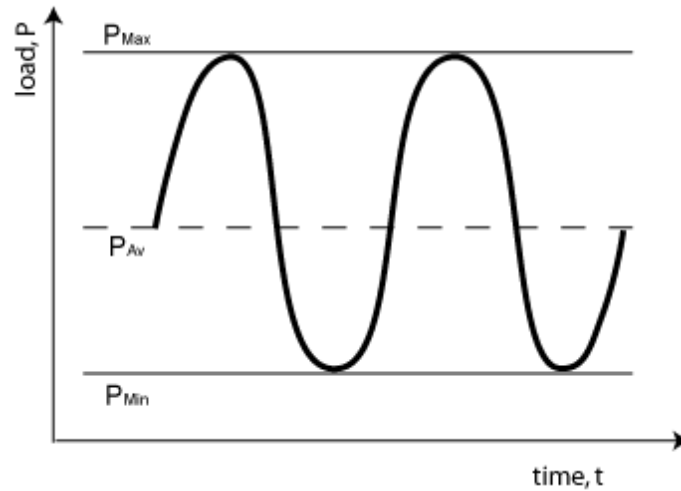


**Figure 9.2:** *Cyclic load-time profile used in laboratory experiment.*

The first type is characterized by relatively high stress (load) levels (equal to or higher than the yield stress of the material) and by a relatively small number of cycles to failure (hundreds to few thousands). On the other hand, the high cycle fatigue is characterized by low stress levels and by a very large number of cycles to failure (thousands to millions).

Although in these type of experiments the quantities typically measured are the number of cycles to crack initiation [52] and the fracture length as a function of the total number of cycles, at the moment we are only interested in propagating a natural crack until a certain point without breaking the specimen. Several tests have been performed using reinforced and unreinforced CT-specimen, with the aim of finding the good conditions (frequency, number of cycles, maximum and minimum load) which allow a stable crack propagation. Finally the best parameters to obtain a cracked specimen are shown in Table 9.2. In particular the maximum

$P_{Max}(N)$	$P_{Min}(N)$	$P_{Av}(N)$	$Amp.(N)$	$\nu(Hz)$
135	35	85	50	3

**Table 9.1:** *Parameters used in the fatigue crack propagation test to obtain a stable crack evolution in the specimen*

and minimum applied load correspond respectively to 30% and to 10% of the critical load ( $P_c$ ), which is the load associated to specimen rupture. This last value has been determined by loading several unreinforced specimens (seven) from zero load to the point of complete failure. The average value of  $P_c$  is found to be 350 N. The total number of cycles however, is not indicated because it depends on the type of tested specimen (with or without fiber) and on the environmental conditions (room temperature, humidity, etc.) and may have great variations from one specimen to another. Indicating by  $a$  the distance between the application point of the load and the front of the fracture (see Fig.9.4), with the conditions in Table

9.2 an unstopped fatigue test of three days is usually required to obtain a fracture length of 4 mm in an unreinforced specimen. Two or three time more is necessary when the CT-specimen contains a reinforcing optical fiber.

### 9.3 Optical FBG sensor glued on the back face of the specimen

Since this experiment is particularly difficult and a new mould is necessary to prepare the CT-specimen with an embedded fiber, the FBG has been initially glued on the back face of the specimen as indicated in Fig.9.3. The fiber was attached by using the same mixture of

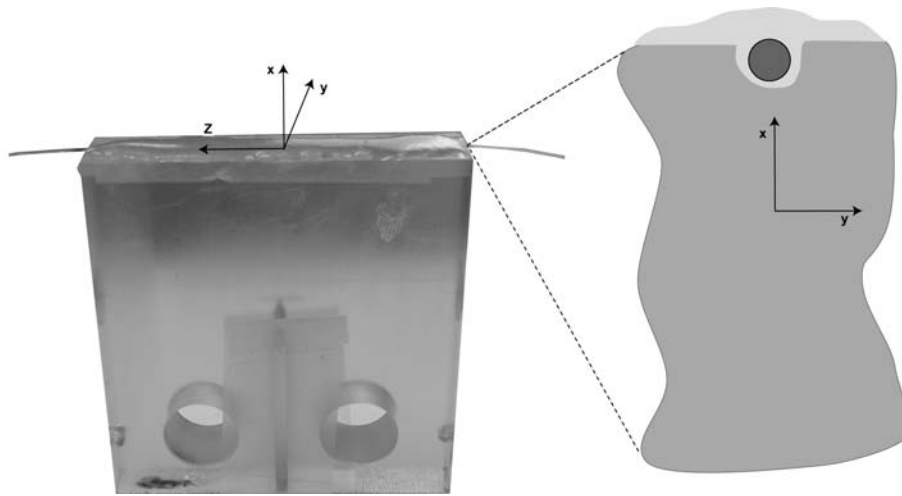


**Figure 9.3:** *CT-specimen used in the preliminary test. The optical fiber containing a 1.4 mm-length FBG is positioned on the back face of the specimen and glued using epoxy.*

epoxy used for the specimen, but was not post-cured to avoid another thermal treatment to the matrix material. Actually the optical sensor is attached to the specimen only after a crack of a desired length has propagated via a fatigue test (Fig.9.4). This greatly reduces the possibilities of accidental breaking during the manipulation phases of the specimen. Nevertheless, to reach a sufficient level of polymerization and to assume a certain stability of the material properties, after gluing the fiber, an interval of one week is imposed before measuring the strain with the FBG.

The fiber used in the first pilot test was equipped with a 1.4 mm-long-grating positioned at the origin of the system of coordinates and aligned along  $z$  (Fig.9.3). To ensure and maintain the correct alignment a groove of 0.15 mm depth was machined on the face of the specimen where the fiber was to be located.

The test was organized as follows:

- Before loading the specimen, a measurement of the deformation applied on the grating was done to have a new reference state of the sensor.

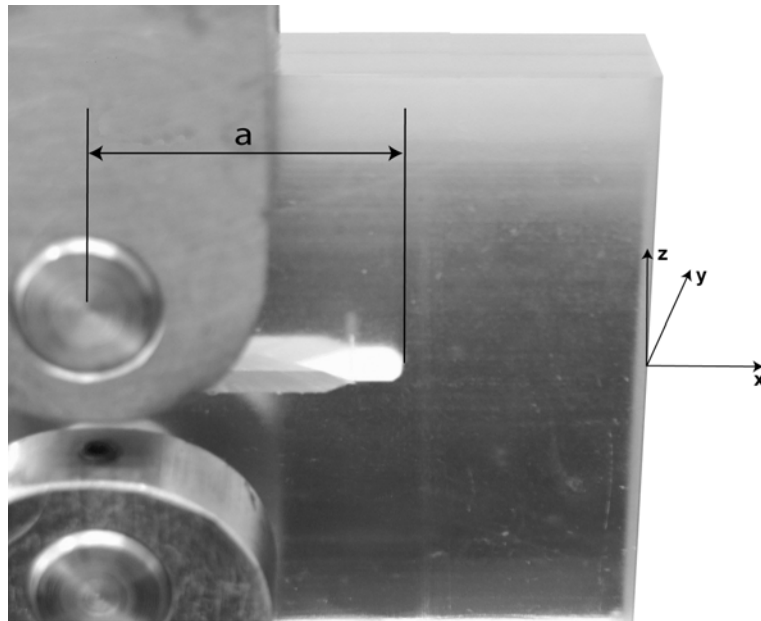


**Figure 9.4:** Compact tension specimen during the test of fatigue crack propagation. The final length  $a$  of the fracture before stopping the test was 25.6 mm.

- Starting from an applied load of 10 Newtons, the CT-specimen was loaded up to 100 Newtons in ten equally spaced intervals.
- At each step, when a stable value of the load was reached, an optical measurement of the reflected signal from the grating was performed using the OLCR technique and the experimental strain evolution due to the applied force could be retrieved at the FBG position.
- The specimen was finally unloaded.

A special stand to manually load the sample was used for this experiment (Fig.9.5). In general, it was not possible to use a hydraulic machine (as in the case of the fracture propagation) to better control the loading process since the vibrations produced would have affected the optical measurements.

Following the experimental procedure mentioned before, different values of strain have been measured at the point corresponding to the origin of the coordinates for each applied load (see Fig.9.4). In order to verify the results the test has been repeated twice respecting a time interval of one week. A summary is presented in Fig.9.6. It is easy to note that in the case of the curve B (the second test in order of time) the values of strain are slightly higher (in absolute value) than in the case A. Although care was taken to reproduce as much as possible the same test conditions (specimen orientation, loading speed and value of the force at the moment of the measurement, room temperature, grips alignment, etc.), some differences inevitably remain, thus justifying the variations between the corresponding values shown in

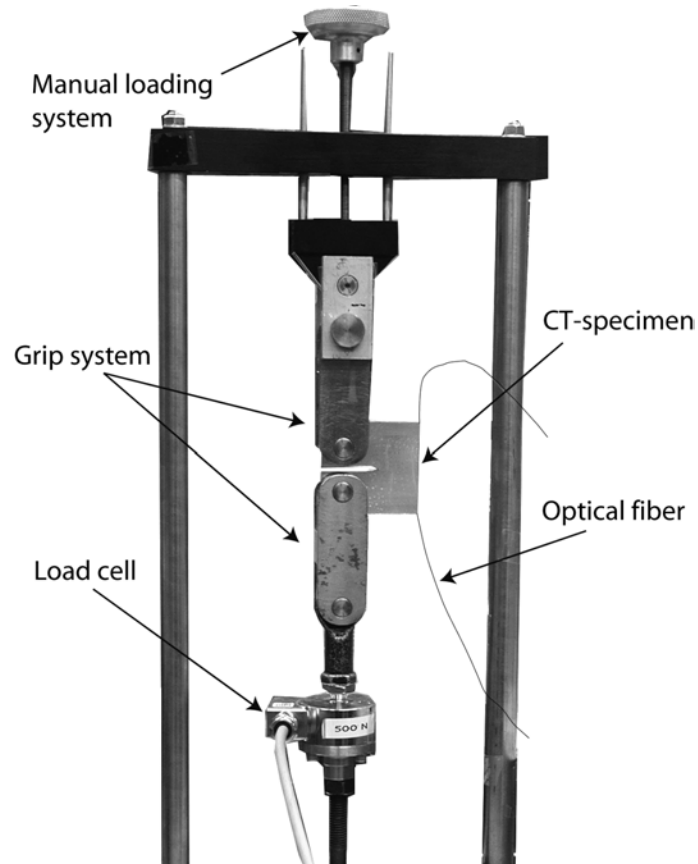


**Figure 9.5:** Special stand used to manually load the compact tension specimen.

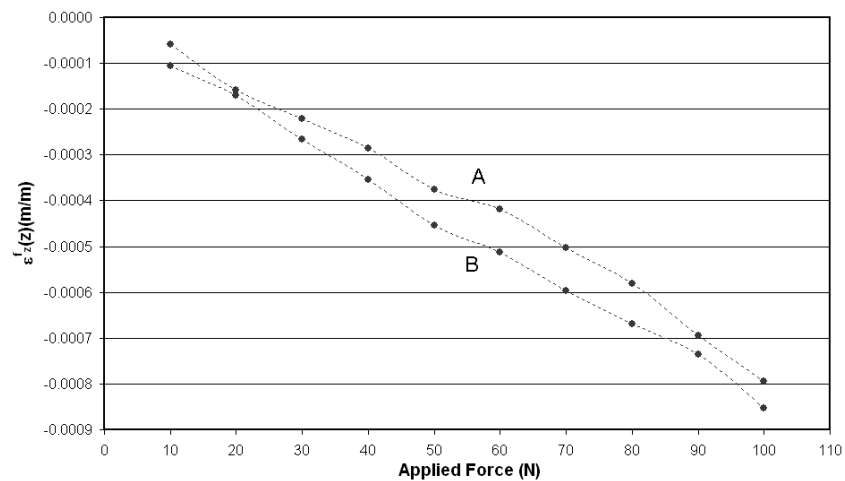


**Figure 9.6:** Strain measured at the origin of the system of coordinates shown in Fig.9.3 by using a 1.4-mm-long-grating. The results correspond to two different tests (A and B) performed on the same specimen and in the same conditions.

the curves of Fig.9.6. Although the complete system is not automatically controlled, the curves show the same trend and only in one case (applied force equal to 60 N) the differences between the experimental strains goes up to 18%.

In view of the encouraging results obtained with the previous test and to exploit as much as possible the FBG capabilities, the same procedure has been followed to test another specimen. In this second case a 13-mm-long grating placed in the same position was used with the aim to obtain a distributed measurement of strain (instead of singular points) along the axial direction  $z$  for each different applied load. Since the grating used this time is longer than that of the previous test, this experiment is slightly more difficult, because the optical measurement of the reflected signal takes more time. During the OLCR scan in fact, the specimen continues to relax and the load decreases affecting in this way the very high-sensitive optical measurements. Despite the aforementioned problem, as shown in Fig.9.7 the results achieved in this second case are quite good. It is worth noting that the results should be

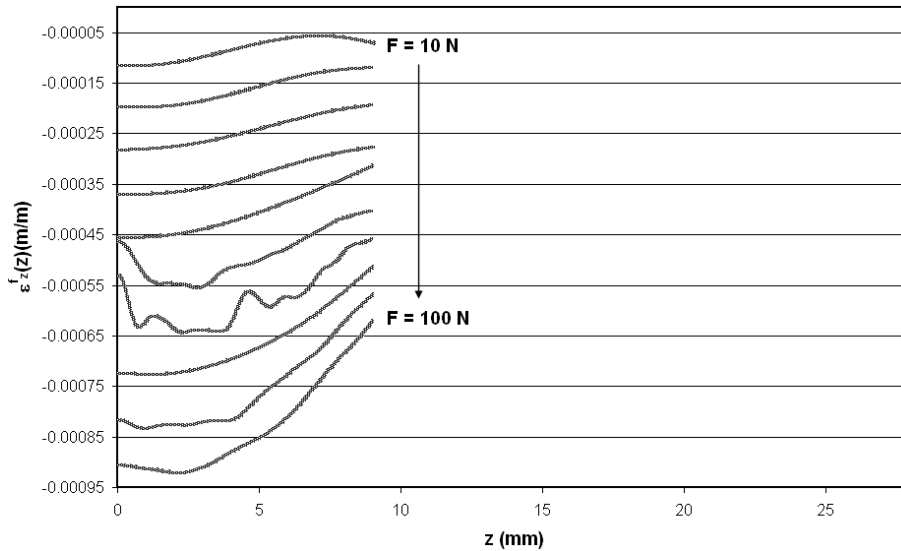


**Figure 9.7:** Strain measured along the axial direction  $z$  by using a 13-mm-long-grating. The grating center is slightly displaced respect to the origin of the coordinate system.

symmetric with respect to the plane  $z=0$ . Therefore, the grating center is slightly displaced (3 mm) in the positive direction of the  $z$ -axis, thus explaining the non-symmetric length of strain distribution's curves. A similar displacement (4 mm) has also been observed for the grating of 1.4 mm. This explains the fact that strains measured with the short FBG are situated in a position corresponding to 4 mm for the long FBG. This assessment has also been confirmed by OLCR measurement of the two exact positions of the gratings. This simple comparison underlines one of the advantages coming from the use of long instead of short FBG for this kind of application.

## 9.4 3-D Finite Element modeling of the CT-specimen

To generalize and verify the results experimentally obtained, a 3-D modeling of the CT-specimen is proposed. Due to the symmetries in the sample's geometry only a quarter of the specimen needs to be modeled (Fig.9.8). Quadratic hexahedric elements have been used to

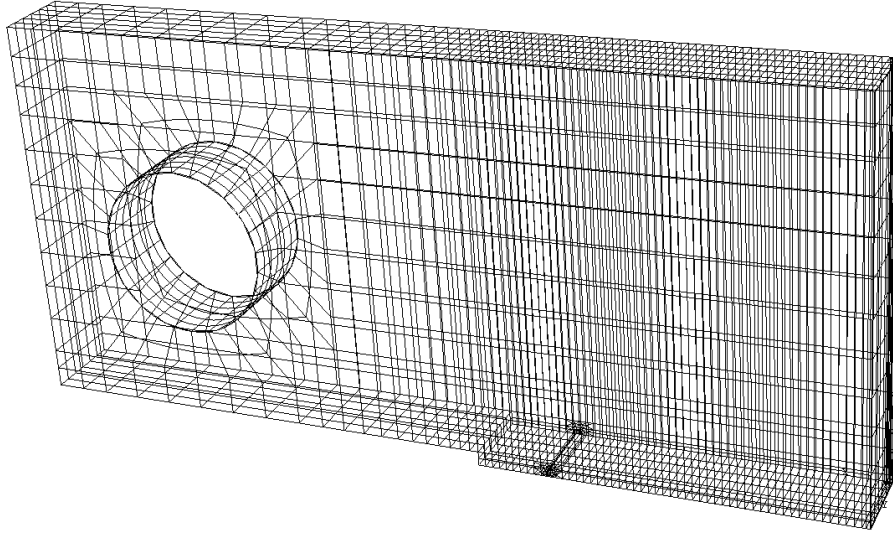


**Figure 9.8:** *A quarter of the modeled CT-specimen.*

mesh the main part of the specimen while quadratic wedge elements have been chosen for the fiber domain and for the crack tip region. In addition other kinds of mesh refinement and element order have been checked to ensure the quality of the results.

To apply the traction force, both contact and the distributed coupling tool [38] have been successfully implemented in the model. The first methodology permits one to model the contact between a shape-retaining surface (which simulates the pin in the grip system of Fig.9.4) and the surface of the specimen's hole (Fig.9.9) thus eliminating the problem of modeling and meshing the pin of metal. The force is then directly applied on the rigid surface by using a coupling with the reference point (which corresponds to the application point of the force) and via the contact conditions between this surface and the specimen is finally transferred to the sample. Nevertheless, since there were no differences in the results, the application load procedure can be simplified by imposing a coupling directly between the reference point and the surface of the hole (Fig. 9.10). The results obtained by the FE model are presented in Fig.9.11 and in Fig.9.12 in the case of the short and long grating respectively. A good agreement is found between the experimental and the numerical data.

### 9.4.1 3-D model parameterization

To improve the simulation results a series of geometric parameters have been introduced into the FE model.



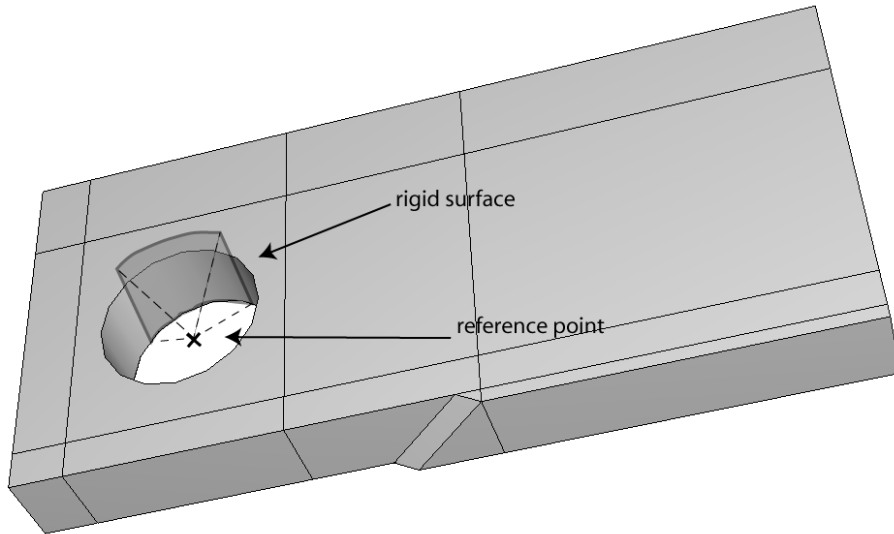


**Figure 9.9:** First approach used to model the traction applied to the CT-specimen via the contact tool and the distributed coupling between a reference point and a rigid surface.

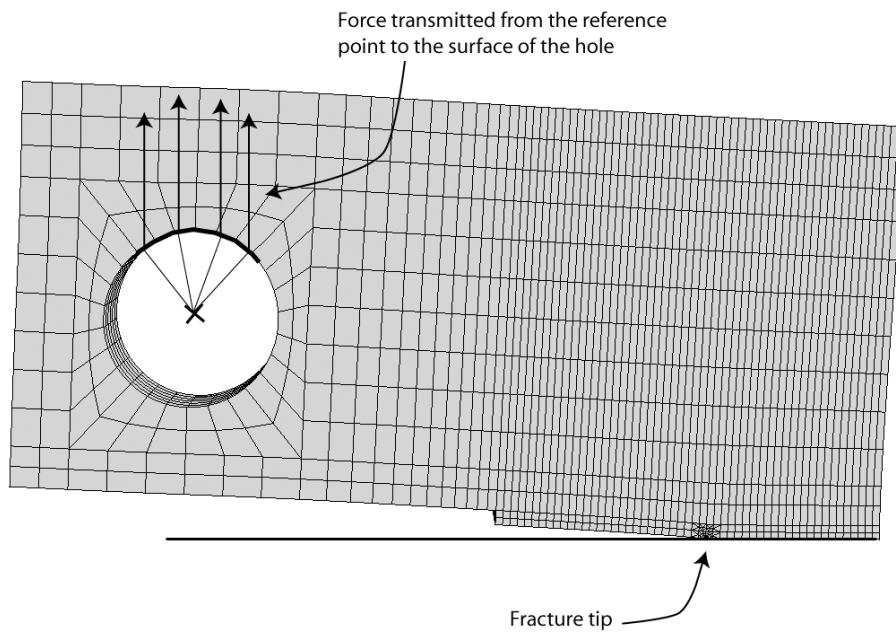


**Figure 9.10:** Illustration of the load transfer process from the reference point to the hole's surface.

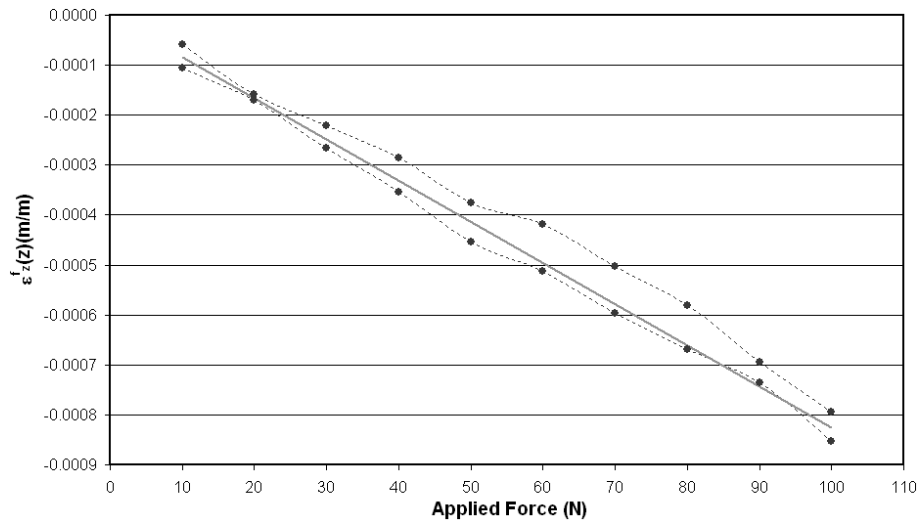


**Figure 9.11:** Comparison between the numerical simulation (continuous line) and the two experimental results coming out from the 1,4-mm-long grating placed at 4 mm from the origin of the system of coordinates along the  $z$ -direction.

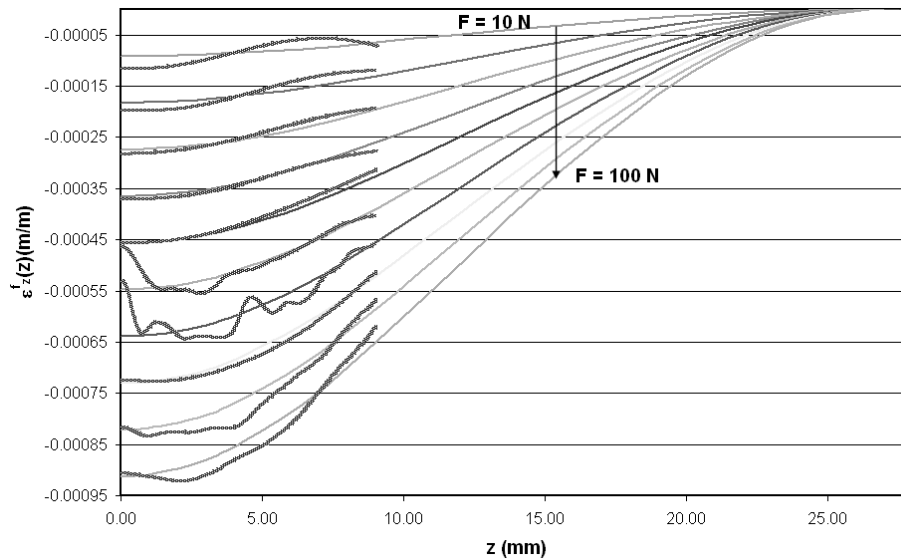


**Figure 9.12:** Comparison between the numerical (continuous lines) and the experimental (bold line) distributions obtained by the 13-mm-long grating along the axial direction  $z$ .

The first parameter considered in the model is the fiber inclination, which allows to take into account a possible variation in the depth of the groove machined on the back face of the specimen. A maximum difference of  $\pm 0.1$  mm between the entry and exit point of the fiber at the top and the bottom end of the specimen can be considered admissible (see Fig.9.13). Taking into account the eventual fiber misalignment, a region of possible values of strain can

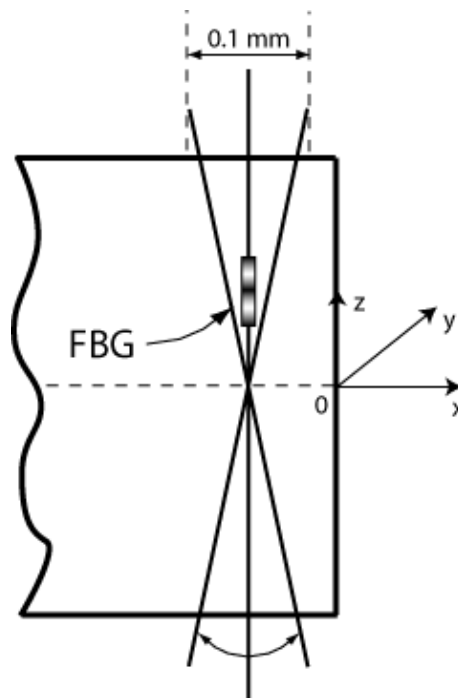


**Figure 9.13:** Schematic explaining the possible error committed in the vertical alignment of the optical fiber. Depending on the grating position, the variation in the strain response could be important.

be identified whose limits are directly related to the extreme positions assumed by the fiber. (see Fig.9.14). As it easy to verify, in one case the change in the fiber orientation has an important effect on the experimental results.

Another parameter related to the fiber is represented by its vertical position here indicated by  $D_N$  (see Fig.9.1). It becomes particularly useful to study the deformation behavior of the specimen as a function of the fiber location within the specimen and will be used later to validate the new analytical approach based on the beam theory and proposed to model the compact tension geometry.

Although the crack length  $a$  is itself a parameter, more important is the possibility to correctly reproduce the exact shape of the crack front. To do this, the form of the front can be manually imposed on the FE model by using a spline tool available in Abaqus [38] and used to define profiles having non-conventional geometry. Based on experimental observations, the exact positions of some points that are on the fracture tip can be easily identified. These points are then correctly located in the model and the form of the front finally retrieved by using a

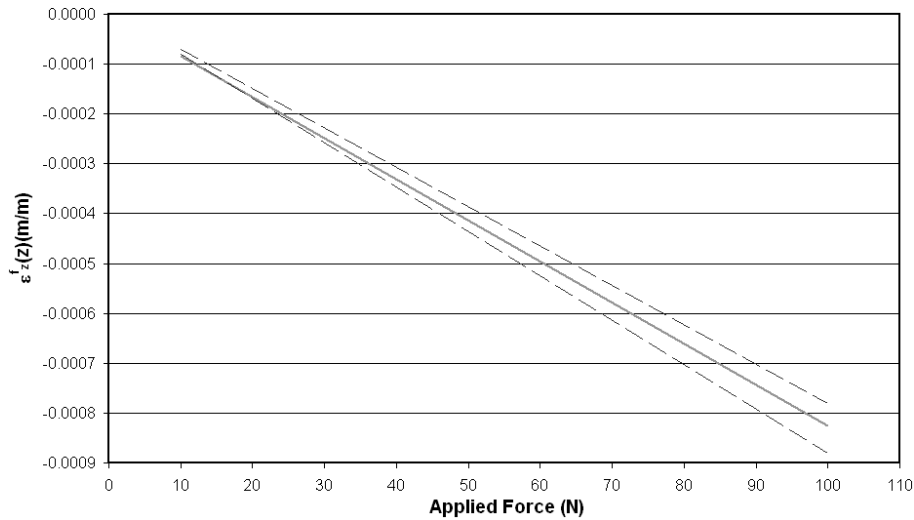


**Figure 9.14:** Numerical strain evolution (continuous line) for a short grating located at 4 mm along the axial direction  $z$  and the possible corresponding variations (dashed lines) due to a misalignment of the fiber.

spline interpolation. Even if there is a dependence on the number of available points, by using seven experimental data trough the specimen thickness, the crack tip can be reproduced with a sufficient level of accuracy.

In the following, a brief numerical analysis reveals the effects in terms of strain distribution that the front profile may have along the core of the fiber. As indicated in Fig.9.15 and Fig.9.16 four different front shapes which can be experimentally observed during fatigue crack propagation tests are taken into account.

The fiber position  $D_N$  is equal to 2.5 mm while the crack length calculated in the plane  $z = 0$  is fixed to 23.2 mm. The fracture front is in the influence region of the reinforcement. For a traction force  $F$  equal to 200 N, the strain distributions which would be measured along the core of the fiber are plotted in the subsequent Fig.9.17.

This analysis clearly highlights that at a distance greater than 5 mm from the plane  $z = 0$  (i.e. the plane containing the fracture) there are no appreciable differences between the distribution associated to the different shapes of the crack. Nevertheless, in a region very close to the fiber these differences become important, and a maximum strain variation of the order of  $1000\mu\epsilon$  can be calculated from one shape to another. In particular, Fig.9.18 and Fig.9.19 clearly indicate a dependence of the strain distribution on the derivative respect to the  $y$ -coordinate of the fracture profile. In fact, even if the Front A subtends a smaller area than the Front B, it generates greater deformation along the reinforcement.

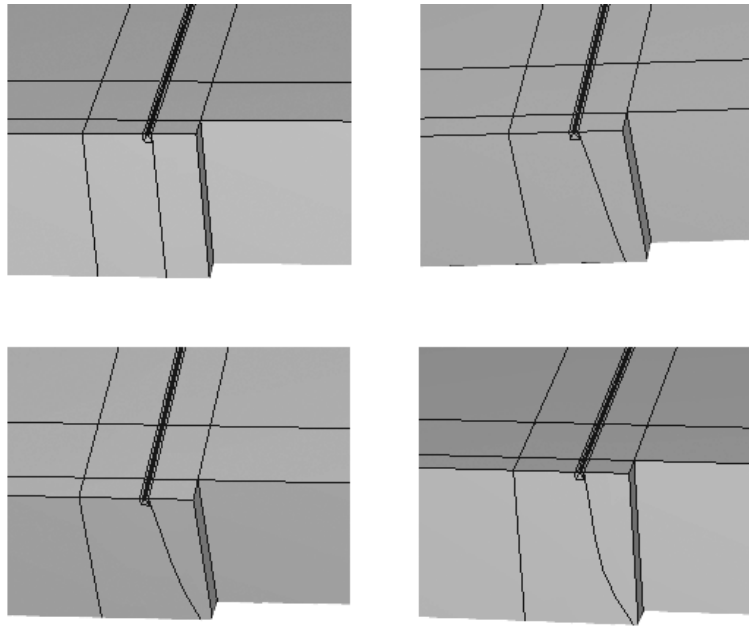


**Figure 9.15:** Four different shapes of the crack front simulated in the FE model.

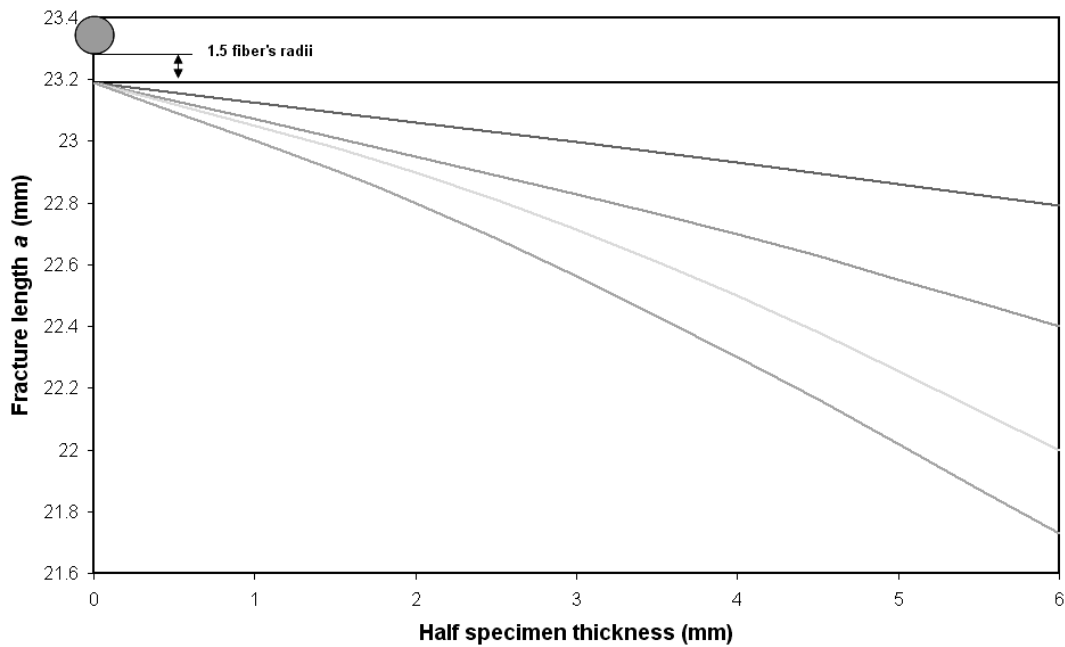


**Figure 9.16:** Plot of the crack fronts shown in Fig.9.15.

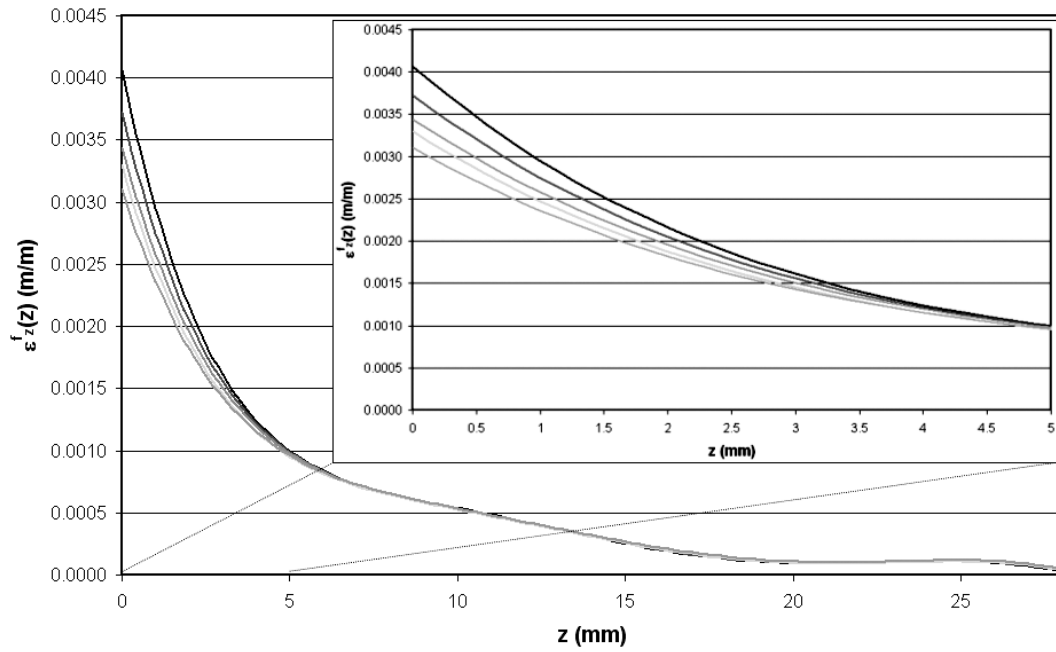


Figure 9.17: Strain evolutions as functions of the front shapes represented in Fig.9.16.

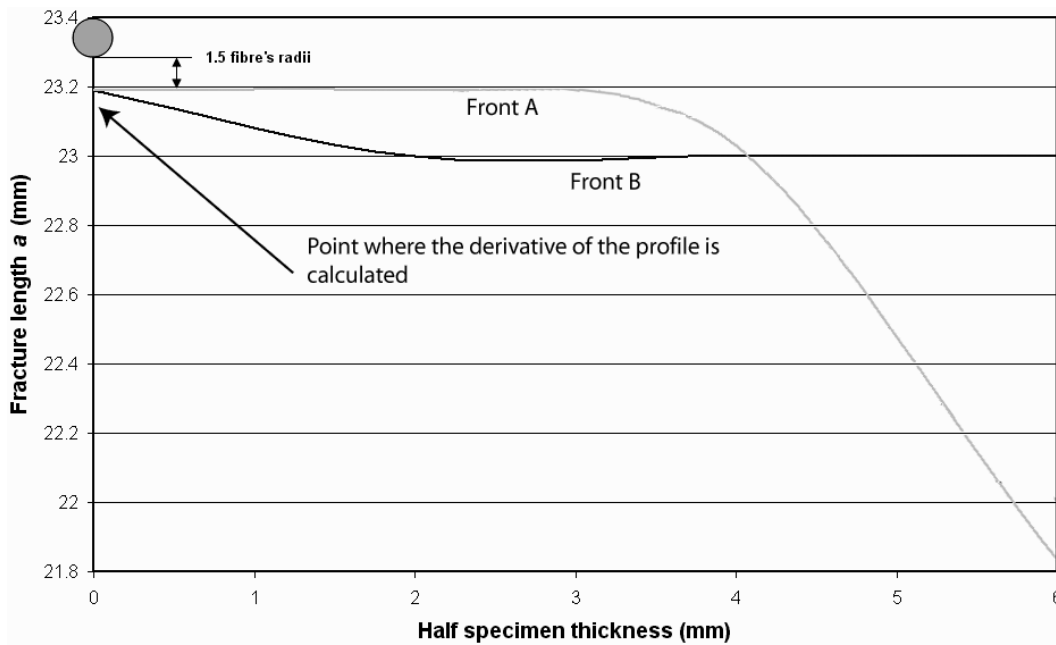
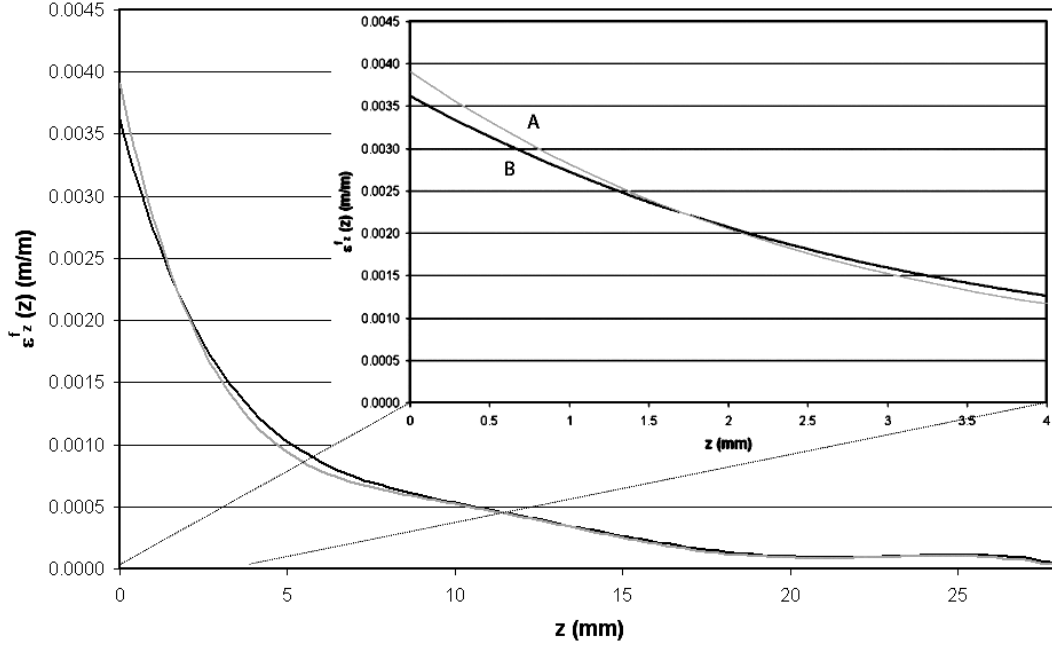


Figure 9.18: Simulated crack fronts used to underline the dependence of the strain on the derivative of the fracture profile.



**Figure 9.19:** Strain evolutions as functions of the front shapes represented in Fig.9.18.

## 9.5 Analytical modeling of the CT-specimen

In this section we propose an analytical modeling of the compact tension specimen inspired to the beam theory used to treat reinforced concrete structures [55]. The main hypothesis used in the model is the planarity of a given internal section of the beam when deformed under a certain load. This implies that the strain evolves linearly along the section maintaining a constant value in the transversal direction as indicated in Fig.9.20. Considering the plane of symmetry  $z = 0$  as shown in Fig.9.20 the previous hypothesis is absolutely acceptable.

When a given load is applied to the specimen the structure equilibrium requires that the sum of the total forces and moments be equal to zero all over the section. In view of the parameters and the reference system introduced in Fig.9.20 the following equations have to be satisfied:

$$\begin{aligned} \sum F_{\xi} &= 0 \\ \sum F\zeta &= 0 \end{aligned} \quad (9.5.1)$$

or

$$\begin{aligned} \int_0^{\zeta_L} tE_e\phi(\zeta_n - \zeta)d\zeta - \sum_{i=1}^n A_{f(i)}E_e\phi(\zeta_n - \zeta_{f(i)}) + \sum_{i=1}^n A_{f(i)}E_{f(i)}\phi(\zeta_n - \zeta_{f(i)}) - F &= 0 \\ \int_0^{\zeta_L} tE_e\phi(\zeta_n - \zeta)\zeta d\zeta - \sum_{i=1}^n A_{f(i)}E_e\phi(\zeta_n - \zeta_{f(i)})\zeta_{f(i)} + \sum_{i=1}^n A_{f(i)}E_{f(i)}\phi(\zeta_n - \zeta_{f(i)})\zeta_{f(i)} + \\ - F(b - \zeta_n) &= 0 \quad i=1, \dots, N \end{aligned} \quad (9.5.2)$$

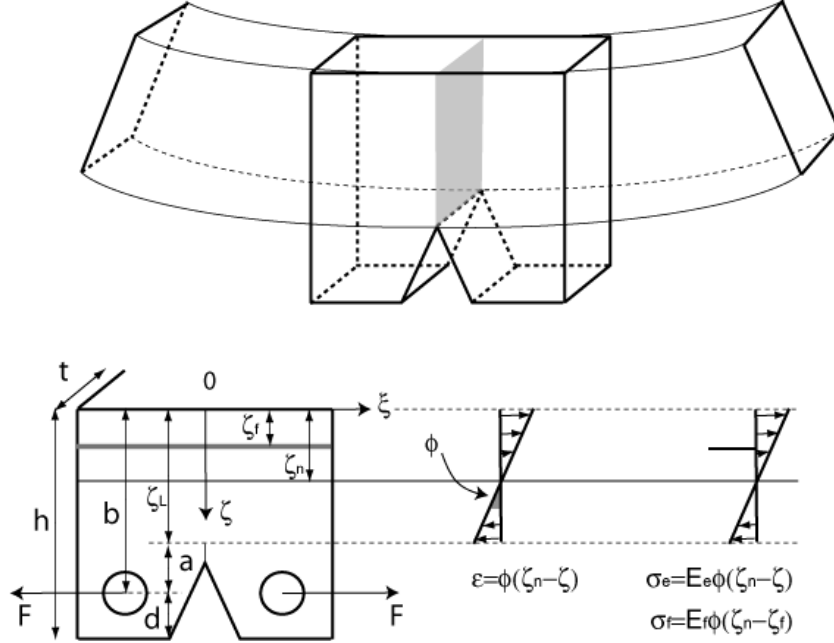


**Figure 9.20:** The CT-specimen viewed as part of a beam. The strain  $\epsilon$  and the stress  $\sigma$  are supposed to vary linearly along the section.

where  $E_e$  and  $E_{f(i)}$  are the Young moduli of the epoxy matrix and of the  $i^{th}$  glass fiber respectively,  $A_{f(i)}$  is the area of the  $i^{th}$  fiber section,  $t$  is the thickness of the specimen,  $\phi$  is the curvature's angle of the section,  $F$  the force used to open the crack,  $\zeta_n$  is the position of the neutral axis and  $\zeta_{f(i)}$  is the position of the  $i^{th}$  reinforcing fiber. The sums take into account the case having more than one fiber embedded into the specimen (in the following development only one fiber will be taken into account).

For a given crack length and defined geometrical parameters, the relations 9.5.2 constitute a system of two equations in the two unknowns  $\phi$  and  $\zeta_n$ . By solving the first equation with respect to  $\phi$  and by substituting into the second of 9.5.2 the exact position of the neutral axis can be retrieved as a function only of the geometrical and mechanical parameters. In particular:

$$\phi = \frac{2F}{-tE_e\zeta_L^2 + 4\pi E_e r_f^2 \zeta_f - 4\pi E_f r_f^2 \zeta_f - 4\pi E_e r_f^2 \zeta_n + 4\pi E_f r_f^2 \zeta_n + 2tE_e \zeta_e \zeta_n}$$

$$\zeta_n = \frac{(-12\pi(b - \zeta_n)E_e r_f^2 + 12\pi(b - \zeta_n)E_f r_f^2 + 6t(b - \zeta_n)E_e \zeta_n - ((12\pi(b - \zeta_n)E_e r_f^2 + 12\pi(b - \zeta_n)E_f r_f^2 + 6t(b - \zeta_n)E_e \zeta_n)^2 - 4(12\pi E_e r_f^2 + 12\pi E_f r_f^2 + 6tE_e \zeta_n)(3t(b - \zeta_n)E_e \zeta_L^2 + - 2tE_e \zeta_L^3 - 12\pi(b - \zeta_n)E_e r_f^2 \zeta_f + 12(b - \zeta_n)E_f r_f^2 + 12\pi E_e r_f^2 \zeta_f^2 - 12\pi E_f r_f^2 \zeta_f^2))^{1/2})}{2(-12\pi E_e r_f^2 + 12\pi E_f r_f^2 + 6tE_e \zeta_L)}$$

$$(9.5.3)$$



Finally a back substitution in the system allows to calculate the curvature's angle and by using the relations in Fig.9.20 the strain and the stress evolution in the matrix and in the fiber domain along the direction  $\zeta$ . A comparison between this original approach proposed to model the compact tension specimen and the numerical simulations results is presented in Fig.9.21. It is important to underline that when the crack front is not too close to the fiber

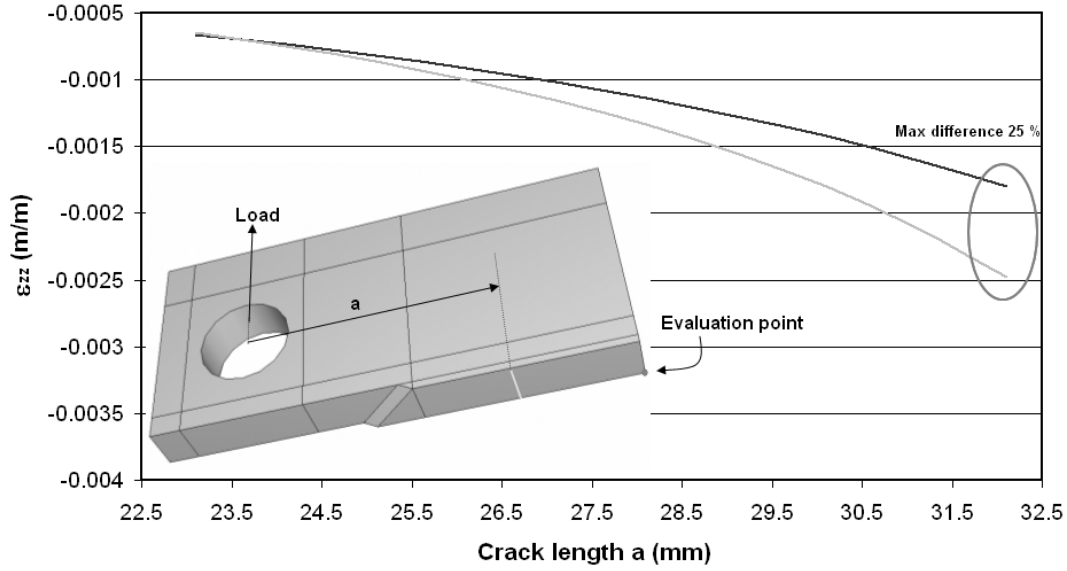


**Figure 9.21:** Evolution of the maximum value of strain calculated at the origin of the coordinates as function of the crack length  $a$  by using the FE model (black line) and the proposed new approach (grey line) respectively

(up to distances of the order of 2 cm) the model predictions and the numerical simulations differ of less than 20%. This is particular encouraging, because this approach can be also used to predict the length of a crack based only on the strain coming out the FBG sensor. To this purpose, the ligament  $\zeta_L$  (Fig.9.20) which corresponds to the length of the ideal beam section, is expressed as a function of the crack length  $a$  as follow:

$$\zeta_L = h - d - a \quad (9.5.4)$$

A substitution in Eq.9.5.2 allows now to express the angle  $\phi$  and the position of the neutral axis  $\zeta_n$  as a function of  $a$  as well. The length of the fracture  $a$  can be finally retrieved by finding the root in (terms of  $a$ ) of the following equation:

$$\sigma_f - \sigma_f^{Exp} = E_f \phi(\zeta_n - \zeta_L) - \sigma_f^{Exp} = 0 \quad (9.5.5)$$

where  $\sigma_f^{Exp}$  is the experimental value of strain measured in the plane of the fracture via the FBG sensor. We have applied this process to calculate the fracture length in a CT-specimen loaded with a force of 100 N. The experimental measurement of the fracture length gave 38.2 mm while the analytical model has predicted a length of 38.4 mm with an error of only 0.5 %.

Although certain simplified hypotheses have been introduced into the model (the stress and the strains are considered constant through the section and the singularity at the crack tip is not taken into account) the analytical and experimental results are in a very good agreement.

## 9.6 CT-specimen containing an embedded optical fiber

A second series of experimental tests have been conducted on a compact tension specimen reinforced with an embedded optical fiber Fig9.22. Two specimens have been prepared with fiber containing FBG sensors of different lengths: one of 1.4-mm-length and the other with a 13-mm-long grating. The grating is located in the plane  $z=0$  and the parameter  $D_N$  (see Fig.9.1) is fixed equal to 2.5 mm. The tests have been carried out as follows:

- Since this time the grating is embedded into the specimen, a measurement of the strain along the grating has been done during the fabrication steps of the sample: before embedding, after curing, after post-curing and after the specimen machining. The strain reference state corresponds to the strain after the specimen machining.
- A fatigue crack propagation test is run to create and increase a natural crack up until a desired length is reached.
- For a given crack length, three different levels of force (10 N, 50 N, 100 N) are applied to the specimen.
- At each step, when a stable value of the load is reached, an optical measurement of the reflected signal from the grating is performed by using the OLCR technique and the experimental strain evolution only due to the applied force can be retrieved at the FBG position.
- By continuing the fatigue crack propagation test, the fracture length is advanced towards the fiber.
- The loading procedure and the OLCR measurements are repeated as indicated at third and fourth point.
- The test is stopped when the crack has advanced past the fiber.
- The specimen is finally unloaded and used in an eventual post-mortem analysis (i.e. after a complete failure).

Five different crack lengths have been considered, namely  $a = 21.6$  mm,  $a = 22.8$  mm,  $a = 24.1$  mm,  $a = 24.4$  mm and  $a = 24.6$  mm. The evolutions of the maximum strain level measured during the fabrication process of the sample and a subsequent comparisons with the numerical simulations are presented in the following series of images for the CT-specimen with an embedded 1.4-mm-long-grating (Fig.9.23 to Fig.9.26).

Unfortunately the maximum fracture length reached in this test was 24.4 mm because the specimen broke during the following fatigue test. Nevertheless interesting information has

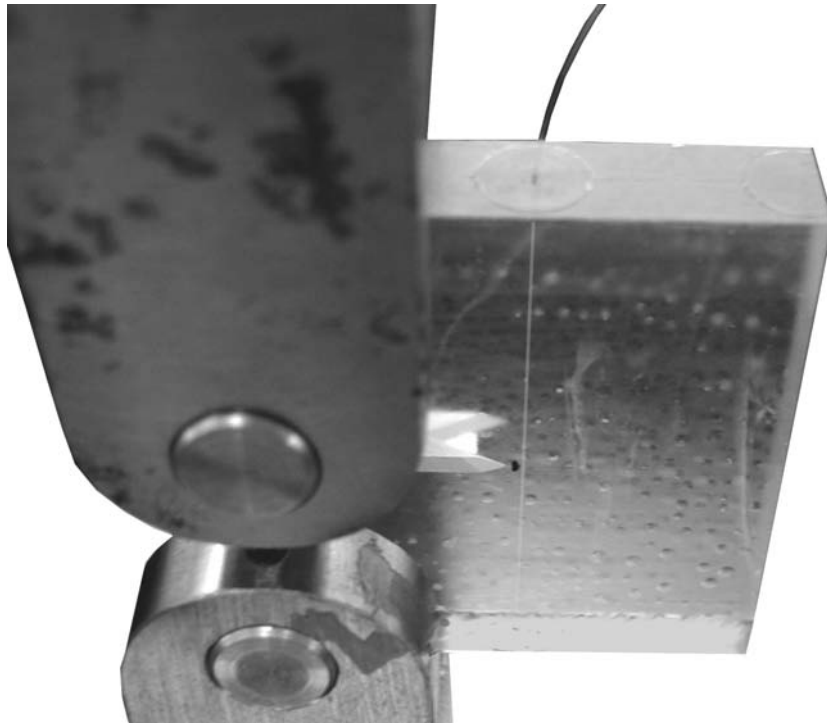


**Figure 9.22:** *Fatigue crack propagation test on a CT-specimen with an embedded optical fiber. A natural crack is visible in the notch.*

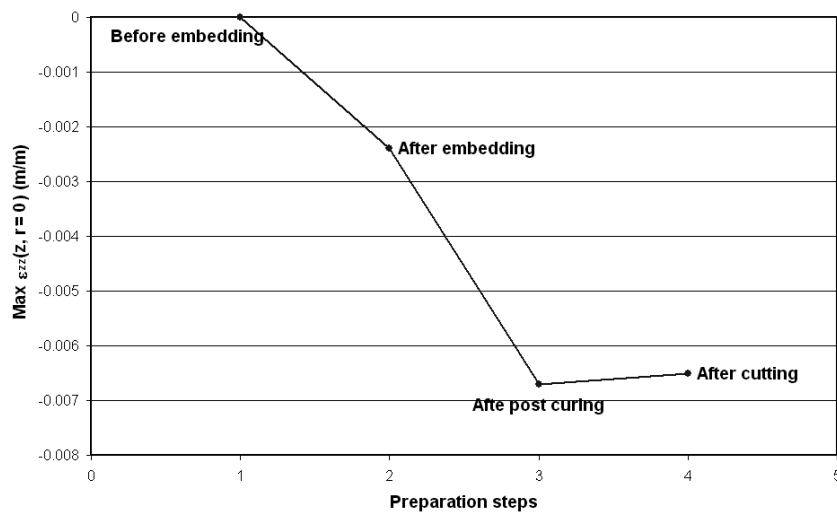


**Figure 9.23:** *Evolution of the maximum value of strain calculated during the specimen preparation.*

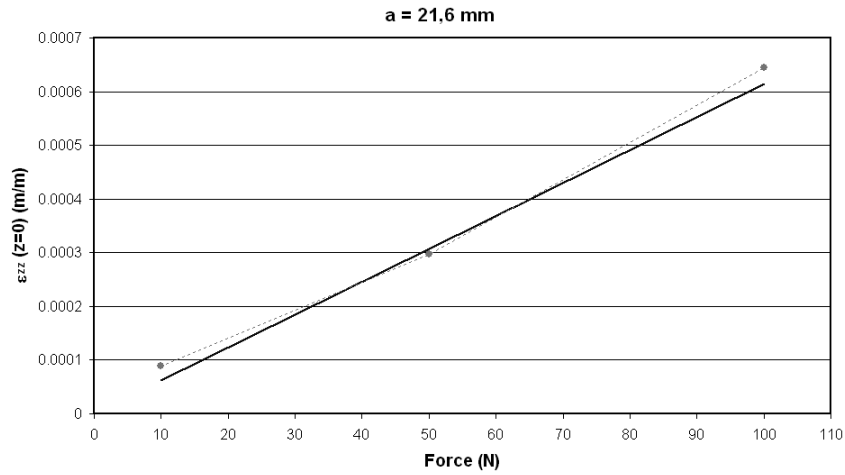


**Figure 9.24:** Comparison between the experimental (dashed line) and numerical (continuous line) maximum strain values for a crack length  $a$  of 21.6 mm.

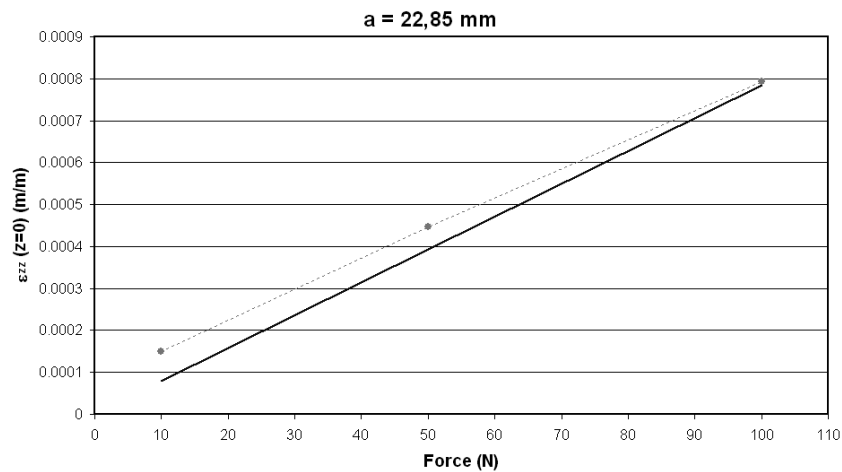


**Figure 9.25:** Comparison between the experimental (dashed line) and numerical (continuous line) maximum strain values for a crack length  $a$  of 22.85 mm.

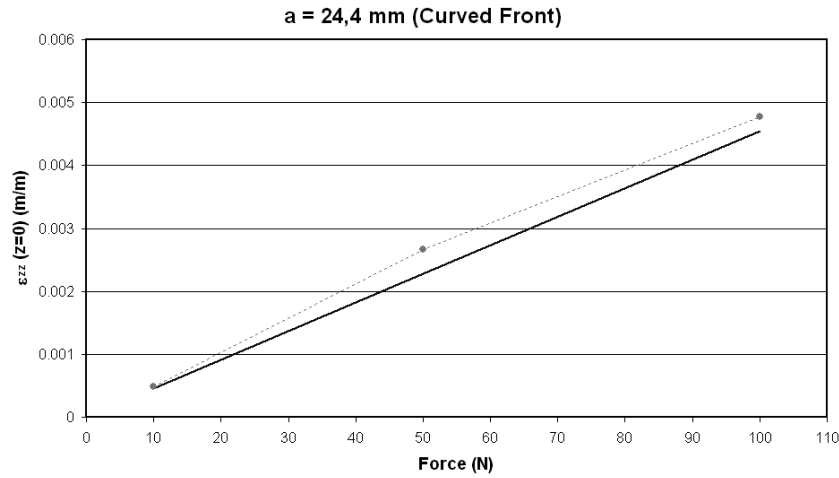


**Figure 9.26:** Comparison between the experimental (dashed line) and numerical (continuous line) maximum strain values for a crack length  $a$  of 24.4 mm.

been obtained from the microscopical observations of the fracture surface overall about the exact profile of the crack in a region close to the fiber. As highlighted in Fig.9.27 the interaction between the reinforcing fiber and the crack generates an important modification on the curvature of the crack tip with obvious effects on the local stress field. The same observation have already been reported in [57] but now, by using the embedded FBG sensors, a direct experimental measurement of these variations becomes possible thus supporting and providing data to the theoretical and analytical treatment [84] of the fiber-crack interaction process. The same test has been repeated on a CT-sample containing a longer FBG (13 mm). The experimental and numerical results are all summarized and compared in a series of diagrams: (Fig.9.28 to Fig.9.33) Although the presented results refer to preliminary tests, they clearly show the potential represented by the embedded FBG sensor to study advanced problems in the fracture mechanics domain (crack-fiber interaction, bridging forces, matrix-fiber interface properties, etc) of composites materials.

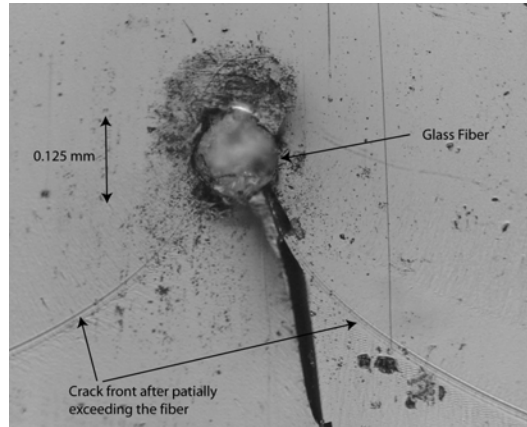


**Figure 9.27:** Profile of the curved crack front interacting with the reinforcing glass optical fiber. The black line behind the fiber can be explained noting that the fracture front is not coplanar anymore when pass the fiber. In the region of conjunction a sort of deep valley is created thus reflecting the light in a different direction.

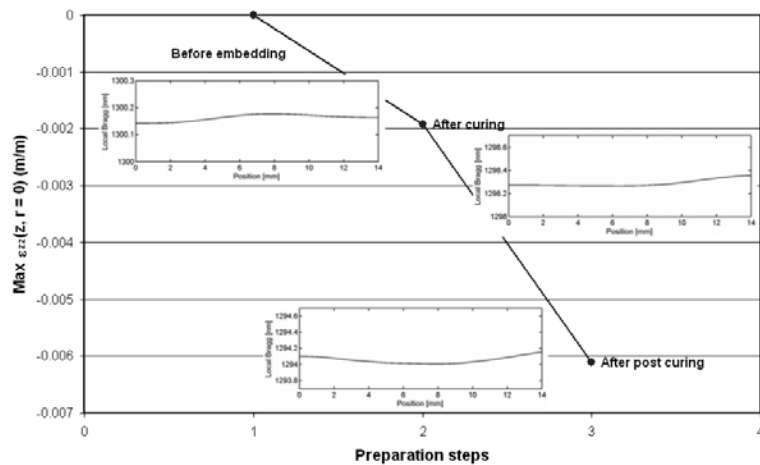


**Figure 9.28:** Evolution of the maximum strain value calculated during the specimen preparation. Since the grating length is 13 mm, the complete wavelength evolutions along the gratings are presented in the insets of the figure. Notice that a practically constant distribution of wavelength corresponds to a constant strain in the central region of the specimen.

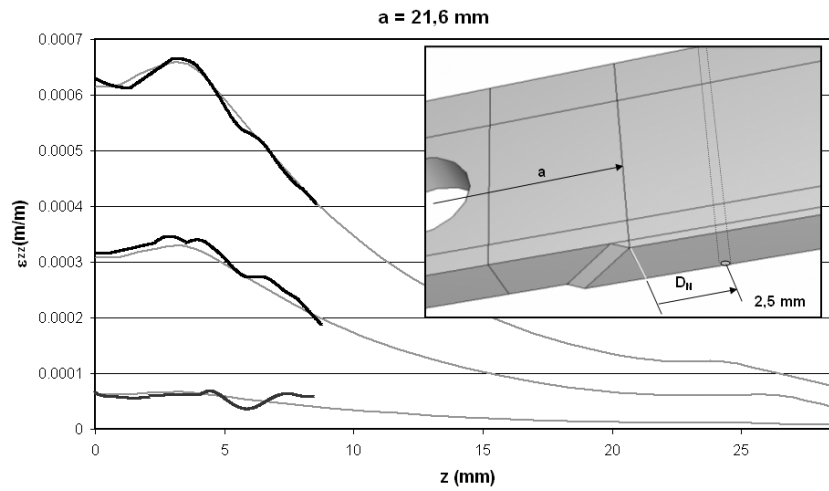


**Figure 9.29:** Comparison between the experimental (bold lines) and numerical (normal lines) strain distributions along the axial direction  $z$  (i.e. along the core of the fiber) for a crack length  $a$  of 21.6 mm measured by a 13-mm-long-grating. Each curve refers to a given applied load: 10 N (lower curves) 50 N (in the middle) and 100 N (upper curves).

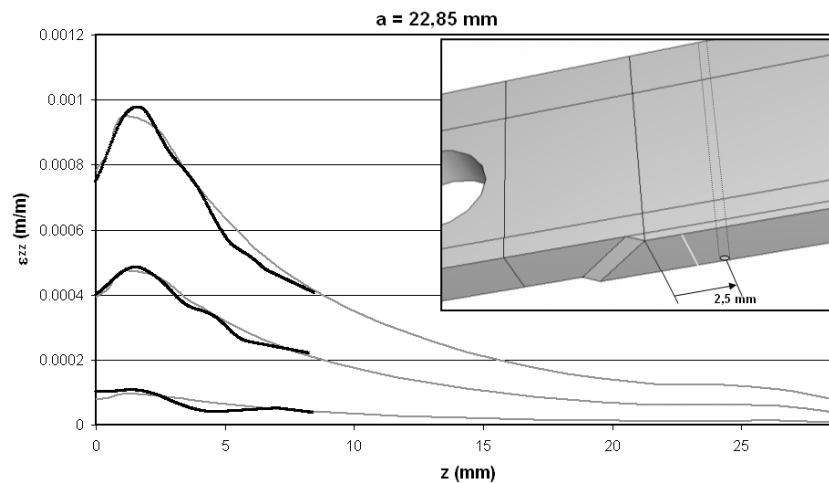


**Figure 9.30:** Comparison between the experimental (bold lines) and numerical (normal lines) strain distributions along the axial direction  $z$  (i.e. along the core of the fiber) for a crack length  $a$  of 22,85 mm measured by a 13-mm-long-grating. Each curve refers to a given applied load: 10 N (lower curves) 50 N (in the middle) and 100 N (upper curves).

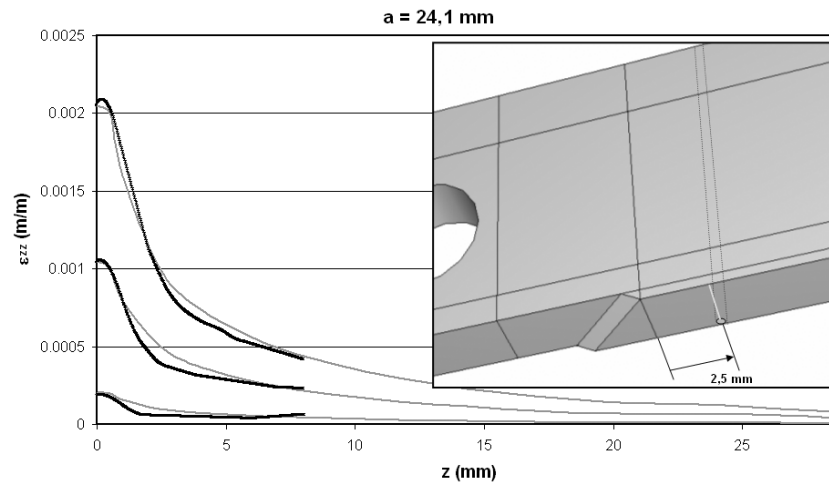


**Figure 9.31:** Comparison between the experimental (bold lines) and numerical (normal lines) strain distributions along the axial direction  $z$  (i.e. along the core of the fiber) for a crack length  $a$  of 24.1 mm measured by a 13-mm-long-grating. Each curve refers to a given applied load: 10 N (lower curves) 50 N (in the middle) and 100 N (upper curves).

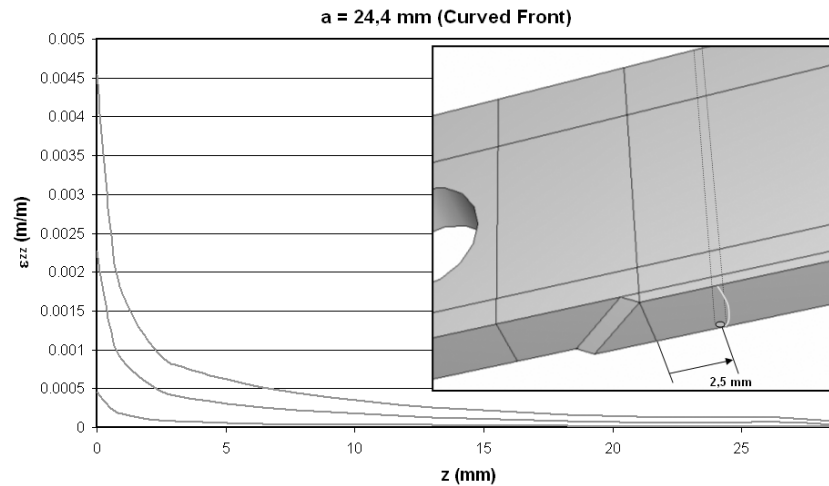


**Figure 9.32:** Numerical (normal lines) strain distributions along the axial direction  $z$  (i.e. along the core of the fiber) for a crack length  $a$  of 24.4 mm measured by a 13-mm-long-grating. Each curve refers to a given applied load: 10 N (lower curves) 50 N (in the middle) and 100 N (upper curves). This case was experimentally analyzed only by using a short grating but the entire distributions are reported for thoroughness. Let notice the exact form of the fracture front simulated by the model.



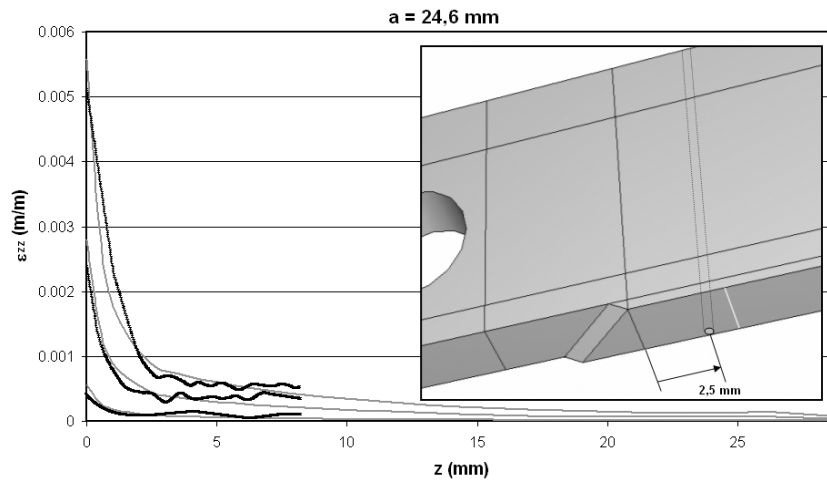


**Figure 9.33:** Comparison between the experimental (bold lines) and numerical (normal lines) strain distributions along the axial direction  $z$  (i.e. along the core of the fiber) for a crack length  $a$  of 24.6 mm measured by a 13-mm-long-grating. Each curve refers to a given applied load: 10 N (lower curves) 50 N (in the middle) and 100 N (upper curves).

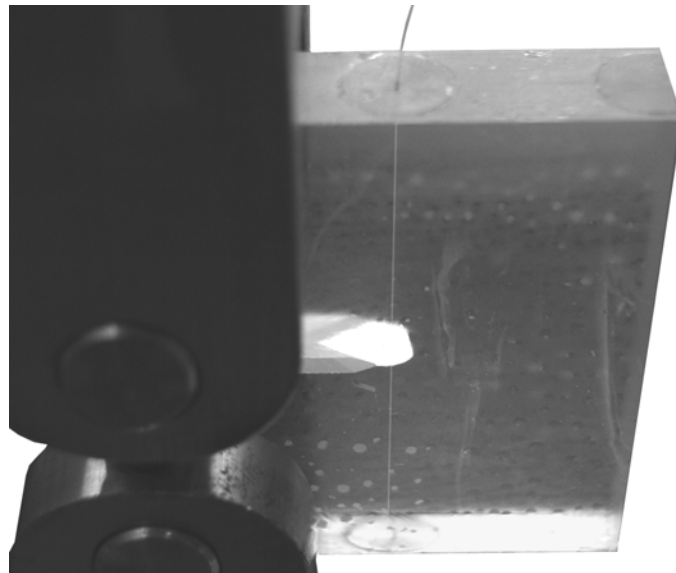


**Figure 9.34:** A photograph of a cracked compact tension specimen. The crack has exceeded the fiber and it works as a bridge between the two surfaces of the fracture. The bridging force along the fiber can be calculated using the deformation data plotted in Fig. 9.33.



# Chapter 10

## Summary and future work

From an experimental mechanics point of view, Bragg gratings are of great interest as embedded strain sensors for two main reasons: the first is that they can be used to carry out key experiments to address issues that are difficult or impossible to investigate with other means; the second is that they provide a practical sensing tool in structural monitoring applications. Both of these areas have been considered in this work on the use of FBG sensors.

### 10.1 Summary

Long gage fiber Bragg grating sensors and new Optical Low Coherence Reflectometry Technique are initially used to characterize the longitudinal evolution of the residual strains (stresses) along a reinforcing glass fiber included in a polymeric material during the manufacturing process without the need of any initial assumption. By combining this technique with the layer-peeling algorithm, the direct reconstruction of the optical period of the grating is possible and, this way, the strain distribution along the fiber is immediately retrieved without any a priori hypothesis on the strain profile. In particular, for given geometrical dimensions of the specimen (length  $L \geq 40mm$ ), a fourth order evolution function characterizes the distribution of stresses along the axial fiber direction. The form of the function has been determined from the distributed grating measurements. This is not the case when the inverse T-Matrix based approach is used to obtain the same results. In fact, since the complex coupling coefficient is not experimentally measured, it would be difficult to solve the problem of the uniqueness of the solution and directly calculate the local values of strain that really build-up along the sensor. The support of the FE method is then necessary to integrate the initial lack of information.

Since the FBG directly measures the deformation applied along its axis, the transversal evolution of stresses has been obtained by measuring the perturbations of the initial residual stress field as a consequence of the introduction of a series of circular deep cracks machined in the radial direction of the specimen. A modified version of the Crack Compliance Method to take into account the available distributed measurements of strain is thus proposed to retrieve

the initial residual stress profile present in the region of the crack plane before cutting. The new approach is more efficient because it allows the retrieval of the stress profile by only one crack, thus reducing the experimental errors that generally affect this technique. The important objective of the thesis to establish a reliable experimental method using FBG sensors in conjunction with other more traditional techniques to characterize the behavior of composites has thus been obtained.

The effect of a machined longitudinal crack has been also analyzed. The study revealed that no transversal effects are measured by the grating likely because of the fiber stiffness. Nevertheless, a small axial relaxation due to the bending effect which results from the loss of axisymmetry conditions of the cylindrical specimen was successfully measured.

For the purpose of the analysis, the effective volume reduction undergone by the epoxy matrix during the polymerization process is simulated via an equivalent thermo-elastic problem by introducing a shrinkage function  $S_m(r, z)$ . Though some differences (overall at the ends of the specimen) are present due to simplified assumptions (the variable separation hypothesis is likely valid only at the center of the specimen) a good correlation between experimental and FE results has been obtained. Moreover, the numerical predictions are found to be in good agreement compared with some representative analytical models proposed in literature.

In the final part of the thesis, two feasibility studies have been carried out using FBG sensors in structural-monitoring inspired applications. In the first case, an FBG glued on the surface of a CT-specimen was used to inspect and to detect the effects of the presence of a natural crack propagated during a fatigue test. In the second case, the Bragg grating was directly embedded into the specimen, providing fundamental information on the study of the stress field around a crack tip as it interacts with the reinforcing sensing fiber. A simple theoretical approach based on the beam theory has been used to model these experiments. The main goal of the model is the possibility to monitor the fracture length starting from the FBG strain measurements thus realizing a first realistic step towards the development of an embedded sensor based technique for fiber-reinforced composites that are self-evaluating.

These results demonstrate that, accompanied by an appropriate model, the internal strain measurements from embedded FBG sensors, can become a powerful technique to characterize deformation and fracture behavior at various scales of polymeric composite materials.

## 10.2 Perspectives

Future work can be carried out on various aspects of the research presented herein. The OLCR is a very powerful technique for measuring strain distributions with high resolution in static configurations, but is not practical for dynamic measurements. Efforts have to be made in this direction to improve the existing optical techniques or to find new experimental methods.

From the point of view of FBG signal interpretation, some questions remain open relative to their response to non-uniform axial strain fields (very high gradient) and transversal non-homogeneous strains (birefringence effects). Ideally, a general model including both effects needs to be developed and systematically applied to interpret measured Bragg data from embedded sensors. Nevertheless, the present work has shown that an adequate model of the stress transfer from the host material to the embedded sensor is required in all cases. In fact, if such a model is available, experimental results can be compared and validated with numerical predictions.

Fiber optic sensor reliability in the long term is another open question, particularly due to applications in severe environments and loading conditions, such as impact-induced structural damage or high-frequency cyclic loading. There are several failure modes of the sensors themselves (e.g. micro-bending along the optical fiber, degradation of the fiber properties due to chemical reactions or moisture, etc) which could be incorrectly interpreted as a failure of the host material and must therefore be considered if the sensor is to provide reliable indications on the composite's state of stress. It may be particularly important to account for micro-bending effects in future work on bridging forces in actual composite structures. Despite these challenges the methodology proposed in this thesis opens a great number of possibilities in the field of fracture mechanics.

In the case of real composite applications, the measurements obtained from an FBG when it is embedded close to other reinforcements would be useful in order to detect and to characterize fiber interaction and to optimize the composite structure. This could be used as a starting point for the generalization of real composites, where the reinforcing fibers are generally smaller and have a higher volume fraction.

Finally, in the case of adaptive composites or self-evaluating materials, further progress towards model smart structures can be made. The continuous monitoring of distributed strains could be used to control the reactions within a system in order to maintain the internal stresses at a chosen level thus avoiding catastrophic and dangerous failures.



## Appendix A

# The T-Matrix reconstruction based approach for the analysis of other distributions of strain

As well explained in Chapter 3 the main problem in using the T-Matrix approach is represented by the need of a priori knowledge of the complex coupling coefficient along the grating length. This in practice corresponds to the knowledge of the local Bragg wavelength or the strain distribution along the sensor. On the contrary, when all the data are given both the possible reconstruction methods result very efficient and not appreciable differences can be evidenced in the results. In this section the analysis via T-Matrix of the grating response in the case of the cylindrical specimen with a circular radial crack and in the case of the CT-specimen is proposed, but in order to show the advantages of the direct OLCR based method only the physical parameters are provided to the model.

### The cylindrical specimen with a radial circular crack

The reflected spectrum from a grating embedded in cylindrical specimen where a circular crack of 12 mm depth is machined in radial direction is shown in Fig.A.1. Instead of using

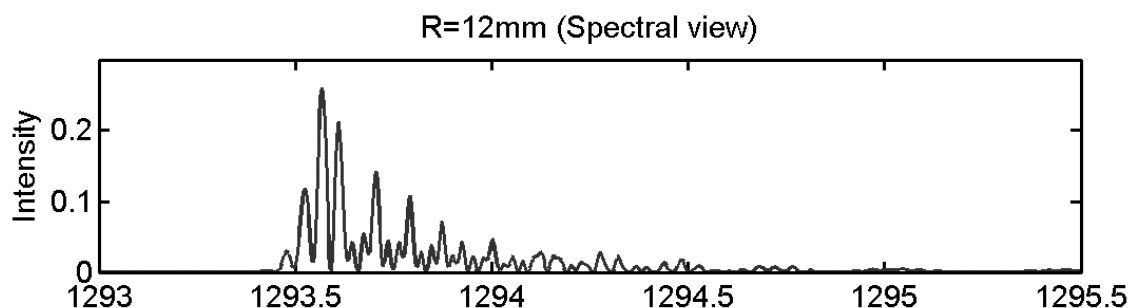


**Figure A.1:** Reflected spectrum from an FBG of 25-mm-length embedded in a cylindrical specimen with a machined circular crack of-12-mm depth.

the real distribution of local Bragg wavelength depicted in Fig.6.5 a Gaussian evolution is taken into account (FigA.2) This distribution is particularly interesting especially thanks to

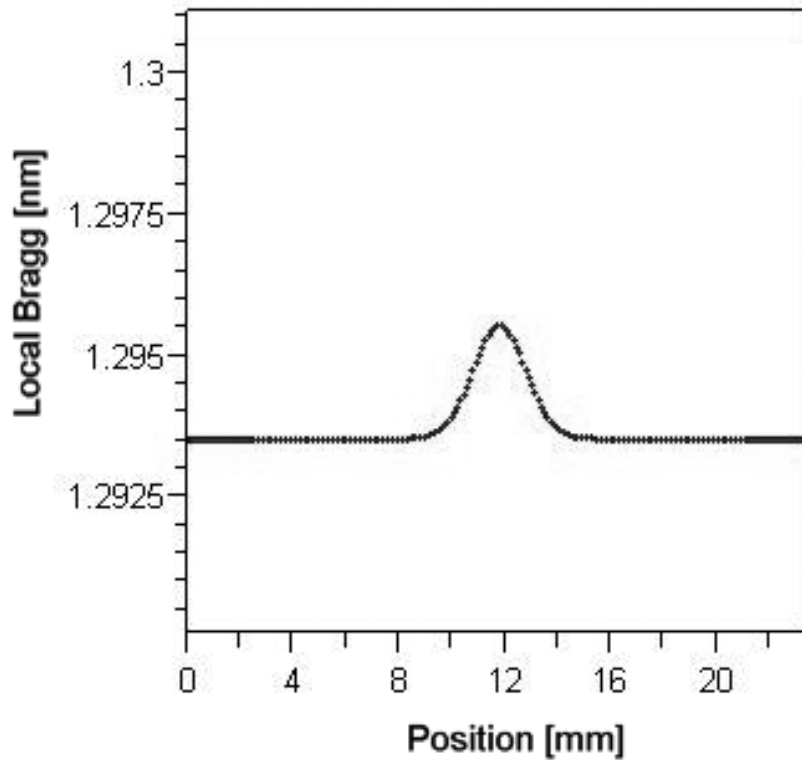


**Figure A.2:** *The Gaussian piecewise constant evolution chosen to represent a realistic distribution of the Bragg wavelength along the FBG. The center of the grating corresponds to the center of the specimen.*

the central peak that gives indications on the presence of regions with high gradient variations.

Though the curve in Fig.A.2 can be assumed realistic and not far from the real wavelength evolution (see Fig.6.5 for comparison), the reconstructed spectrum shows important differences when compared with the real one (Fig.A.3). This is probably due to the aforementioned high gradient zones, where the decomposition by piecewise constant functions is often difficult to correctly realize (e.g number  $N$  of sub-domains and determination of their amplitude  $\Delta$ ). As it easy to verify, the reconstructed spectrum only corresponds partially to the measured one, thus meaning that the chosen wavelength distribution correctly represents the real evolution only in certain regions of the grating. The same conclusion can be applied to the strain distribution obtained from the wavelength evolution by using Eq.3.2.4.

### **The Compact Tension specimen**

More difficult results the reconstruction process in the case of the cracked CT-specimen reinforced with an embedded optical fiber (see Chapter 9). When the crack length  $a$  is equal to



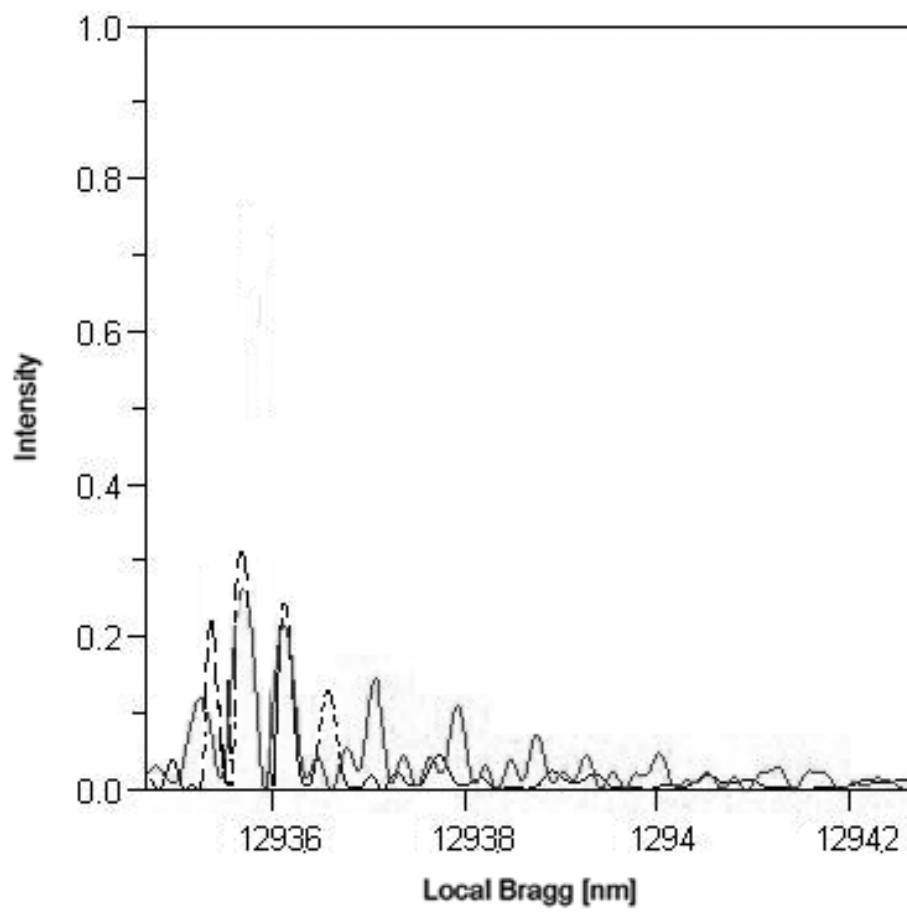


**Figure A.3:** Comparison between the measured spectrum (grey line) and the reconstructed spectrum (dashed line) via the T-Matrix approach in the case of the cylinder with a circular radial crack.

24.1 mm and the applied load is 50N the reflected spectrum and the local Bragg distribution correctly measured via the OLCR have the following form:

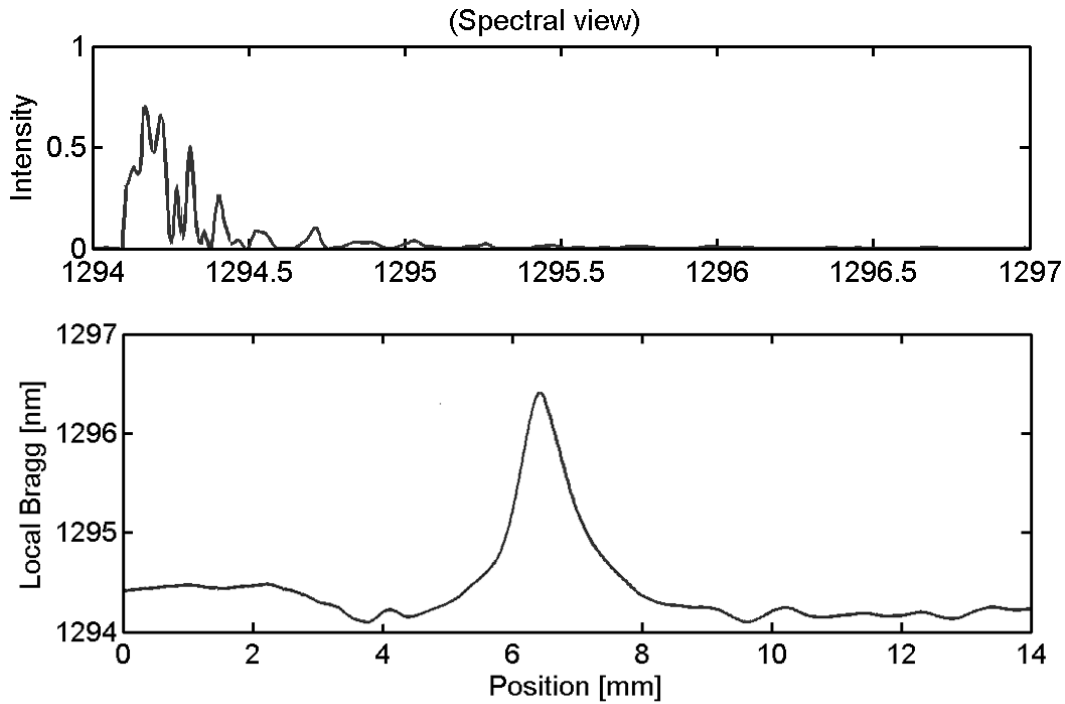


**Figure A.4:** *Spectrum and local Bragg wavelength evolution retrieved via the OLCR in the case of the cracked CT-specimen reinforced with an embedded optical fiber.*

Also in this case, we choose a Gaussian evolution to describe the wavelength distribution along the grating length for which the piecewise constant approximating function is shown in Fig.A.5. This is a typical case where the approximating function presented in Fig.A.5 could be obtained by using the FE method. In fact, by simulating the CT-specimen geometry and the load configuration, the FE model provides the distribution of strain along the fiber core which can be translated in wavelength distribution by using Eq.3.2.4. This distribution is then used as the input data for the T-Matrix reconstruction process to simulate the reflected spectrum by the FBG sensor. Nevertheless, due to the highly pronounced peak at the center of the distribution, the simulated spectrum presents important differences respect to the simulated one (Fig.A.6).

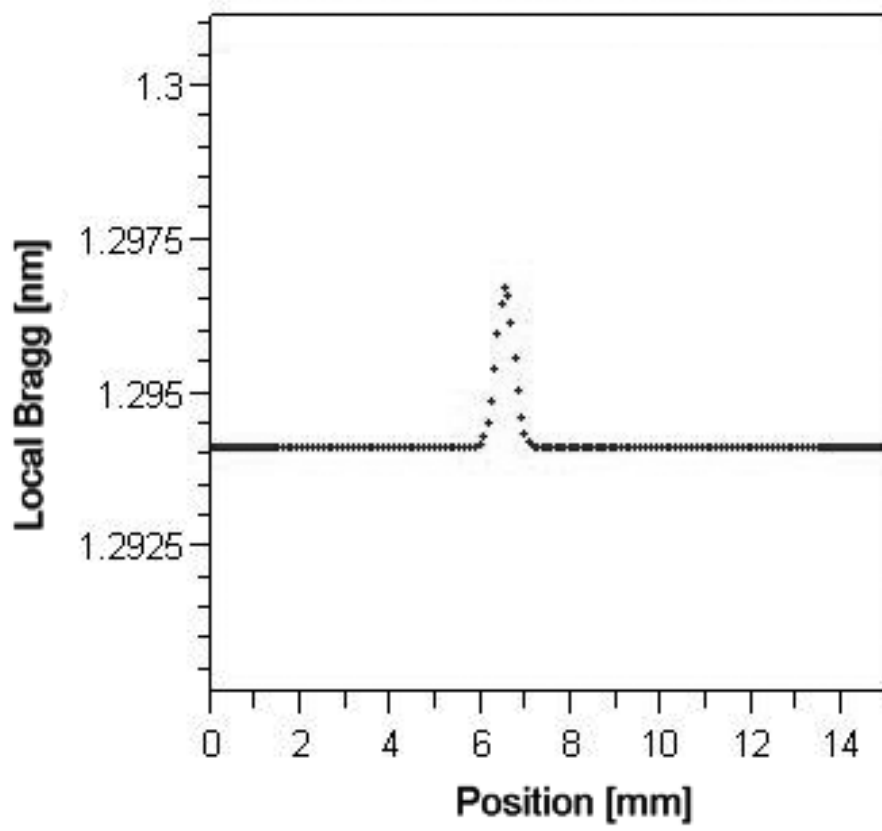


**Figure A.5:** Piecewise constant function used to approximate the local Bragg wavelength evolution along the core of the embedded optical fiber.

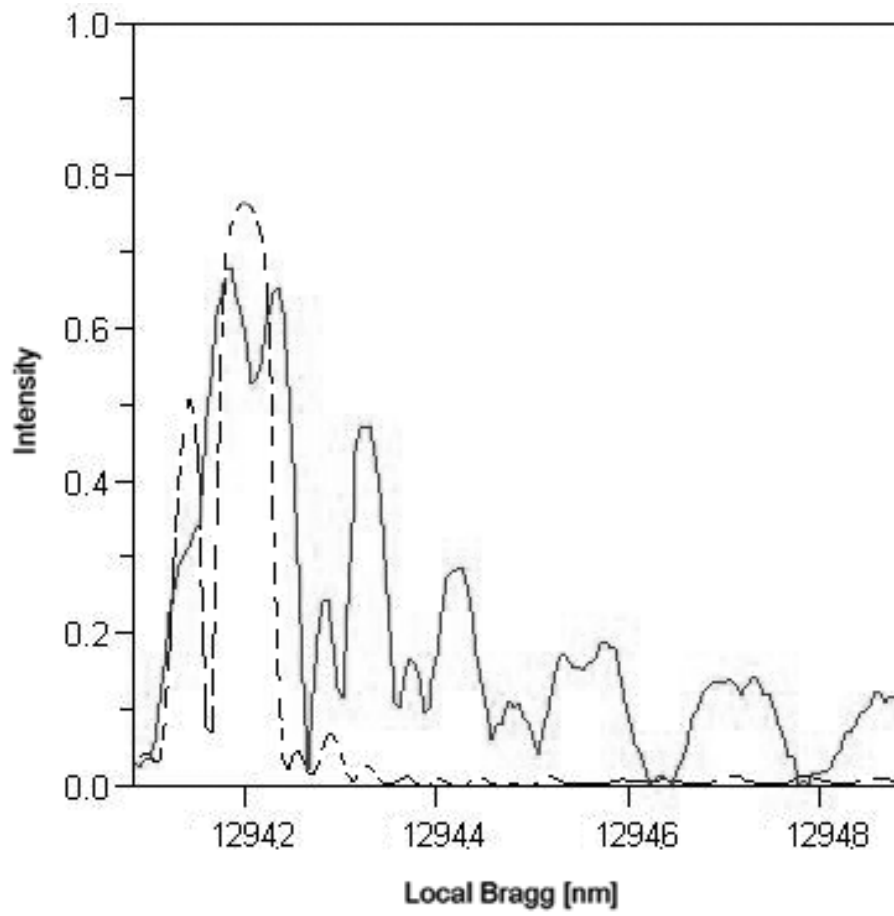


**Figure A.6:** Comparison between the real measured spectrum (grey line) and the simulated one (dashed line) via the T-Matrix reconstruction method.

# Bibliography

- [1] *Annual Book of ASTM Standards. Designation: D 695-96.* ASTM International, 100 Barr Harbor Drive, West Conshohocken, U.S.A., 1996.
- [2] *Dow Stewardship Manual.* Dow Chemical Corporation, 4502 Ashman Street, P.O. Box 1206, Midland, MI 48642, U.S.A., 2003.
- [3] E. Acerbi. *Metodi e strumenti di misura.* Città Studi Edizioni, Milano, 1994.
- [4] T.L. Anderson. *Fracture Mechanics.* CRC Press, Boston, 2000.
- [5] N.K. Anifantis, P.A. Kakavas, and G.C. Papanicolaou. Thermal stress concentration due to imperfect adhesion in fiber-reinforced composites. *Composites Science and Technologies*, 57(6):687–697, 1997.
- [6] D.R. Askeland. *The Science and Engineering of Materials.* PWS Publishing Company, Boston, 1994.
- [7] J.A. Barnes and G.E. Byerly. Formation of residual stresses in laminated thermoplastic composites. *Composites Science and Technologies*, 51(4):479–494, 1994.
- [8] P. Bérest and V. Gérard. Remarques sur les contraintes résiduelles. *Comptes Rendus Mécanique*, 331:455–460, 2003.
- [9] M. Born and E. Wolf. *Principles of Optics.* Cambridge University Press, London, 7th. edition, 2001.
- [10] F. Bosia. *Internal Strain Measurements in Composite Laminate using Fibre Bragg Grating sensors.* Ph.d. thesis, EPFL, 2002.
- [11] J. Botsis. *Mechanics of fracture and fatigue.* Course Notes, EPFL, 1998.
- [12] B. Budiansky, A.G. Evans, and J.W. Hutchinson. Fiber-matrix debonding effects on cracking in aligned fiber ceramic composites. *Internal Journal of Solids and Structures*, 32(3-4):315–328, 1995.
- [13] B. Budiansky, J.W. Hutchinson, and A.G. Evans. Matrix fracture in fibre-reinforced ceramics. *Journal of the Mechanics and Physics of Solids*, 34(2):167–189, 1986.

- [14] H.F. Bueckner. A novel principle for the computation of stress intensity factor. *Zeitschrift für Angewandte Mathematik und Mechanik*, 50:529–546, 1970.
- [15] C.D. Butter and G.B. Hocker. Fibre optics and strain gauge. *Applied Optics*, 17(18):2867–2869, 1978.
- [16] P. Caldirola, M. Fonatnesi, and E. Sironi. *Elettromagnetismo*. Masson, Milano, 1993.
- [17] Y.S. Chai and Y.W. Mai. New analysis on the fiber push-out problem with interface roughness and thermal residual stresses. *Journal of Materials Science*, 36(8):2095–2104, 2001.
- [18] T. Chen, G.J. Dvorak, and Y. Benveniste. Stress fields in composites reinforced by coated cylindrically orthotropic fibers. *Mechanics of Materials*, 9:17–32, 1990.
- [19] T.W. Clyne and S.C. Gill. Sprayed coatings and their effects on interfacial adhesion. *Journal of Thermal Spray Technology*, 5(4):1–18, 1996.
- [20] F. Colpo, L. Humbert, P. Giaccari, and J. Botsis. Characterization of residual strains in an epoxy block by embedded fbg sensor and olcr technique. *Composites Part A: Applied Science and Manufacturing*, 2005.
- [21] B.D. Cullity. *Elements of X-Ray diffraction, 2nd edn.* Addison-Wesley, New York, 1978.
- [22] I.M. Daniel and O. Ishai. *Engineering Mechanics of Composites Materials*. Oxford University Press, New York, 1994.
- [23] W. Du, X.M. Tao, H.Y. Tam, and C.L. Choy. Fundamentals and applications of optical fiber bragg grating sensors to textile structural composites. *Composite Structures*, 42:217–229, 1998.
- [24] T. Erdogan. Fiber grating spectra. *Journal of Lightwave Technology*, 15(8):1277–1294, 1997.
- [25] J.D. Eshelby. The determination of the elastic field of an ellipsoidal inclusion, and related problems. *Proceeding of the Royal Society of London. Series A, Mathematical and Physical Sciences*, 241(1226):376–396, 1957.
- [26] J.D. Eshelby. The elastic field outside an ellipsoidal inclusion. *Proceeding of the Royal Society of London. Series A, Mathematical and Physical Sciences*, 252(1271):561–569, 1959.
- [27] T. Fett and D. Munz. *Stress Intensity Factor and Weight Functions*. Computational Mechanics Publications, Southampton, U.K., 1997.
- [28] I. Finnie and W. Cheng. Residual stress measurement by introduction of slots or cracks. In H. Nisitani, M.H. Aliabadi, S.I. Nishida, and J.J. Cartwright, editors, *Localized Damage: Computer Aided Assessment and Control*. Computational Mechanics Publications Southampton, Boston, 1996.

- [29] I. Finnie and W. Cheng. A summary of past contribution on residual stresses. *Material Science Forum*, 404-407:509–514, 2002.
- [30] S. Finnie, W. Cheng, I. Finnie, J.M. Drezet, and M. Gremaud. The computation and measurement of residual stresses in laser deposited layers. *Journal of Engineering Materials and Technology*, 125:302–309, 2003.
- [31] J.F. Flavenot. *Handbook of measurement of residual stresses*. J. Lu, Lilburn, GA, 1996.
- [32] E.S. Folias. On the stress singularities at the intersection of a cylindrical inclusion with the free surface of a plate. *International Journal of Fracture*, 39:25–34, 1988.
- [33] E.S. Folias, M. Hohn, and T. Nicholas. Predicting crack initiation in composites material systems due to a thermal expansion mismatch. *International Journal of Fracture*, 93(1-4):335–349, 1998.
- [34] P. Giaccari. *Fiber Bragg grating characterization by optical low-coherence reflectometry and sensing applications*. Ph.d. thesis, EPFL, 2003.
- [35] P. Giaccari, G.R. Dunkel, L. Humbert, J. Botsis, H. G. Limberger, and R. P. Salathe. On a direct determination of non-uniform internal strain fields using fibre bragg gratings. *Smart Materials and Structures*, 14, 2005.
- [36] P. Giaccari, H. G. Limberger, and R. P. Salathe. Local coupling-coefficient characterization in fiber bragg gratings. *Optics Letters*, 28(8):598–600, 2003.
- [37] K.T.L. Grattan and T. Sun. Fiber optic sensor technology: an overview. *Sensors and Actuators*, 82:40–61, 2000.
- [38] Hibbitt, Karlsson, and Sorensen. *Abaqus user's manual, Version 6.5*. Hibbitt, Karlsson & Sorensen, Inc., U.S.A., 2004.
- [39] K.O. Hill, F. Fujii, D.C. Johnson, and B.S. Kawasaki. Photosensitivity on optical fibre waveguides; application to reflection and filter fabrication. *Applied Physics Letters*, 32, 1978.
- [40] K.O. Hill and G. Metz. Fibre bragg grating technology: fundamentals and overview. *Journal of Lightwave Technology*, 15(8):1263–1276, 1997.
- [41] K.R. Hiremath, R. Stoffer, and M. Hammer. Coupled mode theory and fdtd simulations of the coupling between bent and straight optical waveguides. In *IEEE/LEOS Symposium*, Benelux, 2003.
- [42] T.J.R. Hughes. *The Finite Element Method*. Dover Publications Inc., New York, 2000.
- [43] D. Hull and T.W. Clyne. *An introduction to composite materials*. Cambridge Solid State Science Series, second edition, 1996.

- [44] L. Humbert, J. Botsis, and F. Bosia. Modelling of residual stresses acting on a low-birefringence fibre bragg grating sensor embedded in an epoxy matrix. *in SPIE 10th. Annual International Symposium on Smart Structures and Materials*, March 2003.
- [45] C.J. Humphreys and E.G. Bithell. *Electron diffraction techniques*. Oxford University Press, Oxford, 1992.
- [46] I.S. Jones and G. Rothwell. Reference stress intensity factor with application to weight functions for internal circumferential cracks in cylinders. *Engineering Fracture Mechanics*, 68:435–454, 2001.
- [47] S.P. Kovalev, P. Miranzo, and M.I. Osendi. Finite element simulation of thermal residual stresses in joining ceramics with thin metal interlayers. *Journal of American Ceramic Society*, 81(9):2342–2348, 1998.
- [48] J.M. Lopez-Liguera. *Handbook of optical fiber sensing technology*. Wiley, New York, 2002.
- [49] J. Mackerle. Fem and bem analysis and modelling of residual stresses: a bibliography (1998-1999). *Finite Element in Analysis and Design*, 37(3):253–262, 2001.
- [50] C. Mattheck, P. Morawietz, and D. Munz. Stress intensity factors for sickle-shaped cracks in cylindrical bars. *International Journal of Fracture*, 7(1):45–47, 1985.
- [51] A.S. Maxwell and A. Turnbull. Measurement of residual stress in engineering plastics using the hole-drilling technique. *Polymer Testing*, 22(2):231–233, 2003.
- [52] L.N. McCartney and P.M. Cooper. A new method of analysing fatigue crack propagation data. *Engineering Fracture Mechanics*, 9:273–290, 1977.
- [53] R.M. Measures. *Structural Monitoring with fibre optic technology*. Academic Press, 2001.
- [54] T. Meshii and W. Katsuhiko. Stress intensity factor for a circumferential crack in a finite-length thin-walled cylinder under an arbitrary biquadratic stress distribution on the crack surfaces. *Engineering Fracture Mechanics*, 68:975–986, 2001.
- [55] A. Migliacci and F. Mola. *Progetto agli stati limite delle strutture in cemento armato*. CEA, Milano, 1985.
- [56] Y. Mikata and M. Taya. Stress field in a coated continuous fiber composite subjected to thermo-mechanical loading. *Journal of Composite Materials*, 19:554–579, 1985.
- [57] T.M. Mower and A.S. Argon. Experimental investigation of crack trapping in brittle heterogeneous solids. *Mechanics of Materials*, 19:343–364, 1995.
- [58] P.C. Paris. *The mechanics of fracture propagation and solutions to fracture arrester problems*. Document D2-2195, The Boeing Company, 1957.



- [59] D.M. Parks. A stiffness derivative finite element technique for determination of crack tip stress intensity factors. *International Journal of Fracture*, 10:487–502, 1974.
- [60] M.W. Paterson and J.R. White. Layer removal analysis of residual stress: Part 2. a new procedure for polymers mouldings with depth varying young's modulus. *Journal of Materials Science*, 24(10):3521–3528, 1989.
- [61] K. Peters, M. Studer, and J. Botsis. Embedded optical optical fibre bragg grating sensor in a non uniform strain field: measurements and simulations. *Experimental Mechanics*, 41:19–28, 2001.
- [62] M.B. Prime. Measuring residual stress and the corresponding stress intensity factor in compact tension specimen. *Fatigue Fracture Engineering and Material Structures*, 22:195–204, 1999.
- [63] M.B. Prime. Residual stress measurement by successive extension of a slot: the crack compliance method. *Applied Mechanics Review*, 52:75–96, 1999.
- [64] M.B. Prime and M.R. Hill. Residual stress, stress relief and inhomogeneity in aluminium plate. *Scripta Materialia*, 46(1):77–82, 2002.
- [65] M.B. Prime, V.C. Prantil, P. Rangaswamy, and F.P. Garcia. Residual stress measurements and prediction in an hardened steel ring. *Material Science Forum*, 347-349:223–228, 2000.
- [66] M.Y. Quek. Analysis of residual stresses in a single fibre-matrix composite. *International Journal of Adhesion and Adhesives*, 24(5):379–388, 2004.
- [67] Y.J. Rao. In-fibre bragg grating sensor. *Measurements Science and Technology*, 8:355–375, 1997.
- [68] J.R. Rice. Some remarks on elastic crack-tip stress fields. *International Journal of Solids and Structures*, 8:751–758, 1972.
- [69] F.K. Richtmyer, E.H. Kennard, and J.N. Cooper. *Introduction to modern physics*. Tata McGraw-Hill, NewDelhi, 6th. edition, 1996.
- [70] S. Rosati. *Fisica Generale*. Casa Editrice Ambrosiana Milano, Milano, 2-nd. edition, 1998.
- [71] V.P. Shchepinov and V.S. Pisarev. *Strain and Stress Analysis by Holographic and Speckle Interferometry*. John Wiley & Sons, New York, 1996.
- [72] J. S. Sirkis. Unified approach to phase-strain-temperature models for smart structure interferometric optical fiber sensors. 1. development. *Optical Engineering*, 32(4):752–761, 1993.

- [73] J. Skaar, L. G. Wang, and T. Erdogan. On the synthesis of fiber bragg gratings by layer peeling. *Ieee Journal of Quantum Electronics*, 37(2):165–173, 2001.
- [74] A.W. Snyder and J.D. Love. *Optical Waveguide Theory*. Chapman & Hall, London New York, 1983.
- [75] M. Steinzig, G. Hayman, and M.B. Prime. Verification of a technique for holographic residual stress measurement. *Residual Stress Measurement and General Nondestructive Evaluation*, 429, 2001.
- [76] M.A. Stone, I.F. Schwartz, and H.D. Chandler. Residual stresses associated with post-cure shrinkage in grp tubes. *Composites Science and Technologies*, 57(1):47–54, 1997.
- [77] M. Studer. *Etude des forces pontantes dans un matériau composite á l'aide des réseaux de Bragg dans des fibres optiques*. Ph.d. thesis, EPFL (Switzerland), 2001.
- [78] A. Svandro. In-plane dynamic speckle interferometry: comparison between a combined speckle interferometry / speckle correlation and an update at the reference image. *Applied Optics*, 43(21):5381–5385, 1993.
- [79] H. Tada, P.C. Paris, and J.R. Irwing. *The Stress Analysis of Cracks Handbook*. ASME International, New York, 2000.
- [80] R.J. Van Steenkiste and G.S. Springer. *Strain and Temperature measurement with Fiber Optic Sensor*. Technomic Publishing Co. Inc., Lancaster, U.S.A., 1997.
- [81] I.V. Varfolomeyev. Weight function for external circumferential cracks in hollow cylinders subjected to axisymmetric opening mode. *Engineering Fracture Mechanics*, 60(3):333–339, 1998.
- [82] P.J. Withers and H.K.D.H. Bhadeshia. Free content residual stress. part ii: Nature and origins. *Material Science and Technology*, 10:366–375, 2001.
- [83] P.J. Withers and H.K.D.H. Bhadeshia. Residual stresses. part i: Measurements techniques. *Material Science and Technology*, 17:355–365, 2001.
- [84] G. Xu, A.F. Bower, and M. Ortiz. The influence of the crack trapping on the toughness of fiber reinforced composites. *Journal of Mechanics and Physics of Solids*, 46(10):1815–1833, 1998.

# Curriculum Vitæ

*Born:* 13-01-1975, Cittiglio (Varese, Italy)  
*Nationality:* Italian  
*Address:* Via Carcano 15, 21100 Varese (Italy)  
*Telephone:* +39 0332 834630, +41 693 2996  
*E-mail:* fabiano.colpo@epfl.ch

## ***Qualifications:***

- Laurea di Dottore in Fisica, from University of Milan (Italy).
- Scientific Maturity, from Liceo Scientifico Statale di Gavirate (Varese, Italy).

## ***Post-graduate experiences:***

- June 2002-present: Ph.D. student in mechanical engineering. Thesis topic: *Residual stress characterization in a single fiber composite specimen by using FBG sensors and OLCR Technique.*
- January 2002-June 2002 Professor of mathematics and physics at the Technical Secondary School of Informatics (Varese).
- March 2001-January 2002: Military service in the Special Corp of V.A.M. of the Italian Air Force. Dismissed with merit and mention.
- November 2000-March 2001: Oracle Database Programmer. Nous Informatics (Milan).
- December 2000-June 2002: Professor of mathematics and physics at the European Center for the University Courses Preparation (CEPU) (Varese).

## ***Further education:***

- December 2005: Course on Extended Finite Element Method (X-FEM), EPFL.
- May 2004: Course on LabView Programming, EPFL.
- January-May 2003: Course on Fracture Mechanics, EPFL.
- January-May 2003: Course on Computational Solid Mechanics, EPFL.
- October-January 2003: Course on Mechanics of Composite Materials, EPFL.

- December 2002: Course on LabView Imaq Vision Builder, EPFL.
- September-October 2001: European Diploma in Informatics, Head Quarter of the Italian Air Force, Milan.
- April 1997: Course on Radio-protection systems, University of Milan.

***Languages:***

- Italian mother language.
- Fluency in French.
- Good knowledge of English.

***Computer skills:***

- Extensive abilities ranging from finite-element analysis programs (Abaqus), to Mathematica, Matlab, and various Mac OS X and MS Windows software packages. Scientific programming in Fortran.
- Good knowledge of L<sup>A</sup>T<sub>E</sub>X language.
- Good knowledge of SQL / PL-SQL languages.

***Publications:***

*Journal papers*

- M. Giudici, F. Colpo, G.S. Ponzini, G. Parravicini. Calibration of groundwater recharge and hydraulic conductivity for the aquifer beneath the city of Milan (Italy). *Impact of Human Activity on Groundwater Dynamics*, 269: 43-50, 2001.
- J. Botsis, L. Humbert, F. Colpo. Embedded fiber Bragg grating sensor for internal strain characterization in polymeric material. *Optics and Lasers in Engineering*, 2005.
- F. Colpo, L. Humbert, P. Giaccari, J. Botsis. Characterization of residual strains in an epoxy block by embedded FBG sensor and OLCR technique. *Composites A*, 37(4): 652-661, 2005.

*Conference papers*

- J. Botsis, F. Colpo, L. Humbert. Residual strain characterization using an embedded FBG sensor: measurements and simulations. *Proceedings of Society of Plastic Engineering (ANTEC)*. Chicago, USA (2004).
- F. Colpo, G. Dunkel, L. Humbert, J. Botsis. Residual stress and debonding analysis using a Fiber Bragg Grating in a model composite specimen. *Proceedings of 12th Smart Structures and Materials International Symposium (SPIE)*. San Diego, USA (2005).

- F. Colpo, L. Humbert, J. Botsis. Residual stresses in a two phase concentric cylinder configuration. *Proceedings of 11th International Conference on Fracture (ICF)*. Torino, Italy (2005).

***Presentations and Conferences:***

- EUROMECH 453, International Conference on Composite Materials. Saint-Etienne, France (2003).
- ANTEC, Society of Plastic Engineering. Chicago, USA (2004).
- COMPTTEST 2004, Composites Testing and Model Identification. Bristol, UK (2004).
- SPIE's 12th Smart Structures and Materials International Symposium. San Diego, USA (2005).
- ICF, 11th International Conference on Fracture. Torino, Italy (2005).